**Joana Isabel Lázaro Almeida**

Mestre em Engenharia Biomédica

# Advances in solar-pumped laser efficiency and brightness

Dissertação para obtenção do Grau de Doutoramento
**Engenharia Física**

Orientador:  Dawei Liang,
Professor auxiliar,
Universidade Nova de Lisboa

Júri:

Presidente: Prof. Doutora Maria Adelaide de Almeida Pedro de Jesus
Arguente(s): Prof. Doutor Zhao Changming
Prof. Doutor Gonçalo Nuno Marmelo Foito Figueira
Vogais:  Prof. Doutor José Luís Campos de Oliveira Santos
Prof. Doutora Maria Adelaide de Almeida Pedro de Jesus
Prof. Doutor Dawei Liang
Prof. Doutor Pedro Manuel Cardoso Vieira

**FCt** FACULDADE DE
CIÊNCIAS E TECNOLOGIA
UNIVERSIDADE NOVA DE LISBOA

**Setembro, 2017**

**Advances in solar-pumped laser efficiency and brightness**

# ACKNOWLEDGEMENTS

# ABSTRACT

Advances in both solar-pumped laser efficiency and brightness are herein presented. Several solar laser prototypes with both end-side-pumping and side-pumping configurations were studied and developed to efficiently pump small diameter Nd:YAG laser rods, leading to substantial increase in solar laser collection efficiency and brightness, which have gained international recognitions.

All the design parameters were optimized in ZEMAX$^©$ non-sequential ray-tracing software. LASCAD$^©$ laser cavity analysis software was then used to optimize the laser resonator parameters. Based on the numerically optimization of the solar laser system, the solar laser prototypes were designed and built in Lisbon. Solar energy collection and concentration were achieved through the PROMES-CNRS heliostat-parabolic system, NOVA Fresnel lens system, and the recently new NOVA heliostat-parabolic system. Measurements of the solar input / laser output performance, beam quality $M^2$ factors, and laser beam profiles for both multimode and fundamental mode regime were performed and compared with that of the numerical results.

13.9 W/m$^2$ solar laser collection efficiency was achieved in 2013, through PROMES heliostat-parabolic mirror system, by end-side-pumping a 5 mm diameter, 25 mm length Nd:YAG laser rod. This result was further increased to 21.1 W/m$^2$, in 2015, within the same solar facility. In 2016, 25 W/m$^2$ collection efficiency was reported, by end-side-pumping a thinner laser rod through NOVA heliostat-parabolic mirror system. In addition to the enhancement of solar laser collection efficiency, the thermal performance of end-side-pumped solar laser was also substantially improved. In 2017, record solar laser collection efficiency of 31.5 W/m$^2$ was reported by end-side-pumping a 4 mm diameter, 35 mm length Nd:YAG laser rod in PROMES-CNRS heliostat-parabolic mirror system. Also, record slope efficiency of 8.9% was achieved.

A substantial progress in solar laser beam brightness with Fresnel lens was reported in 2013, through the first TEM$_{00}$-mode solar laser. 1.9 W solar laser brightness was registered, being 6.6 times more than the previous record. The adoption of an asymmetric laser resonator, for maximum extraction of TEM$_{00}$-mode solar laser, was also essential for improving significantly the solar laser brightness. By side-pumping a 3 mm diameter, 30 mm length Nd:YAG rod with a double-stage rectangular light guide / 2D-CPC concentrator, 4.0 W solar laser brightness was reported in 2015, doubling the previous record with Fresnel lens. TEM$_{00}$-mode solar laser collection efficiency of 4.0 W/m$^2$ was obtained by side-pumping a Nd:YAG grooved rod in 2016. Most recently, by end-side-pumping a 4 mm diameter, 35 mm length, Nd:YAG rod, the TEM$_{00}$ mode solar laser collection efficiency was almost doubled, reaching 7.9 W/m$^2$. Record-high solar laser brightness of 6.5 W was also achieved.

Advances in solar laser beam stability were also achieved by developing sculptured twisted light guides for efficient uniform redistribution of pump light into a thin and long laser rod. In addition to this, we were also able to demonstrate the first emission of doughnut shaped solar laser beam, which may widen the applications areas of solar-pumped lasers.

The research efforts performed during this work for enhancing both solar laser efficiency and beam brightness are explained. Experimental results are discussed and future suggestions are proposed.

# RESUMO

Nesta dissertação são apresentados os avanços na eficiência e brilho de laser bombeado por luz solar. Vários protótipos de laser solar, com configurações de bombeamento longitudinal e lateral, foram estudados e desenvolvidos para bombear eficientemente cilindros de Nd:YAG de pequeno diâmetro, levando a um aumento substancial da eficiência de colecção e brilho de laser solar, tendo ganho reconhecimento internacional.

Os parâmetros do desenho dos protótipos foram optimizados no software de traçado de raios não-sequencial ZEMAX$^©$. Por sua vez, os parâmetros da cavidade de ressonância foram optimizados pelo software de análise de cavidade laser LASCAD$^©$. Com base na optimização numérica do sistema de laser solar, os protótipos foram então projectados e construidos. Para colectar e concentrar a energia solar para bombeamento foram utilizados os sistemas: heliostato - espelho parabólico de PROMES-CNRS, lente de Fresnel da NOVA, e heliostato - espelho parabólico da NOVA, recentemente construído. Em termos experimentais, foram efectuadas medições do desempenho da potência de laser em função da potência de bombeamento, factores $M^2$ de qualidade do feixe laser, e perfil do feixe laser, em regime multimodo e de modo fundamental. As medições experimentais desenvolvidas foram também comparadas com os resultados numéricos.

Laser solar com eficiência de coleção de 13.9 W/m$^2$ foi conseguido em 2013, utilizando uma cavidade laser com configuração de bombeamento longitudinal - lateral para bombear um cilindro de Nd:YAG com 5 mm de diâmetro e 25 mm de comprimento, no sistema de heliostato - espelho parabólico de PROMES-CNRS. Este resultado foi posteriormente melhorado para 21.1 W/m$^2$, em 2015, na mesma instalação de energia solar. Em 2016, 25 W/m$^2$ de eficiência de coleção foi registado, utilizando uma cavidade laser com configuração de bombeamento longitudinal - lateral para bombear um cilindro fino, no sistema heliostato - espelho parabólico da NOVA. Além do aumento da eficiência de coleção, o desempenho térmico do laser solar com este tipo de configuração foi melhorado substancialmente. Em 2017, foi conseguida uma eficiência de coleção recorde de 31.5 W/m$^2$, através do bombeamento longitudinal - lateral de um cilindro de Nd:YAG de 4 mm de diâmetro e 35 mm de comprimento, no sistema de heliostato - espelho parabólico de PROMES-CNRS. Foi também registada uma eficiência de declive recorde de 8.9%.

Em 2013, foi conseguido um progresso substancial em brilho de laser solar com lente de Fresnel, através do primeiro laser solar de modo TEM$_{00}$. 1.9 W de brilho de laser solar, 6.6 vezes maior que o recorde anterior, foi registado. A utilização de cavidade de ressonância assimétrica para máxima extracção de laser de modo TEM$_{00}$ foi também essencial para melhorar significativamente o brilho de laser solar. Através do bombeamento lateral de um cilindro de Nd:YAG com 3 mm de diâmetro e 30 mm de comprimento, foi registado 4.0 W em brilho de laser, em 2015, duplicando o recorde anterior com lente de Fresnel. Em 2016, foi obtido um record de 4.0 W/m$^2$ em eficiência de coleção de laser solar de modo TEM$_{00}$, através do bombeamento lateral de um cilindro de Nd:YAG. Mais recentemente, ao bombear lateralmente um cilindro de Nd:YAG de 4 mm de diâmetro e 35 mm de comprimento, a eficiência de coleção de laser solar de modo TEM$_{00}$ foi quase duplicada, atingindo 7.9 W/m$^2$. Recorde em brilho de laser solar de 6.5 W foi também obtido.

Os avanços na estabilidade de laser solar foram também obtidos com a produção de guias de luz torcidas para uma redistribuição uniforme e eficiente no bombeamento de um cilindro de laser fino

e longo. Foi também possível realizar a primeira emissão de laser solar em forma de donut, o que pode alargar as áreas de aplicação dos lasers bombeados por luz solar.

Nesta dissertação, é abordado o trabalho desenvolvido para aumentar a eficiência e brilho do feixe de laser solar. Os resultados experimentais são debatidos e propostas futuras para o melhoramento do desempenho do laser solar são também sugeridas.

# CONTENTS

XIII

# LIST OF FIGURES

XVII

XVIII

# LIST OF TABLES

XXII

# LIST OF PUBLICATIONS

## PUBLICATIONS INCLUDED IN THE PHD THESIS

This PhD thesis is based on the following publications in peer-reviewed journals:

I.     Mehellou, S., Liang, D., <u>Almeida, J</u>., Bouadjemine, R., Vistas, C. R., Guillot, E. Rehouma, F. (2017) Stable solar-pumped $TEM_{00}$-mode 1064 nm laser emission by a monolithic fused silica twisted light guide. *Sol. Energ.***155**, 1059-1071. doi: 10.1016/j.solener.2017.07.048

II.    Bouadjemine, R., Liang, D., <u>Almeida, J.</u>, Mehellou, S., Vistas, C. R., Kellou, A., Guillot, E.,(2017) Stable $TEM_{00}$-mode Nd:YAG solar laser operation by a twisted fused silica light-guide. *Opt. Laser Tech.* **97**, 1-11. doi:10.1016/j.optlastec.2017.06.003

III.   Liang, D., <u>Almeida, J.</u>, Vistas, C. R., Guillot, E. (2017) Solar-pumped NdYAG laser with 31.5 $W/m^2$ multimode and 7.9 $W/m^2$ $TEM_{00}$-mode collection efficiencies. *Sol. Energ. Mat. Sol. Cells* **159**, 435-439. doi:10.1016/j.solmat.2016.09.048

IV.   Liang, D., <u>Almeida, J.</u>, Vistas, C. R. (2016) 25 $W/m^2$ collection efficiency solar-pumped Nd:YAG laser by a heliostat-parabolic mirror system. *Appl. Opt.* **55**, 7712-7717. doi:10.1364/AO.55.007712

V.    Vistas, C. R., Liang, D., <u>Almeida, J.</u>, Guillot, E. (2016) $TEM_{00}$ mode Nd:YAG solar laser by side-pumping a grooved rod. *Opt. Commun.* **366**, 50-56. doi:10.1016/j.optcom.2015.12.038

VI.   Liang, D., <u>Almeida, J.</u>, Vistas, C. R., Oliveira, M., Gonçalves, F., Guillot, E. (2016) High-efficiency solar-pumped $TEM_{00}$-mode Nd:YAG Laser. *Sol. Energ Mat. Sol. Cells* **145**, 397-402. doi:10.1016/j.solmat.2015.11.001

VII.  <u>Almeida, J.</u>, Liang, D., Vistas, C. R., Bouadjemine, R., Guillot, E. (2015) 5.5 W continuous-wave $TEM_{00}$-mode Nd:YAG solar laser by a light guide / 2V pump cavity. *Appl. Phys. B - Lasers and Optics* **121**, 473-482. doi:10.1007/s00340-015-6257-z

VIII. <u>Almeida, J.</u>, Liang, D., Vistas, C. R., Guillot, E. (2015) Highly efficient end-side-pumped Nd:YAG solar laser by a heliostat-parabolic mirror system. *Appl. Opt.* **54**, 1970-1977. doi:10.1364/AO.54.001970

IX.   Liang, D., <u>Almeida, J.</u>, Vistas, C. R., Guillot, E. (2015) Solar-pumped $TEM_{00}$ mode Nd:YAG laser by a heliostat-parabolic mirror system. *Sol. Energ. Mat. Sol. Cells* **134**, 305-308. doi:10.1016/j.solmat.2014.12.015

X.    <u>Almeida, J.</u>, Liang, D., Guillot, E., Hadi, Y. (2013) A 40W cw Nd:YAG solar laser pumped through a heliostat: a parabolic mirror system. *Laser Phys.* **23**, 065801. doi:10.1088/1054-660X/23/6/065801

XI.   Liang, D., <u>Almeida</u>, J. (2013) Solar-pumped $TEM_{00}$ mode Nd:YAG laser. *Opt. Express* **21**, 25107–25112. doi: 10.1364/OE.21.025107

Other relevant publications in peer-reviewed journals during the PhD project:

XII. Oliveira, M., Liang, D., <u>Almeida, J.</u>, Vistas, C. R., Gonçalves, F., Martins, R. (2016) A path to renewable Mg reduction from MgO by a continuous-wave Cr:Nd:YAG ceramic solar laser. *Sol. Energ. Mat. Sol. Cells* **155**, 430-435 doi:10.1016/j.solmat.2016.06.046

XIII. Vistas, C. R., Liang, D., <u>Almeida, J.</u> (2015) Solar-pumped $TEM_{00}$ mode laser simple design with a grooved Nd:YAG rod. *Sol. Energ.* **122**, 1325-1333. doi:10.1016/j.solener.2015.10.049

XIV. Liang, D., <u>Almeida, J.</u>, Vistas, C. R., Guillot, E. (2015) Solar-pumped $TEM_{00}$ mode Nd:YAG laser by a heliostat-parabolic mirror system. *Sol. Energ. Mat. Sol. Cells* **134**, 305-308. doi:10.1016/j.solmat.2014.12.015

XV. <u>Almeida, J.</u>, Liang, D. (2014) Design of $TEM_{00}$ mode side-pumped Nd:YAG solar laser. *Opt. Commun.* **333**, 219 225. doi:10.1016/j.optcom.2014.07.091

XVI. Liang, D., <u>Almeida, J.</u>, Garcia, D.(2014) Design of high-power, high-brightness Nd:YAG solar laser. *Appl. Opt.* **53**,1856-1861. doi:10.1364/AO.53.001856

XVII. Liang, D., <u>Almeida, J.</u> (2013) Multi Fresnel lenses pumping approach for improving high-power Nd:YAG solar laser beam quality. *Appl. Opt.* **52**, 5123-5132 doi:10.1364/AO.52.005123

XVIII. Liang, D., <u>Almeida, J.</u>, Guillot, E.(2013) Side-pumped continuous-wave Cr:Nd:YAG ceramic solar laser. *Appl. Phys. B - Lasers and Optics* **111**, 305-311. doi:10.1007/s00340-013-5334-4

# ACRONYMS

**AM0** Air Mass Zero atmospheres

**AM1.5** Air Mass 1.5 atmospheres

**AR** Anti Reflection

**AUTOCAD** AUTO Computer Aided Design

**BPM** Beam Propagation Method

**CMOS** Complementary Metal Oxide Semiconductor

**CNRS** Centre National de la Recherche Scientifique

**CPC** Compound Parabolic Concentrator

**Cr** Chromium

**EU** European Union

**FEA** Finite Element Analysis

**FFT** Fast Fourier Transform

**GSGG** Gadolinium Scandium Gallium Garnet

**HR** High reflection

**LASCAD** LASer Cavity Analysis and Design

**LSC** Luminescent Solar Concentrator

**MSSF** Medium Size Solar Furnace

**Nd** Neodymium

**NIR** Near Infra Red

**PMMA** PolyMethylMethAcrylate

**PR** Partial Reflection

**PROMES** PROcédés, Matériaux et Énergie Solaire

**RoC** Radius of Curvature

**SFERA** Solar Facilities for the European Research Area

**TEM** Transverse mode

**UV** UltraViolet

**VECSEL** Vertical External Cavity Surface Emitting Lasers

**YAG** Yttrium Aluminum Garnet

# 1 INTRODUCTION

The conversion of sunlight into laser light by direct solar pumping is of ever-increasing importance, since broad-band solar radiation, the most plentiful available form of energy, can be converted into coherent, collimated and narrow-band radiation. Compared to electrically powered lasers, solar laser is much simpler and reliable due to the complete elimination of the electrical power generation and conditioning equipments, offering the prospect of a drastic reduction in the cost of coherent optical radiation for high-average-power applications, leading to numerous environmental and economical benefits in the years to come.

Solar laser is a natural candidate for applications where sunlight is plentiful and there are few other energy sources available. Thus, it is a future emerging technology for space-based applications *(1,2)* where extended run times are required and where compactness, reliability, and efficiency are critical. As solar energy is the main continuous energy source in space, it can be used to pump solid-state lasers either directly or indirectly. In indirect solar pumping, the solar radiation illuminates solar cells to produce electricity, which powers diode lasers. However, direct solar pumping saves two energy conversion steps and thus is inherently more efficient, much simpler and more reliable. A significant shortcoming of semiconductor arrays is their limited life time and performance degradation over time, that seems to scale with the level of average output power. For high-power laser systems, the lifetime of these devices is one of the major factors limiting the lifetime of a laser system or even an entire system to the order of round about 3 years *(3)*. Entirely avoiding semiconductor laser arrays by direct solar pumping of solid - state lasers exhibits potential to overcome the current limitations, enabling reliable space borne laser operation over a multitude of years. Since strength of sunlight in space is about twice that on the Earth, and there are four or five times the hours of sunlight due to the absence of clouds energy, space - based solar power generation would be a major step forward in terms of fulfilling energy needs. Among the potential space applications of solar lasers are remote sensing from space, deep space communications, wireless space power laser beaming *(4)*, asteroid deflection, fuel-free photonic thrusters *(5)*, orbital space debris removal *(6,7)*. Solar laser has also large potentials for terrestrial applications such as material laser-based processing, micro/nano-material production and renewable energy cycles. Particular attention has been recently paid to the renewable magnesium (Mg) - hydrogen ($H_2$) cycle that might lead us to future fossil-fuel-free Mg-based civilization *(2,8)*. Large amounts of heat and $H_2$ are given off from the reaction of Mg with water. Mg has great potential as an energy source because it has an energy storage density about ten times higher than that of $H_2$. It can be easily stored and transported in the form of 'pellets' and when necessary reacts with water to produce both $H_2$ and thermal energy for fuel cell vehicle applications. However, about 4000 K is necessary for MgO reduction *(9)*. Since there is no practical way of reaching this temperature by directly focusing sunlight onto MgO with conventional optics, solar-powered lasers with excellent beam quality become essential, since they can be focused to a small spot, exceeding 4000 K. The MgO residue can hence be refined back to Mg by laser radiation *(8,9)*.

The idea of solar-pumped lasers (solar lasers) appeared no long after the invention of laser *(10)*. The first studies on solar lasers have been described in the literature since 1962 *(11)*. The first solar-pumped laser was reported in 1963 by Kiss et al. using calcium fluoride ($CaF_2$) crystal doped with divalent dysprosium ($Dy^{2+}$:$CaF_2$) at liquid neon (Ne) temperature *(12)*. Shortly thereafter, systems using the Sun to pump solid *(13)* liquid *(14)* and gaseous *(15,16,17,18,19)* active media were considered. However, research into solar pumped lasers has essentially converged in systems with solid-state materials operating in a continuous wave (cw) mode. Among various laser materials, solid lasers appear to be most attractive because of their inherent high energy density and compactness, their relatively low pumping threshold, and their potential for efficient solar-to-laser power conversion. Since the first Sun-pumped neodymium yttrium aluminum garnet (Nd:YAG) laser reported by Young in 1966 *(13)*, optical and laser material advances have continued to improve the solid-state solar laser performance *(20)*. Nevertheless, additional focusing systems are required to collect and concentrate solar radiation because natural sunlight does not provide power density sufficient enough to produce laser. Parabolic mirrors have long been explored to achieve tight focusing of incoming solar radiation *(21,22,23,24,25)*. By mounting directly a 4 mm diameter, 75 mm length Nd:YAG single-crystal rod within a 50 mm diameter water-cooled flow tube at the focus of a 78.5 $m^2$ area parabolic mirror, 18 W multimode solar laser power was successfully produced in 1984 *(21)*, leading to 0.23 $W/m^2$ laser collection efficiency – defined as solar laser power achieved per unit area of a primary collector ($W/m^2$). With CPC (Compound Parabolic Concentrator) secondary and tertiary concentrators, solar laser collection efficiencies were gradually boosted to 6.7 $W/m^2$ in 2003 *(25)*. Previous limitations in the size of Fresnel lenses made solar-pumped laser efforts relatively unsuccessful in their early stage. Nevertheless, most of the technologically significant effort has occurred during the past ten years, after the adoption of Fresnel lenses as primary solar concentrators *(26)*, boosting significantly the solar laser efficiency. 18.7 $W/m^2$ solar laser collection efficiency was firstly reported in 2007 by pumping a 3–9 mm diameter and 100 mm length Chromium (Cr) co-doped Nd:YAG ceramic laser rod with a 1.4 $m^2$ area Fresnel lens *(26)*. The progress with Fresnel lens and Cr:Nd:YAG ceramic laser medium has revitalized solar laser researches, revealing a promising future for renewable recovery of Mg from MgO *(8,9,27,28)*. 19.3 $W/m^2$ laser collection efficiency was later achieved in 2011 by exciting a 4 mm diameter, 25 mm length Nd:YAG single-crystal rod through a 0.64 $m^2$ area Fresnel lens in direct solar tracking mode *(29)*. This result triggered the discussions about which medium between Cr:Nd:YAG ceramics and Nd:YAG single-crystal was more suitable for solar lasers. Consequently, in 2012, record-high collection efficiency of 30.0 $W/m^2$ was attained by pumping a 6 mm diameter, 100 mm length Nd:YAG single-crystal rod through a 4 $m^2$ area Fresnel lens *(30)*, while the laser output power was unexpectedly worse when pumping a Cr:Nd:YAG ceramic rod. Most recently, both 31.5 $W/m^2$ multimode and 7.9 $W/m^2$ $TEM_{00}$ mode solar laser efficiencies were achieved by pumping a 4 mm diameter, 35 mm length Nd:YAG single-crystal rod through a heliostat-parabolic mirror system *(31)*. Compared with parabolic mirror systems, the use of Fresnel lenses reduces complexity, weight and cost of solar lasers. However, there still exists practical inconveniences regarding the use of Fresnel lens solar laser systems in direct solar tracking applications *(26,29,30)* where a solar laser head usually moves together with the whole solar tracking structure. An optical fiber thus becomes necessary for the transportation of solar laser radiation to a fixed target position away from both the solar laser head and solar tracker, therefore degrading the efficiency of the whole solar laser system due to optical fiber transmission loss. This advantage becomes much more pronounced when a Mg reduction vacuum chamber is to be installed nearby. Moreover, Fresnel lenses cause the dispersion of the solar radiation spectrum along its focal zone *(32)*, impairing the efficient light concentration to a thin laser rod. Minimizing a laser rod volume reduces cost, and reducing the diameter makes the rod more resistant to thermal

stress *(25)*. Also, as the rod acts as an aperture, by pumping a small diameter laser rod, high-order resonator modes can be suppressed by large diffraction losses, and beam quality improves.

Despite the strong desire to achieve high solar laser efficiency *(26,29,30,31,33,34,35)*, more attention should also be paid to the solar laser beam quality in order to attain tight focusing, which is very important for most laser applications. For these reasons, we have insisted on enhancing the solar laser efficiency and brightness by pumping small diameter Nd:YAG rods through heliostat–parabolic mirror systems *(31,36,37,38,39,40,41)*.

The brightness is one of the most important parameters of a laser beam. It is given by the laser power divided by the product of the beam spot area and its solid angle divergence. This product is proportional to the square of beam quality factor $M^2$. Brightness figure of merit is thus defined as the ratio between laser power and the product of $M_x^2$ and $M_y^2$ factors *(25)* – parameter that quantifies the laser beam quality. The highest brightness figure of merit of an end-pumped solar laser is 0.086 W with Fresnel lens *(29)*. Despite the successful production of 120 W cw end-pumped solar laser power in 2012, very large beam quality factors, $M_x^2 = M_y^2 = 137$, have also been measured *(30)*, resulting in a dismal brightness figure of merit of only 0.0064 W. 0.29 W solar laser beam brightness figure of merit was achieved in 2011, by side-pumping a 4 mm diameter Nd:YAG rod through the heliostat – parabolic mirror system in PROMES-CNRS *(36)*. This remained as a record-high value until 2013, through the first report of $TEM_{00}$ mode solar laser *(42)* by our research team. Gaussian $TEM_{00}$ mode beams are by far the most common laser beam shape used in materials processing *(43)*, since it produces the smallest beam divergence, the highest power density, and thus highest brightness and ability to be focused to a diffraction-limited spot.

For these reasons, the main objective of this work was to enhance both the solar laser efficiency and solar laser brightness, which are essential for the above mentioned applications. Several solar pumping prototypes with end-side-pumping and side-pumping configurations have been proposed. All the design and solar laser parameters were firstly numerically optimized through ZEMAX[©] and LASCAD[©] software, respectively. The final set-ups were designed and built in Lisbon, according to the optimized parameters of the numerical analysis. The final tests of the solar laser performances were mainly carried out at PROMES-CNRS, through the participation in R&D projects supported by SFERA I and SFERA II projects (Solar Facilities for the European Research Area, 7th Framework Program of the EU), where the solar energy collection and concentration was achieved by the horizontal-axis Medium Size Solar Furnace (MSSF) solar facility *(44)*. From 2015 to 2017, solar laser prototypes were also performed at the NOVA Solar Laser Laboratory, due to the recently new construction of NOVA heliostat-parabolic mirror system. Measurements of the solar laser output performance, including multimode and $TEM_{00}$ mode laser powers, beam quality factors $M^2$, brightness figure of merit, were performed and compared with that of numerical analysis. The solar laser performance through Fresnel lenses system was also studied and tested. Significant progresses in both solar laser efficiency and brightness are herein reported, which are explained in detail in CHAPTER 5 and CHAPTER 6, respectively.

## 1.1  OUTLINE

This dissertation is divided into nine chapters:

**CHAPTER 2** covers the fundamental concepts of solid-state lasers. The solar-pumped lasers concept is also described, including an overview of the suitable laser materials for solar-pumped lasers and a State-of- the Art.

**CHAPTER 3** describes in more detail the solar energy collection and concentration systems utilized for the solar laser prototypes.

**CHAPTER 4** presents the modeling tools for the numerical optimization of the proposed solar laser schemes.

**CHAPTER 5** describes the efforts for enhancing the solar laser collection efficiency, reported in the papers III, IV, VIII, X of the list of publications.

**CHAPTER 6** describes the efforts for enhancing the solar laser brightness, reported in the papers VI, VII, IX, XI of the list of publications.

**CHAPTER 7** is dedicated to the presentation of two laser prototypes to increase the stability of solar lasers, which is essential to obtain stable $TEM_{00}$-mode solar laser, and thus, high brightness solar laser beams. This was also reported in papers I and II in the list of publications.

**CHAPTER 8** presents the report of doughnut-shape solar laser beam production, which is also a very important class of beams for many applications, enabling novel fundamental insights in light-matter interactions.

**CHAPTER 9** presents the conclusions of this work. Future perspectives on how to improve both the solar laser efficiency and brightness are also discussed.

The highlights and publications obtained during the PhD project are presented in the **ANNEXES**.

# 2 SOLID-STATE LASERS

In this chapter, the basics of solid-state laser physics that are necessary in order to understand this work will be presented. It will start with the interaction of light and matter. The influence of the characteristics of the pumping source, pumping cavity, active medium and resonance cavity on the performance of the solid state lasers are described. It is also established the correspondence between these characteristics with the main parameters involved in the processes of energy conversion from pump input to laser radiation. This will be followed by an introduction of solar-pumped lasers, where it is described the solid state materials utilized for solar lasers, including their main advantages and disadvantages, ending with the state-of-the art of this technology, from the first solid-state solar-pumped laser to the most recent reports in 2017.

## 2.1 LIGHT AND MATTER INTERACTION

The mechanism of a laser is based on the interaction of light and matter. If electromagnetic radiation interacts with matter, intra-ionic and inter-ionic processes occur. To understand the properties of laser, the focus here will be on the relevant intra-ionic processes. They can be either radiative, when photons are involved, or non-radiative, when phonons are involved. Atomic systems such as atoms, ions, and molecules can exist only in discrete energy states. A change from one energy state to another - called a transition - is associated with either the absorption or the emission of a photon, as represented in FIG. 2.1. An electromagnetic wave whose frequency, $\upsilon$, corresponds to an energy gap of such an atomic system can interact with it. The wavelength of the absorbed or emitted radiation is given by Bohr's frequency relation:

$$\Delta E = E_2 - E_1 = h\nu_{21} \tag{2.1}$$

where $E_2$ and $E_1$ are two discrete energy levels, in which $E_2 > E_1$, $\upsilon_{21}$ is the frequency, and $h$ is Planck's constant ($6.626 \times 10^{-34}$ J.s).
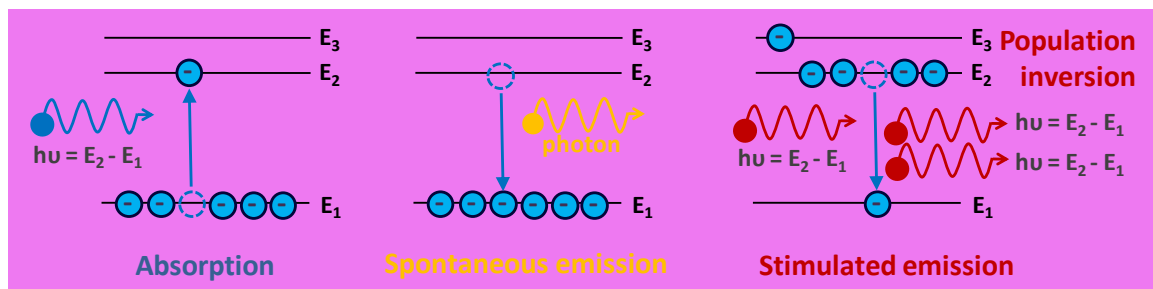


**FIG. 2.1** - Intra-ionic radiative processes.

In this context, a laser medium can be considered an assemble of many identical atomic systems. When a large collection of similar atoms is in thermal equilibrium at temperature $T$, the relative populations of any two energy levels $E_1$ and $E_2$, such as the ones shown in Fig. 2.1, must be related by the Boltzmann ratio:

$$\frac{N_2}{N_1} = \frac{g_2}{g_1}\frac{N_2'}{N_1'} = \frac{g_2}{g_1}\exp\left(\frac{-(E_2-E_1)}{kT}\right) \tag{2.2}$$

where $N_1$ e $N_2$ are the number of atoms of the relative energy levels, $E_1$ e $E_2$; when two or more states have the same energy, the respective level is called degenerate - represented by g; the states of the same energy level, for example $E_1$, will be equally populated, therefore $N_1 = g_1 N_1'$.

## ABSORPTION

At thermal equilibrium, the lower energy states ($E_1$) in the medium are more heavily populated than the higher energy states ($E_2$ or $E_3$). An electromagnetic wave interacting with the laser system will raise the atoms (ions, molecules) from lower to higher energy levels and thereby experience absorption. In this case, the population of the lower level, $N_1$, will be depleted at a rate proportional both to the radiation density $\rho(v)$ and to the population of that level:

$$\frac{\partial N_1}{\partial t} = -B_{12}\rho(v)N_1 \tag{2.3}$$

$B_{12}$ is a constant of proportionality with dimensions $cm^3/s^2.J$, related to the probability per unit frequency that transitions are induced by the effect of the field.

## SPONTANEOUS EMISSION

After an atom has been raised to the upper level by absorption, the population of the upper level decays spontaneously to the lower level at a rate proportional to the upper level population:

$$\frac{\partial N_2}{\partial t} = -A_{21}N_2 \tag{2.4}$$

where $A_{21}$ is a constant of proportionality with dimension $s^{-1}$, related to the spontaneous transition probability to a lower level within a unit of time. Spontaneous emission is then characterized by the lifetime of the electron in the excited state, after which it will spontaneously return to the lower state and radiate away the energy. Contrary to the stimulated emission, spontaneous emission can occur without the presence of an electromagnetic field, where the emitted quanta is incoherent. Thus, the $A_{21}$ Einstein coefficient represents a loss term and introduces into the system photons that are not phase-related to the incident photon flux of the electric field, which means that the spontaneous process represents a noise source in a laser.

## STIMULATED EMISSION

The acronym laser derives its name from: Light Amplification by Stimulated Emission of Radiation. Thus, as shown in FIG. 2.1, the operation of a laser requires that higher energy levels are more populated than the ground-state level, causing population inversion. This is achieved by an external pump source that supplies the energy required to transfer atoms (ions, molecules) from

a lower energy level to a higher one. In this case, an electromagnetic wave of appropriate frequency, incident on the "inverted" laser material, will be amplified. The stimulated emission is, in fact, completely indistinguishable from the stimulating radiation field, which has the same directional properties, same polarization, same phase, and same spectral characteristics. These facts are responsible for the extremely high degree of coherence which characterizes the emission from lasers.

Analogously to the absorption process, in the stimulated emission the population of the higher level, $N_2$, will be depleted at a rate proportional both to the radiation density of the radiation field $\rho(v)$ and to the population of that level, according to:

$$\frac{\partial N_2}{\partial t} = -B_{21}\rho(v)N_2 \tag{2.5}$$

where $B_{21}$ is a constant of proportionality with same conditions as $B_{12}$, from eq. (2.3). The Einstein coefficients for stimulated emission and absorption are equal ($B_{21} = B_{12}$) when there is no degeneracy or if the levels have unequal degeneracy.

### 2.1.1 POPULATION INVERSION

Population inversion is clearly an abnormal situation, since it is never observed at thermal equilibrium (FIG. 2.2(a)). Thus, to populate a higher energy level is required a source of energy – pump energy to replenish the supply of upper-state atoms (FIG. 2.2(b)). The point at which the population of both states is equal is called the inversion threshold and the laser material is then transparent to the incident radiation. Nevertheless, spontaneous emission tends always to return the energy level populations to their thermal equilibrium values, which means that population inversion is not possible with materials of only two energy levels, even with higher pump energy density (FIG. 2.2(c)).
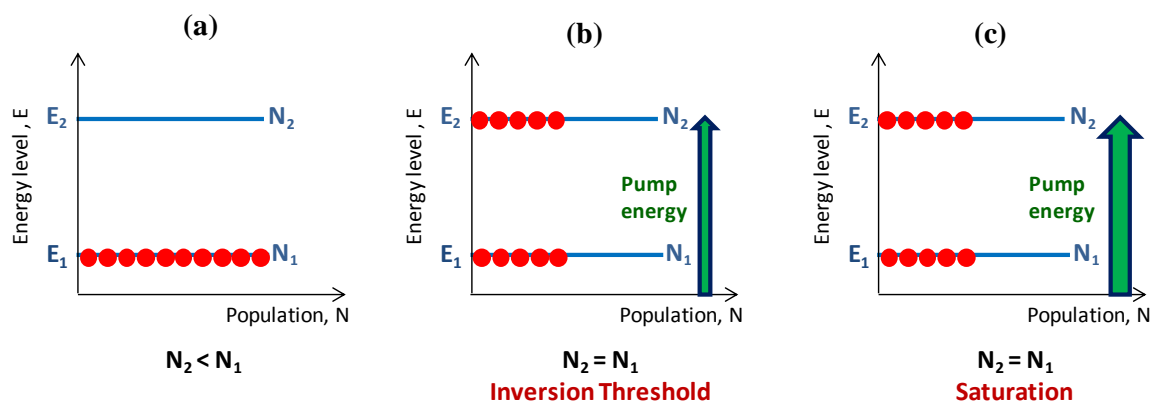


**FIG. 2.2** - Relative populations in two energy levels **(a)** for thermal equilibrium, **(b)** for inversion threshold and **(c)** saturation in transition processes.

The pumping and laser processes in real laser systems typically involve a very large number of energy levels, with complex excitation processes and cascaded relaxation processes among all these levels. Operation of a laser material is properly described only by a many level energy diagram.

## 2.1.2 METASTABLE STATE

The existence of a metastable level is necessary for laser action. The relatively long lifetime of the metastable level provides a mechanism by which inverted population can occur, as demonstrated in FIG. 2.3. Most transitions of ions show rapid non-radiative decay, because the coupling of the internal atomic oscillations to the surrounding lattice is strong. Radiative decay processes occur, but most have short lifetimes and broad linewidths. Only a few transitions of selected ions in solids turn out to be decoupled from the lattice vibrations, which have a radiative decay that leads to relatively long lifetimes.

In three and four level laser systems, illustrated in FIG. 2.3, the $3 \to 2$ and $1 \to 0$ transition frequencies fall within the frequency range of the vibration spectrum of the host crystal lattice. For this reason, these transitions can relax extremely rapidly by direct non-radiative decay, emitting a phonon to the lattice vibrations with lifetimes $\tau_{32}$, $\tau_{10} \approx 10^{-8}$ to $10^{-11}$ s. Nevertheless, the transitions $3 \to 0$ , $3 \to 1$ , $2 \to 0$ ,and $2 \to 1$, with larger energy gaps, often correspond to transition frequencies that are higher than the highest possible vibration frequency of the crystal lattice. Since the lattice cannot accept phonons at those high frequencies, these transitions cannot relax via simple single-phonon spontaneous emission, but relax either by radiative photon emission or by multiple-phonon processes, which are relatively weak compared to direct single-phonon relaxation. Therefore, these transitions will have much slower relaxation rates ($\tau_{21} \approx 10^{-5}$ to $10^{-3}$s). The energy levels from the pump band, $E_3$, will then relax mostly into the metastable level, $E_2$, which has a long lifetime because there are no other levels located close below it, into which it can decay directly.
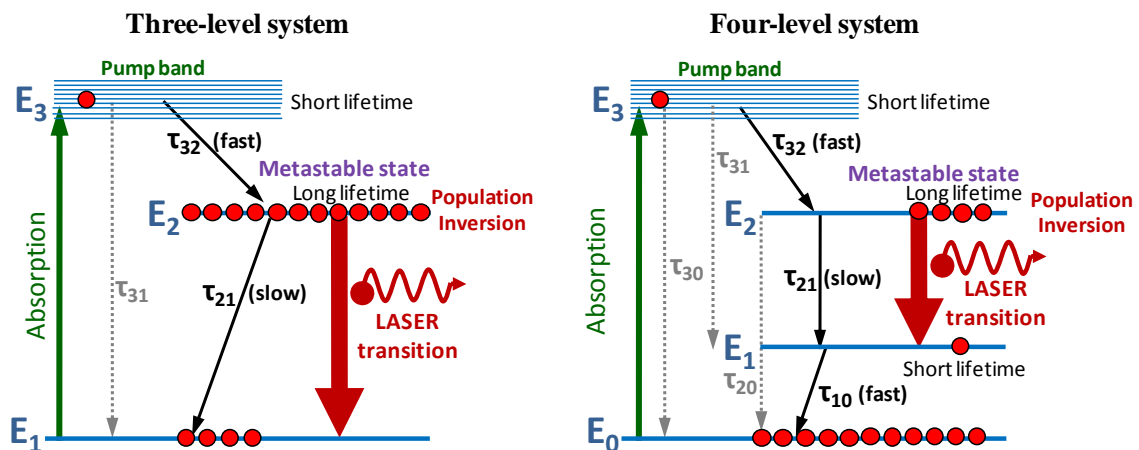


**FIG. 2.3** - Schematic energy level diagram of a three and four-level laser system.

In the absence of a metastable level, the ions which become excited by pump radiation and are transferred to a higher energy level will return either directly to the ground state by spontaneous radiation or by cascading down on intermediate levels, or they may release energy by phonon interaction with the lattice. Thus, population inversion cannot occur.

## 2.2  LASER OSCILLATOR

For a laser device, in addition to a laser material and pump energy to maintain a non-equilibrium state, it is also necessary to have a feedback mechanism for radiation to build up the amplified optical field. This requirement can be obtained by placing the laser medium into a laser resonator, as shown in FIG. 2.4.

The pump energy inverts the electron population in the laser material, leading to energy storage in the upper laser level (FIG. 2.4(b)-(f)). The role of the resonator, or resonant cavity, is to maintain an electromagnetic field configuration whose losses are replenished by the amplifying medium through stimulated emission. Thus, the resonator defines the spectral, directional, and spatial characteristics of the laser radiation, and the amplifying medium serves as the energy source. It is composed of two (or more) opposing mirrors (plane-parallel or curved) at right angles to the axis of the active material, enabling the laser beam to travel back and forth through the laser material, increasing the amplification of stimulated radiation (FIG. 2.4(c)-(f)). The amount of feedback is determined by the reflectivity of the mirrors. Lowering the reflectivity of the mirrors is equivalent to decreasing the feedback factor. One cavity mirror is high-reflection coated (about 100% reflectivity) for the laser emission wavelength, while the mirror (output coupler) must be only partial reflection coated for the same wavelength, for a fraction of the radiation to "leak out" from the oscillator. Laser output emission occur (FIG. 2.4(f)) if the feedback and the gain are sufficiently large to compensate the internal losses of the system.
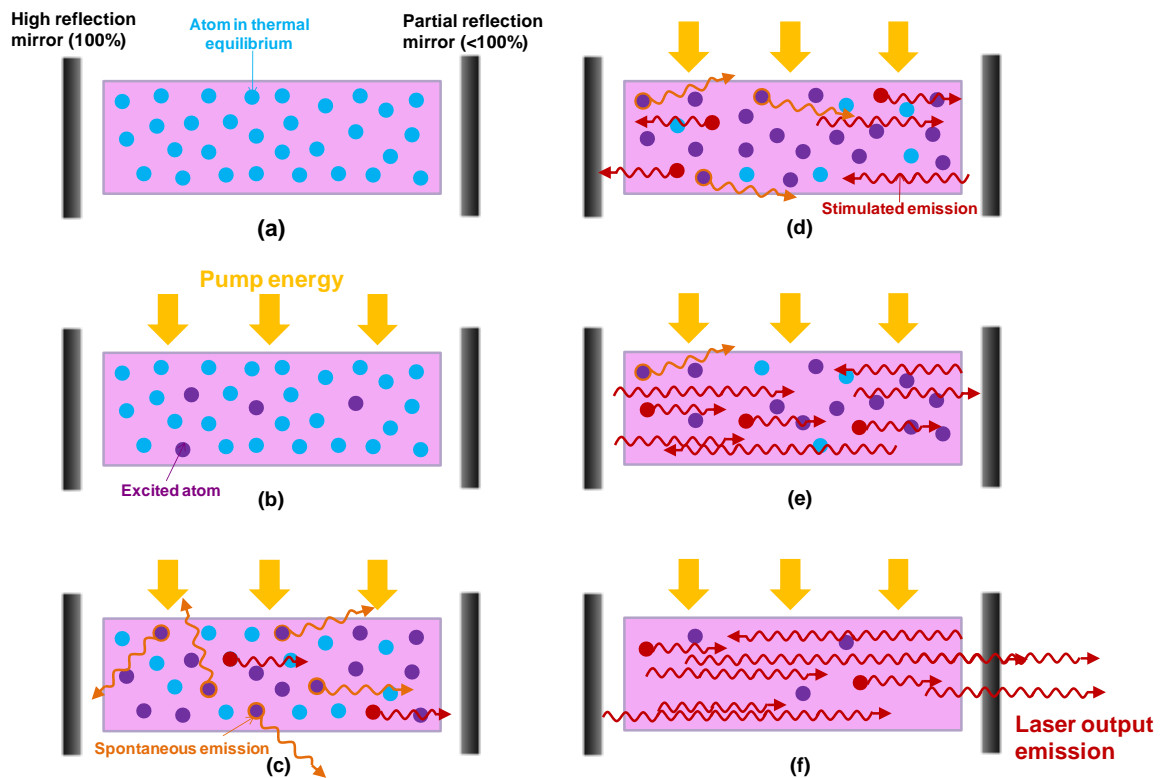


**FIG. 2.4** - Schematic scheme of laser oscillation operation through a resonant cavity.

## 2.2.1 CONVERSION OF PUMP INPUT TO LASER OUTPUT ENERGY

To achieve a desired output performance with the maximum system efficiency it is of utmost importance to understand the dependency and interrelationship of the laser system design parameters and design issues which may help in the optimization of the overall laser efficiency. This can be represented by the energy diagram schematically illustrated in FIG. 2.5.
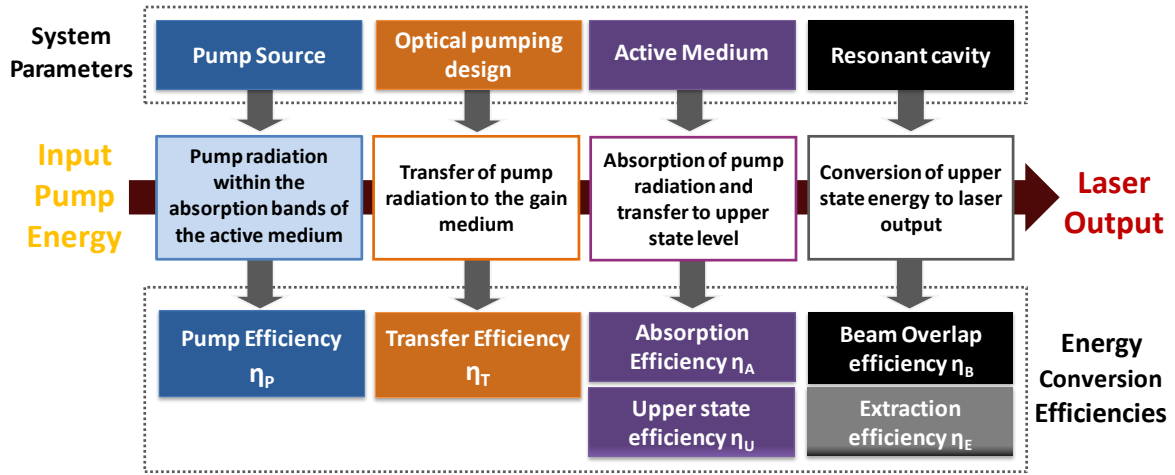


**FIG. 2.5** - Energy conversion process in a solid-state laser system.

### CONVERSION OF INPUT DELIVERED FROM THE PUMP SOURCE TO USEFUL PUMP RADIATION

The useful radiation is defined as the radiation emission from the pump source that falls into the absorption bands of the laser medium. The pump source efficiency, $\eta_P$, is therefore the fraction of input power, $P_{in}$, that is emitted as optical radiation within the absorption region of the active medium, $P_P$, as defined by eq. (2.6):

$$\eta_P = \frac{P_P}{P_{IN}} \tag{2.6}$$

In the case of electrical-pumped lasers the spectral output power of the pump source can be also defined as the product of the electrical-to-optical power efficiency, $\eta_{EO}$, and the fraction of the emitted radiation which matches the absorption bands of the active medium, $\eta_{OVP}$, also designated as overlap efficiency:

$$\eta_{P_{EL}} = \eta_{EO}\eta_{OVP} \tag{2.7}$$

However, since the pump source of solar-pumped lasers is the Sun, they don´t rely on electrical power. Therefore, the pump power efficiency is only affected by the overlap efficiency as follows

$$\eta_{P_{SL}} = \eta_{OVP} = \frac{\int_{\lambda_1}^{\lambda_2} g_\lambda d\lambda}{\int_0^\infty g_\lambda d\lambda} \tag{2.8}$$

where $g_\lambda$ is spectral irradiance of the pumping source and $\lambda_1$ to $\lambda_2$ is the wavelength range within the absorption bands of the active medium. For Nd:YAG solid-state laser material, which is the

most widely used laser material for solar-pumped laser, the overlap between the absorption spectrum of Nd:YAG and the emission spectrum of solar radiation is only $\eta_{OVP} = 0.16$ *(45)*.
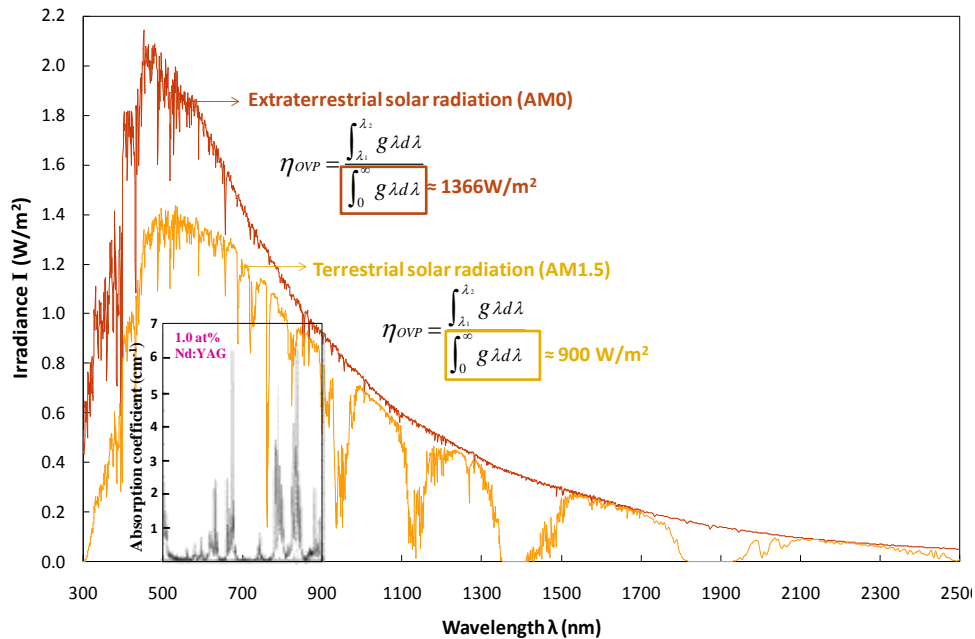


**FIG. 2.6** - Standard solar emission spectrum in space (AM0) and on the Earth (AM1.5) *(46)*, and Nd:YAG absorption bands *(47)*.

## TRANSFER OF THE USEFUL PUMP RADIATION EMITTED BY THE PUMP SOURCE TO THE ACTIVE MEDIUM

The energy transfer efficiency, $\eta_T$, from the useful pump radiation, $P_P$, to the active medium is defined as:

$$\eta_T = \frac{P_T}{P_P} \tag{2.9}$$

where $P_T$ is the fraction of the radiation transferred into the laser material. This process is influenced by geometrical shape of the concentrating optics and pump cavity, diameter of the pump source and laser rod, as well as the separation distance between them, reflectivity of pump walls, absorption losses in the optical components and coolant fluid, radiation losses through spaces in the pump cavity.

## ABSORPTION OF PUMP RADIATION BY THE ACTIVE MEDIUM AND TRANSFER OF ENERGY TO THE UPPER LASER LEVEL

This energy conversion process can be divided into two steps. The first one has to do with the absorption of the incident pump radiation into the active medium (eq. 2.10) while the second is related with the fraction of the absorbed radiation that is transferred to the upper laser level of the active medium (eq. 2.11).

The absorption efficiency, $\eta_A$, is then defined as the ratio of absorbed power, $P_A$, to the useful pump power incident on the active medium, $P_T$, being a function of the absorption coefficient and the path length of the active medium.

$$\eta_A = \frac{P_A}{P_T} \tag{2.10}$$

The upper state efficiency, $\eta_U$, is defined as the fraction of the absorbed pump power, $P_A$, which is emitted at the laser transition, $P_U$. This efficiency is the product of two contributing factors, the quantum efficiency, $\eta_Q$, and the quantum defect efficiency, $\eta_S$, also referred as Stokes factor.

$$\eta_U = \frac{P_U}{P_A} = \eta_Q \eta_S \tag{2.11}$$

The quantum efficiency is the ratio between the number of photons contributing to laser emission and the number of pump photons ($\eta_Q = 0.9$ for Nd:YAG *(48)*). This factor is affected by non-radiative processes such as multi-phonon transitions and energy transfer processes *(49)*. The Stokes factor is the ratio of the photon energy emitted at the laser transition, $h v_L$, to the energy of a pump photon, $h v_P$

$$\eta_S = \left( \frac{h v_L}{h v_P} \right) = \frac{\lambda_P}{\lambda_L} \tag{2.12}$$

where $\lambda_P$ and $\lambda_L$ are the pump transition and laser wavelengths, respectively. In solar-pumped lasers, the pump wavelength is defined as the mean absorbed and intensity-weighted solar radiation wavelength (eq. 2.13)

$$\lambda_P = \frac{\int_{a.b}^{a.b} g_\lambda \lambda d\lambda}{\int_{a.b}^{a.b} g_\lambda d\lambda} \tag{2.13}$$

where a.b. (the sign under the integral) indicates that the integration is performed over the laser absorption bands only. Since the laser wavelength of Nd:YAG laser material is $\lambda_L = 1064$ nm, for solar-pumped Nd:YAG laser, $\eta_S = 0.62$ is find based on $\lambda_P = 660$ nm *(22)*. In most lasers, the laser wavelength is longer than the pump wavelength (except in upconversion lasers), which means that the energy of the laser photons is smaller than that of the pump photons. As a consequence, the upper state efficiency could not be 100% even if every pump photon could be converted into a laser photon. The difference in the photon energies is the quantum defect, $q$

$$q = h v_P - h v_L = h v_P \left( 1 - \frac{h v_L}{h v_P} \right) = \left( 1 - \frac{\lambda_P}{\lambda_L} \right) = 1 - \eta_S \tag{2.14}$$

Both quantum defect and Stokes factor are not related to the quantum efficiency, since the latter refers to the average number of output photons, contributing to the laser emission, per pump photon, rather than to the photon energies.

### CONVERSION OF THE UPPER STATE ENERGY TO LASER OUTPUT

The efficiency of this process can be divided into beam overlap efficiency, $\eta_B$, and the extraction efficiency, $\eta_E$. The first one expresses the spatial overlap between the resonator modes and the pumped region of the laser medium, which can be given by an overlap integral

$$\eta_B = \frac{\int I_{PM}(r) I_{RM}(r) 2\pi r dr}{\int I_{RM}{}^2(r) 2\pi r dr} \tag{2.15}$$

where $I_{PM}$ represents the absorbed pump intensity distribution and $I_{RM}$ the resonator mode intensity distribution. The beam overlap efficiency is strongly dependent on the resonator parameters (radius of curvature of the mirrors, cavity length), rod diameter and pumping configuration.

In solid-state lasers, optical pumping leads to a radial temperature gradient in the laser rod. As a result, in high-average laser power systems, the laser rod acts like a positive thick lens with an effective focal length, which is inversely proportional to pump power *(48,50)*. Pump induced fluctuations on the rod focal length will hence exert strong influence on resonator modes configuration and stability, giving rise to thermally stable zones *(48,50)*. Conventionally, lasers are designed to operate at the middle of thermally stable zones, where the fundamental mode size  is insensitive to thermal  perturbation *(48,51)*. Since the TEM$_{00}$ mode Gaussian beam has the smallest beam radius and divergence in a resonator, if the transverse dimension of the gain region is much larger than the TEM$_{00}$ mode size, laser oscillates at several modes *(48)*. Thus, in case of a uniformly pumped gain medium operated in a highly multimode resonator a beam overlap efficiency equal to unit ($\eta_B = 1$) can be reached. However, to achieve laser operation in fundamental mode, classically a pinhole with similar diameter to the fundamental mode size is inserted inside the laser resonant cavity to prevent higher-order modes from oscillating, considerably reducing the laser extraction efficiency because of poor utilization of the stored energy in the active medium. Thus, a suitable resonator design for efficient energy conversion to the TEM$_{00}$ mode must maximize the overlap integral of the resonator TEM$_{00}$ mode and the pump profile while simultaneously utilizing only the rod to apodize higher-order spatial modes *(52)*. In side-pumped solar lasers, the adoption of an asymmetric resonator configuration with concave end mirrors of large radius of curvature (RoC) has shown to provide a large spatial overlap between the fundamental mode and pump mode volumes , as shown in FIG. 2.7. The use of small diameter laser rods played a crucial role. Since the laser rod acts as an aperture, high-order resonator modes can be easily suppressed with small diameter rod due to large diffraction losses, improving thus the beam quality and contributing largely on the efficient extraction of TEM$_{00}$ laser power *(31,37,38,39,40,41,42)*.



**FIG. 2.7** - Schematic diagram of the TEM$_{00}$-mode beam propagation along the asymmetric laser resonator with large RoC (radius of curvature) end mirrors. L$_1$ and L$_2$ represent the separation length of the high reflection (HR) mirror and partial reflection (PR) mirror, respectively, to the end face of the laser rod with length L$_R$.

The ratio L$_1$/L$_2$ is a key parameter for achieving the optimum mode overlap, as shown in FIG. 2.8. High multimode, low TEM$_{00}$ mode laser output power levels can be achieved with relatively small L$_1$/L$_2$ ratio, as for L$_1$/L$_2$ = 1, where TEM$_{00}$ mode radius, $\omega_0$, poorly matches the laser rod radius. However, this comes at the expense of high M$^2$ beam quality values and thus poor laser beam quality. As L$_1$/L$_2$ increases, the TEM$_{00}$ mode size within the rod enhances and higher-order modes are suppressed by large diffraction losses. Consequently, spatial overlap between

TEM$_{00}$ mode and pump mode volumes becomes larger and fewer higher-order modes oscillate. As pump power increases towards the resonator stability limit, $\omega_0$ increases further until laser oscillation is only possible for the lowest-order mode: TEM$_{00}$ mode.
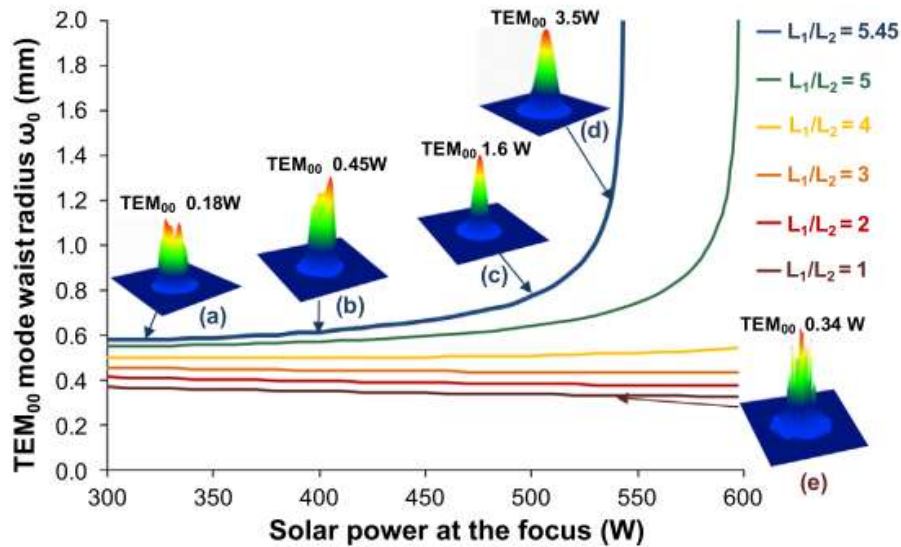


**FIG. 2.8** - Solar-pumped TEM$_{00}$ mode beam waist radius $\omega_0$ in the rod as function of solar power at the focus, for different $L_1/L_2$ resonators, numerically obtained by LASCAD$^{©}$ analysis *(40)*. **(a)–(d)** output laser beam profiles at different pump powers for $L_1/L_2 = 5.45$ resonator. **(e)** Output laser beam profile for $L_1/L_2 = 1$ resonator.

A strong dependence of the beam overlap efficiency on the radius of curvature (RoC) of end mirrors has been also observed in solar-pumped laser designs *(53,54)*. In solar lasers, small laser oscillation mode occurs along the central region of the laser rod when using small RoC mirrors, which causes a large mismatch with the pumped volume. Thus, for the maximum extraction of TEM$_{00}$ solar laser power from all the available absorbed solar pump power within the rod, it is preferable to adopt large RoC mirrors.

The extraction efficiency, $\eta_E$, describes the fraction of total available upper state power, $P_{Uavail}$, which appears at the output of the laser, $P_{OUT}$.

$$\eta_E = \frac{P_{OUT}}{P_{Uavail}} \tag{2.16}$$

The sum of absorption, scattering, and diffraction losses for laser emission wavelength within the active medium constitutes the most important part of round-trip resonant cavity losses. Imperfect high reflection (HR) and anti reflection (AR) coating losses of both laser medium and resonator cavity mirrors are also an important portion of the round-trip losses. For example, for a Nd:YAG laser rod of length $L_R = 50$ mm, the amount of absorption and scattering losses is $2\alpha L_R = 3.0\%$, where $\alpha$ represents the absorption coefficient of the laser medium for the laser wavelength. Assuming 0.4% of imperfect HR and AR coating loss, the round-trip losses increases to 3.4%. The diffraction losses depend on rod diameter, resonator length and radius of curvature of the resonator mirrors. Usually the diffraction losses of a large diameter rod within a short resonator are very small, even with large concave RoC end mirrors *(53,54)*.

The overall laser system efficiency, $\eta_{Sys}$, of a solid-state laser is given by the product of the individual efficiency factors above mentioned: $\eta_P$ - pump efficiency, $\eta_T$ - transfer efficiency, $\eta_A$ - absorption efficiency, $\eta_Q$ - quantum efficiency and $\eta_S$ - Stokes efficiency, $\eta_B$ - beam overlap efficiency and $\eta_E$ - extraction efficiency.

$$\eta_{Sys} = \eta_P \eta_T \eta_A \eta_Q \eta_S \eta_B \eta_E = \frac{P_{OUT}}{P_{IN}} \tag{2.17}$$

### 2.2.1.1  SLOPE EFFICIENCY

An indication of the reduction of available output power due to losses in resonator can be obtained from the coupling efficiency, $\eta_C$, through eq. (2.18).

$$\eta_C = \frac{T}{\delta + T} \approx \frac{-\ln R}{\delta - \ln R} \tag{2.18}$$

where $T$ is the transmission of the output end mirror, and R the reflectivity of the output mirror. $\delta$ defines the round-trip losses, which reduces the available output power.

$$\delta = 2\alpha l + \delta_D + \delta_M \tag{2.19}$$

$2\alpha l$ represents the two-way loss within the laser medium, $\delta_D$ represents the diffraction losses and $\delta_M$ the absorption and scattering losses at the mirrors.

The slope of the output versus input curve of a laser, $\eta_{Slope}$, is directly proportional to the coupling efficiency, whereas the overall system efficiency of a laser is directly proportional to the extraction efficiency

$$\eta_{Slope} = \eta_P \eta_T \eta_A \eta_Q \eta_S \eta_B \eta_C = \eta_P \eta_T \eta_A \eta_Q \eta_S \eta_B \left( \frac{-\ln R}{\delta - \ln R} \right) \tag{2.20}$$

The slope efficiency can also be given as

$$\eta_{Slope} = \frac{P_{OUT}}{P_{IN} - P_{TH}} \tag{2.21}$$

where $P_{TH}$ is the pump power required to achieve laser emission threshold.

### 2.2.1.2  LASER OUTPUT POWER

The laser output power, $P_{OUT}$, can be expressed in terms of input pump power and measurable quantities by Eq. (2.22)

$$P_{OUT} = (-\ln R) \left( \frac{\eta_P \eta_T \eta_A \eta_Q \eta_S \eta_B}{\delta - \ln R} P_{IN} - A I_S \right) \tag{2.22}$$

where $I_S$ is the saturation intensity ($I_S \approx 2.2$ kW/cm$^2$ for a lamp-pumped cw Nd:YAG laser *(48)*) and $A$ the cross-section area of the laser rod. For solar-pumped lasers the laser output power can be defined by eq. (2.23), where the pump efficiency, $\eta_P$, is replaced by the overlap efficiency, $\eta_{OVP}$:

$$P_{OUT} = \left(-\ln R\right)\left(\frac{\eta_{OVP}\eta_T\eta_A\eta_Q\eta_S\eta_B}{\delta - \ln R} P_{focus} - AI_S\right) \tag{2.23}$$

In this case, $P_{focus}$ represents the collected solar power at the focus, which has been widely used for defining the slope efficiency in many publications on solar-pumped lasers *(21,22,26,29)*. The respective threshold pump power at the focus, $P_{TH}$, can also be found using Eq. (2.24):

$$P_{TH} = \left(\frac{\delta - \ln R}{\eta_P\eta_T\eta_A\eta_Q\eta_S\eta_B} AI_S\right) \tag{2.24}$$

### 2.2.1.3 COLLECTION EFFICIENCY

The collection efficiency, *CE*, is defined by the ratio between the laser output power and the area of the primary solar concentrator *(55)*, which has been a desirable goal in solar-pumped lasers *(25,26,29,30,31,35)* in order to get more laser power as well as to save primary mirror area. Thus, we have insisted in enhancing the solar laser collection efficiency.

$$CE = \frac{P_{OUT}}{A_{collection}} \tag{2.25}$$

## 2.3 SOLAR-PUMPED LASERS

## 2.3.1 LASER MATERIALS

Gas, liquid, and solid lasers have all been considered as candidate for solar lasers. Nevertheless, among various laser materials, solid lasers appear to be most attractive because of their inherent high energy density and compactness, their relatively low pumping threshold, and their potential for efficient solar-to-laser power conversion. To improve the efficiency of solar-pumped lasers, the selection of a suitable crystal is the most important factor.

### 2.3.1.1 ND:YAG

The Nd:YAG laser material is by far the most commonly used type of solid-state laser. It possesses a combination of properties uniquely favorable for laser operation. Despite the small overlap between the Nd:YAG absorption spectrum and the solar emission spectrum *(47)*, as shown in FIG. 2.6, Nd:YAG has been demonstrated as the best material under highly intense solar pumping *(13,21,25,29,30,31,35)* because of its excellent characteristic on thermal conductivity (K = 14 W/m.K *(48)*), high quantum efficiency and fracture strength ($\sigma_{max}$ = 180 – 210 N/mm$^2$ *(48)*) compared to other host materials.

The Nd:YAG is a four-level laser system, as depicted in FIG. 2.9, except for the 946 nm transition, offering substantial laser gain even for moderate excitation levels and pump intensities. Furthermore, the cubic structure of YAG favors a narrow fluorescent linewidth, which results in high gain and low threshold for laser operation. In a four-level laser medium, the lower laser level is well above the ground state and, thus, is quickly depopulated by multi-phonon transitions. This

means that reabsorption of the laser radiation can be avoided and a lower threshold pump power can be achieved, making it easier to obtain stimulated emission with low power pumping. Also, due to the broadband pump absorption of Nd:YAG laser mediums and four-level characteristics, they can be lamp-pumped or solar-pumped *(48,49)*.
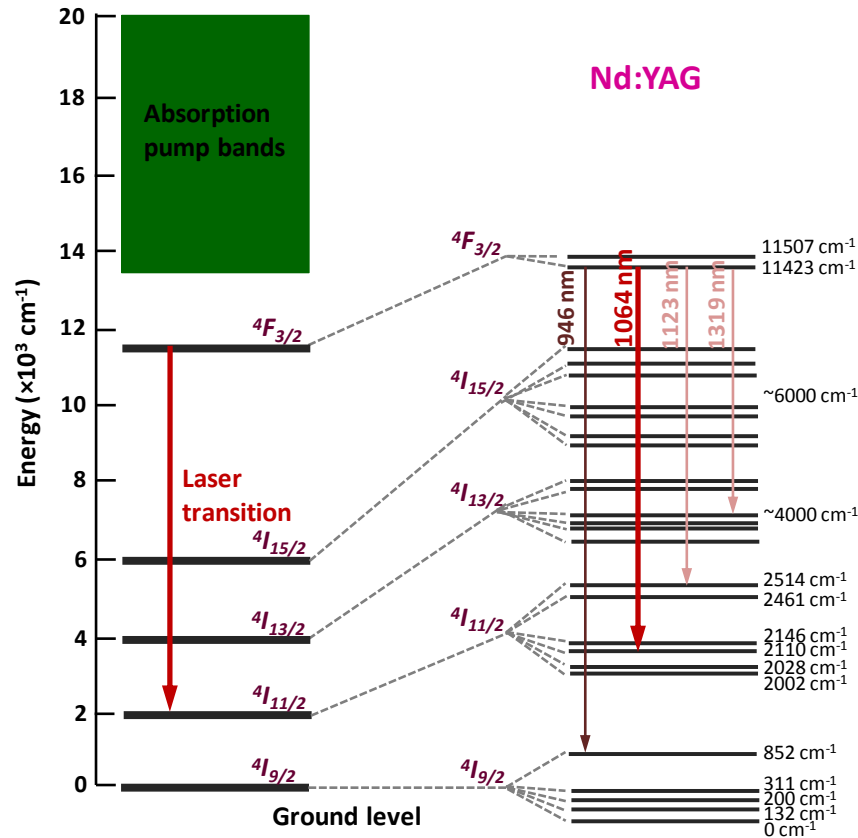


**Fig. 2.9** - Energy level diagram of Nd:YAG *(48,49)*.

The most common Nd:YAG emission wavelength is 1064 nm, which have much higher gain compared to other laser emission wavelengths. Other emission lines are at 946, 1123, and 1319 nm, where Nd:YAG is a quasi-three-level laser system at the 946-nm transition. A quasi-three-level laser system is an intermediate situation between three and four-level systems, where the lower laser level is so close to the ground state that an appreciable population in that level occurs in thermal equilibrium at the operating temperature, requiring significantly higher pump intensities, compared to four-level laser systems. All other emission lines of Nd:YAG are four-level transitions. Some of these, such as the one at 1123 nm, are very weak, so that efficient laser operation on these wavelengths is difficult to obtain *(48,49)*.

### 2.3.1.2 Cr:Nd:YAG

To improve the efficiency of $Nd^{3+}$- doped YAG laser, cross-pumped $Cr^{3+}$ and $Nd^{3+}$ co-doped YAG ceramic material has attracted more attentions for solar pumping in recent years *(26,28,56)*. The sensitizer $Cr^{3+}$ ions have broad absorption bands in the visible region. The absorption spectra of 0.1 at% Cr:1.0 at% Nd:YAG ceramics has two broad absorption bands at approximately 440 nm ($^4A_2$ to $^4T_1$) and 600 nm ($^4A_2$ to $^4T_2$ ) *(47,57)*. It can be seen as the superposition of the absorptions of Nd:YAG and Cr:Nd:YAG, as shown in Fig. 2.10.
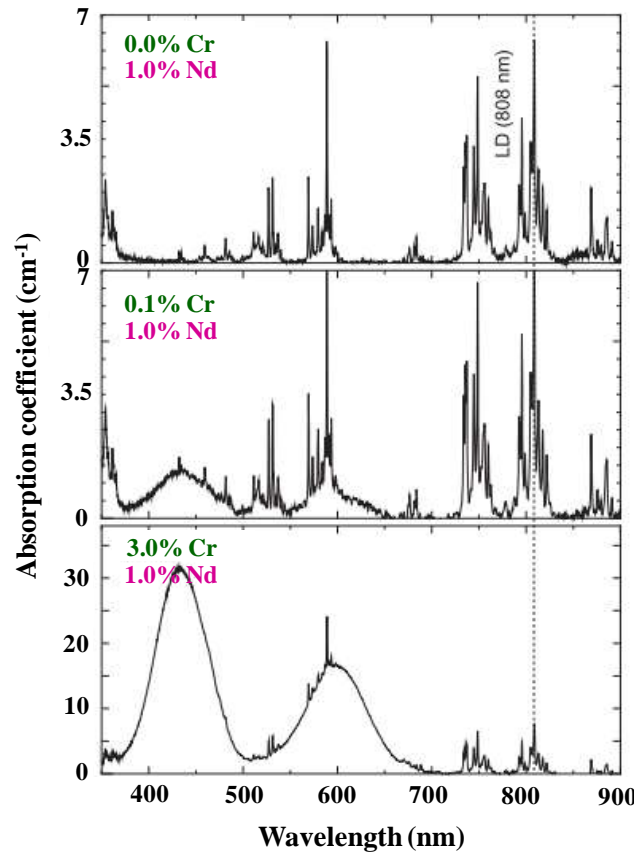
**FIG. 2.10** - Absorption spectra of the 0.0%Cr^{3+}/1.0% Nd[3+]:YAG, 0.1% Cr^{3+}/1.0% Nd[3+]:YAG, and 3.0% Cr^{3+}/1.0% Nd[3+]:YAG *(47)*.

By the $^4T_2$ to $^4A_2$ transition of Cr^{3+}ions, energy is transferred from Cr^{3+} to Nd[3+] ions *(47,57)*. It has been known that doping Cr^{3+} ions in a Nd:YAG crystal enhances absorption in the visible spectrum considerably, as shown in FIG. 2.10, so that increased energy coupling from solar radiation to the laser medium is expected. A 24% overlap between the absorption spectrum of the 0.1 at.% Cr: 1.0 at.% Nd:YAG medium and the solar emission spectrum is estimated *(57)*. For single-shot laser operation with a 0.1 at% Cr^{3+} and 1.0 at% Nd[3+] co-doped YAG ceramic rod, the laser efficiency is found to be more than twice that of a 1.0 at% Nd[3+]:YAG ceramic rod. At low repetition rates, the average output power of Cr:Nd:YAG rod is higher than that of Nd:YAG. However, this tendency gradually decreases with increasing repetition rates *(57)*. Very large, continuous absorption by $^4T_1$ and $^4T_2$ bands are seen for the 3.0% Cr specimen. The photon absorption coefficient of the 3.0% Cr codoped YAG ceramic was 12 times larger than that of a Nd:YAG crystal. On the other hand, a relatively high loss of 0.052 cm$^{-1}$ occurs at the lasing wavelength, which is a serious drawback when considering it as the medium for solar-pumped lasers *(47)*. Therefore, while it is clear about the effectiveness of Nd:YAG single-crystal rods for solar laser operation, there still exist some concerns about the advantages of Cr:Nd:YAG ceramic medium. Despite the interests in Cr:Nd:YAG ceramic medium, solar laser researchers have achieved significant laser efficiencies with different Nd:YAG single-crystal rods *(25-27,32)*. Although the slightly high conversion efficiency of the Cr:Nd:YAG ceramic rod for the side-pumping configuration *(56)* it presented, unexpectedly, much worse laser output performance in end-pumping approach *(30)*.

### 2.3.1.3  ALEXANDRITE

Alexandrite ($Cr^{3+}:BeAl_2O_4$ Cr-doped Chrysoberyl) has a number of superior thermo-mechanical properties that make it particularly attractive as a laser gain medium for high power/energy operation. Its thermal conductivity (23 W/m.K) is almost twice that of Nd:YAG. Additionally, its fracture resistance is five times that of Nd:YAG. Alexandrite is strongly birefringent, giving highly linearly-polarized laser emission, and eliminating depolarization problems. Its long upper-state (room-temperature) lifetime ~260μs allows for good energy storage potential, making it advantageous for Q-switched operation. The stimulated emission cross-section for alexandrite is low ($0.7x10^{-20}cm^2$) requiring high pump fluence for efficient gain extraction, but this is offset by alexandrite's extraordinarily high optical damage threshold ($>270Jcm^{-2}$) *(48,58,59,60,61,62)*. The broad emission bands of alexandrite in the visible enables use of a variety of pump sources, including flash lamps, Hg and Xe lamps, sunlight. Using these pump sources, tens of Watts of cw output power have been obtained from alexandrite lasers *(59,60,63)*. There are only a few studies on cw diode-pumped alexandrite lasers *(64,65,66,67)* and only one on Sun-pumped alexandrite laser by Lando *et. al.* in 1999 *(68)*.

Solid-state laser materials with broadband absorption in the visible range, such as alexandrite, have shown interesting features for solar-pumped lasers *(22,69)*. Alexandrite is projected to have the highest slope efficiency for solar pumping. However, its high threshold pump intensity makes this laser material a real challenge for solar-pumped lasers *(22,68,69)*.
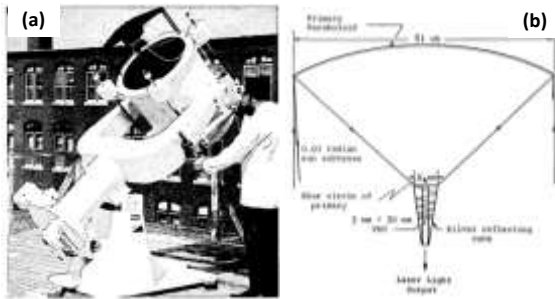
### 2.3.1.4  ND:CR:GSGG

Neodymium: chromium: gadolinium scandium gallium garnet (Nd:Cr:GSGG) is projected to have the next highest efficiency and the lowest threshold for solar pumping *(22,69)*. Nevertheless, Nd:Cr:GSGG crystals are more difficult to operate at high power input levels than Nd:YAG. Several factors contribute to this fact: GSGG has a lower thermal conductivity than YAG, therefore higher thermal gradients develop in GSGG for the same amount of deposited power. GSGG has a smaller fracture resistance and therefore will support a smaller thermal load. The co-doping of GSGG with Cr and Nd allows for a stronger absorption of the input radiation, however there is an accompanying increase in the heat deposited in the crystal; this is even more accentuated since the additional Cr bands are at low wavelengths and therefore a larger energy gap between absorption and emission wavelengths exists *(70)*.

## 2.3.2  STATE-OF-THE-ART

An historical point of view of solar-pumped lasers, containing the most important remarks in this area, are summarized below in TABLE 2.1.

**TABLE 2.1** - Important remarks for development of solar-pumped lasers

| Year | Researchers team | State-of-the-Art of solar-pumped lasers | Type of active medium |
|------|------------------|------------------------------------------|-----------------------|
| **1963** | **Kiss et al.**<br>Princeton, USA | **First solar-pumped solid-state laser**<br><br>The first solar-pumped solid-state laser was reported by Kiss et al. in 1963 *(12)*, using a $Dy^{2+}$-doped $CaF_2$ crystal with liquid neon in a 14-in. aperture spherical mirror. Laser action was registered at 2.36 μm with an estimated absorbed power at threshold of 3W. | **Solid-state laser**<br>$Dy^{2+}$-doped $CaF_2$ |
| **1966** | **Young**<br>American Optical Company, USA | **First solar-pumped 1 W cw Nd:YAG laser**<br><br>The first solar-pumped neodymium-doped: YAG solid-state laser was reported by Young in 1966 *(13)*. 1 W of cw laser output has been obtained at room temperature by using a modified Cassegrain Sun-tracking telescope consisting of a 61-cm diameter paraboloidal primary mirror collector.<br><br><br>**FIG. 2.11** - **(a)** Photograph and **(b)** Design of the Nd:YAG solar laser scheme *(13)*. | **Solid-state laser**<br>Nd:YAG |
| **1983** | **Schneider et al.**<br>University of Florida, USA | **First solar-pumped liquid laser concept**<br><br>The goal of Schneider et al. was to develop a solar-pumped liquid laser that can be scaled up to high power for space applications *(14)*. By using Xenon flash pumping to simulate the solar irradiance provided by the solar concentrator, lasing of liquid phosphor $POCl_3:Nd^{3+}:ZrCl_4$ was achieved. The estimated laser output energy was about 2J. | **Liquid laser**<br>$POCl_3:Nd^{3+}:ZrCl_4$ |

## 18 W cw Nd:YAG solar laser power

**Arashi et al.**

Tohoku University, Japan
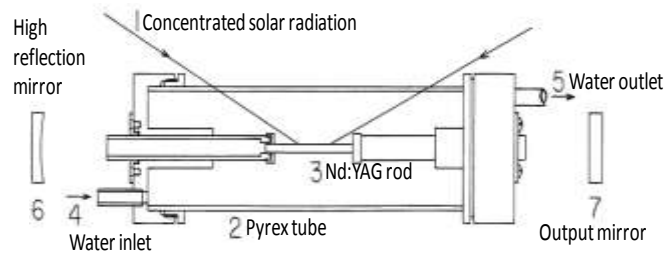
FIG. 2.12 - Solar-pumped Nd:YAG laser head *(21)*

**Solid-state laser**

Nd:YAG

After Young's work there was little progress in the field of solar-pumped solid-state laser research until 1984, when Arashi et al. reported a 18 W cw laser using Nd:YAG *(21)*, by mounting directly a 4 mm diameter, 75 mm length Nd:YAG single-crystal rod within a 50 mm diameter water-cooled flow tube at the focus of a 78.5 $m^2$ area parabolic mirror. However, only 0.23 $W/m^2$ solar laser collection efficiency was achieved in this case.

## First blackbody solar-pumped $CO_2$ laser concept

**Insuik** and **Christiansen**

University of Chicago, USA

This researchers thought of using sunlight to heat a blackbody *(17)*, which will start to emitt IR thermal radiation, since blackbody radiations usually peak at IR region for color temperature less than 3000 K. The laser tube can then be placed inside the blackbody cavity. This scheme would allow the entire solar flux to contribute to the lasing because of the thermodynamics of the blackbody cavity. To proof this concept, they used an electrically heated oven to simulate the solar heated blackbody cavity, obtaining a laser output power of about 4.5 mW.

**Gas laser**

$CO_2$
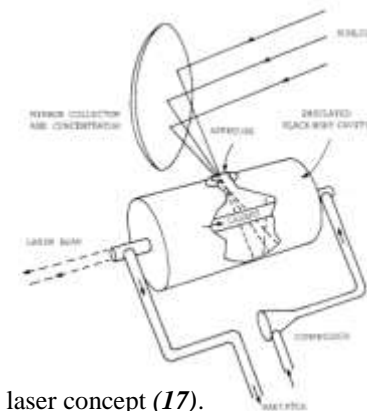


FIG. 2.13 - Blackbody-pumped solar laser concept *(17)*.

**1986**

**DeYoung** and **Weaver**

NASA Langley Research Center, USA
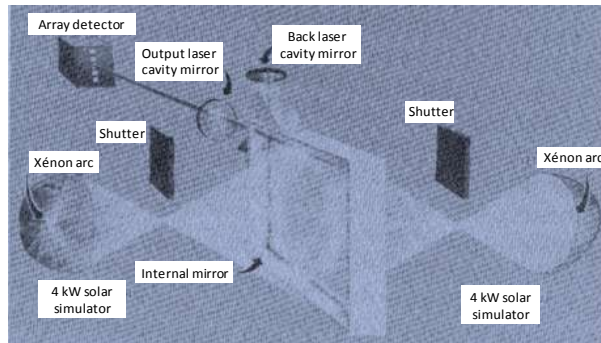


**First solar- simulated pumped iodine laser**

Solar-pumped lasing of perfluorobutyl iodide (n-$C_4F_9I$) *(18)* and pentafluoroethyl iodide ($C_2F_5I$) *(19)* has been achieved, approaching a laser threshold of 100 solar constants (135 kW/m$^2$ at AM0), by simulating the sunlight spectrum with two xenon arc solar simulators. 525 mW *(18)* and 350 mW *(19)* laser power was mesured, respectively.

**Gas laser**

n-$C_4F_9I$
$C_2F_5I$

**FIG. 2.14** - Schematic representation of the experimental setup *(18)*.

---

**1988**

**Weksler** and **Shwartz**

Weizmann Institute of Science, Israel

**60 W cw Nd:YAG solar laser power**

Stable 60 W cw output power was obtained with a slope efficiency exceeding 2% with direct solar pumping of a Nd:YAG rod laser through a compound parabolic concentrator (CPC), which was designed to increase the solar radiation coupled into the laser rod *(22)*. The results were also consistent with predictions based on a solar-pumped laser model for solid-state laser materials with broadband absorption characteristics (e.g., alexandrite and Nd:Cr:GSGG).



1 - laser rod
2 - cooling sleve
3 - 2D-CPC
4,5 - resonator mirrors
6 - CPC output
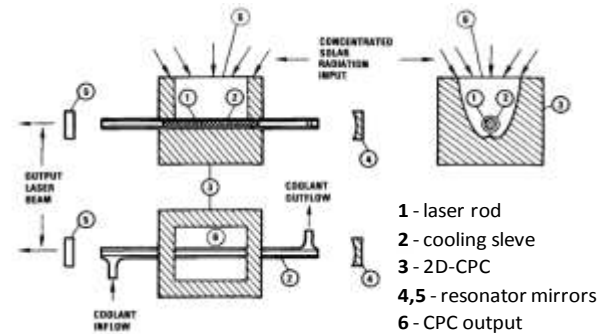
**Solid-state laser**

Nd:YAG

**FIG. 2.15** -The laser head and resonator *(22)*.

## 4.7 W/m² Nd:YAG solar laser collection efficiency

**1996**

**Jenkins et al.**

University of Chicago, USA

In the first solar-pumped Nd:YAG laser systems, there was a tendency to increase the laser output power. However, the collection efficiency was very low, with only 1.56 W/m² from the highest laser power of 60W *(22)*. Concerned with this problem, Jenkins et al. have designed and demonstrated a solar pumped Nd:YAG laser with 4.7 W/m² collection efficiency *(24)*. The laser was side-pumped in a quasi-cw mode by the High-Flux Solar Furnace (HFSF) at the National Renewable Energy Laboratory.

**Solid-state laser**

Nd:YAG

---

**1999**

**Lando et al.**

Weizmann Institute of Science, Israel
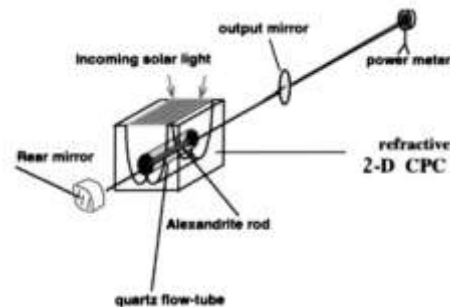


**FIG. 2.16** - Schematic illustration of the solar-pumped alexandrite laser *(68)*.

## Visible solar-pumped solid-state laser

In 1999, Lando et al. reported on two visible solar pumped lasers: a red alexandrite laser with a potential tunability range between 700 and 818 nm, and a frequency doubled Nd:YAG laser operating at 532 nm *(68)*. Highly concentrated solar energy was obtained by a 3-stage concentrator. An output power of up to 12 W was obtained from the alexandrite laser. For Nd:YAG second harmonic generation, output powers of 4.1 W and 8.7 W were respectively achieved through passive and active Q-switching.

**Solid-state laser**

Nd:YAG

Alexandrite

---

## 6.7 W/m² Nd:YAG solar laser collection efficiency

**2003**

**Lando et al.**

Weizmann Institute of Science, Israel

In 2003, Lando et al. improved the Nd:YAG solar laser collection efficiency to 6.7 W/m² *(25)*, by using a 6.75 m² segmented primary mirror mounted in direct-tracking mode and a secondary 3D-CPC conjugated with a 2D-CPC concentrator. A comprehensive study of solar-pumped laser beam quality and brightness was also reported, achieving 0.032 W brightness figure of merit.
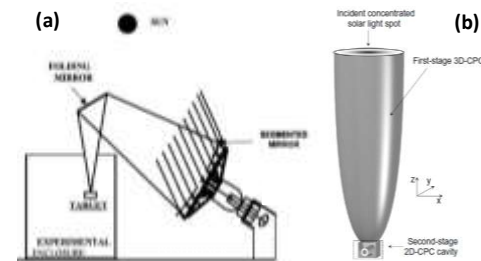


**FIG. 2.17** - **(a)** The primary concentrator mirror **(b)** The double-stage concentrator *(25)*.

**Solid-state laser**

Nd:YAG

**Study of a conical-toroidal mirror resonator for solar-pumped thin-disk lasers**

A conical-toroidal mirror resonator combined with a Nd/Cr-codoped GSGG thin disk was proposed *(71)*. Unlike the conventional thin-disk lasers, the optical ray path inside the media has radial direction, parallel to the face of the disk, which is suitable for solar pumping because the pump light could be irradiated to the wide surface of the disk.

**Endo**

Tokai University, Japan

FIG. 2.18 - Schematic of a resonator with a conical-toroidal reflector and a thin-disk *(71)*.

**Solid-state laser**

Cr:Nd:GSGG

**2007**

**18.7 W/m$^2$ Cr:Nd:YAG solar laser collection efficiency with Fresnel lens**

Even though parabolic mirrors have been explored to achieve tight focusing of incoming solar radiation, the adoption of a Fresnel lens as a primary solar concentrator in 2007 by Yabe et. al. has boosted significantly the solar laser collection efficiency to 18.7 W/m$^2$ *(26)*. This has revitalized solar laser researchers, revealing a promising future for renewable recovery of Mg from MgO. It was also the first time that Cr:Nd:YAG laser was tested to improve the efficiency of Nd$^{3+}$-doped YAG laser due to the enhanced absorption of sunlight spectrum compared with Nd:YAG.

**Yabe et al.**

Tokyo Institute of Technology, Japan



FIG. 2.19 - Test system for laser from natural sunlight *(26)*.

**Solid-state laser**

Cr:Nd:YAG

**2011**

**Liang** and **Almeida**

Universidade NOVA de Lisboa, Portugal
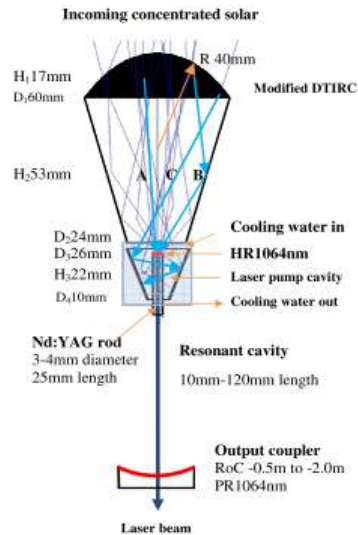
**19.3 W/m² Nd:YAG solar laser collection efficiency with Fresnel lens**

19.3 W/m² solar laser collection efficiency was later achieved by our research team in 2011 *(29)* exciting a 4 mm diameter, 25 mm length Nd:YAG single-crystal rod through a 0.64 m² area Fresnel lens. Considerable enhancement in laser beam quality was achieved, leading to record brightness figure of merit of 0.086W *(29)*. Substantial reduction in threshold pump power to 94 W was also reported. These results triggered the discussions about which medium between Cr:Nd:YAG ceramics and Nd:YAG single-crystal was more suitable for solar-pumped lasers *(30,56,72)*.

**FIG. 2.20** - The solar laser head positioned in the focal zone *(29)*

**Solid-state laser**

Nd:YAG

**Highlights:** This research was featured in *Towards Megawatt Solar Powered Lasers for Magnesium Production and future space applications*, in Nextbigfuture website *(2)*

**2012**

**Dinh et al.**

Tokyo Institute of Technology, Japan

**30 W/m² record -high Nd:YAG solar laser collection efficiency with Fresnel lens**

In 2012, record-high collection efficiency of 30.0 W/m² was attained by pumping a 6 mm diameter, 100 mm length Nd:YAG single-crystal rod through a 4 m² area Fresnel lens *(30)*. The collection efficiency with the Nd:YAG rod was also unexpectedly better than that with Cr:Nd:YAG ceramic rod.
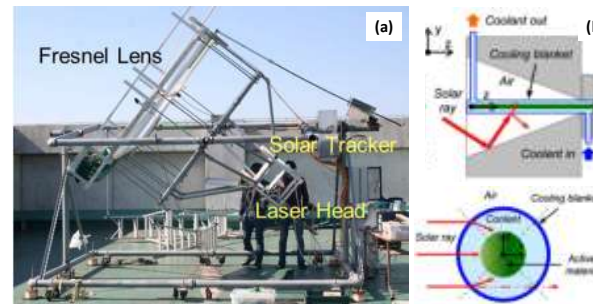


**FIG. 2.21 - (a)** 2 m × 2 m Fresnel lens. **(b)** Liquid light-guide lens configuration *(30)*.

**Solid-state laser**
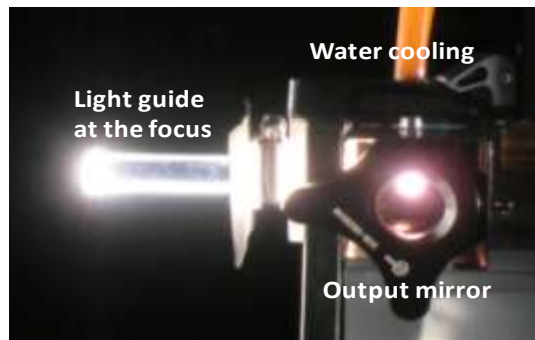
Nd:YAG

**FIG. 2.22** - Photograph of the Nd:YAG laser head at the focus of the PROMES-CNRS MSSF *(36)*.

**0.29 W solar laser beam brightness**

Significant improvement in solar-pumped laser beam brightness has been achieved by us in 2012 *(36)*. By side-pumping of a 4 mm diameter, 30 mm length Nd:YAG single-crystal rod with the PROMES-CNRS horizontal-axis MSSF solar facility *(44)*, 0.29 W brightness figure of merit was achieved, being 3.4 times higher than the previous record *(29)*. Also, solar laser collection efficiency of 9.6 W/m$^2$ was registered, surpassing by 1.4 times the previous record with parabolic mirror system in 2003, by Lando et al. *(25)*.

**Almeida et al.**

Universidade NOVA de Lisboa, Portugal

**Solid-state laser**

Nd:YAG

**New concept of solar-pumped disk laser**

In 2012, we have also proposed a new concept of applying thin-disk laser technology *(73)*, initially developed for diode-pumped laser systems *(74,75)*, to solar-pumped lasers, through Fresnel lenses. A multi-Fresnel lens scheme is used for side-pumping a single-crystal Nd:YAG disk. Compared to the previous solar-pumped thin-disk laser concept *(71)*, this approach is much more effective in alleviating the thermal management problems in solar-pumped disk lasers.

**Liang** and **Almeida**

Universidade NOVA de Lisboa, Portugal
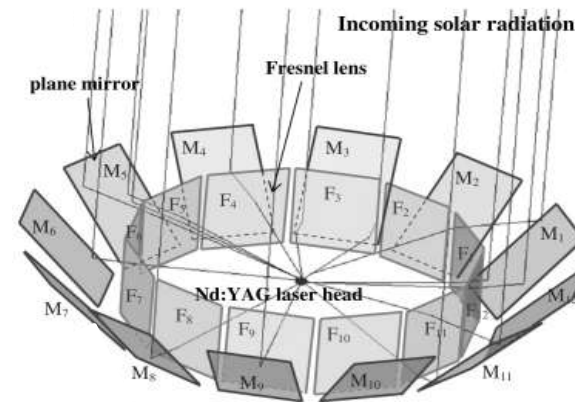


**FIG. 2.23** - Multi plane mirror — Fresnel lens scheme for solar-pumped disk laser *(73)*

**Solid-state laser**

Nd:YAG

**Highlights:** The publication regarding this concept *(73)* was selected for inclusion in Spotlight on Optics, OSA journals *(76)*

**First solar-pumped fiber laser**

**Mizuno et al.**

Toyota Central Research and Development Laboratories, Inc., Japan

Toyota Technological Institute, Japan
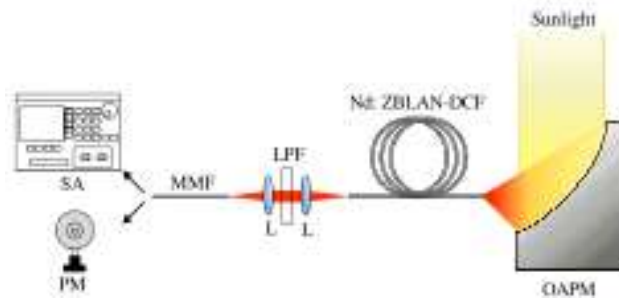


**FIG. 2.24** - Schematic set-up of the solar-pumped fiber laser experiment *(77)*.

Also in 2012, Mizuno et al. demonstrated the realization of a solar-pumped fiber laser operating under natural sunlight using a Nd-doped fluoride optical fiber as a laser medium *(77)*. Their intention was to exploit the very large surface-area-to-volume ratio of the fiber media to remove the need for active cooling. 0.57 mW output power was measured *(77)*, resulting in only 0.3 $W/m^2$. Indeed, directing all excitation light into the core of the fiber is challenging because its size for a single-mode fiber is smaller than the smallest solar image capable of being provided by typical optical mirrors or lenses.

**Fiber laser**

Nd:ZBLAN-DCF

---

**First side-pumped Cr:Nd:YAG solar laser**

**2013**

**Liang et al.**

Universidade NOVA de Lisboa, Portugal

PROMES-CNRS, France

To clarify the advantages of Cr:Nd:YAG ceramics rods in solar-pumped lasers, a fused silica light guide is coupled to a compound V-shaped cavity within which a 7 mm diameter 0.1 at.% Cr:1.0 at.% Nd:YAG ceramic rod is uniformly side-pumped through the MSSF solar facility *(56)*. 33.6 W cw laser power and 2.6% slope efficiency were achieved, resulting in a general improvement compared to the last year's results *(36)*. On contrary, highly intense solar end-pumping will inevitably raise the thermal load of the ceramic rod, hampering the Cr:Nd:YAG solar laser efficiency.
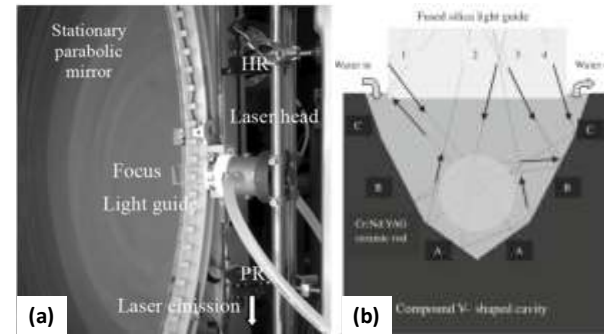


**FIG. 2.25** - **(a)** The Cr:Nd:YAG laser resonator within the MSSF solar facility **(b)** Compound V-shaped pump cavity *(56)*.

**Solid-state laser**

Cr:Nd:YAG

---

**Highlights:** The publication regarding this report *(56)* was selected by Renewable Energy Global Innovations as a Key Scientific Article *(78)*.

**13.9 W/m$^2$ Nd:YAG solar laser collection efficiency with parabolic mirror system**

**Almeida et al.**

Universidade NOVA de Lisboa, Portugal



We have also reported a significant improvement in solar laser collection efficiency through a heliostat–parabolic mirror system in PROMES-CNRS, by end-side pumping a Nd:YAG single-crystal rod *(33)*. 40 W cw laser power was measured, leading to 13.9 W/m$^2$ collection efficiency and 2.9% slope efficiency.

**Solid-state laser**

Nd:YAG

**FIG. 2.26** - The Nd:YAG laser head at the focus of the PROMES-CNRS MSSF *(33)*.

This progress was featured in Laser Physics Highlights of 2013 *(79)*.

**First TEM$_{00}$-mode solar laser/ 1.9 W solar laser brightness**

**Liang** and **Almeida**

Universidade NOVA de Lisboa, Portugal

Also in 2013, a substantial progress in solar laser beam brightness with Fresnel lens was reported by us, through the first generation of TEM$_{00}$-mode solar laser *(42)*. 2.3 W continuous-wave TEM$_{00}$-mode solar laser power (M$^2 \leq$ 1.1) was produced, corresponding to 1.9 W laser beam brightness figure of merit, which was 6.6 times larger than the previous record *(36)*. The fundamental mode slope efficiency of 0.7% and the collection efficiency of 2.93 W/m$^2$ were achieved.
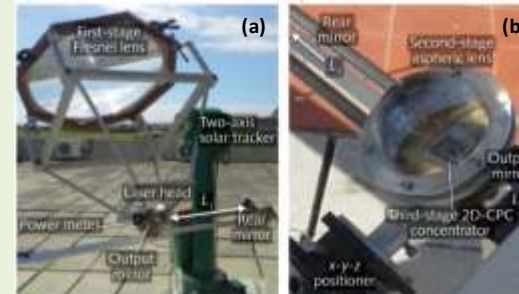


**FIG. 2.27** - (a) The solar-pumped TEM$_{00}$ mode Nd:YAG laser system (b) The laser head *(42)*.

**Solid-state laser**

Nd:YAG

**Highlights:** This achievement was highlighted in Laser Focus World *(20)* and featured in *Towards Megawatt Solar Powered Lasers for Magnesium Production and future space applications*, in Nextbigfuture website *(2)*. Also shared in Photonics Online and Photonics Solutions.

**Design of high power, high brightness solar laser**

**Almeida** and **Liang**

Universidade NOVA de Lisboa, Portugal

**Liang et al.**

Universidade NOVA de Lisboa, Portugal

Two solar pumping schemes were proposed by us to both enhance both solar laser efficiency and brightness, by side-pumping uniformly a Nd:YAG rod *(53,54)*. Both are composed of four Fresnel lenses and four secondary fused-silica concentrators. Also, since in FIG. 2.28(b) the secondary concentrators are shifted along the laser rod, followed by four hollow 2D-CPC concentrators, and four V-shaped pumping cavities, it is possible to scale up the solar pumping scheme *(54)*.

**Solid-state laser**
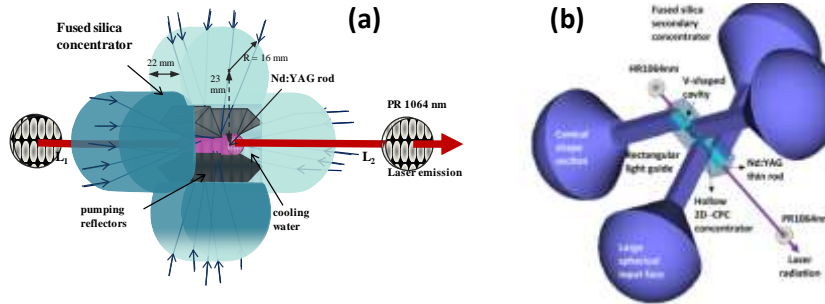
Nd:YAG



**FIG. 2.28** - Detailed view of the solar laser heads *(53,54)*

**2014**

---

**20.3 W cw end-side-pumped Nd:YAG grooved rod with Fresnel lens**

**Xu et al.**

Beijing Institute of Technology, China

Also in 2014, Nd:YAG rod with grooved sidewall has been employed for the first time in a end-pumping solar-pumped laser scheme by Xu et al. *(80)*. The efficiency and beam quality were improved relatively to other unpolished rods. The maximum output power from the grooved rod was more than 50% higher than the maximum output power from the unpolished rod, leading to maximum slope efficiency of 8.34% compared to only 6.13% for unpolished rod.
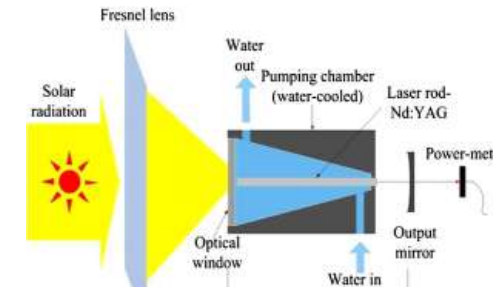


**FIG. 2.29** - Schematic of the solar pumped laser *(80)*.

**Solid-state laser**

Nd:YAG

### 21.1 W/m² solar laser collection efficiency with parabolic mirror system

**Almeida et al.**

Universidade NOVA de Lisboa, Portugal

PROMES-CNRS, France
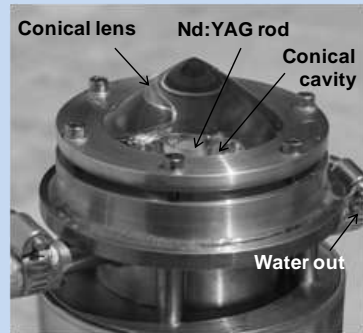


In 2015, we reported a large improvement in both collection and slope efficiencies by end-side-pumping a Nd:YAG solar laser through a heliostat – parabolic mirror system in PROMES-CNRS *(34)*. A 56 W cw laser power was measured, corresponding to 21.1 W/m² record-high solar laser collection efficiency. 4.9% slope efficiency was also calculated, corresponding to 170% enhancement over our previous result with same solar facility *(33)*.

**FIG. 2.30 -** Photograph of the Nd:YAG laser head *(34)*

**Solid-state laser**

Nd:YAG

---

### 4.0 W solar laser brightness

**Liang et al.**

Universidade NOVA de Lisboa, Portugal

PROMES-CNRS, France

In the same year, we have also registered a significant improvement in solar-pumped laser beam brightness by pumping a 3 mm diameter Nd:YAG single-crystal rod through a rectangular fused silica light guide and a 2D-CPC concentrator *(37)*, being also the first time that $TEM_{00}$ solar laser emission was produced with heliostat-parabolic mirror system. 4.4 W continuous-wave $TEM_{00}$ mode 1064 nm solar laser power was produced, attaining 4.0 W laser beam brightness figure of merit, which was 2.1 times higher than the previous record by a Fresnel lens *(37)*.
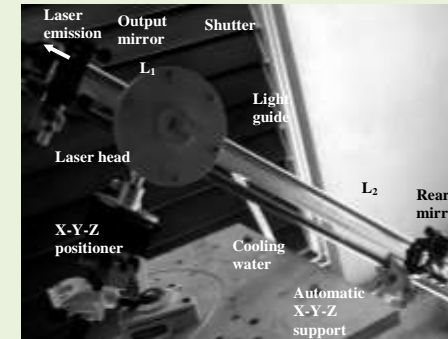


**FIG. 2.31 -** Asymmetric resonator for $TEM_{00}$ mode Nd:YAG laser *(37)*

**Solid-state laser**

Nd:YAG

**5.5 W cw TEM$_{00}$-mode laser power**

**Almeida et al.**

Universidade
NOVA de Lisboa,
Portugal

PROMES-CNRS,
France
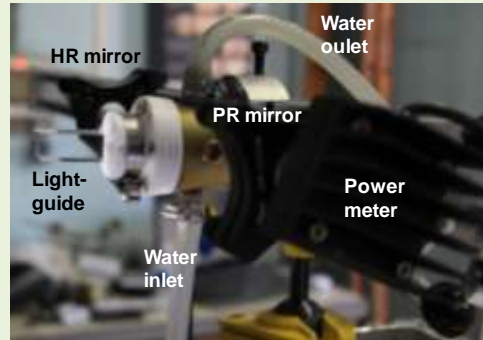


FIG. 2.32 - Solar-pumped TEM$_{00}$-mode Nd:YAG laser system *(38)*.

In 2015, 5.5 W cw TEM$_{00}$-mode solar laser was registered, improving the TEM$_{00}$-mode solar laser power *(38)*. A 4 mm-diameter, 30-mm-length 1.1 at.% Nd:YAG single-crystal rod was pumped by a light guide with a large rectangular cross section, which also enabled a stable uniform pumping profile along the laser rod, resulting also in an enhanced tracking error compensation capacity. 2.84 W/m$^2$ TEM00 mode collection efficiency and 1.27% slope efficiency were found, representing an enhancement of 150% and 157% respectively over that of the previous TEM$_{00}$-mode solar laser, in 2014.

**Solid-state laser**

Nd:YAG

**A path to Solar Pumped Lasers via Radiative Energy Transfer**

**Reusswig et al.**

Massachusetts
Institute of
Technology, USA

Technion-Israel
Institute of
Technology, Israel
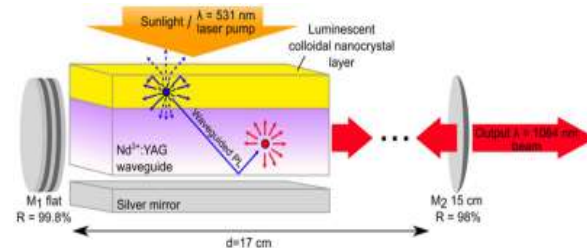


FIG. 2.33 - Illustration of cascade energy transfer for solar pumped lasers *(81)*.

Also in 2015, Reusswig et al. presented an architecture for solar pumped lasers that uses a luminescent solar concentrator (LSC) *(81)* to shift the part of solar spectrum that otherwise could not be absorbed by the active medium, to the frequency range where active medium has strong absorption bands, thereby increasing the pumping efficiency of the laser. In this case, a 750-μm-thick Nd$^{3+}$-doped YAG planar waveguide was sensitized by a luminescent CdSe/CdZnS (core/shell) colloidal nanocrystal, yielding a peak cascade energy transfer of 14% and an equivalent quasi-CW solar lasing threshold of 23 W/cm$^2$, approximately 230 suns.

**Solid-state laser**

Nd:YAG

CdSe/CdZnS

**Design of solar-pumped semiconductor laser**

**Quarterman** and **Wilcox**

University of Dundee, United Kingdom

In order to find a solution to achieve simultaneously a high efficiency and beam quality of solar lasers in a scalable manner, Quarterman and Wilcox have proposed a new solar laser architecture, by a VECSEL *(82)*, also known as semiconductor disk lasers. Diode-pumped VECSELs proven capability for high power and efficiency, and good beam quality *(83,84)*. But, primarily due to their broadband optical absorption and very short absorption lengths, VECSELs can be highly attractive candidates for solar - pumped semiconductor lasers *(85,86)*.
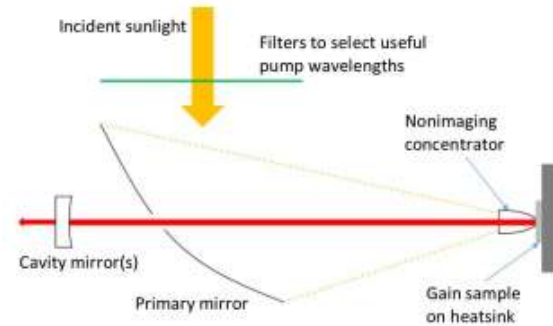
**Semiconductor laser**

VECSEL InGaAs, GaAsP active region



**FIG. 2.34 -** Example of a system where a two-stage solar concentrator i**s** used to pump a VECSEL *(82)*.

---

**2016**

**Liang et al.**

Universidade NOVA de Lisboa, Portugal

PROMES-CNRS, France
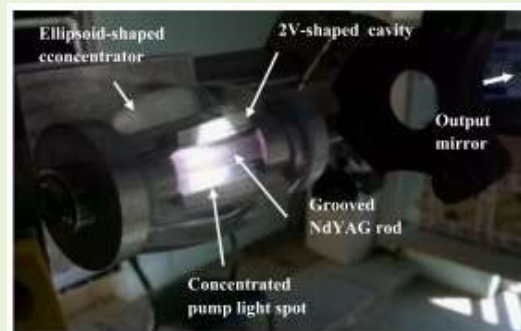


**4.0 W/m² TEM$_{00}$-mode collection efficiency**

In 2016, through the same solar facility of PROMES-CNRS, record TEM$_{00}$-mode laser collection efficiency of 4.0 W/m² was obtained by side-pumping a 4 mm diameter, 34 mm length grooved Nd:YAG rod with an ellipsoid-shaped fused silica secondary concentrator and a 2V-shaped pumping cavity *(41)*. Record TEM$_{00}$-mode laser slope efficiency of 2.36% was also achieved.

**Solid-state laser**

Nd:YAG

**FIG. 2.35** - The solar laser head composed of the ellipsoid-shape fused silica concentrator and 2V-shaped cavity for efficiently side-pumped a grooved Nd:YAG rod *(41)*.

### Nd:YAG solar laser efficiency enhancement using Cr:LiCAF frequency down-shifter

**Payziyev** and **Makhmudov**

Uzbekistan Academy of Sciences, Uzbekistan

Payziyev and Makhmudov studied the possibility of increasing the Nd:YAG solar laser efficiency with the use of Cr:LiCAF as an external solar spectrum frequency converter *(87)*. It was shown that the use of frequency down-shifter increased 2.4 and 1.9 times more the Nd:YAG laser efficiency through end-pumping and side-pumping configurations, respectively.
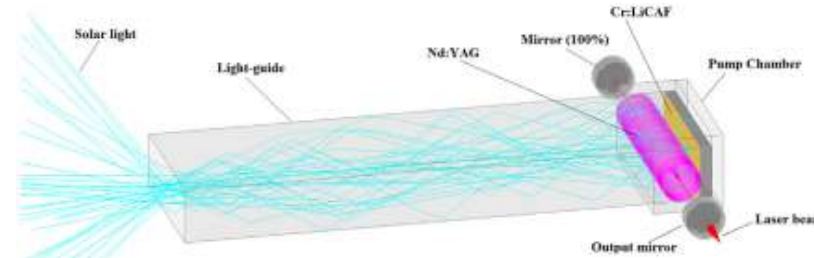


**FIG. 2.36** - Side-pumped laser design with a frequency converter *(87)*.

**Solid-state laser**

Nd:YAG

Cr:LiCAF

---

### 25 W/m$^2$ solar collection efficiency with parabolic mirror system

**Liang et al.**

Universidade NOVA de Lisboa, Portugal
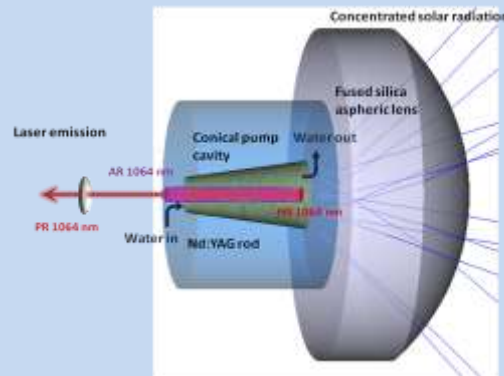


**FIG. 2.37** - Design of novel Nd:YAG laser head *(35)*.

Also in 2016, a new progress in solar laser collection efficiency was reported, by using the heliostat-parabolic mirror system of Universidade NOVA de Lisboa *(35)*. A large aspheric fused silica lens was used to couple efficiently the concentrated solar radiation from the focal zone of a 1.5 m diameter primary concentrator into a 4mm diameter, 35mm length Nd:YAG single-crystal rod. 29.3 W continuous-wave laser power was measured, attaining 25.0 W/m$^2$ solar laser collection efficiency, corresponding to 19% increase over the previous record with parabolic mirror. 5.1% record slope efficiency was also measured.

**Solid-state laser**

Nd:YAG

| | | |
|---|---|---|
| **2017** | **Liang et al.**<br><br>Universidade NOVA de Lisboa, Portugal<br><br>PROMES-CNRS, France | **Record 31.5 W/m² multimode and 7.9 W/m² TEM₀₀-mode solar collection efficiencies** |

**Record 31.5 W/m$^2$ multimode and 7.9 W/m$^2$ TEM$_{00}$-mode solar collection efficiencies**

Most recently, by end-side-pumping the 4 mm diameter 35 mm length Nd:YAG single-crystal rod with PROMES-CNRS heliostat-parabolic mirror solar energy concentration system, significant progresses in both multimode and fundamental mode regimes were reported *(31)*. Maximum multimode solar laser power of 37.2 W was registered, corresponding to record-high collection efficiency of 31.5 W/m$^2$ and 8.9% slope efficiency. By adopting the asymmetric large-mode resonator cavity, 9.3 W cw TEM$_{00}$-mode (M$^2$ ≤1.2) solar laser power and consequently 7.9 W/m$^2$ fundamental-mode laser collection efficiency was registered, doubling the previous record with parabolic mirror *(41)*.
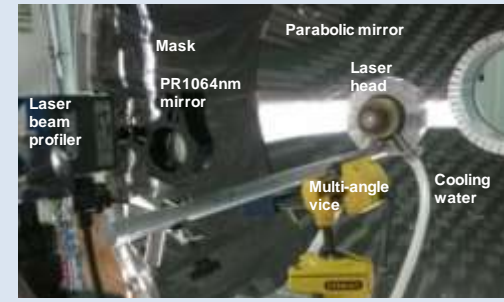


**FIG. 2.38** - TEM$_{00}$-mode laser power in PROMES-CNRS solar facility *(31)*.

**Solid-state laser**

Nd:YAG

This substancial progress was reported in both Renewable Energy Global Innovations *(88)* and Laser Focus World *(89)*.

**Mehellou et al.**

Universidade NOVA de Lisboa, Portugal

PROMES-CNRS, France

**Stable TEM$_{00}$-mode solar laser operation**

Also in PROMES-CNRS at the same year, very stable TEM$_{00}$-mode solar laser operation was achieved by using a twisted fused silica light-guide to uniformly side-pumping a thin and long Nd:YAG rod *(90,91)*. Excellent TEM$_{00}$-mode laser beam profile at M$^2$ ≤ 1.05 and very good output power stability of less than 1.6% were achieved. Heliostat orientation error dependent laser power variation was considerably less than previous solar laser pumping schemes.



**FIG. 2.39** - Solar laser system with the twisted fused silica light-guide for the extraction of stable TEM$_{00}$-mode laser power *(91)*.

**Solid-state laser**

Nd:YAG

### Low-concentrated solar laser (SPL) with a fiber laser

**Masuda et al.**

Toyota Motor Corporation, Japan

Tokai University, Japan

In 2017, Masuda et al. were devoted to reduce significantly the lasing threshold of present-day solar-pumped lasers at a extremely low concentration factor by using a fiber laser with transverse excitation geometry *(92)*. With the proposed system, it was demonstrated a solar lasing threshold at a concentration factor of two orders of magnitude smaller than that of conventional solar-pumped lasers, resulting however in a dismal slope efficiency of only $3.6 \times 10^{-5}$%.
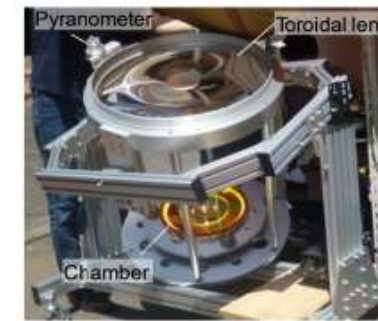
**Fiber laser**

Nd$^{3+}$-doped silica fiber



**FIG. 2.40** - Photo of the solar-pumped fiber laser *(92)*.

### Multi-amplifier laser system with white-light pumping

**Saiki et al.**

Kansai University, Japan

Institute for Laser Technology, Japan

Osaka University, Japan
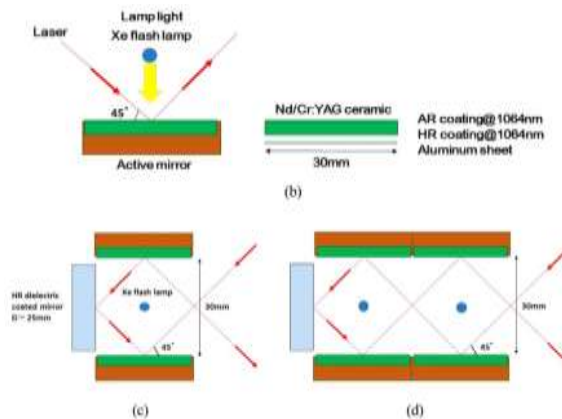


The amplification property of Nd/Cr:YAG ceramics under quasi-solar light pumping was studied *(93)*. For simulating the solar pumping source, a Xe flash lamp was used. A seed cw laser with a 1064 nm wavelength was amplified by multi-stage Nd/Cr:YAG ceramic active mirror amplifiers. At a pumping laser power of 340 W/cm$^2$, the temperature of the ceramic disk was 100 °C, and an output laser peak power of 1.6 kW was achieved. The evaluated optical-optical conversion efficiency for the volume of ceramics in which the laser passes was 63%.

**Solid-state laser**

Cr:Nd:YAG

**FIG. 2.41** - Experimental setup (a) Measurement system. (b) Structure of single active-mirror amplifier. (c) Two-stage active-mirror amplifier system. (d) Four-stage active-mirror amplifier system *(93)*.

The remarks shadowed at light blue, green and orange colors are addressed and discussed in CHAPTER 5, CHAPTER 6, and CHAPTER 7, respectively.

As observed in TABLE 2.1, solar laser has more than 50 years of history. The first report of solar-pumped laser occurred shortly after the invention of laser, in 1963 by Kiss et al. *(12)*, while in 1966 Young *(13)* succeeded with the first solar-pumped Nd:YAG solid-state laser. After Young's work there was little progress in the field of solar-pumped solid-state laser research until 1984, when the group of Arashi et al. *(21)* reported the development of a solar-pumped Nd:YAG laser. Liquid and Gas lasers have also been considered as candidates for solar lasers *(14,17,19)*. However, solar laser research has essentially converged in systems with bulk solid-state medium, essentially Nd:YAG and Cr:Nd:YAG. In the first solar-pumped Nd:YAG laser systems, between 1966 and 1988, there was a tendency to increase the laser power output power *(13,21,22)*. However, the most important parameter for the assessment of solar laser is its efficiency, which was not seriously considered until 1996 by Jenkins et al. *(24)* who reported a substantial increase in solar laser output per unit collection area, which was further improved to 6.7 $W/m^2$ in 2003 by Lando et al. *(25)*. This has remained a record value until 2007, when the solar laser collection efficiency was boosted to 18.7 $W/m^2$ by Yabe et al. *(26)* with the adoption of Fresnel lens as primary concentrator and Cr:Nd:YAG as active medium. This has revitalized the solar laser researchers, and in 2011 the Nd:YAG solar collection efficiency was boosted to 19.3 $W/m^2$ by Liang and Almeida *(29)*. This result raised doubts about which laser material, between Nd:YAG and Cr:Nd:YAG *(56)*, would be more suitable for solar-pumped lasers. In 2012, 30 $W/m^2$ Nd:YAG solar laser collection efficiency was further boosted by Dinh et al *(30)*, being unexpectedly better than that with Cr:Nd:YAG. Slope efficiency of 8.6% was also achieved. These values remained records until 2017 within the framework of this PhD *(31)*.

As noted above, the most significant improvements in solar laser efficiency have occurred in the past ten years with the adoption of the economically competitive Fresnel lenses as primary concentrators. However, this has put aside the advantages of parabolic mirrors for solar laser research. Thus, one of the main objectives of this PhD project was to improve the solar laser efficiency with the use of parabolic mirror systems, as summarized in TABLE 2.1 and explained in detail in Chapter 5. Solar laser beam brightness is also a very important parameter, which has been neglected until 2003 by Lando et al. *(25)* and more seriously considered in 2012 by Almeida and Liang *(36)*. For these reasons, another important objective of this PhD project was to boost the solar laser beam brightness, whose efforts are summarized in TABLE 2.1 and addressed in Chapter 6. The solar laser beam stability is also an essential parameter, but it has not been highly regarded. However, in 2017 very stable $TEM_{00}$ mode solar laser stability was reported under this PhD project. The efforts for this achievement are described in detail in Chapter 7.

It is worth noting that above mentioned developments in the solar laser performance has also unleashed the interests of solar laser research groups from other countries to study and develop novel solar laser concepts with new types of laser materials, as summarized in TABLE 2.1: solar-pumped fiber lasers *(77,92)*; solar-pumped Vertical External Cavity Surface External Laser *(82)*; a path for high efficient solar-pumped laser via Luminescent Solar Concentrators *(81)* and frequency energy converter *(87)*; solar laser amplification by multi-stage Cr:Nd:YAG ceramic disks *(93)*.

The booming of solar-pumped lasers in these recent years offers bright prospects for the development of solar laser performances in the years to come, as well as the extension of solar laser application areas.
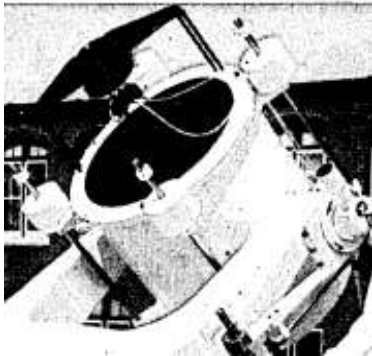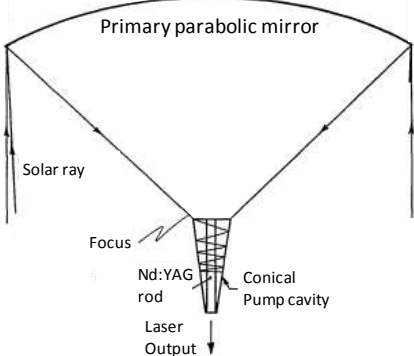
## 2. SOLID-STATE LASERS
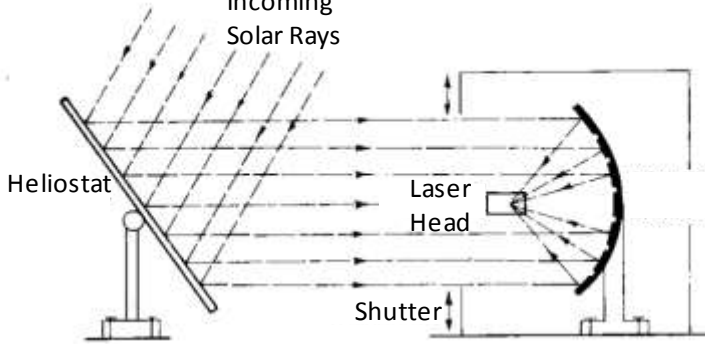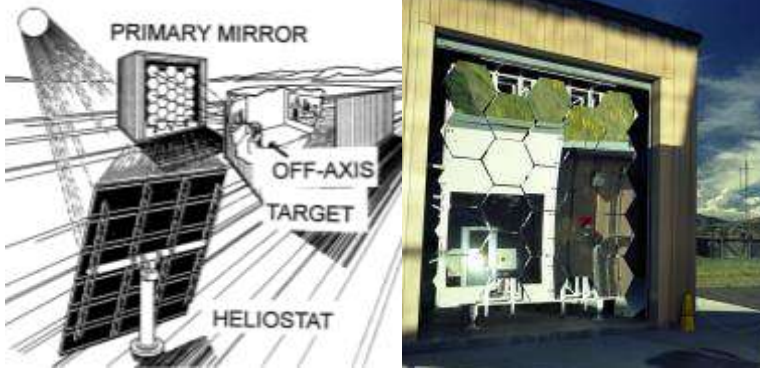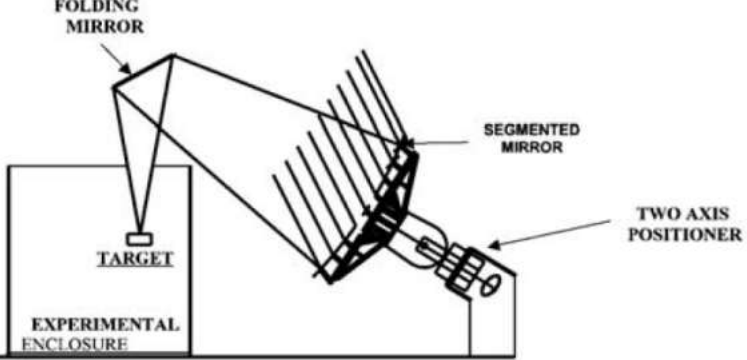
# 3 SOLAR ENERGY COLLECTION AND CONCENTRATION SYSTEMS FOR SOLAR LASERS

Most solar-pumped lasers require a concentration factor in the order of thousands to obtain a sufficient gain in the irradiated active medium. Therefore, high solar concentration optics are needed. As verified in the previous Chapter, the solar laser collection efficiency has been dramatically increased after the utilization of Fresnel lenses as primary solar concentrators *(26)*, which, in our opinion, led the other solar researchers to put aside the advantages of the parabolic mirrors. Although Fresnel lenses are cost-effective, the largely dispersed radiation distributed along its focal zone hampers further efficient light concentration to a small and thin active medium. Thus, to achieve higher solar laser efficiency with Fresnel lens, larger rod is more suitable *(26,30,80,94)*, which in turn makes it less resistant to thermal stress. Parabolic mirrors, instead, allow to achieve a tight focusing of incoming solar radiation. It is therefore very meaningful to improve the performance of solar-pumped lasers through parabolic mirrors.

The solar energy collection and concentration systems utilized in solid-state solar-pumped lasers, from 1966 to 2017, are described below, in TABLE 3.1.

**TABLE 3.1** - Solar collectors and concentrators for solid-state solar lasers.

| Year/ Advances/ Researchers | Solar Energy and Concentration Solar Laser Systems |
|---|---|
| | **Parabolic Mirror Systems** |
| **1966**<br><br>**First 1 W cw Nd:YAG solar laser**<br><br>*Young (13)*<br>AO | **Modified Cassegrain sun-tracking telescope**<br><br><br><br>**Direct tracking mode**<br><br>Primary concentrator: 61 cm diameter; **0.29 m$^2$** collection area; f/1.5 |

| | |
|---|---|
| **1988** | **WIS Solar Furnace** |
| 60 W Nd:YAG solar laser |  |
| *Weksler & Shwartz (22)* WIS | **Indirect tracking mode** <br> Segmented Primary concentrator: 600 spherical mirrors; **38.5 m²** collection area |
| **1996** | **NREL High-Flux Solar Furnace (HFSF)** |
| **4.7 W/m²** collection efficiency |  |
| *Jenkins et al. (24)* UChicago | **Indirect tracking mode** (off-axis) <br> Segmented Primary concentrator: 25 hexagonal segments; **12.1 m²** collection area; 7.3 m focal length |
| **2003** | **WIS Astigmatic Corrected Target Aligned (ACTA) Solar Concentrator** |
| **6.7 W/m²** collection efficiency <br><br> 0.032 W solar laser beam brightness |  |
| *Lando et al. (25)* WIS | **Direct tracking mode** <br> Segmented Primary concentrator: 61 hexagonal segments; **6.75 m²** collection area; 8.5 m focal length |
| **2012** | **PROMES-CNRS Medium Size Solar Furnace (MSSF)** |

| | |
|---|---|
| **0.29 W** solar laser beam **brightness**<br><br>**9.6 W/m²** collection efficiency<br><br>*Almeida et al. (36)*<br>NOVA<br><br>**2013 - 2017**<br>During PhD | <br>**Indirect tracking mode**<br>Primary concentrator: **2 m diameter** parabolic mirror; 0.85 m focal length |
| | **Fresnel Lens Systems** |
| **2007**<br><br>**18.7 W/m²** collection efficiency<br><br>*Yabe et al. (26)*<br>TITech |  **TITech Fresnel Lens System**<br><br>**Direct tracking mode**<br><br>Primary concentrator:<br>1.33 × **0.98 m²** collection area;<br>1.2 m focal length |
| **2011**<br><br>**19.3 W/m²** collection efficiency<br><br>*Liang et al. (26)*<br>NOVA | **NOVA Fresnel Lens System**<br><br>**Direct tracking mode**<br><br>Primary concentrator:<br>**0.636 m²** collection area;<br>1.2 m focal length<br><br> |
| **2012**<br><br>**30 W/m²** collection efficiency<br><br>8.6% slope efficiency<br><br>*Dinh et al. (26,95)*<br>TITech |  **TITech Fresnel Lens System**<br><br>**Direct tracking mode**<br><br>Primary concentrator:<br> **4 m²** collection area;<br>2 m focal length |

The solar facilities utilized in this work are described in the present Chapter. Solar energy collection and concentration is achieved through: PROMES-CNRS MSSF solar facility and the

recently new NOVA heliostat-parabolic mirror system. Before its final construction, the solar laser performance was also studied through NOVA Fresnel lens system. For a better understanding of the advantages of these systems, the physical fundamentals of both parabolic mirror and Fresnel lens systems are also addressed in the next subchapters.

## 3.1 PARABOLIC MIRRORS

The equation that defines a parabola with the vertex at $(x, y) = (0,0)$ is given by:

$$y = ax^2 \tag{3.1}$$

In which $a$ is the aperture of the parabola and it is related to the focal length $f$ through:

$$f = \frac{1}{4a} \tag{3.2}$$

Thus, the shape of the parabola as a function of its focal length is obtained by:

$$x^2 = 4y.f \tag{3.3}$$

The concentration of sunlight by a parabolic mirror is schematically represented in FIG. 3.1, which shows how the reflected radiation from the rim of the parabola determines the width of the focal zone.
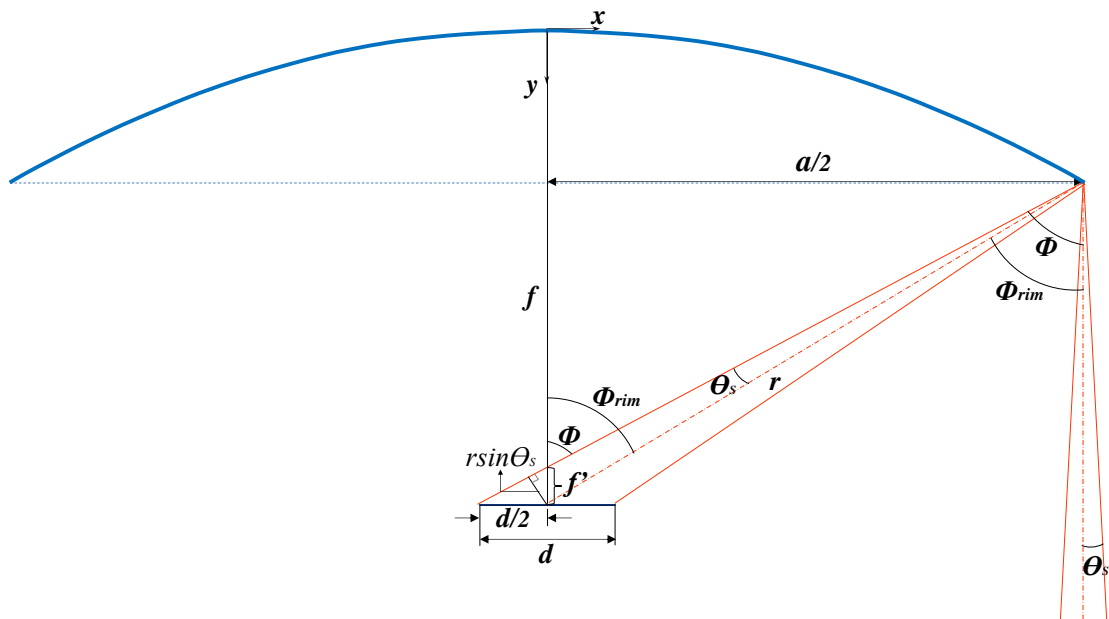


**FIG. 3.1** - Concentration of sunlight by a parabolic mirror of focal length $f$ and rim angle $\Phi rim$.

A parabola focuses rays parallel to its axis into its focal point. However, due to the superior diameter of the Sun relative to Earth, Sun rays are not parallel, making an apparent half-angle $\Theta s$ of 0.267° in relation to Earth. In this case, the focal width becomes a range defined by $d$. Since the parabolic mirror has rotational symmetry about its axis, $d$ also represents the diameter of the image formed at its focus. The width of the focus $d$ is given by:

$$d = 2f'\tan\phi = 2f'\frac{\sin\phi}{\cos\phi} \tag{3.4}$$

where $\phi = \phi_{rim} + \theta_s$ is the angle between the y-axis and the reflected ray with angle $\theta_s$. $\Phi_{rim}$ is the rim half angle. Since $f' = r\sin\theta_s / \sin\phi$, $d$ can be expressed by:

$$d = \frac{2r\sin\theta_s}{\cos\phi} \tag{3.5}$$

The aperture of the parabolic mirror $a$ is given by:

$$a = 2r\sin\phi_{rim} \tag{3.6}$$

Therefore, Eq. (3.5) can then be rewritten to obtain the width of the focus $d$ as a function of the aperture of the parabolic mirror $a$, through eq. (3.7):

$$d = \frac{a\sin\theta_s}{\sin\phi_{rim}\cos(\phi_{rim} + \theta_s)} \tag{3.7}$$

From eq. (3.7) and FIG. 3.1, we can verify that for the same focal length $f$ the width of the focus increases with increasing aperture of the parabolic mirror and, consequently, with increasing rim angle.

Once the PROMES-CNRS parabolic mirror has much smaller diameter and focal length compared to the other conventional parabolic mirrors, as shown in TABLE 3.1, small diameter laser rods can be more efficiently pumped, favoring the solar laser beam quality.

## 3.1.1 PROMES-CNRS HELIOSTAT - PARABOLIC MIRROR SYSTEM
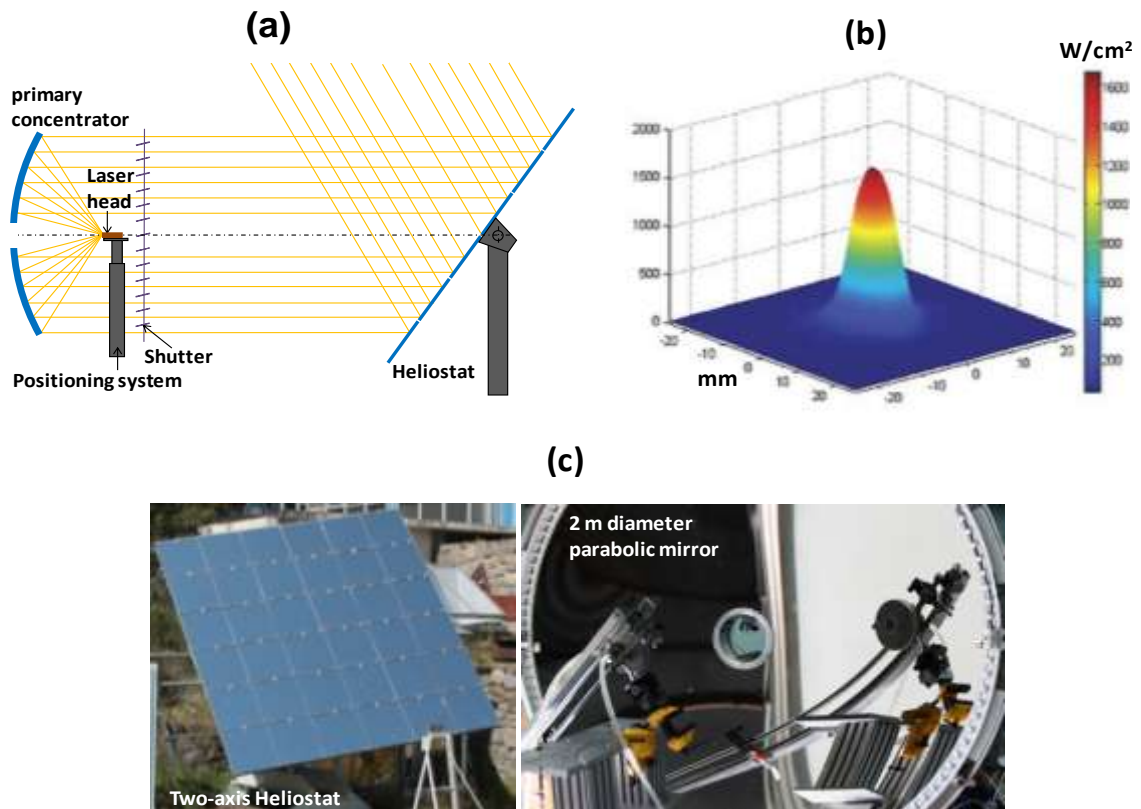


**FIG. 3.2** - **(a)** Scheme, **(b)** Flux distribution at the focus and **(c)** photograph of the PROMES - CNRS MSSF solar system.

A large plane mirror with 36 small flat segments (0.5 m × 0.5 m each), mounted on a two-axis heliostat, redirects the incoming solar radiation toward the horizontal axis primary parabolic mirror with 2 m diameter, 60° rim angle and 850 mm focal length, as shown in FIG. 3.2. All the mirrors are back-surface silver-coated. Due to iron impurities within the glass substrates of plane and parabolic mirrors (with 5 and 10 mm thickness, respectively), along with more than 70-year usage, only 59 % of incoming solar radiation is effectively focused to the focal zone. Two sliding doors and a shutter with motorized blades regulate the incoming solar power from the heliostat. On high solar insolation days, more than 1.8 kW solar powers can be focused into a 15 mm diameter wide light spot, reaching the peak flux of 16 W/mm$^2$ (*44,96*).

Since 2011, our solar laser research proposals to SFERA (*P11030100000127*, *Laser-Osci-Amp*) and SFERA2 (*P1404090033, P1502270118, P1602010181*, *P1701190231*) FP7 European project have all been accepted by the SFERA and SFERA2 user´s evaluation experts committee. This has lead to the main advances in solar laser performances in the list of publications I (*90*), II (*91*), III (*31*), V (*40*), VI (*41*), VII (*38*), VII (*34*), IX (*37*) X (*33*), described in CHAPTERS *5* to *7*.

## 3.1.2 NOVA HELIOSTAT - PARABOLIC MIRROR SYSTEM

A large plane mirror with 4 segments (1.16 m × 1.27 m each), mounted on a two-axis heliostat (Dezhou Gaokeli Hydraulic Co. Ltd., China), redirected the incoming solar radiation towards a stationary parabolic mirror with 1.5 m diameter, 0.66 m focal length and 60° rim angle. An effective collection area of 1.77 m$^2$ is hence calculated. All the mirrors were back-surface silver coated. The plane mirror segments were provided by FLABEG Solar GmbH & Co KG, Germany. Their glass substrate was 4 mm thick, with low iron content, which allowed 93.5% reflectance of the incoming radiation. Parabolic mirror's glass substrate was 10 mm thick, with high iron content, reducing the mirror's reflectivity to about 80%. About 75% of incoming solar radiation was hence effectively focused to the focal zone. For the clear sunny days in Lisbon maximum terrestrial solar irradiance can reach about 900 W/m$^2$. In this case, more than 1.1 kW solar power can be focused into a 8 mm full width at half maximum diameter (FWHM) light spot with near-Gaussian distribution, reaching the peak flux of 12.6 W/mm$^2$, as shown in FIG. 3.3.
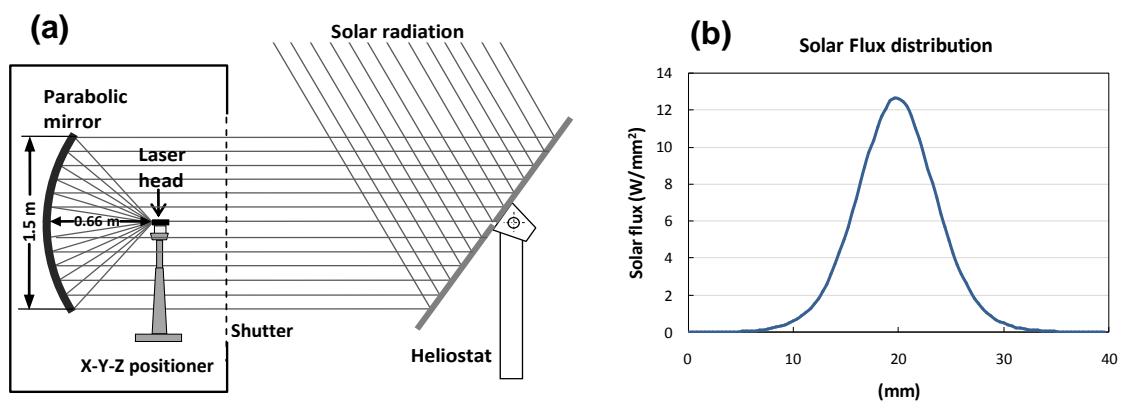


FIG. 3.3 - (a) Scheme of the NOVA heliostat-parabolic mirror system. (b) Solar flux distribution of the heliostat-parabolic mirror, considering an irradiance of 900 W/m$^2$ in ZEMAX analysis.

The NOVA heliostat - primary concentrator system was recently built in the campus of NOVA, within the project PTDC/FIS/122420/2010. The process of construction (in FIG. 3.4) involved a significantly delayed (but justified) authorization by NOVA due to: the choice of the solar furnace

sit within our University campus, a huge amount of civil work, considerable delays in the delivery of solar equipments, in both installation, and calibrations of heliostat and the solar furnace, the mounting of high-reflectance solar mirrors etc, so it only until most recently in 2014  that we have finally succeded in building the first solar furnace with automatic solar heliostat tracking system in Portugal. Therefore, the main achievements in solar lasers within NOVA solar facility were only reported from 2015 to 2017.
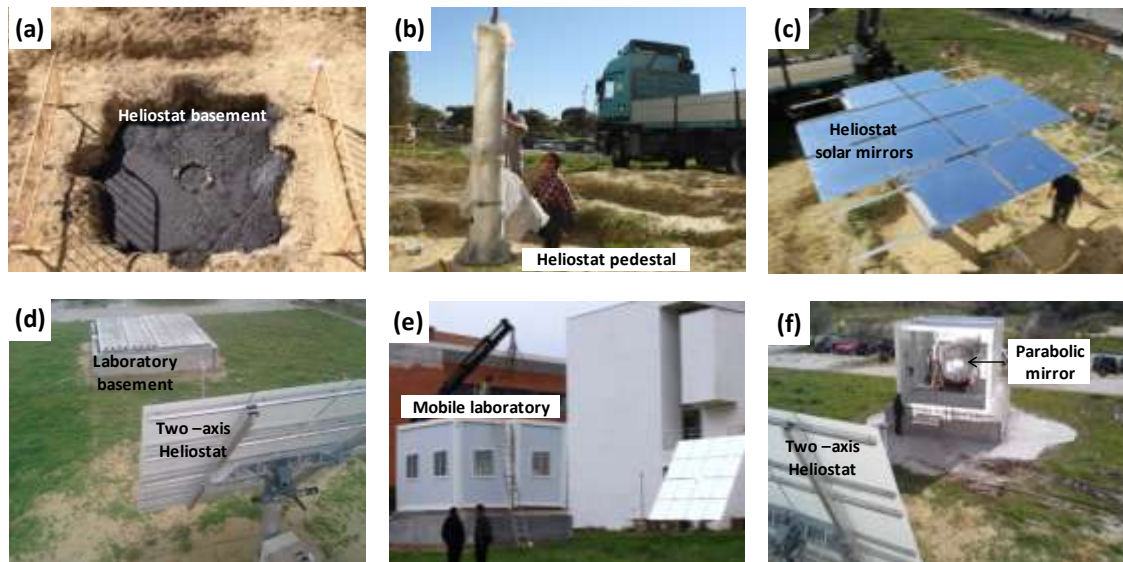


FIG. 3.4 - The construction of the first automatic solar furnace in Portugal: (a) Preparation of the heliostat basement. (b) Installation of the heliostat pedestal. (c) Mounting of heliostat solar mirror. (d) Preparation of laboratory basement. (e) Installation of the mobile laboratory. (f) Finally built heliostat-parabolic mirror system.

## 3.2  FRESNEL LENSES

The Fresnel lens is a lens resembling of a plano-convex or plano-concave lens flattened, which was developed to reduce the amount of glass material needed to build a conventional lens.
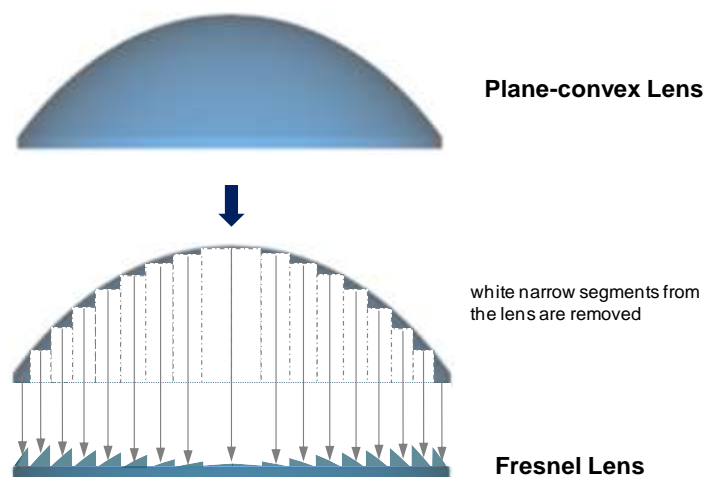


FIG. 3.5 - Schematic design of a Fresnel lens from its corresponding aspheric lens.

As observed in FIG.3.5, each groove of the Fresnel lens represents a narrow curved segment of the conventional lens, translated towards its planar surface. Thus, the surface of a Fresnel lens consists of a series of concentric rings, each corresponding to the curvature of a conventional lens of equal diameter, but without the material of the full body of the corresponding conventional singlet.

The main disadvantage of Fresnel lenses is the chromatic aberration, which leads to a significant decrease in the energy efficiency in concentrating solar radiation. Due to the different refractive index of the lenses at different wavelengths the focal length of the Fresnel lens is highly dependent on solar spectrum wavelength, especially in UV and visible region as observed in FIG. 3.6. This strong variation of the focal length causes large dispersions of the concentrated solar radiations along the optical axis of the Fresnel lens, becoming more difficult to efficiently pump a small diameter laser rod.
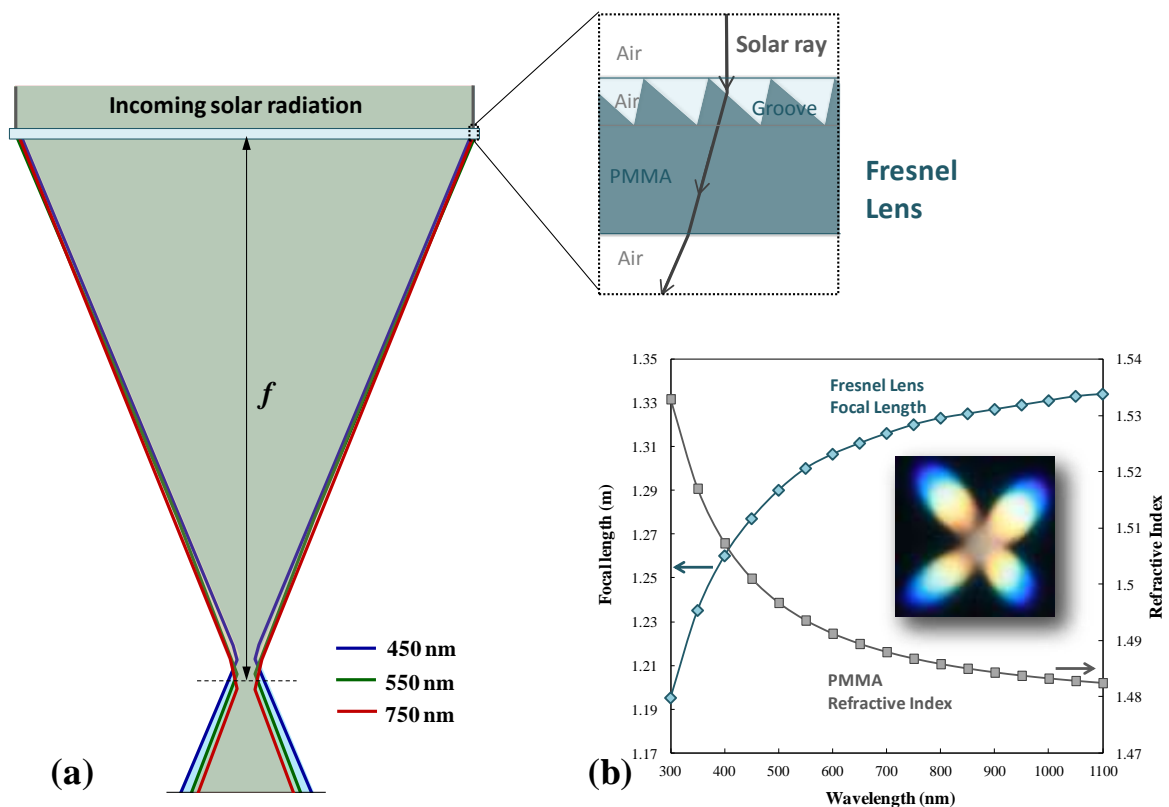


**FIG. 3.6** - (a) Schematic design of the chromatic aberration of a Fresnel lens. (b) Wavelength dependency of both the focal length and the refractive index of the 1.1 m diameter NOVA Fresnel lens with 1.3 m principal focal length $f$. The inset photograph shows its chromatic aberration, slight below of the principal focal length.

## 3.2.1 NOVA FRESNEL LENSES SYSTEM

Fresnel lenses recently have been one of the best choices because of the advantages such as small volume, light-weight, mass production with low cost as well as effectively increase the energy density *(97)*. For these reasons, solar laser researchers, including us, have also adopted Fresnel lens as primary solar concentrators to make solar laser prototypes economically competitive *(26,29,30,80)*.

Most Fresnel lens designers of concentrated solar energy applications choose Polymethylmethacrylate (PMMA) material, because of its high optical quality combined with

less costly manufacturing technologies *(97)*. PMMA is a light-weight clear and stable polymer with optical characteristics nearly similar to that as glass. It is resistant to sunlight, remaining thermally stable up to at least 80 ºC. Its special transmissivity matches the solar spectrum: PMMA is transparent at visible and near infrared wavelengths, but absorbs the infrared radiation beyond 2200 nm and cut undesirable UV solar radiation below 350 nm.

The NOVA Fresnel lenses are mounted on a two-axis solar tracker that follows automatically the Sun's movement, as shown in FIG. 3.7. The solar tracker is supplied by Shandong Huayi Sunlight Solar Energy Industry Co., Ltd. The Fresnel lenses are supplied by Nihon Tokushu Kogaku Jushi Co., Ltd. (FIG. 3.7 (a)) and Shandong Yuying Optical Instruments Co., Ltd. (FIG. 3.7 (b)).
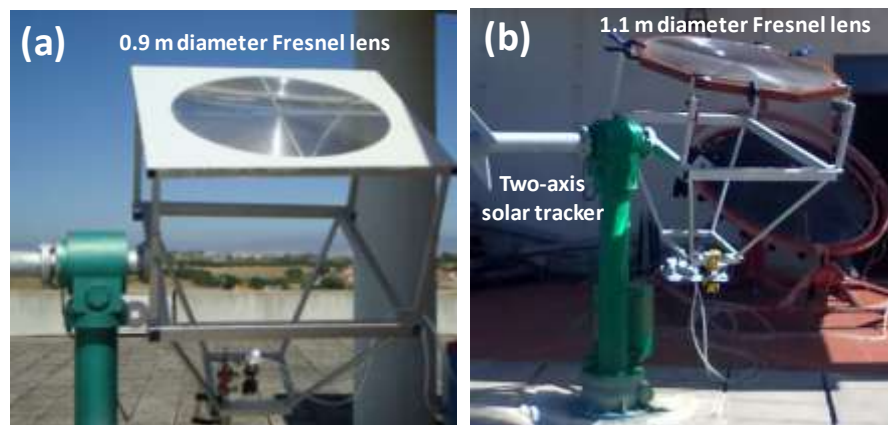


**FIG. 3.7** - NOVA Fresnel lens system with **(a)** 0.9 diameter and **(b)** 1.1 diameter.

For 890 W/m² solar irradiance, in August 2011 and 2013, the concentrated solar power at the focal spot averaged over 2 min was 445W and 590 W for the 0.9 m diameter and 1.0 m diameter Fresnel lenses, respectively. The measured full width at half maximum is 12 mm and 13 mm at the minimum focal waist, respectively. The measured transmission efficiency in direct solar tracking was 78.6% *(29)* and 76% *(42)*, respectively, being only slightly higher than with NOVA heliostat-parabolic mirror solar facility. Yet, the measured transmission efficiency of the Fresnel lenses in indirect tracking mode, through NOVA heliostat, is about 72%, becoming slightly lower than that with NOVA heliostat-parabolic mirror.

Despite our substantial progresses in both solar efficiency and brightness with parabolic mirrors, the utilization of Fresnel lenses before the final construction of NOVA heliostat-parabolic mirror systems was also very important to us, leading to record achievements: Solar laser collection efficiency in 2011 *(29)* and solar laser brightness in 2013 *(42)*. The latter was also highlighted in Laser Focus World *(20)*, and it is described in detail in CHAPTER *6*.

During this PhD project, several solar laser prototypes were developed according to the above mentioned solar concentrators to achieve the proposed objectives, which are described in detail in Chapters 5 to 8. But first, for the design and optimization of the prototypes modeling tools were used, which are presented in the next chapter (Chapter 4).

# 4 MODELING TOOLS FOR SOLAR LASERS

In this chapter, the tools for design, modeling and optimization of the laser system, used in this doctoral programme, will be introduced. The design parameters of all the solar pumping systems were firstly optimized through ZEMAX$^©$ non-sequential ray-tracing software. Laser resonator parameters were then modeled by LASer Cavity Analysis and Design (LASCAD$^©$) codes to optimize the laser output power and beam quality. After the optimization of the solar laser system design, AUTOCAD$^©$ software was used to design the mechanical components the solar laser head for its final machining.

## 4.1  ZEMAX$^©$ - MODELING OF THE SOLAR LASER SYSTEM

ZEMAX$^©$ is a program which can model, analyze, and assist in the design of optical systems. The Non-Sequential mode, utilized in the solar-pumping system modeling, makes the operation of the program easier for systems which are non-imaging. In this method, the rays are traced only along a physically realizable path until they intercept an object. The ray then refracts, reflects, or it is absorbed, depending upon the properties of the object struck. The ray then continues on a new path. In non-sequential ray tracing, rays may strike any group of objects in any order, or may strike the same object repeatedly; depending upon the geometry and properties of the objects. For this reason, the non-sequential simulations usually require longer time to obtain accurate results. All the non-sequential objects can be divided into three types: Sources, geometric optical elements and detectors, as illustrated in 4.1.
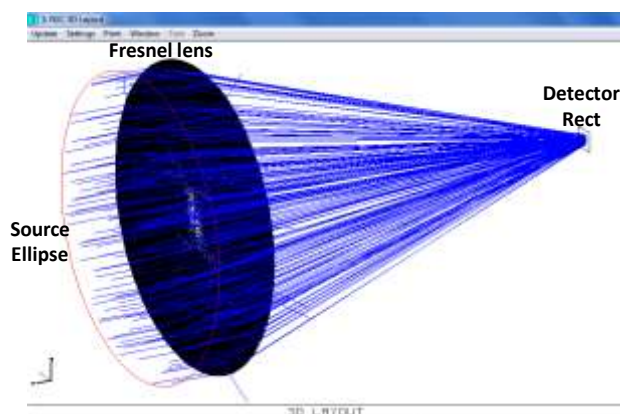


**FIG. 4.1** - Non-sequential objects of ZEMAX$^©$ software to model a Fresnel lens solar system.

Sources are the objects utilized to emit the rays of the simulation, thus representing the pumping sources. The geometric optical elements define the optical components in which the emitted rays are absorbed, refracted, reflected, diffracted, dispersed, divided, etc. These objects represents in this case the components of the solar energy collection and concentration system and the solar laser head components. The detectors objects define the qualitative and/or quantified information of the incident rays. With these objects it is possible to design and parameterize the whole optical system, which transfer the pump energy into the active medium of the solar laser.

### 4.1.1 SOLAR PUMPING SOURCE

There exist several types of source objects in ZEMAX$^{©}$. However, only the "Source Ellipse" is utilized for defining the solar pumping source, as shown in FIG. 4.2.
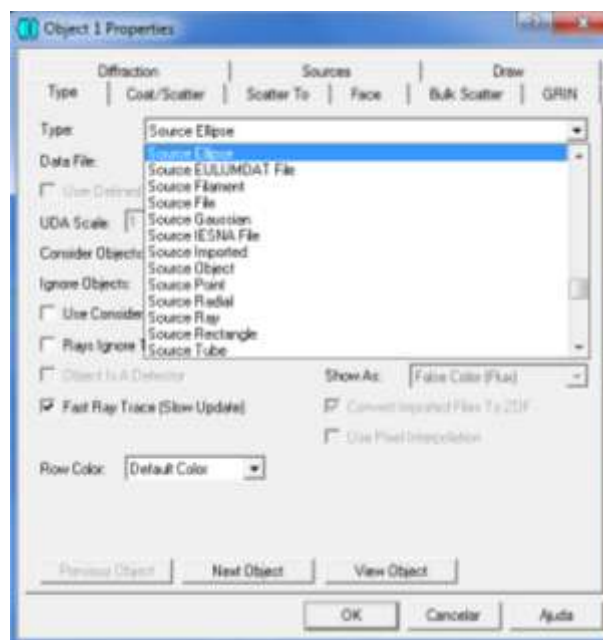


**FIG. 4.2** - Source objects in ZEMAX$^{©}$.

The specific characteristics of each object are defined in the Non-Sequential Components Editor, as observed in FIG. 4.3.



| Object Type | X Position | Y Position | Z Position | Tilt About X | Tilt About Y | Tilt About Z |
|---|---|---|---|---|---|---|
| 1 Source El.. | 0.000 | 2023.000 | 0.000 | 90.000 | 0.000 | 0.000 |

| Object Type | Material | # Layout Rays | # Analysis Rays | Power(Watts) | Wavenumber | Color # |
|---|---|---|---|---|---|---|
| 1 Source El.. | -- | 200 | 5000000 | 91.500 | 0 | 0 |

| Object Type | X Half Width | Y Half Width | Source Distance | Cosine Exponent | Gauss Gx | Gauss Gy |
|---|---|---|---|---|---|---|
| 1 Source El.. | 450.000 | 450.000 | 0.000 | 8.000E+004 | 0.000 | 0.000 |

**FIG. 4.3** - List of some the parameters of the source ellipse for the solar pumping source in the Non-Sequential Component Editor.

There are parameters common to all the three types of objects (Sources, geometric optical elements and detectors) such as the position (X, Y, Y position) and direction (Tilt about X, Y, Z), and there are parameters common only to the sources. These parameters are:

- **Layout** and **Analysis Rays**, which define how many random rays to launch from the source when creating layout plots and when performing analysis, respectively. To accurately compute quantitative energy distributions on the detectors, it generally requires a larger number of rays than the qualitative analysis of the layout plots. This is why the number of layout and number of analysis rays are defined separately in the source parameter listing. The number of rays used in the simulation process is a critical parameter throughout the process of modeling the system. On one hand, a reduced number of analysis rays in the simulations reduces time but the accuracy of the results is also low. On the other hand, a number too high leads to more accurate results, but the time spent in each simulation is also increased. Therefore there is an optimum number to be used in each simulation, which can vary from hundreds of thousands for low complexity optical systems to several million for more complex systems. The procedure for obtaining the optimum number of analysis rays consists in its progressive increase until the power incident / absorbed by the detectors, as well as the power distribution, converge.

- **Power** (units), which is the total power over the defined range of the source.
  The terrestrial solar irradiance of 900 W/m$^2$, in Lisbon area, in Summer is considered in ZEMAX$^©$ software. Moreover, for the modeling of a solar laser system, the effective pump power of the light source has also to take into account the overlap between the absorption spectrum of the active medium and the solar emission spectrum, which is considered as 16% *(45)* for the Nd:YAG. Thus, for the modeling of the Nd:YAG solar laser system, the source power is calculated by the product of the source area ($\pi\times0.45^2$ m$^2$ = 0.636 m$^2$) with the terrestrial irradiance, and the overlap between the Nd:YAG absorption spectrum and absorption spectrum: $P_{source}$= 0.636 m$^2\times$900W.m$^{-2}\times$0.16 $\approx$ 91.5 W.

- **Wavenumber**. To use when tracing random rays. Zero means polychromatic; which chooses ray wavelengths randomly with the weighting defined on the wavelength data editor, as shown in FIG. 4.3.

- **Color #**. The pen color to use when drawing rays from this source. If zero, the default color will be chosen.

The other parameters have source type specific meanings. The parameters to define the source ellipse are:

- **X-Half Width** and **Y-Half Width** in lens units, defined in millimeters (mm) in this case. The Source Ellipse is a flat elliptical surface. Thus, since the amount of radiation collected is relative to the collection area of the primary concentrator, which is usually circular, the dimensions of the solar pumping source are similarly defined to those of the primary concentrator, in order to simplify the parameterization of the solar system, as observed in FIG. 4.3. By defining the same X, Y Half-Width of 450 mm, as shown in FIG. 4.3, it means that the solar radiation is collected by a circular primary concentrator with 900 mm diameter.

- **Source Distance**, which is the distance along the local z axis from the apparent source point to the location of the source object, defined by zero in this case.

- **Cosine Exponent**:
  Although the origin of each ray launched lies on the surface of the ellipse with a uniform distribution, the distribution of the rays may emit in a cosine distribution of the form

$$I(\theta) = I_0 (\cos\theta)^{Cn}$$

(4.1)

where Cn is cosine exponent, which may be any value greater than or equal to unity. When using this mode (Cn is not zero), the source acts like a diffuse cosine source. The larger Cn, the narrower the distribution becomes. The apparent half angle of +- 0.27° subtended by the Sun has to be considered in the analysis of our solar laser system, which is defined by the Cosine Exponent = 80000 (FIG. 4.3).

- **Gaussian Gx** and **Gy** are the X and Y terms, if the rays emit a Gaussian distribution. In this case, these terms are ignored, the rays of the solar source have a cosine distribution.

- **Source X** and **Y** are the X and Y coordinates of the point that emits the rays, which is ignore in this case, since the solar source is not considered as a point.

In the case of a solar-pumped Nd:YAG laser system modeling, for Nd:YAG laser medium, 22 absorption peaks are defined in ZEMAX$^{©}$ numerical data. The central wavelengths of these peaks are 527, 531, 568, 578, 586, 592, 732, 736, 743, 746, 753, 758, 790, 793, 803, 805, 808, 811, 815, 820, 865, and 880 nm *(34,35)*. Spectral irradiance (W/m$^2$/nm) values corresponding to the above mentioned 22 peak absorption wavelengths could be consulted from the standard solar spectrum for 1.5 air mass (AM1.5) *(98)* and saved as source wavelength data in ZEMAX$^{©}$ software, as shown in FIG. 4.4.



**FIG. 4.4** - Solar source wavelength data, for solar-pumping of a Nd:YAG laser.

## 4.1.2 SOLAR ENERGY COLLECTION AND CONCENTRATION SYSTEM AND SOLAR LASER HEAD

Parabolic mirrors and Fresnel lenses systems, as well as the laser head components, are modeling through the different non-sequential geometrical optical components, as observed in FIG. 4.5. The ZEMAX$^{©}$ tool has an extensive list of objects with geometric shapes that can be used to absorb, reflect refract the rays emitted by the source object, depending on the function for which it is intended to function.
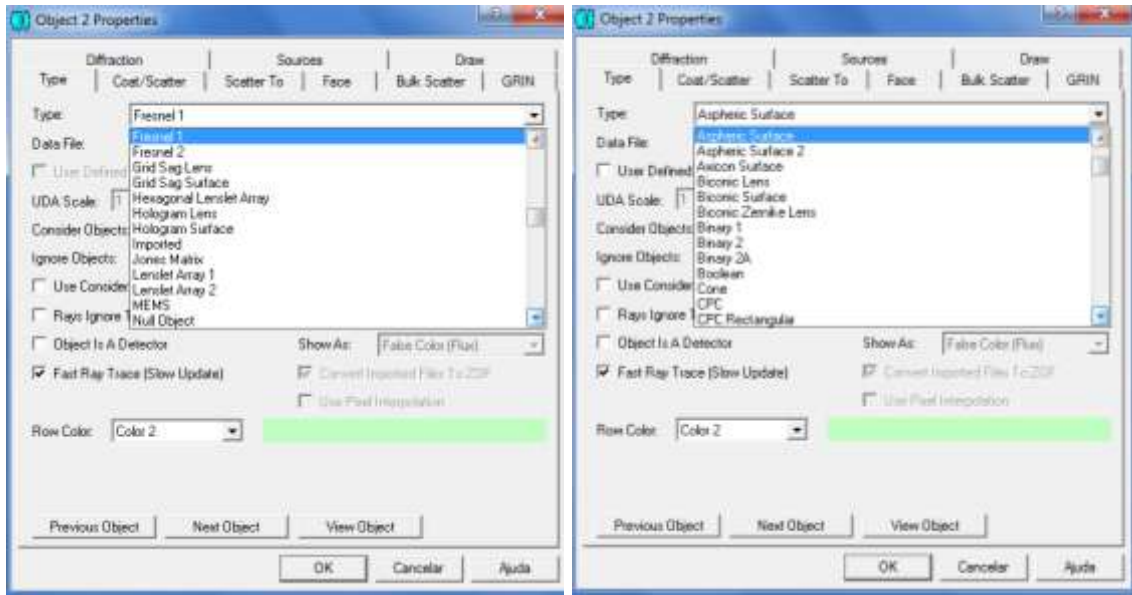
FIG. 4.5 - Geometrical optical objects in ZEMAX$^{©}$. *Fresnel 1* and *Aspheric Surface* represent the objects selected to model the Fresnel lens and Parabolic mirror systems, respectively.

AUTOCAD© software was also used to carry out the design of some laser head components, which geometry does not exist in the list of objects of ZEMAX$^{©}$, and which had been exported to the ZEMAX$^{©}$ environment.

The properties of reflection, absorption or refraction of the objects are parameterized according to the selected material in the editor menu of non-sequential components, as shown in FIG. 4.6.



FIG. 4.6 - Selection of the *Material* parameters in the Non-Sequential Component Editor.

If the object has the function of only absorbing the *ABSORB* function must be selected in material box. If the object has the properties of only reflecting, such as the Aspheric Surface for the modeling of the parabolic mirror, the *MIRROR* function must be selected. However, in the case of a refractor material, such as the laser rod, all the characteristics must be defined through the *Glass Catalog* menu, in FIG. 4.7, within which it is possible to update the values or create new materials, depending on the specific need of each case. One of the parameters that can be changed is the absorption / transmission spectrum of the material, which depends on the wavelength, doping material, absorption coefficient, the temperature and the distance traveled by the radiation inside the material. The transmission spectrum of 1.0 at% Nd:YAG laser material, at a temperature of 300º K, is shown in FIG. 4.7.
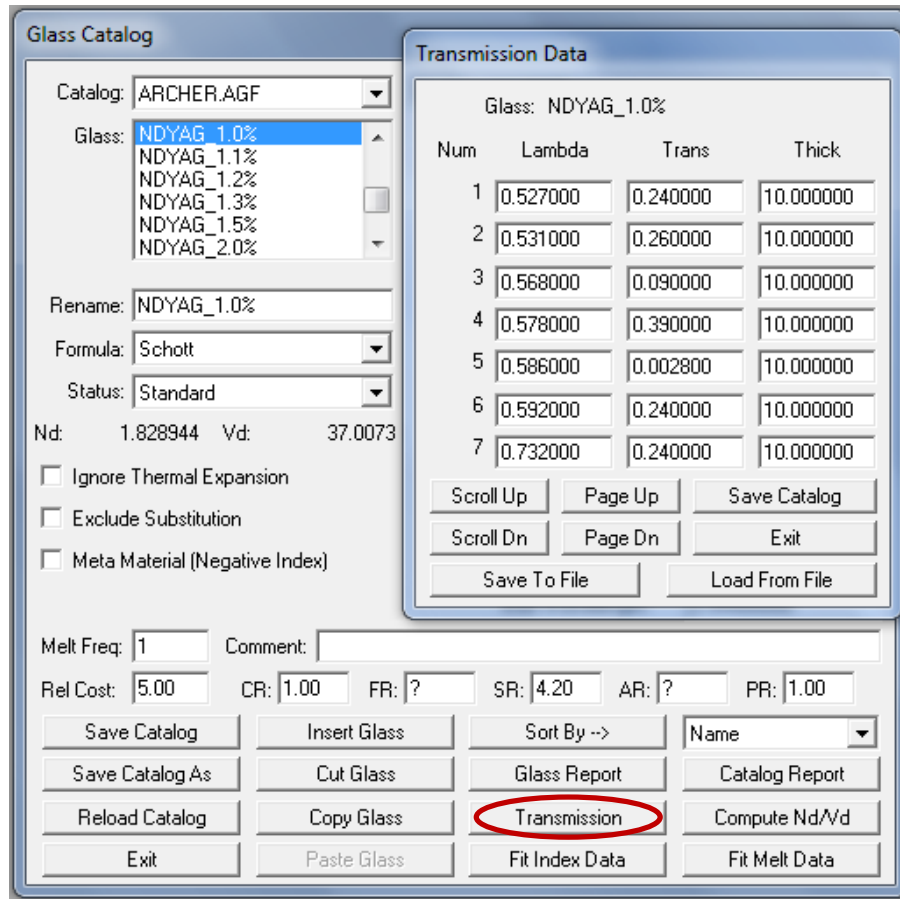
**FIG. 4.7** - Transmission data of the Nd:YAG laser material.

### 4.1.3 DETECTORS - ABSORBED PUMP POWER ANALYSIS

To provide the information of the incident or absorbed pump power it is necessary to use the detector objects in ZEMAX©. For example, to detect the numerical information at the focus of the primary concentrator, illustrated in FIG. 4.1, a *detector rect* is usually utilized. The rectangular detector allows to record more amount of data, such as the incident power and angle, the bidimensional power distribution and the profile of incident/absorbed power in the area defined by the detector. This type of detector can be placed either inside or outside of an object and have the function of absorbing, reflecting or not have any effect on the incident radiation. The shape of the detector is, however, limited to a rectangular surface defined by the user. The image resolution can be adjusted by parameterizing the number of pixels of the detector, taking into account the influence on the total time required for each simulation. For the analysis of the incident or absorbed pump power within the laser material, as well as the pump profile in FIG. 4.8, a *detector volume* is used in this case. Similar to the rectangular detector, the detector volume is limited to the shape of a rectangle. However, with this detector it is possible to add a new dimension to obtain the power information, since it has a parallelepiped shape, whose dimensions are defined by the user, as well as the number of voxels. The resolution of the volume detector has also a great influence on the calculation time of each simulation. In ZEMAX© non-sequential ray-tracing, the *detector volume* of the laser rod is divided into a total of 18,000 voxels. The path length in each voxel is then found. With this value and the effective absorption coefficient of the Nd$^{3+}$:YAG material, its absorbed

solar pump power within the laser medium can be numerically calculated by summing up the absorbed pump radiation of all zones.
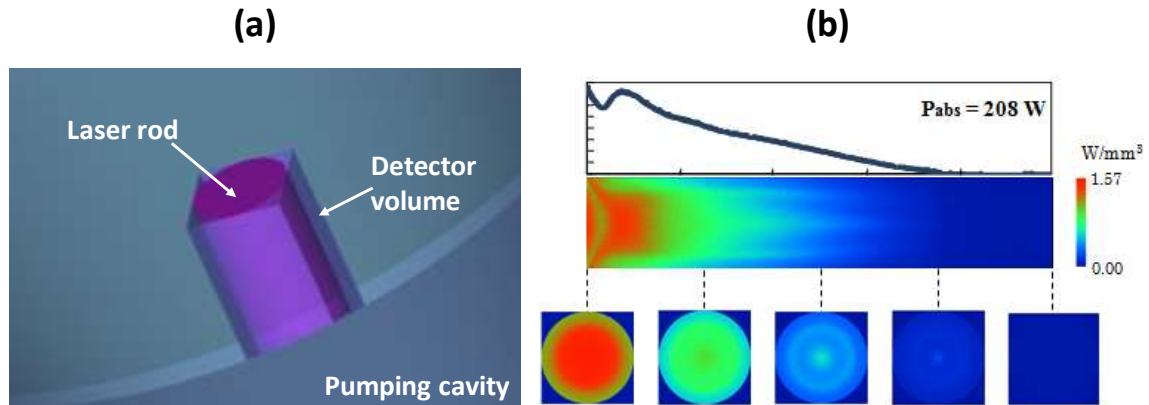


**FIG. 4.8** - (**a**) Design of the active medium and *detector volume* in ZEMAX$^{©}$ software. (**b**) Absorbed pump flux distributions along five transversal cross sections and one central longitudinal cross section of an end-side-pumped Nd:YAG rod *(34)*, obtained by ZEMAX$^{©}$ numerical simulation through the *detector volume*.

The absorbed pump flux data from the ZEMAX$^{©}$ analysis is then processed by LASCAD$^{©}$ software to study the laser beam parameters and quantify the thermal effects applied in the active medium.

## 4.2 LASCAD$^{©}$ - MODELING OF THE SOLAR LASER RESONANT CAVITY

LASCAD$^{©}$ software allows the combination of several simulation tools to optimize the laser resonator design: The Thermal and Structural Finite Element Analysis (FEA); the ABCD Gaussian Beam Propagation Code; and the propagation algorithm of non-Gaussian beams – the Beam Propagation Method (BPM). Thus, it is possible to model resonant cavities through the analysis of: the thermal lensing effects, which is one of the key problems in solid-state lasers; multimode and TEM$_{00}$ mode output power and laser efficiency; laser beam quality and profile, as well as laser beam propagation outside the laser cavity, taking into account several laser parameters, such as reflectivity, radius of curvature and distance between cavity components, diffraction losses, gain saturation, etc.

### 4.2.1 FINITE ELEMENT ANALYSIS (FEA) OF THERMAL EFFECTS

The Finite Element Analysis (FEA) computes the heat, temperature and stress induced parameters in the laser crystal, taking into account the laser material parameters, pump configuration and cooling geometry. LASCAD$^{©}$ provides several pre-defined models of typical configurations, as shown in FIG. 4.9(a). However, the pumping scheme may have very particular characteristics, which are not defined in the pre-defined models of LASCAD$^{©}$, as in the case of solar-pumped lasers. Thus, to accurately model the solar laser systems, it is possible to import files from ZEMAX$^{©}$ (or TracePro$^{©}$) ray-tracing software, whose content is the three-dimensional distribution of the absorbed pump power by the active medium defined in ZEMAX$^{©}$, shown in

FIG. 4.9(b). The cooling parameters of the active medium, as well as the material properties, are respectively defined in the *Boundaries* and *Material Param*eter menus (FIG. 4.10).
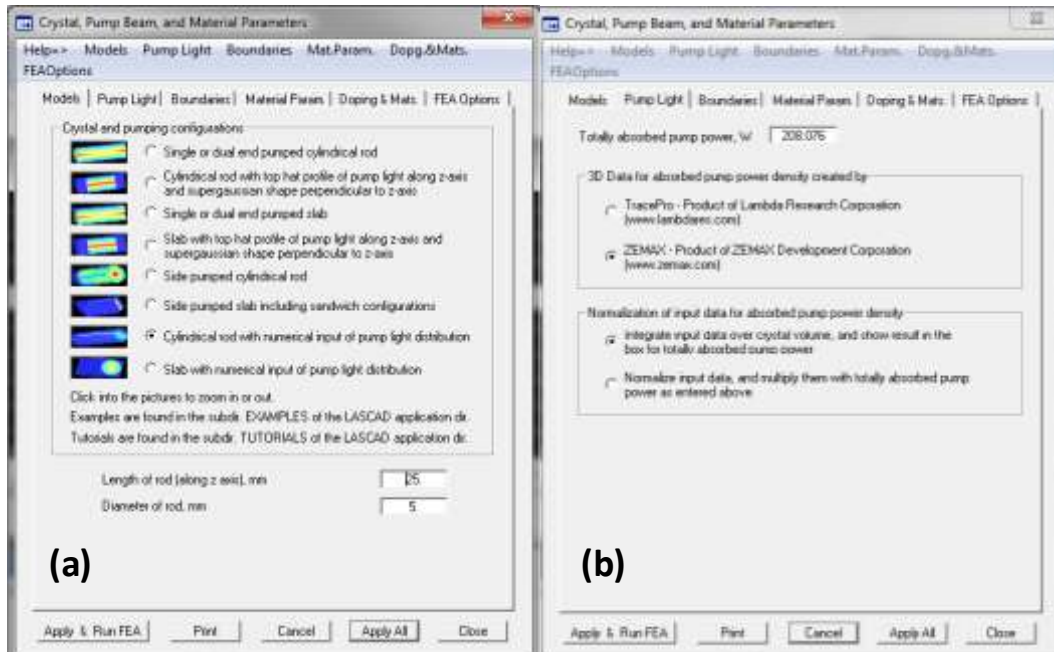


**FIG. 4.9** - **(a)** Crystal and pumping configuration models of LASCAD© software. **(b)** Laser pumping parameters, obtained through ZEMAX© data file.
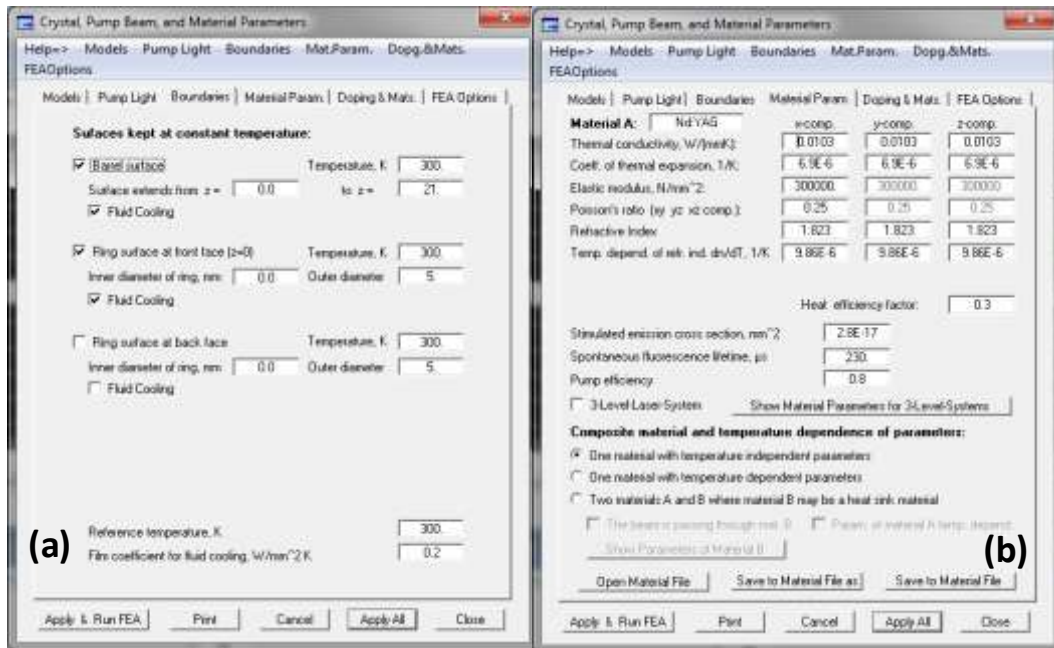


**FIG. 4.10** - **(a)** Cooling parameters of an end-pumped laser system in reference *(34)* **(b)** Nd:YAG laser material parameters.

Finally, the simulation conditions, such as resolution and number of iterations are defined in Tab *FEA options*. After defining all the parameters related to pumping, active medium and cooling, thermal and structural analysis by finite elements (FEA) can be started. The thermal analysis is carried through in three steps: 1. determination of heat load distribution, 2. solving of the 3D

differential equations of heat conduction, and 3. solving of the differential equation of structural deformation *(99)*. The differential equations of heat conduction are given by:

$$-div\left[\kappa(T)\nabla(T)\right]=Q(x,y,z) \tag{4.2}$$

where $\kappa$ is the coefficient of thermal conductivity; $T$ is the constant temperature of the active medium surface, defined in LASCAD[©] (in tab *Boundaries*); $Q(x, y, z)$ is the heat load distribution in the active medium , resulting from either the pre-defined laser scheme models in LASCAD[©] or the ZEMAX[©] ray-tracing analysis.

The differential Equations of Structural Deformation are given by strain-stress relation:

$$\left(\varepsilon_{ij}\right)=\left(\alpha_x,\alpha_y,\alpha_z\right)\!\left(T-T_0\right)+\frac{1}{E}C^{-1}\left(\sigma_{ij}\right) \tag{4.3}$$

where $\varepsilon_{ij}$ is the strain tensor given by:

$$\left(\varepsilon_{ij}\right)=\frac{1}{2}\left(\frac{\partial u_i}{\partial x_j}+\frac{\partial u_j}{\partial x_i}\right) \tag{4.4}$$

$\alpha_i$ is the coefficient of thermal expansion, $E$ the elastic modulus, $\sigma_{ij}$ the stress tensor and $u_i$ the displacement.

To solve these differential equations, the LASCAD[©] FEA code discretizes the laser crystal into a tri-dimensional grid (FIG. 4.11), whose resolution is defined by the user, and iterates through these a defined amount of times. The accuracy of the results depends directly on the grid resolution, as well as on the simulation time.
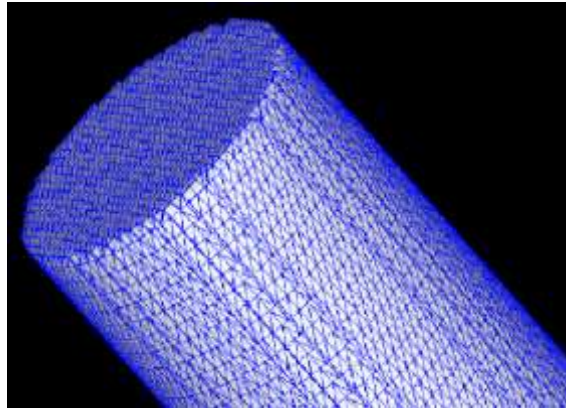


**FIG. 4.11** - Semi-unstructured grid in case of a laser rod.

Running the FEA generates the data used for simulating thermal lensing within the laser cavity. It also produces three dimensional representations of the crystal heat load, temperature and stress, as shown in FIG. 4.12), relying on the above equations which describe heat conduction, structural deformation and absorption *(99)*. The remaining results of the algorithms within LASCAD[©] depend on the results from the FEA.
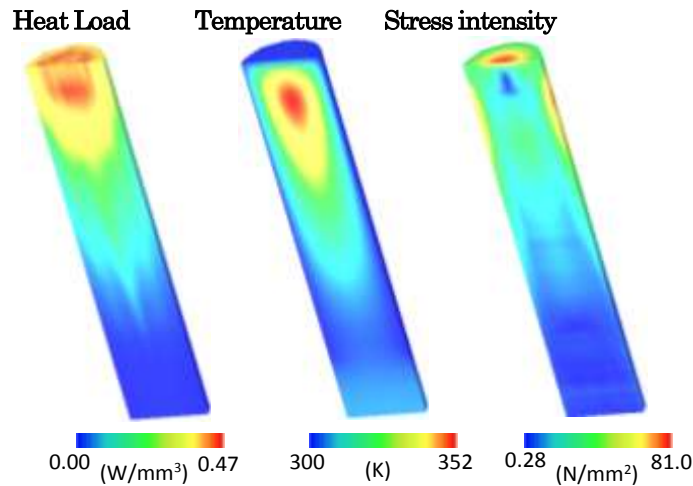
FIG. 4.12 - Heat load, temperature and stress intensity distributions, numerically simulated in LASCAD© for a 5 mm diameter, 25 mm length Nd:YAG rod *(34)*.

## 4.2.2  GAUSSIAN ABCD MATRIX APPROACH

When using the FEA mesh results, the thermal lensing element can be defined by parabolic approximation, as shown in FIG. 4.13. In the same way, a fit of the deformed end faces of the crystal is accomplished.
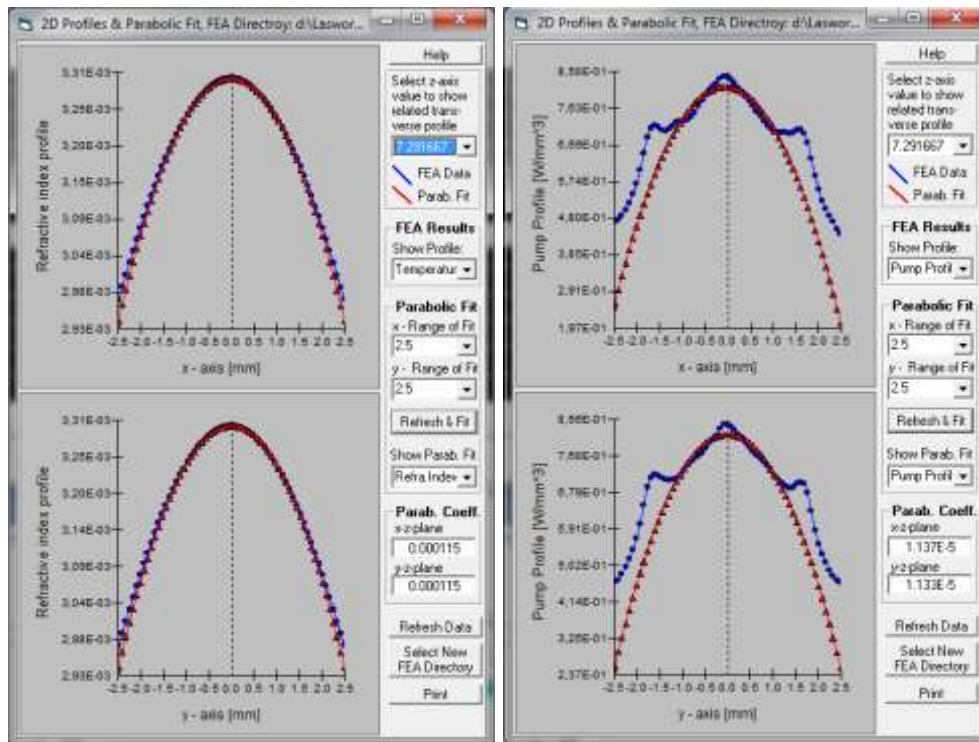


FIG. 4.13 - Parabolic approach for determination of the representative element of the active medium inside the resonant cavity.

With the obtained parabolic coefficients, it is possible to model the resonant cavity through the Gaussian beam propagation matrix algorithm (ABCD code). To visualize the results of the ABCD matrix approach, fundamental mode spot size, as well as multimode, are displayed along the

resonator axis. To account for astigmatic, the computations are carried through simultaneously in two planes perpendicular to the resonator axis, as shown in FIG. 4.14.
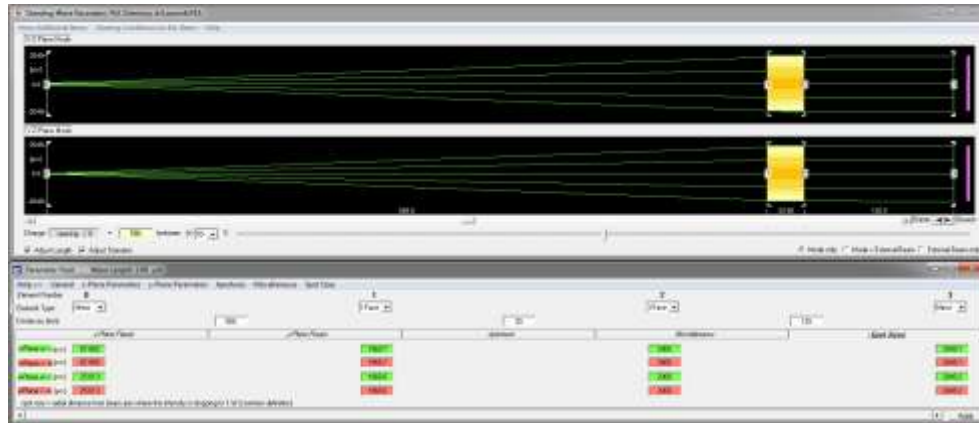


**FIG. 4.14** - Representation of the resonant cavity and laser beam in the propagation planes X-Z and Y-Z for the efficient production of fundamental mode solar laser power *(38)*.

Through the Gaussian modes distribution and absorbed pump power distribution it is possible to calculate the multimode or TEM$_{00}$-mode laser power in continuous - wave (cw) or pulsed operation mode through Laser Rate Equations *(100)*. The laser emission curve as a function of either the power absorbed or the reflectivity of the output coupler can be visualized, as shown in FIG. 4.15(a) and FIG. 4.15(b), respectively. In addition, it is possible to optimize the laser resonator by changing its length, angle between the various components, applying mirrors or lenses, changing the focal length of the components, etc.



(a)

(b)
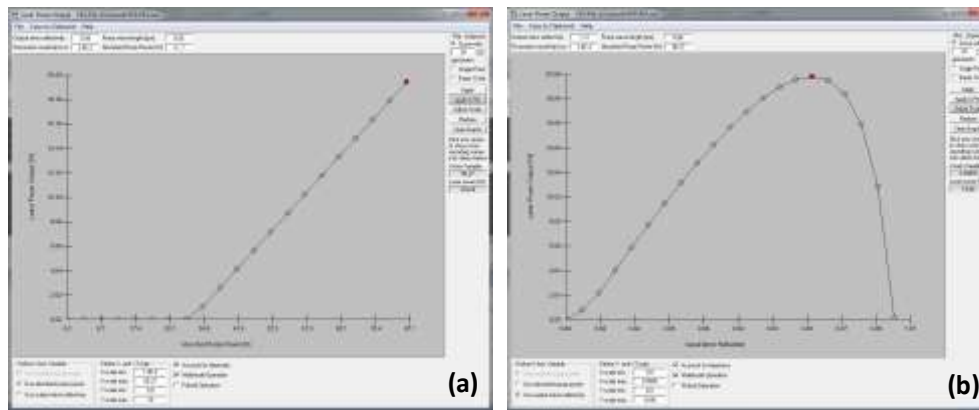
**FIG. 4.15** - Numerically calculated laser output power as function of **(a)** the absorbed pump power and **(b)**the reflectivity of the output coupler, for Ref. *(38)*.

In LASCAD$^{©}$ analysis, the laser power output, $P_{out}$, is obtained by computing the number of laser photons passing the output coupler per time unit through the power output relation:

$$P_{out} = h\upsilon_L S_L \frac{c(-\ln(R_{out}))}{2\tilde{L}}$$

(4.5)

where $h$ is the Planck´s constant, $\upsilon_L$ the frequency of laser light, $S_L$ the number of photons passing the output coupler, $c$ the vacuum speed of light ($2.998 \times 10^8$ m/s), $R_{out}$ the reflectivity of the output mirror, and $\tilde{L}$ the optical path length of the resonant cavity, which is given by

$$\tilde{L} = L_{\text{Re}\,s} + nL_A - L_A \tag{4.6}$$

where $L_{Res}$ is total cavity length and $L_A$ is the active medium length. $n$ is the refractive index of the laser material.

The number of photons in the laser resonant cavity can be obtained through the equation (4.7):

$$S_L = \tau_c \eta_p S_P \iiint \frac{p_0(x,y,x)}{1 + \dfrac{n}{c\sigma\tau S_L s_0(x,y,z)}} dV \tag{4.7}$$

This equation can be solved by iterative integration, where the integral extends over the volume of the active medium. $\tau_c$ is the mean life time of laser photons in the laser resonant cavity; $\eta_p$ is the pump efficiency; $S_p$ is the total number of pump photons absorbed in the crystal per unit of time; $p_0(x,y,z)$ is the absorbed pump power density distribution normalized over the crystal volume; $\sigma$ the stimulated emission cross section; $\tau$ is the spontaneous fluorescence life time of upper laser level; and $s_0(x,y,z)$ the normalized distribution of the laser photons.

## 4.2.3 LASER BEAM PROPAGATION METHOD (BPM)

In cases where parabolic approximation and ABCD matrix code are not sufficient, FEA results can be used as input for a Fast Fourier Transform (FFT) split-step Beam Propagation Method (BPM) *(101)*. This code provides a full 3D simulation of the interaction of a wavefront propagating through the hot, thermally deformed laser crystal. Based on the principle of Fox and Li *(102)*, a series of round-trips through the resonator is computed, which finally converges to the fundamental mode, FIG. 4.16 (a), or to a superposition of higher-order transverse modes. The intensity profile at the output mirror, as it develops with increasing number of iterations is also demonstrated as the computation is running, as observed in FIG. 4.16(b). The BPM code also takes into account the gain dynamics and diffraction effects, due to the finite extension of apertures and mirrors.
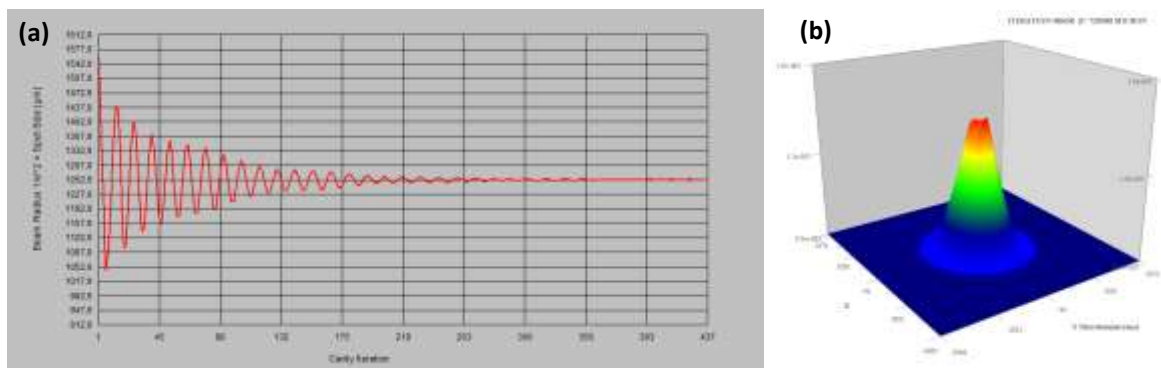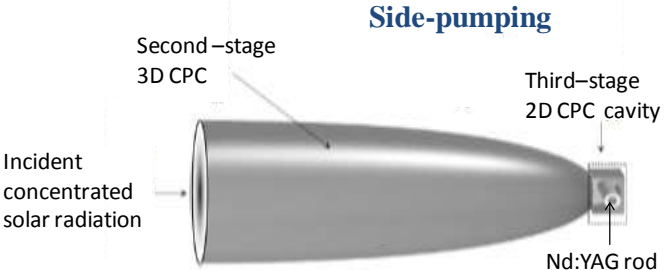


**FIG. 4.16** - **(a)** BPM Laser Beam Radius over cavity iteration and **(b)** output mirror beam profile, for ref. *(38)*.
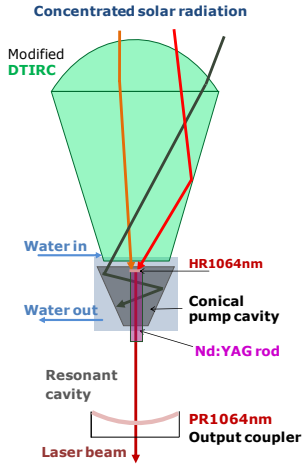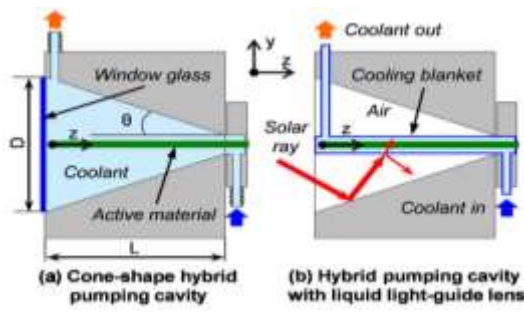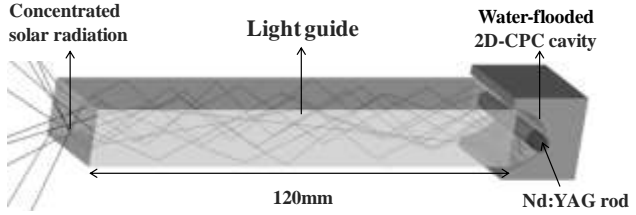
Based on the numerical optimization of the solar laser systems in both ZEMAX© and LASCAD©, the solar laser heads and laser resonator mechanics were design in AUTOCAD© and then produced in Lisbon. The description of the solar laser prototypes developed to improve the solar laser efficiency, beam brightness, and beam stability, as well as its experimental results, are described in Chapters 5, 6, and 7, respectively.

# 5 ADVANCES IN SOLAR LASER EFFICIENCY

Collection efficiency is generally regarded as a primary figure of merit for lasers. The main problem preventing wide spreading of solar-pumped lasers today is its relatively low efficiency, compared to diode-pumped lasers. Since 1996, the main efforts of solar laser researchers have been made to improve both the solar laser slope and collection efficiencies *(24,25,26,29,30,36)*, as shown in TABLE 5.1. In 2012, solar laser researchers, from Tokyo Institute of Technology (Japan), reported a record solar laser collection efficiency of 30 W/m$^2$, by a Fresnel lens system, in direct tracking mode *(30)*. This was the highest value until 2017, when our solar laser research team has reached 31.5 W/m$^2$ by using, instead, a heliostat-parabolic mirror system *(31)*. Although this value was only 5% higher than the previous record with Fresnel lens as primary concentrator *(30)*, it has however a three-fold increase compared to the solar laser collection efficiency with parabolic mirror in 2012, within the same solar facility *(36)*.

**TABLE 5.1** - Previous advances in solar laser efficiency and respective solar laser head configurations.

| Year / Advances / Researchers | Solar Laser Head Configuration |
|---|---|
| **1996**<br><br>**4.7 W/m²** collection efficiency with **parabolic mirror**<br><br>*Jenkins et al. (24)* UChicago | **Side pumping**<br><br>• Primary stage concentrator:<br>12.1 m² Segmented Parabolic Mirror<br><br>• 10 mm diameter Nd:YAG rod |
| **2003**<br><br>**6.7 W/m²** collection efficiency with **parabolic mirror**<br><br>*Lando et al. (25)* WIS | <br>**Side-pumping**<br>Second−stage 3D CPC · Third−stage 2D CPC cavity · Incident concentrated solar radiation · Nd:YAG rod<br><br>• Primary stage concentrator: 6.75 m² Segmented Parabolic Mirror<br>• Second-stage 3D - CPC |

| | |
|---|---|
| | • 2D-CPC pump cavity<br>• 10 mm diameter, 100 mm Nd:YAG rod |
| **2007**<br><br>**18.7 W/m²** collection efficiency with **Fresnel lens**<br><br>*Yabe et al. (26)* TITech | **End-side pumping**<br>• Primary stage concentrator: 1.3 m² Fresnel lens<br>• No secondary concentrator<br>• Conical pump cavity<br>• 9 mm diameter, 100 mm length Cr:Nd:YAG rod |
| **2011**<br><br>**19.3 W/m²** collection efficiency with **Fresnel lens**<br><br>3.5% slope efficiency<br><br>*Liang et al. (29)* NOVA | <br>**End-side pumping**<br>• Primary stage concentrator: 0.64 m² Fresnel lens<br>• DTIRC secondary concentrator<br>• Conical pump cavity<br>• 4 mm diameter, 25 mm length Nd:YAG rod |
| **2012**<br><br>**30 W/m²** collection efficiency with **Fresnel lens**<br><br>8.6% slope efficiency<br><br>*Dihn et al. (26,95)* TITech | **End-side pumping**<br><br>• Primary stage concentrator: 4 m² Fresnel lens<br>• No secondary concentrator<br>• Conical pump cavity<br>• 6 mm diameter, 100 mm length Nd:YAG rod |
| **2012**<br><br>**9.6 W/m²** collection efficiency with **Parabolic mirror**<br><br>*Almeida et al. (36)* NOVA | **Side pumping**<br><br>• Primary stage concentrator: 2.88 m² Parabolic mirror<br>• Second-stage light guide / 2D-CPC pump cavity<br>• 4 mm diameter, 30 mm length Nd:YAG rod |

In this chapter, the efforts performed during this PhD doctoral programme for enhancing the solar laser collection efficiency are addressed and discussed.

# 5.1  13.9 W/M$^2$ SOLAR LASER COLLECTION EFFICIENCY

A large improvement in solar laser collection efficiency, with parabolic mirror as primary concentrator, was reported by pumping a 5 mm diameter, 25 mm length Nd:YAG rod through the PROMES-CNRS MSSF solar facility *(33)*.

## 5.1.1  END-SIDE-PUMPING SCHEME WITH CONICAL LIGHT-GUIDE

As shown in FIG. 5.1, the concentrated solar radiation at the focus is first collected by the circular input face of the fused silica light guide with conical shape. It is then transmitted to the light-guide output section with 3D-CPC profile, which further compresses the solar pump light onto the 1064 nm HR (high reflection) end face of the rod. The laser head, along with the fused silica light guide, is mounted on an automatic X–Y–Z axis mechanical support and positioned at the focus of the parabolic mirror.
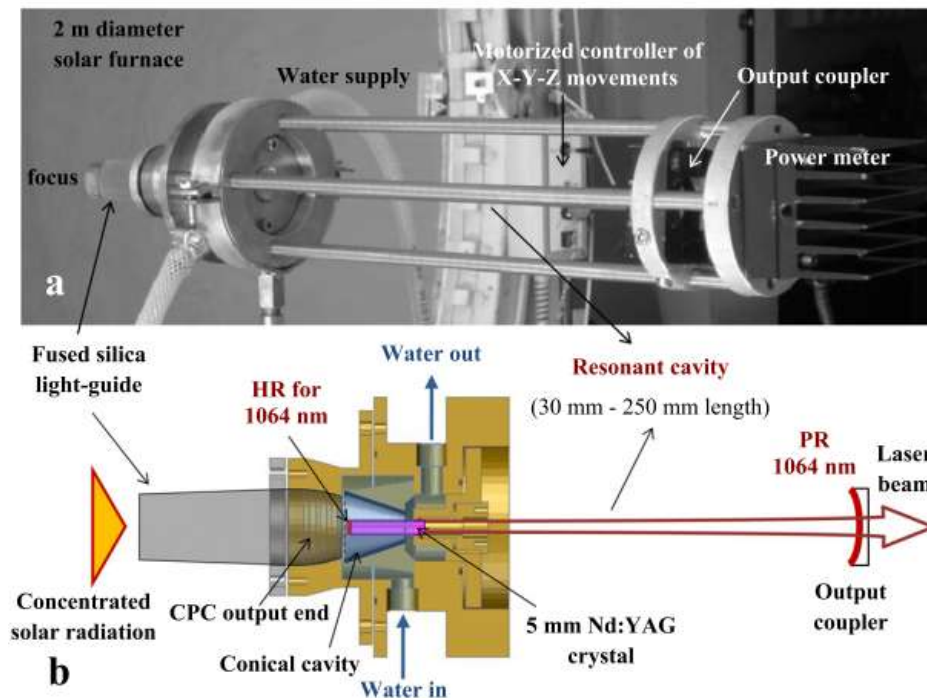


**FIG. 5.1** - **(a)** The Nd:YAG laser head positioned at the focus of the PROMES-CNRS 2 m diameter parabolic mirror. **(b)** The mechanical structure of the Nd:YAG laser head. Both the 1064 nm HR coating and the output coupler form the laser resonant cavity .

Fused silica is an ideal optical material for Nd:YAG laser pumping since it is transparent over the visible spectrum. Moreover, it has a low coefficient of thermal expansion and it is resistant to scratching and thermal shock *(103)*. For manufacture of the light guide, a 99.995% optical purity fused silica rod with 25 mm diameter and 100 mm length was supplied by Beijing Kinglass Quartz Co., Ltd. It was first ground and polished to produce the 3D-CPC (Compound Parabolic

Concentrator) form output end with $D_2 = 25$ mm / $D_3 = 20$ mm input / output diameters and $L_2 = 20$ mm length. The 3D-CPC was used to convert the rays from the large-input aperture of the conical light guide, emitting into a smaller angle of $35°$ maximum, to a small-output aperture emitting into a larger angle of $45°$ maximum, thus the source étendue is preserved. This preservation implies that irradiance is larger at output aperture than at the entrance aperture, leading to a net concentration of the pump radiation *(104)*. Although the production of CPC optical surfaces is usually carried out by expensive single-point machining techniques, it is possible to approximate the complex surfaces of the CPC by means of a limited number of simpler shapes without severe efficiency losses *(105)*. This can simplify the production process of the light guide with 3D-CPC output end. The conical section of the light guide was then machined and polished to dimensions of $D_1 = 22$ mm / $D_2 = 25$ mm input / output diameters and $L_1 = 50$ mm length. The polished light guide was finally cut away from the rest of the fused silica rod. Both the input and output ends of the light guide were finally ground and polished.

For end pumping, one part of the radiation is directly focused onto the 1064 nm HR end face of the rod by the total internal reflections from the side walls of the light guide. The HR coating reflects the 1064 nm wavelength oscillating laser power within the resonant cavity, but allows the passage of other pumping wavelengths. Another part of the radiation not hitting the HR end face of the rod is also guided into the small conical cavity, with $D_4 = 22$ mm / $D_5 = 9$ mm input / output diameters and $L_3 = 19.5$ mm length, which ensures efficient side pumping to the laser rod due to multi-pass absorption of the pump radiation caused by the zigzag passage of the rays within the cavity. The inner wall of the pumping cavity is bonded with protective silver-coated aluminum foil with 94% reflectivity.
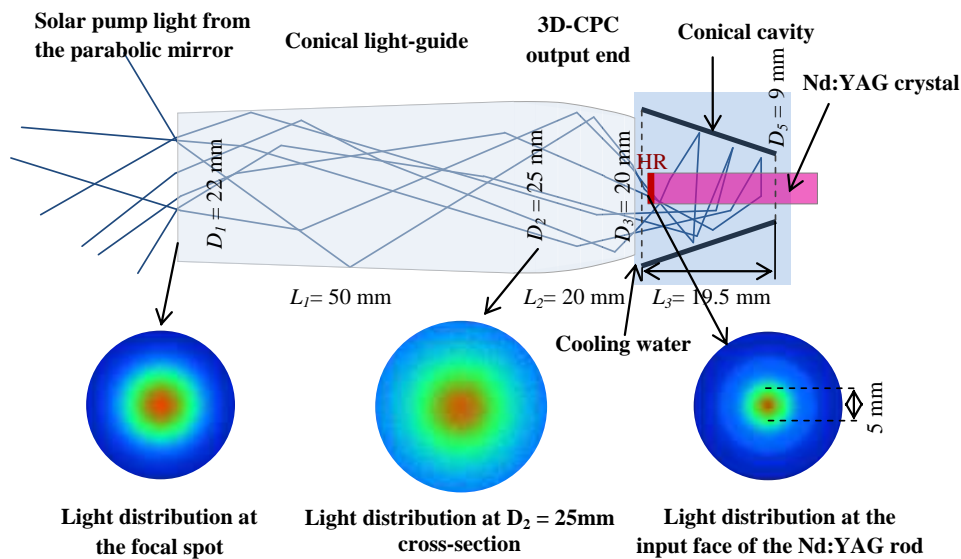


**FIG. 5.2** - The conical-shaped fused silica light guide with 3D-CPC output end coupled to the conical pump cavity where the 5 mm diameter Nd:YAG laser rod is efficiently pumped.

Since large concentration factors are needed for most solar-pumped lasers, a more aggressive cooling system is also of utmost importance in this type of lasers. Thus, all the solar laser setups presented in this thesis are actively cooled by cooling water at 6 l.min$^{-1}$ flow rate. Maximum contact between the coolant and the rod is essential for removal of the generated heat. The light-guide end face is in direct contact with the cooling water, ensuring efficient light coupling from the guide to the rod. Both fused silica material and cooling water are useful for partially preventing both UV solarization and IR heating of the laser rod. The fused silica light guide is also important

in preventing the possible heating of ultra-high solar flux at the focus to the mechanical structure of the laser head.

The 1.0% Nd:YAG single-crystal rod was supplied by Altechna Co. Ltd. The upper end face of the rod was high reflection coated (HR) for the laser emission wavelength (R >99.8% @1064 nm). The lower end face was anti-reflection (AR) coated for the same wavelength (R < 0.2% @1064 nm). The output coupler was partial reflection coated (PR). The optical laser resonator was formed by both the 1064 nm HR reflector and the PR output coupler and its length could be varied from 30 mm to 250 mm. In LASCAD$^{©}$ analysis, output couplers of different reflectivity (R) and different radius of curvature (RoC) were tested individually to maximize the multimode laser power. An average solar pump wavelength of 660 nm *(22)* and a round-trip loss of 2.1% were assumed in LASCAD$^{©}$ analysis.

### 5.1.2 SOLAR LASER EXPERIMENTAL RESULTS

In PROMES-CNRS horizontal axis MSSF solar facility, two sliding doors and a shutter with motorized blades are used to regulate the incoming solar power from the heliostat. By varying the rotation angle of the shutter, different input solar power and output laser power were, respectively, measured with a Molectron PowerMax 500D and a Thorlabs PM1100D power meter. Direct solar irradiance is measured simultaneously during lasing with a Kipp&Zonen CH1 pyrheliometer on a Kipp&Zonen 2AP solar tracker. It varied between 950 and 1020 W/m$^2$ during the experiments. Three −1 m RoC output couplers with 90%, 94% and 98% reflectivity, respectively, were used to study the solar input / laser output performance. A resonator cavity length of 125 mm was adopted in this case.

For the solar irradiance of 990 W/m$^2$ in Odeillo July 2012, about 1680 W of solar power was collected in the focal zone. To achieve the maximum laser power the shutter was totally removed. 40.1 W was measured in this case, for a −1 m RoC output coupler with 94% reflectivity. 13.9 W/m$^2$ collection efficiency was hence calculated, corresponding to an improvement of 145% over the previous result *(36)*. This result agrees well with the numerically predicted 39.8 W of laser power for the same resonator configuration. It is, however, limited by the practical reflectivity of both the heliostat and the parabolic mirror.
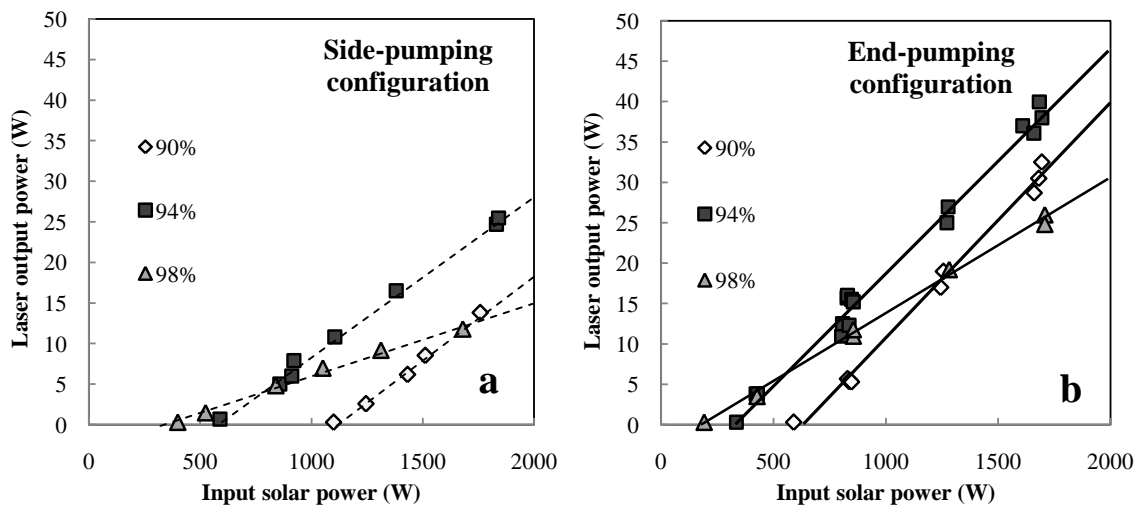


**FIG. 5.3** - Solar input / Nd:YAG laser output performance for different output coupler reflectivity from **(a)** the previous side-pumping configuration *(36)* and **(b)** the present end-pumping configuration *(33)*.

As shown in FIG. 5.3, the highest slope efficiency of 2.9% was measured for the 90% output coupler. This value represents an enhancement of 132% over the previous Nd:YAG slope laser efficiency with side-pumping configuration *(36)*. Moreover, lower pump power at the lasing threshold was measured in the focal zone for all the output mirror reflectivities. A lowest threshold pump power of 192 W was measured for the 98% output coupler, which is 209% less than that necessary for our previous Nd:YAG laser *(36)*. The threshold power can be further reduced by increasing the output mirror reflectivity *(48)*.

Our research article, regarding the above mentioned report *(33)*: *A 40 W cw Nd:YAG solar laser pumped through a heliostat: a parabolic mirror system* (Almeida, J., Liang, D., Guillot, E., and Abdel-Hadi, Y., Laser Phys. 23 (2013)) was featured in Laser Physics Highlights of 2013 *(79)*.

# 5.2  21.1 W/M$^2$ SOLAR LASER COLLECTION EFFICIENCY

A double-stage fused silica conical lens / conical cavity was used to end-side pump the 5 mm diameter, 25 mm length, 1.0 at.% Nd:YAG rod *(34)*. The final test of the solar laser output performance was carried out at PROMES-CNRS, using also the horizontal axis MSSF solar facility.

## 5.2.1  END-SIDE-PUMPING SCHEME WITH CONICAL LENS
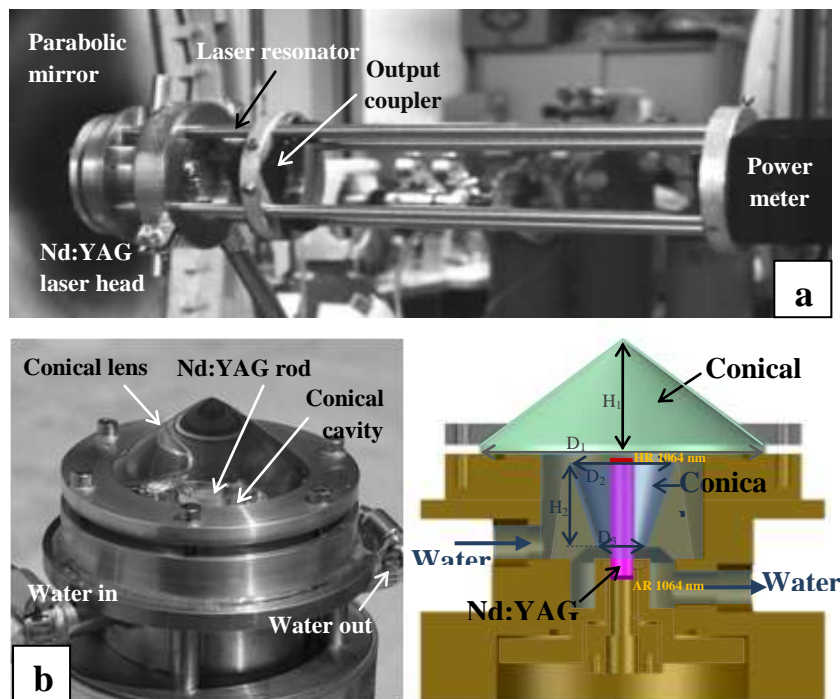


**FIG. 5.4** - **(a)** Nd:YAG laser head positioned at the focus of the PROMES-CNRS 2 m diameter parabolic mirror. **(b)** Photograph and **(c)** mechanical design of the Nd:YAG laser head, composed of the fused silica conical lens, conical pump cavity, and Nd:YAG rod, which was actively cooled by water.

The laser head was also fixed on an X – Y – Z axis positioning system by using a multi-angle vice, ensuring an accurate optical alignment in the focal zone. The laser head was composed of two simple stages: the conical-shaped fused silica lens and the conical-shaped pump cavity, within which the Nd:YAG rod was mechanically mounted.

The conical fused silica lens collected the concentrated solar radiation. Analogously to the previous scheme *(33)*, for end pumping, one part of the radiation is directly focused onto the HR 1064 nm end face of the rod by the conical lens. Another part of the radiation that does not hit the HR 1064 nm end face of the rod is guided into the conical cavity. The zigzag passage of the rays within the small pump cavity ensures the multi-pass side pumping to the rod. The inner wall of the pumping cavity was also bonded with protected silver-coated aluminum foil with 94% reflectivity. The optical laser resonator was also formed by both the HR 1064 nm reflector and the PR 1064 nm output coupler.

## 5.2.2 NUMERICAL OPTIMIZATION OF THE SOLAR LASER PERFORMANCE

The previous solar laser *(33)* used a conical-shaped fused silica light guide with a 3D-CPC output end to couple the concentrated solar radiation into a conical pump cavity, where a 5 mm diameter, 25 mm length Nd:YAG was efficiently end-side pumped. The absorbed pump flux distributions along five transversal cross-sections and one central longitudinal cross-section of the 5 mm diameter, 25 mm length Nd:YAG rod pumped through the present and previous schemes are shown in FIG. 5.5(a) and FIG. 5.5(b) respectively. Red color means near maximum pump absorption, whereas blue means little or no absorption.
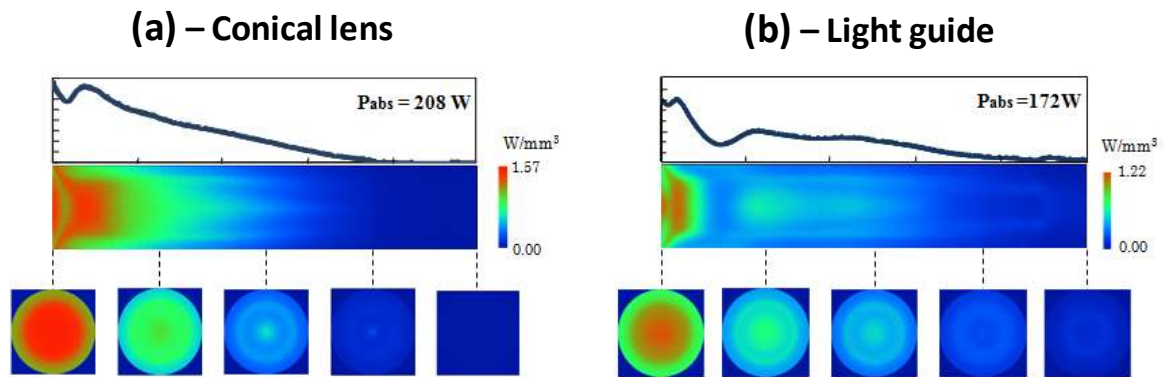


FIG. 5.5 - Absorbed pump flux distribution along the 5 mm diameter, 25 mm length Nd:YAG rod pumped through **(a)** the present double stage conical lens / conical pump cavity and **(b)** the previous double stage conical light guide with 3D-CPC output profile / conical pump cavity *(33)*.

The main contribution to the amount of absorbed pump power within the laser rod comes from end pumping, which leads to a more intense pump flux within the upper-end region of the laser crystal, as observed in FIG. 5.5. Due to the light coupling and focusing capacity of both the fused silica conical lens and the conical pump cavity, 121% more pump power is absorbed by the laser rod pumped through the conical lens.

In LASCAD$^{©}$ analysis, output couplers of different reflectivity (R) and different radius of curvature (RoC) were tested individually to maximize the multimode laser power. For 1600 W solar power at the focus, maximum multimode laser power of 61.6 W was numerically attained with the R = 94%, RoC = -1 m output mirror, as given in FIG. 5.6. The highest slope efficiency of

5.4% was numerically obtained for the R = 90% output coupler. 4.9% slope efficiency was numerically found for the R = 94% output coupler. The threshold pump power of 325 W was achieved in this case. The lowest threshold pump power of 180 W was numerically found for the R = 98% output coupler with 3.2% slope efficiency.



**FIG. 5.6** - Numerically calculated laser output power as function of solar power at the focus, for the RoC = −1 m output mirror with three different reflectivities.

### 5.2.3 SOLAR LASER EXPERIMENTAL RESULTS

To achieve maximum solar laser output power, the R = 94% , RoC = −1 m output coupler was placed 50 mm away from the laser rod. After considering all the shading effects in the primary concentrator, an effective collection area of 2.65 m$^2$ was calculated. For 976 W/m$^2$ solar irradiance, 1526 W was measured at the focus of the primary concentrator. Maximum laser power of 56.0 W was measured in this case. This value was 1.4 times more than that of the previous end-side pumped laser, carried out at PROMES-CNRS *(33)*. A 21.1 W/m$^2$ record solar laser collection efficiency with the heliostat – parabolic mirror system was calculated. Considering the fact that only 59% incoming solar radiation was concentrated at the focus, our collection efficiency represents an important step in competing with the solar lasers pumped by Fresnel lenses.
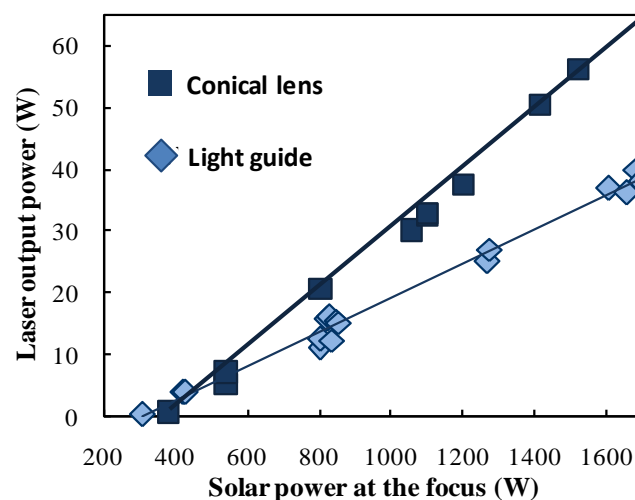


**FIG. 5.7** - Solar input power versus Nd:YAG laser output power achieved by the present *(34)* and previous *(33)* end-side-pumping configurations, for R = 94%, RoC = -1 m output mirror.

A slope efficiency of 4.9% was measured for the R = 94% ,RoC = −1 m output coupler, which agrees well with the numerical data. This value represented an enhancement of 157% over the previous slope efficiency for Nd:YAG laser pumped by the same PROMES-CNRS solar facility.

Laser operation was stable while the shutter was in its maximum opening, producing 56 W cw solar laser power. In this case, the maximum solar power of 1525 W was measured. Nevertheless, in order to achieve more solar power at the focus, the shutter was totally removed. After only about 4 s, drastic reduction in laser power was observed, followed by final laser rod fracture. The main cause is attributed to the inhomogeneous heating of the laser rod, due to its non-uniform absorption pump distribution. Indeed, major damage had occurred in the upper-end region of the laser rod. The main problem hindering laser power and brightness scaling of solar-pumped solid-state lasers is heat generation within the laser medium, which leads to a spatial variation in temperature and, consequently, internal stresses within the laser material. This is especially true for longitudinally pumped high-power lasers, in which the non-uniform pump profile causes a very high pump deposition density and, hence, a high thermal loading density, which can result in fracture of the laser rod *(106,107)*. Even in a water-cooled longitudinally pumped laser rod, increased stress has been observed close to the center of the pumped surface *(107)*, which may be critical for crystal damage in high-power end-pumped laser applications.

## 5.2.4  NUMERICAL ANALYSIS OF THE THERMAL PERFORMANCE

Fig. 5.8 shows the numerical simulation results from LASCAD$^{©}$ analysis of the thermally induced effects in the 5 mm diameter, 25 mm length 1.0 at% Nd:YAG rod, considering 1526 W at the focus of the parabolic mirror. In the analysis, the absorbed pump flux data from ZEMAX$^{©}$ analysis are integrated over the rod volume. A heat efficiency factor – defined by the relative part of the absorbed pump power converted into heat – of 30% for 1.0 at% Nd:YAG under lasing condition *(108)* is considered in LASCAD$^{©}$ analysis.
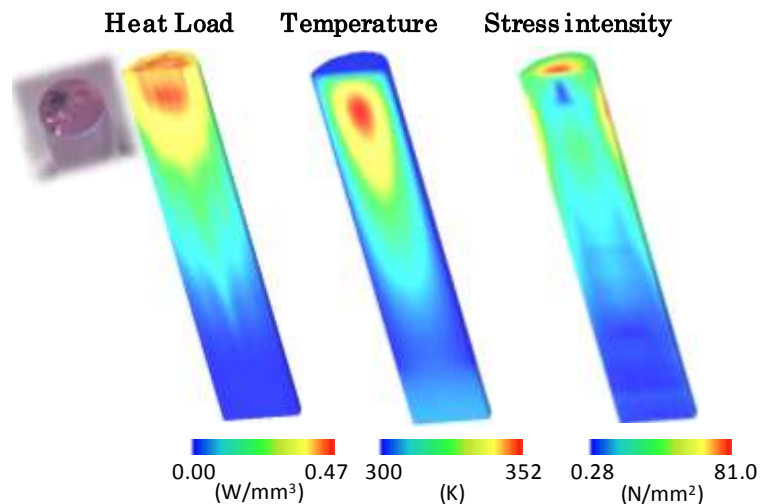


**FIG. 5.8** - Heat load, temperature and stress intensity distributions, numerically simulated in LASCAD$^{©}$ analysis, for the 5 mm diameter, 25 mm length Nd:YAG rod. The inset photograph shows the damaged Nd:YAG laser rod input end.

Major thermal problems occur at the upper-end region of the rod, due to the non-uniform absorbed pump flux distribution. Maximum heat load of 0.47 W/mm$^3$ is numerically calculated. The temperature gradient from the center to the surface of the laser rod reaches 52°C. Maximum stress intensity of 81 N/mm$^2$ is numerically attained, which is still considerably below the stress fracture

limit of about 200 N⁄mm$^2$ for Nd:YAG material *(48)*. The reason for this discrepancy is attributed to the small overlap of only 16% between the absorption spectrum of the Nd:YAG material and the solar emission spectrum *(45)*. The additional 84% unabsorbed solar radiation, ranging between 0.25 μm and 2.5 μm, may also heat the laser rod, causing its final fracture. Cooling water and fused silica material only partially filter the undesirable solar radiations.

To circumvent the thermal-induced stresses in an end-side-pumped solar laser, three different solutions were numerically analyzed: (A) laser rod with lower Nd$^{3+}$ dopant concentration; (B) composite laser rod and (C) thin laser rod:

## A. <u>Laser rod with lower Nd$^{3+}$ dopant concentration</u>

Thermal performances of the 5 mm diameter, 25 mm length Nd:YAG rods with 0.8 to 1.2 at.% Nd$^{3+}$ concentrations are analyzed in TABLE 5.2. Nd:YAG rod with lower dopant concentrations results in slightly better thermal performance. Nevertheless, it also leads to the reduction of absorbed pump power, and therefore laser output power.

**TABLE 5.2** - Thermal performance of the 5 mm diameter Nd:YAG rod as function of the Nd$^{3+}$ concentration.

| Nd concentration (at.%) | 0.8 | 0.9 | 1.0 | 1.1 | 1.2 |
|---|---|---|---|---|---|
| Absorbed pump power (W) | 202 | 207 | 208 | 214 | 217 |
| Heat load (W/mm$^3$) | 0.40 | 0.43 | 0.47 | 0.52 | 0.57 |
| Temperature (K) | 347 | 350 | 352 | 357 | 362 |
| Stress (N/mm$^2$) | 73.7 | 78.5 | 81.0 | 90.9 | 99.2 |
| Laser power (W) | 56.2 | 57.5 | 58.0 | 60.1 | 60.9 |

## B. <u>Composite laser rod</u>
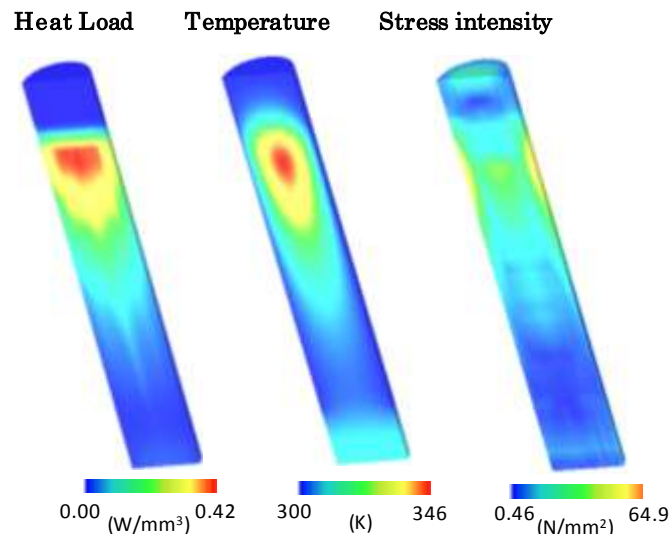


**FIG. 5.9** - Heat load, temperature and stress distributions, numerically simulated for the 5 mm diameter composite YAG / Nd:YAG rod.

Composite rods can provide an effective way to reduce the thermal effects inside longitudinally-pumped laser rods **(107,109)**. The heat load, temperature, and stress intensity distributions are numerically calculated for a 5 mm diameter YAG/Nd:YAG composite rod, with a 5 mm long undoped YAG part and 25 mm long 1.0 at.% Nd:YAG doped part, as shown in FIG. 5.9. Since the undoped region is transparent to the impinging pump radiation, there is no heat load generated at the rod input face. Maximum stress intensity of 65 N/mm$^2$ is located on the lateral surface of the composite rod, which is lower than the 81 N/mm$^2$ for non composite 1.0 at.% Nd:YAG rod. A slightly decreased laser power of 54 W laser output power is numerically calculated for the composite rod.

### C. <u>Thin laser rod</u>

TABLE 5.3 compares the thermal performances of 4 mm, 5 mm diameter rods, all with 25 mm length and 1.0 at% Nd$^{3+}$ concentration.

**TABLE 5.3** - Thermal performances of the 1.0 at% Nd:YAG rod with different diameters.

| Rod diameter (mm) | 4 | 5 |
|---|---|---|
| Absorbed pump power (W) | 173 | 208 |
| Heat load (W/mm$^3$) | 0.53 | 0.47 |
| Temperature (K) | 343 | 352 |
| Stress (N/mm$^2$) | 57.1 | 81.0 |
| Laser power (W) | 52.1 | 58.0 |

For the same doping concentration, the 4 mm diameter Nd:YAG rod absorbs less pump power, producing also less laser power. It can, however, be more easily cooled due to its smaller cross-section, leading to lower temperature gradients and thermally induced stresses, as compared to that of the 5 mm diameter rod in TABLE 5.3. Maximum stress intensity of 57.1 N/mm$^2$ is numerically calculated for the 4 mm diameter rod, which is 30% less that of the 5 mm diameter rod. For these reasons, in the following prototypes we have adopted a longer and thinner laser rod.

## 5.3 25 W/M$^2$ SOLAR LASER COLLECTION EFFICIENCY

We reported an improvement in both solar laser collection efficiency and slope efficiency by using the heliostat-parabolic mirror solar energy collection system of Universidade NOVA de Lisboa **(35)**.

### 5.3.1 END-SIDE-PUMPING SCHEME WITH LARGE ASPHERIC LENS

As shown in FIG. 5.10(a), a large aspheric fused silica lens was used to further concentrate the solar radiation from the focal zone of a 1.5-m-diameter primary concentrator, to a 4-mm-diameter,

35-mm-long Nd:YAG single-crystal rod within a conical pump cavity *(35)*. The large fused silica aspheric lens was 88 mm in diameter, 38 mm in height, 60 mm in front surface radius of curvature. It couples efficiently the concentrated solar radiation from the focal spot to the Nd:YAG rod. For end-pumping, one part of the concentrated radiation is directly focused onto the HR 1064 nm end face of the rod by the aspheric lens. For side-pumping, another part of the radiation that does not hit the HR 1064 nm end face of the rod is guided into the hollow conical cavity with $D_2 = 18$ mm / $D_3 = 9.7$ mm input / output diameters and $H_2 = 18$ mm height. As in the previous schemes, the inner wall of the pumping cavity was bonded with a protected silver-coated aluminum foil with 94% reflectivity. The Nd:YAG rod, the hollow conical pump cavity and the output end face of the fused silica lens were all also actively cooled by water at 6 L /min flow rate. There was 5 mm space between the lens output face and the end face of the rod for the easy exit of cooling water. The 1.0 at.% Nd:YAG single-crystal rod was supplied by Altechna Co. Ltd. The input end face of the rod is HR coated for the laser emission wavelength (HR > 99.8% @ 1064 nm). The output end face is anti-reflection (AR) coated for the same wavelength (R < 0.2% @ 1064 nm). The output coupler was partial reflection (PR) coated for 1064 nm. Analogously to the previous schemes, the optical laser resonator was formed by both the HR 1064 nm reflector and the PR 1064 nm output coupler, as demonstrated in FIG. 5.10 (a).
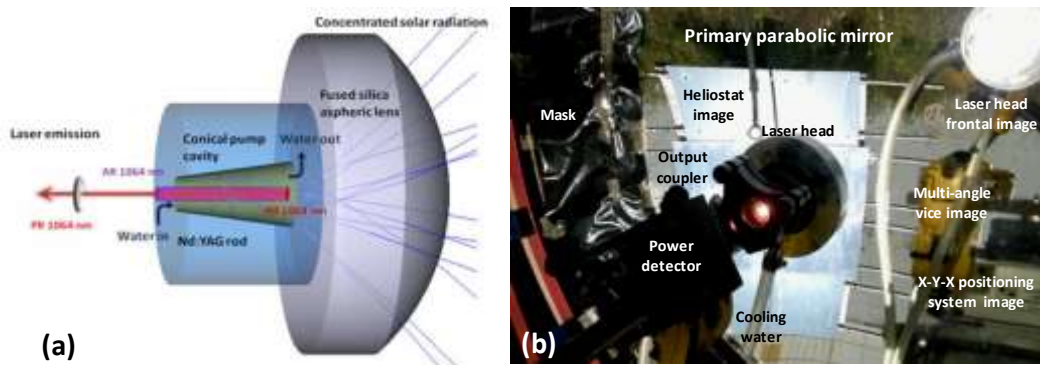


**FIG. 5.10** - **(a)** Design of novel Nd:YAG laser head, composed of the a large fused silica aspheric lens, the conical pump cavity and the Nd:YAG rod, which were all actively cooled by water. **(b)** Stationary Nd:YAG solar laser emitting at the focus of NOVA primary parabolic mirror concentration system.

The laser head was fixed on an X-Y-Z axis positioning system through a multi-angle vice. To avoid overheating the Nd:YAG active medium, the input solar power at focus was actually limited by masking the external annular area of the 1.5 m diameter mirror so that only its 1.28 m diameter central circular area was utilized, as shown in FIG. 5.10(b). 1.17 $m^2$ effective solar radiation reception area was calculated by discounting the shadowing area by both the laser head and its supporting mechanics.

## 5.3.2 NUMERICAL OPTIMIZATION OF THE SOLAR LASER PERFORMANCE

The absorbed pump flux distributions along five transversal and one central longitudinal cross-sections of the 4 mm diameter, 35 mm length Nd:YAG rod are shown in FIG. 5.11. Absorbed pump light distributions presents a strong non-uniform distribution along the thin rod, as shown by the central longitudinal absorbed pump flux distribution along the laser rod. Nevertheless, this was the distribution that ensured the maximum solar laser power.
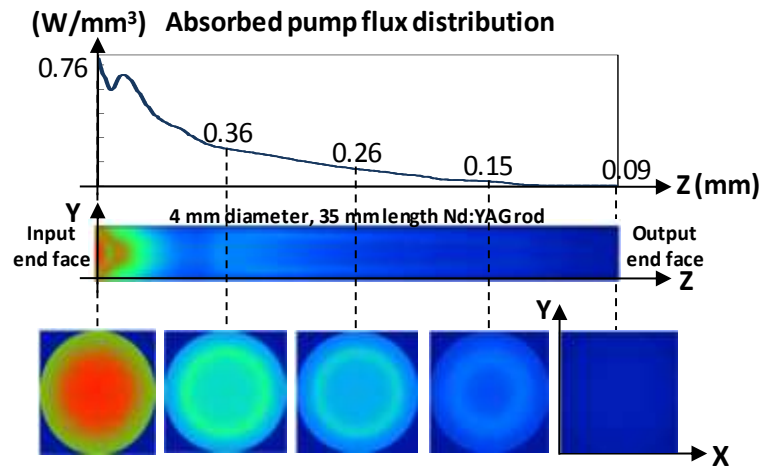
**FIG. 5.11** - Absorbed pump-flux distribution along both one longitudinal central cross-section and five transversal cross-sections of the 4 mm diameter, 35 mm length Nd:YAG rod.

In LASCAD$^{\copyright}$ analysis, output couplers of different reflectivity (R) and different radius of curvature (RoC) were tested individually to maximize the multimode laser power. For typical clear sunny days, with an average solar irradiance of 890 W/m$^2$ in Lisbon, about 780 W solar power can be measured in the focal zone. For short cavity length of $L_1 = 10$ mm, between the AR 1064 nm output end face of the rod and the output coupler, the maximum multimode laser power of 29.6 W was numerically calculated with R = 94% and RoC = -5 m, as shown in FIG. 5.12.



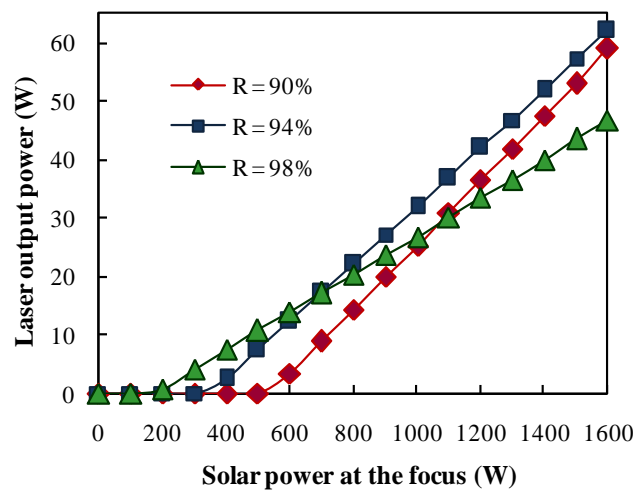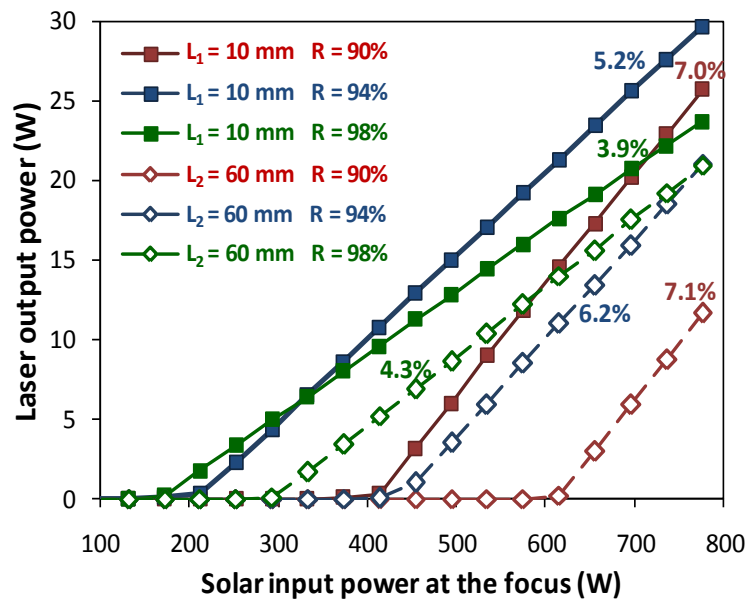**FIG. 5.12** - Numerically calculated laser output power as function of solar power at the focus, for three different reflectivity (R = 90%, 94% and 98%) output mirrors. Laser slope efficiencies are also indicated.

Solar laser output power depends heavily on laser cavity length. When $L_2 = 60$ mm was used in LASCAD$^{\copyright}$ numerical calculations, the maximum solar laser power were reduced to 21 W, 20.9 W and 11.7 W for R = 94%, 98% and 90% respectively. Despite poorer laser output powers at $L_2 = 60$ mm, higher slope efficiencies of 6.2%, 4.3% and 7.1% were found.

### 5.3.3  SOLAR LASER EXPERIMENTAL RESULTS

To achieve maximum solar laser output power, the R = 94% and RoC = -5 m output coupler was placed 10 mm away from the laser rod. 29.3 W cw solar laser power was measured, corresponding to 25.0 W/m$^2$ solar laser collection efficiency with the NOVA heliostat - parabolic mirror system. A slope efficiency of 5.1% was measured for the R = 94%, RoC = -5 m output coupler, as shown in FIG. 5.13, which agreed well with the numerically analyzed data in FIG. 5.13. To test the strong dependency of laser output power on laser resonator cavity length, the R = 94%, RoC = -5 m output coupler was again mounted 60 mm away from the AR 1064 nm output end face of the laser rod. Only 21.5 W cw solar laser power was measured, corresponding to 18.4 W/m$^2$ solar laser collection efficiency with the NOVA heliostat - parabolic mirror system. An enhanced slope efficiency of 6.0% was, however, measured, which was only slightly lower than the numerical data in FIG. 5.13.
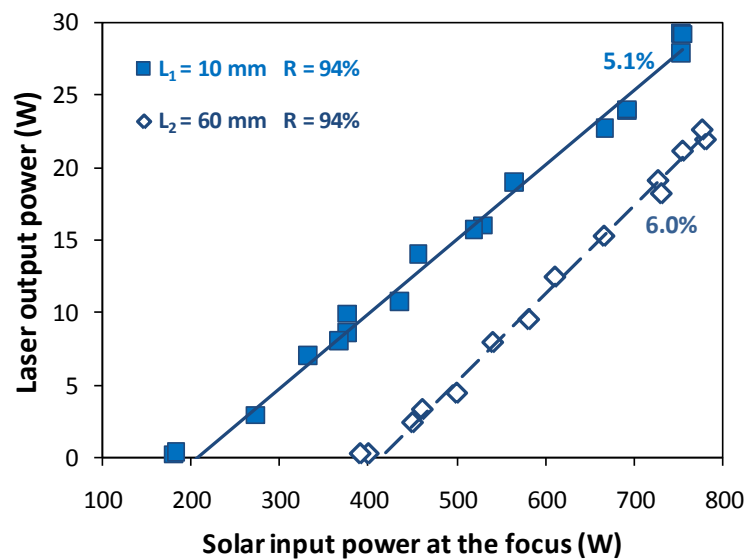


**FIG. 5.13** - Solar laser output power versus solar input power at the focus, achieved by the R = 94%, RoC = -5 m output mirror positioned at different cavity length, L$_1$ = 10 mm and L$_2$ = 60 mm respectively.

Minimizing rod diameter, now 4 mm diameter, makes it more resistant to thermal stress, thus helping to avoid thermal fracture, as happened to our previous 5 mm diameter Nd:YAG rod *(34)*, enabling therefore the use of higher pumping powers. We also experimented pumping the 4 mm diameter rod without masking the mirror. 33 W laser power was obtained in this case without fracturing the rod, so 29.3 W was not the limit of output laser power. It was, however, the most efficient output laser power in terms of laser collection efficiency. The periphery mirror contributes poorly to increasing the laser output due to its high angular input of pump rays. 25.0 W/m$^2$ collection efficiency represents an important step in competing with the direct-tracking solar lasers pumped by Fresnel lenses on a solar tracker.

## 5.4  31.5 W/M$^2$ SOLAR LASER COLLECTION EFFICIENCY

By end-side-pumping the 4 mm diameter 35 mm length Nd:YAG single-crystal rod with the same PROMES-CNRS heliostat-parabolic mirror solar energy concentration system *(31)*,

significant progresses in both multimode and TEM$_{00}$-mode solar laser collection efficiencies were reported here. The last being discussed in CHAPTER 6.

## 5.4.1 END-SIDE-PUMPING SCHEME WITH LARGE ASPHERIC LENS

To reduce the maximum input solar power at the focus, the input solar power at focus was also limited by masking the external annular area of the 2.0 m diameter parabolic mirror so that only its 1.4 m diameter central circular area was utilized, as shown in FIG. 5.14(a). After discounting the shading effects of the large plane solar mirror, the shutter, the X-Y-Z axes positioning system, and multi-angle vice, the 0.3 m diameter central opening on the parabolic mirror and the solar laser head, 1.18 m$^2$ effective solar energy collection area was calculated. The laser head was fixed on the X-Y-Z axes positioning system through the multi-angle vice, ensuring its accurate and easy optical alignment in the focal zone.
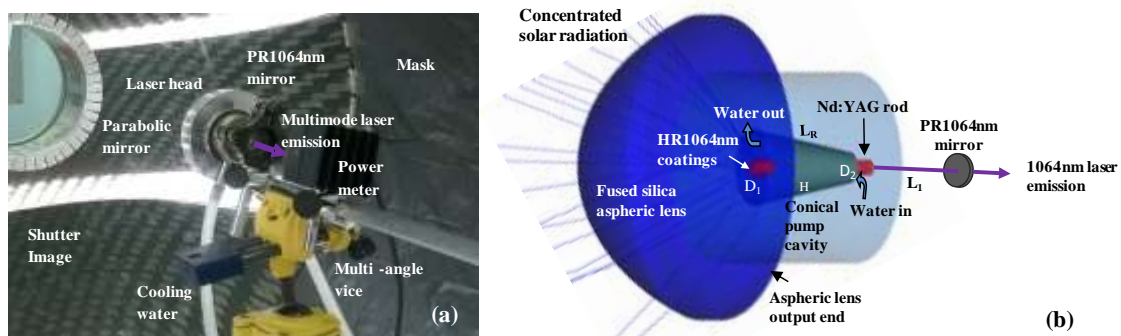


FIG. 5.14 - (a) Laser head and output coupler were separated by 11 mm for producing the maximum multimode laser power . (b) Design of Nd:YAG laser head.

As shown in FIG. 5.14(b), the laser head was composed of the aspheric fused silica lens and the conical-shaped pump cavity, within which the Nd:YAG rod was mounted. The large fused silica aspheric lens was 84 mm in diameter, 38 mm in height, 45 mm in front surface radius of curvature and -0.005 in rear r$^2$ parameter. The output end face of the lens had a plane surface. The aspheric lens coupled efficiently the concentrated solar radiation from the focal zone into the Nd:YAG rod. In this case, there was 10 mm space between the aspheric lens output end face and the HR face of the rod, doubling the space compared to the previous scheme *(35)*, which was more than enough for the exit of cooling water.

## 5.4.2 SOLAR LASER EXPERIMENTAL RESULTS

To achieve maximum solar laser output power, a R = 95%, RoC = -10 m output coupler was mounted 11 mm away from the AR 1064 nm output face of the laser rod, as indicated in FIG. 5.15(a). By varying the rotation angle of the shutter, different input solar power and output laser power were respectively measured with a Molectron PowerMax 500D and a Thorlabs PM1100D power meters, respectively. Direct solar irradiance varied between 950 W/m$^2$ and 1010 W/m$^2$ during the experiments. After considering all the shading effects in the primary concentrator, an effective collection area of 1.18 m$^2$ was adopted. For 1010 W/m$^2$ mid-day solar irradiance, 700 W solar power was measured at the focus of the primary concentrator.

Maximum multimode solar laser power of 37.2 W was successfully registered, corresponding to record-high collection efficiency of 31.5 W/m$^2$. This value was 1.3 times higher than the previous

record with parabolic mirror *(35)*. Threshold laser power of 280 W was also measured, resulting in 8.9% solar laser slope efficiency, as shown in FIG. 5.15. This value represents 1.8 times and 1.4 times improvement over the previous slope efficiencies for Nd:YAG laser pumped within the same PROMES-CNRS solar facility *(34)* and the NOVA solar facility, respectively *(35)*. Output mirror with R = 94%, RoC = -5 m offered a slightly lower slope efficiency of 8.3%.
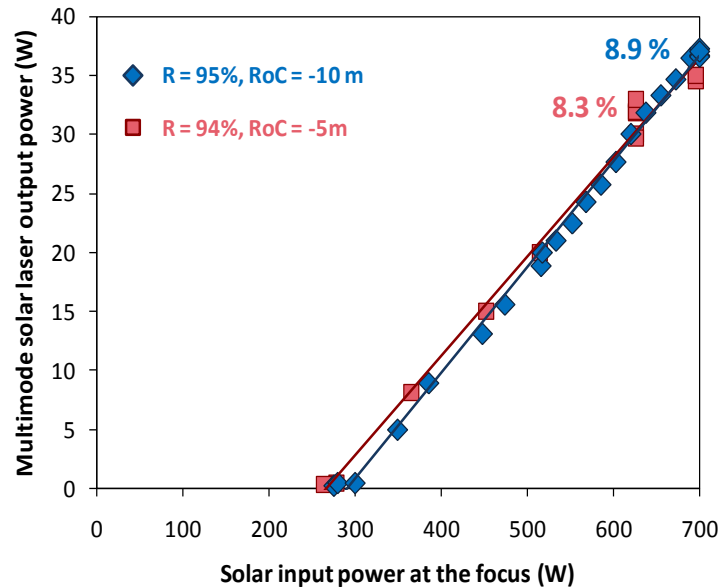


**FIG. 5.15** - Solar laser output power versus solar input power at the focus of the parabolic mirror, for R = 95%, RoC = -10 m and R = 94%, RoC = -5 m output couplers.

Considering the advantage of having a stable laser emission from a stationary solar laser head within the laboratory, rather than a solar laser head mounted onto a mobile solar tracker in outdoor environment *(30)*, our solar laser might represent one-step further towards many interesting applications. This research work was highlighted in both Renewable Energy Global Innovations *(88)* and Laser Focus World *(89)*.

The advances in solar laser efficiency within the framework of this PhD project are summarized below in FIG. 5.16 and compared to the previous records with parabolic mirror and Fresnel lens system. From 2012 to 2017, an almost linear increase in solar laser collection efficiency with parabolic mirror can be observed. When compared to the previous record of 9.6 $W/m^2$ with parabolic mirror system *(36)*, a two-fold and three-fold increase was attained in 2015 and 2017, respectively, during this PhD project. The latter gave rise to a record collection efficiency of 31.5 $W/m^2$. Although it was only slight higher than the record value obtained with Fresnel lens *(30)*, Dinh et al. were favored by using instead a mobile solar tracker. In terms of slope efficiency, a near exponential increase with parabolic mirror system is instead observed, where the most substantial improvement is obtained in 2017 during this PhD project, by reaching a slope efficiency of 8.9%, also even higher than the previous record with Fresnel lens *(31)*.

It is worth noting that these main achievements were obtained by pumping smaller diameter rods when compared to the previous record, which has also lead to meliorate the solar laser beam quality of high efficiency solar-pumping schemes, which was not previously held in high regard.

## 5.5 SUMMARY OF THE ADVANCES IN SOLAR LASER EFFICIENCY
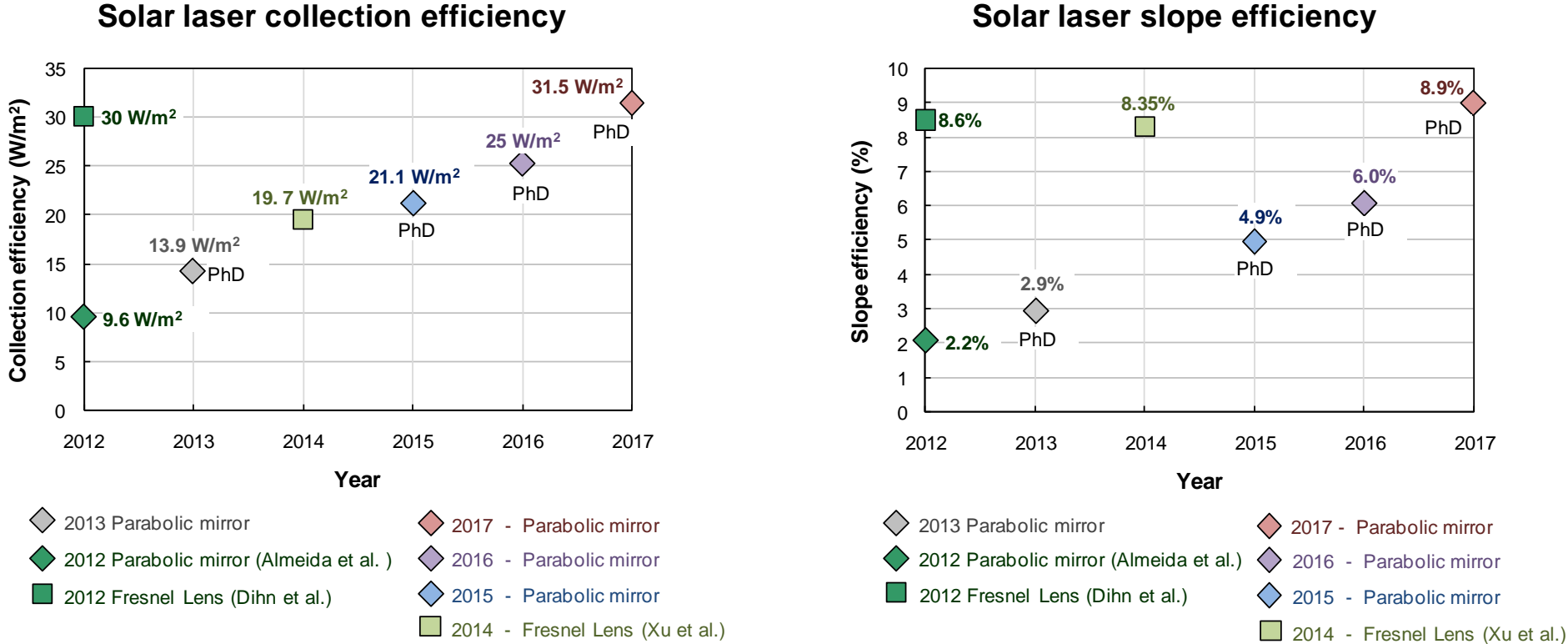


**FIG. 5.16** - Summary of the solar laser collection efficiency and slope efficiency advances during the PhD project and comparison with the previous record.

# 6 ADVANCES IN SOLAR LASER BRIGHTNESS

Two figures of merit are used to characterize the performance of solar lasers. The output power emitted per unit primary collection area, which characterizes the laser efficiency; and second, the output power divided by the square of the $M^2$ beam quality factors, taken as a metric of the potential usefulness of the output. Unfortunately, while solar laser powers of 120 W have been achieved *(30)*, laser beam quality values were very high (meaning a low-quality beam) at 137 for both the X and Y axis, leading to a dismal brightness figure of merit of only 0.0064 W. The substantial improvement in solar brightness was only successful by producing laser output in the lowest fundamental mode, $TEM_{00}$-mode *(31,37,38,40,41,42)*.

In this chapter, the efforts performed during this PhD doctoral programme for enhancing the solar laser brightness are explained.

## 6.1 1.9 W SOLAR LASER BRIGHTNESS / FIRST $TEM_{00}$ MODE SOLAR LASER

Here we show a significant advance in solar-pumped laser beam brightness through the production of $TEM_{00}$-mode solar laser by NOVA Fresnel lens system and a 3 mm diameter Nd:YAG single-crystal rod *(42)*. It was, to the best of our knowledge, the first demonstration of solar laser in fundamental mode.

### 6.1.1 SIDE-PUMPING SCHEME WITH LARGE ASPHERIC LENS

As shown in FIG. 6.1, the solar-pumped $TEM_{00}$ mode Nd:YAG laser system is composed of the first-stage 1.0 diameter Fresnel lens, the laser head and its associated asymmetric optical resonator, all mounted on a two-axis solar tracker that follows automatically the Sun´s movement. The Fresnel lens has 1.0 m diameter and 1.3 m focal length. The measured full width at half maximum is 13 mm at the minimum focal waist. The measured transmission efficiency is 76%. The concentrated solar power at the focal spot averaged over 2 min is 590 W for source sunlight with 890 $W/m^2$ irradiance. Mechanical adjustments in X-Y-Z directions allowed an easy alignment in the focal zone. Coarse angular adjustments were also very helpful for achieving the maximum laser output power. The laser head is composed of the second-stage large fused silica aspheric lens, the

third-stage 2D-CPC concentrator and the V-shaped pumping cavity within which the 3 mm diameter, 30 mm length Nd:YAG rod is mounted.
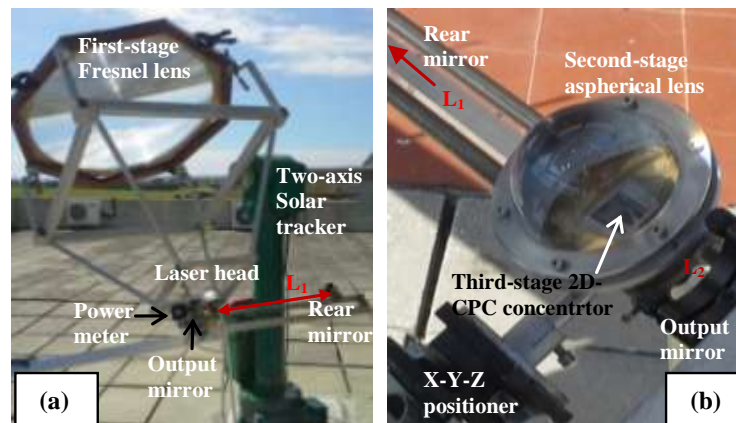


**FIG. 6.1** - **(a)** The solar-pumped $TEM_{00}$ mode Nd:YAG laser system **(b)** The laser head. $L_1$ and $L_2$ represent the separation length of the high reflection (HR) and partial reflection (PR)

The large curved input face of the aspheric lens, the dimensions of the 2D-CPC concentrator are designed to compress the concentrated solar radiations from the focal zone onto the thin laser rod within the V-shaped pumping cavity. To manufacture the large aspheric lens, an 85 mm diameter, 50 mm length fused silica rod of 99.999% optical purity from Beijing Kinglass Quartz Co., Ltd. was ground and polished to its final dimensions.
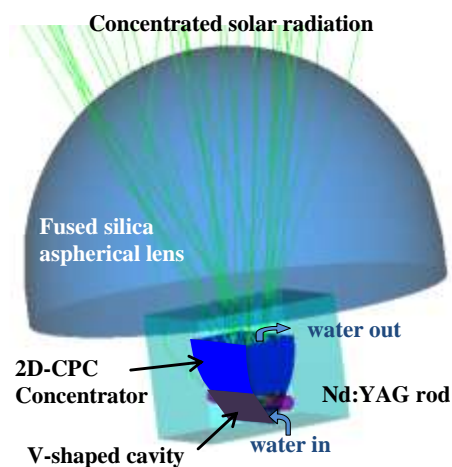


**FIG. 6.2** - Detailed 3D view of the solar laser head.

The 3 mm diameter, 30 mm length Nd:YAG single-crystal rod is supplied by Altechna Co., Ltd. It has 1.0 % $Nd^{3+}$ concentration. Both ends of the rod are AR coated (R < 0.2% @ 1064 nm).

The aspheric input face has 43 mm radius and $r^2$ rear parameter of -0.0005. The third-stage 2D-CPC concentrator has 18 mm × 23 mm large rectangular input aperture, 8 mm × 23 mm narrow rectangular output aperture and is 10 mm in height. The 2D-CPC is used to convert the rays from 18 mm x 23 mm large-aperture emitting into a small angle, $25°$ for example, to 8 mm × 23 mm small-aperture emitting into a large angle, $70°$ for example. The V-shaped cavity is finally used to achieve an efficient multi-pass absorption of the highly concentrated pump radiation from the 8 mm × 23 mm output aperture. The inner wall of both the hollow concentrator and the V-shaped

pumping cavity were bonded with a protected silver-coated aluminum foil with 94% reflectivity. Distilled water with 6 l / min flow rate cools firstly the rod within the V-shaped cavity, then passes through 2D-CPC concentrator and exits the laser head, as illustrated by FIG. 6.2.

## 6.1.1 SOLAR LASER EXPERIMENTAL RESULTS

The optical resonator was comprised of two opposing parallel mirrors at right angles to the axis of the active medium, as shown in FIG. 6.3.
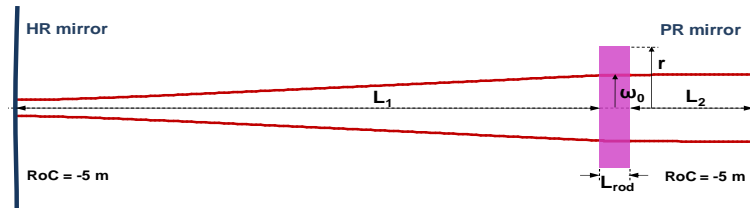


**FIG. 6.3** - Schematic diagram of theTEM$_{00}$-mode beam propagation along the asymmetric laser resonator with large RoC end mirrors, obtained through LASCAD$^©$ analysis.

One end mirror was high reflection coated (HR 1064 nm, 99.98%). The output coupler was partial reflection coated (PR1064 nm, usually 90-98%). The amount of feedback was determined by the reflectivity of the PR mirror. The output mirror is fixed at L$_2$ = 100 mm from the center point of the laser rod, while the HR rear mirror can be positioned at L$_1$ = 100 mm to 675 mm from the same central point.L$_1$/L$_2$ ratio together with HR and PR mirrors reflectivity (R) and radius of curvature (RoC) were optimized to achieve the lowest laser beam divergence and, thus, the highest fundamental mode power. The laser output powers and beam profiles for different L$_1$ (L$_1$ = 100 mm, 200 mm, 300 mm, 400 mm, 500 mm, 600 mm, 625 mm, 650 mm, 675 mm respectively) are all analyzed by LASCAD$^©$ software and confirmed by detailed measurements during the first 20 days of August, 2013, as shown in FIG. 6.4. The laser output power decreases nearly linearly, while the M$^2$ factor decreases more quickly with the increase in L$_1$. The laser beam brightness figure of merit also increases nearly linearly with the increase in L$_1$. On the one hand, 6.17 W solar laser power, M$^2$ = 4.8 are obtained for L$_1$ = 100 mm, resulting in 0.27 W brightness figure of merit; on the other hand, 2.3 W TEM$_{00}$ (M$^2 \leq$ 1.1) fundamental mode laser power is finally measured for L$_1$ = 675 mm, corresponding to the highest brightness figure of merit of 1.9 W.

The laser beam quality factor were determined by the measurement of the beam diameter at 1/e$^2$ on both a near-field position (40 mm from the output coupler) and a far-field position (6000 mm from the output coupler, nearly 9 times of L$_1$). A CINOGY UV-NIR beam profiler - CinCam CMOS was used to measure the laser beam diameters at 1/e$^2$ width. The laser beam divergence $\theta$ is found by adopting the eq. (6.1) in TABLE 6.1, where $\phi_1$and $\phi_2$ mm are the measured laser beam diameters at 1/e$^2$ width, 40 mm and 6 m away from the output mirror respectively and L is the distance between these two points. M$^2$ factor is then calculated by eq. (6.2): $\theta_0 = \lambda/\pi\omega_0$ , where is the divergence of diffraction-limited Gaussian beam for $\lambda$ =1.064 $\mu$m and $\omega_0$ = 650 $\mu$m, as calculated by LASCAD$^©$ laser beam propagation method for the 3 mm diameter, 30 mm length rod. This value can be also calibrated by measuring the laser beam diameter at 1/e$^2$ width 40 mm away from the output coupler, as indicated by FIG. 6.5.
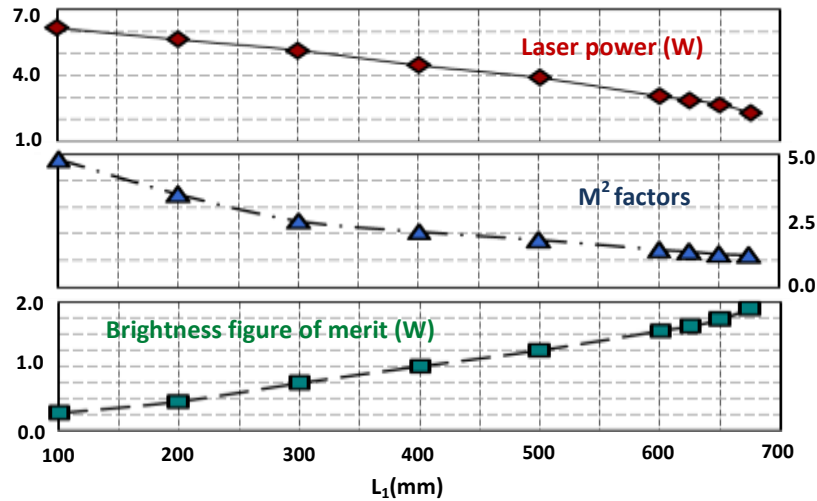
**FIG. 6.4** - Dependence of laser power, $M^2$ factor and brightness figure of merit on resonator length $L_1$ is measured.

**TABLE 6.1** - Equations for laser beam quality measurements.

| Beam divergence | $M^2$ factors | Brightness figure of merit |
|---|---|---|
| $\arctan\theta = (\phi_2 - \phi)_1/2L$ **(6.1)** | $M^2 = \theta/\theta_0$ **(6.2)** | $P_{Laser}/M_x^{\,2}M_y^{\,2}$ **(6.3)** |

Plots of the measured near-field laser beam output pattern (40 mm away from the output coupler) are shown in FIG. 6.5. A close examination of the TEM$_{00}$ mode shows that it differs slightly in laser beam diameters at $1/e^2$ along both X and Y axis. The ellipticity is caused by the slight change in absorbed pump distribution profile within the laser rod, caused by the slight misalignment between the laser head and the optimized focal position of the Fresnel lens. As indicated by FIG. 6.5, the measured average near-filed laser beam diameter is less than 1.44 mm. The measured average laser beam diameter at $1/e^2$ width in far field is 8.15 mm. Since $L = 5960$ mm, $M^2$ factor can easily be determined as 1.09 by using equations (6.1) and (6.2). Considering both the solar tracking error and the laser head misalignment error during the laser emission, $M^2 \leq 1.1$ is finally considered as the final value of our solar laser beam quality factor.
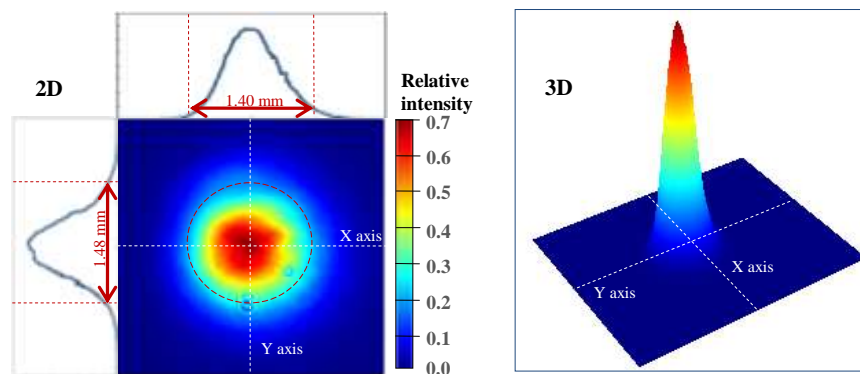


**FIG. 6.5** - Measured output laser beam profile 40 mm away from the output coupler.

A large symmetric cavity with the same total resonator length $L_T = L_1 + L_2 = 775$ mm of asymmetric resonator was also tested. In this case, no TEM$_{00}$ laser beam profile was obtained.

Higher solar laser power of 4.2 W was obtained in this case, but $M_x^2 \approx M_y^2 = 3.2$ factors were determined resulting in less laser beam brightness.

This work was reported as *Novel Lasers: Solar-Pumped Nd:YAG Lasers Getting Brighter* in Laser Focus World *(20)*.

## 6.2  4.0 W SOLAR LASER BRIGHTNESS

Through PROMES-CNRS horizontal-axis MSSF solar facility, we reported a significant advance in solar-pumped laser beam brightness by pumping the 3 mm diameter Nd:YAG single-crystal rod *(37)*.

### 6.2.1  SIDE-PUMPING SCHEME WITH SINGLE LIGHT GUIDE

The solar laser head was composed of the rectangular fused silica light guide, the 2D-CPC secondary concentrator and the V-shaped pump cavity, as indicated in FIG. 6.6.
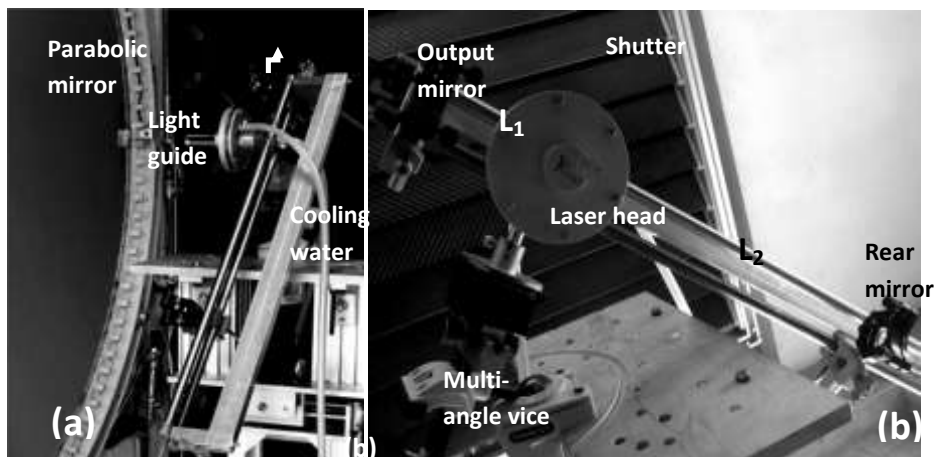


**FIG. 6.6** - Solar-pumped TEM$_{00}$ mode Nd:YAG laser by the PROMES-CNRS heliostat-parabolic mirror system.**(b)** Front-view of the asymmetric laser resonant cavity.

The concentrated solar radiation at the focus of the parabolic mirror is firstly collected by the light guide with 10 mm × 15 mm input end and guided to its 12 mm × 18 mm output end. To manufacture the light guide, a fused silica rod of 99.999% optical purity, with 12 mm × 18 mm rectangular cross section and 100 mm length, is ground and polished to its final dimension. The slightly inclined side faces of the guide (FIG. 6.7) ensure an easy mechanical fixing of the guide to the laser head. The measured transmission efficiency of the light guide is 82 %.

Heliostat orientation errors usually move the center of the absorption distribution within the laser rod, resulting in both less laser output power and a non-uniform beam profile. The light guide with rectangular cross-section is essential to overcoming this problem, serving as a beam homogenizer by transforming the near-Gaussian profile of the concentrated light spot at its input end into a uniform pump light distribution at its output end *(110)*. Uniform absorbed pump distribution along the laser rod is hence achieved. Despite the slight shift of the focal spot at the input face, caused by the orientation error of the heliostat, a uniform reduction in pump flux is

observed at the output end. The absorbed pump profile within the rod, and hence the laser power, is not significantly affected.

The 2D-CPC concentrator has 14 mm × 20 mm rectangular large-input-aperture, 8 mm × 20 mm small-output-aperture and is 10 mm in height. The 60 degree V-shaped cavity is finally used to achieve an efficient absorption of the highly concentrated pump radiation from the 8 mm × 20 mm small-output-aperture. The inner walls of both the 2D-CPC hollow concentrator and the V-shaped pumping cavity were bonded with a protected silver-coated aluminum foil with 94 % reflectivity. Distilled water with 6 Liter / min flow rate cools firstly the rod within the V-shaped cavity, then passes through the hollow 2D-CPC concentrator and exits the laser head from the space between the light guide and the large-input-aperture of the 2D-CPC concentrator. Cooling water also ensures an efficient light coupling from the guide to the rod.
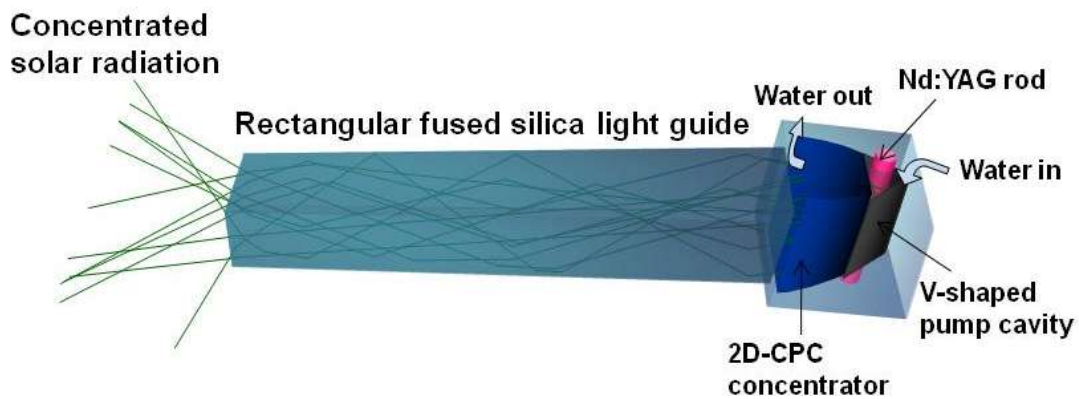


**FIG. 6.7** - 3D view of the solar laser head with the rectangular light guide, the 2D-CPC concentrator and the V-shaped cavity within which the Nd:YAG rod is efficiently pumped.

## 6.2.2 SOLAR LASER EXPERIMENTAL RESULTS

For 2.3 $m^2$ effective collection area and 915W/$m^2$ solar irradiance, the heliostat parabolic mirror system collected 1240W solar power to its focal zone. The output mirror was fixed at $L_1 = 100$ mm from the rod center, while the HR rear mirror could be positioned at $L_2 = 100$ mm to 600 mm from the rod center. A - 5 m RoC output mirror with 94 % reflectivity at $L_1 = 100$ mm and a - 5 m RoC rear mirror at $L_2 = 530$ mm offered the maximum TEM$_{00}$ laser output power of 4.4 W, when pumped by the maximum solar input power of 1115 W. The threshold solar power of 570 W was measured in the focal zone. 0.81 % laser slope and 1.9 W/$m^2$ collection efficiencies were finally calculated. The laser beam quality factors were determined by measuring the beam diameter at $1/e^2$ at both a near-field position (40 mm from the output coupler) and a far-field position near the laboratory ceiling (6.0 m away from the output coupler). Plots of measured near-field laser beam pattern (40 mm from the output coupler) are shown in FIG. 6.8.

$M^2$ factor can be determined as 1.04 (eqs. (6.1) e (6.2)). Considering the heliostat orientation error during laser emission, $M_x^2 \approx M_y^2 \leq 1.05$ are considered as adequate values for describing the laser beam quality. For 4.4 W laser power, 4.0 W beam brightness figure of merit is finally calculated (eq. (6.3)), which is more than the double of the previous record with Fresnel lens **(42)**, discussed in the SUBCHAPTER 6.1, and 13.8 times higher than the previous record with the same solar facility **(36)**.
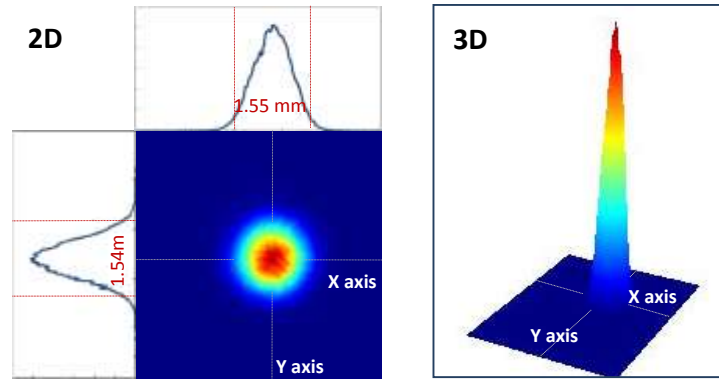
FIG. 6.8 - Measured output laser beam profile 40 mm away from the output coupler, by CINOGY UV-NIR beam profiler - CinCam CMOS .

The TEM$_{00}$ mode laser power collection efficiency of 1.91 W/m$^2$ is still lower than the record value of 2.93 W/m$^2$ by the Fresnel lens **(42)**. Nevertheless, considering the large absorption loss of 41 % from both the heliostat and the parabolic mirror, the results can be considered as an excellent value to promote further researches on TEM$_{00}$mode solar lasers pumped by stationary parabolic mirrors.

## 6.3  5.5 W CW TEM$_{00}$-MODE SOLAR LASER POWER

A double-stage light-guide / 2V-shaped pump cavity is used to efficiently couple and redistribute the concentrated pump light to a 4-mm-diameter, 30-mm-length, 1.1 at.% Nd:YAG single-crystal rod *(38)*.

### 6.3.1  SIDE-PUMPING SCHEME WITH LARGE SINGLE LIGHT GUIDE

The concentrated solar radiation is firstly collected by the rectangular fused silica light guide with 14 mm × 22 mm input end. It is then transmitted along 70 mm length, through total internal reflection, to its 2D-trapezoidal output section with 9 mm × 22 mm output end and 8 mm length, as shown in FIG. 6.10.
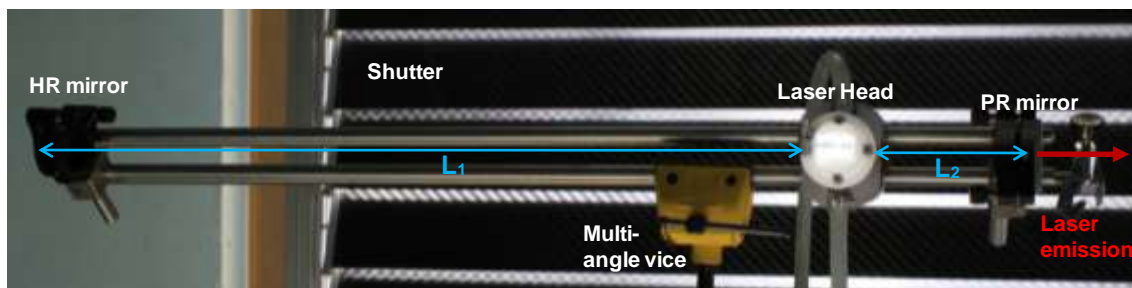


FIG. 6.9 - Front-view of the asymmetric laser resonant cavity for extraction of TEM$_{00}$-mode laser. L$_1$ and L$_2$ represent the separation length of the high reflection (HR) and partial reflection (PR) mirrors to their nearest end face of the laser rod.

To manufacture the light guide, a fused silica rod of 99.999% optical purity (supplied by Beijing Aomolin Ltd.), with 22 mm diameter and 80 mm length, was ground and polished to its final

dimensions. By using a light-guide with large rectangular cross-section, one can attain higher transfer efficiency and smaller tracking error dependent losses compared to that with smaller cross-section, but the efficient light coupling to the laser crystal can be affected by the large output end. It is therefore straightforward to use a closed cavity pumping arrangement, formed by the narrower output section of the light guide and the water-flooded 2V pump cavity, as illustrated in Fig. 6.10. The rod diameter is also a key parameter for achieving high transfer efficiency and reducing the tracking error dependent losses.
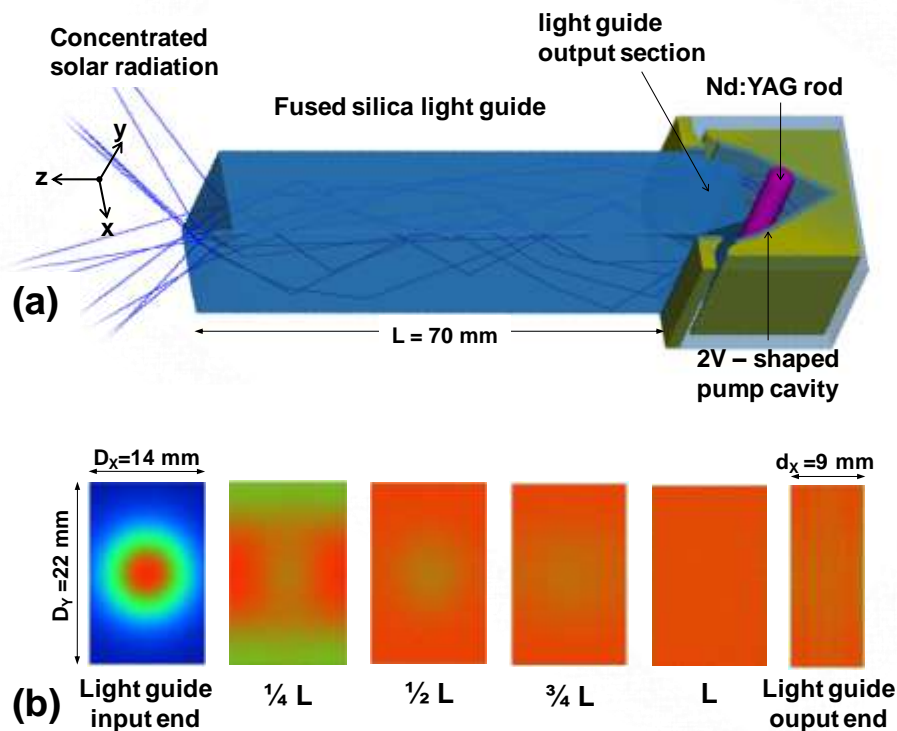


**FIG. 6.10** - **(a)** 3D design of the solar laser head, composed of the rectangular light guide, the 2V-shaped pump cavity and the 4 mm diameter, 30 mm length 1.1 at.% Nd:YAG rod. **(b)** Pump light distribution at different sections along the light guide. Uniform pump light distribution is achieved at L = 70 mm.

For the focal distance of 850 mm, a typical 0.1° tracking error corresponds to approximately 1.5 mm displacement in both X and Y axes. FIG. 6.11 and FIG. 6.12 compares the influence of the combined tracking error displacement on the absorbed pump flux distributions of the Nd:YAG single-crystal rods pumped through the present pumping scheme *(38)* and the previous solar laser side-pumping approach *(37)*, respectively.

The focal spot shift along Y axis results only in a uniform reduction in the pump flux along both rod axes. The focal spot shift along X axis, however, moves the center of the absorbed pump profile along the central cross section of the rod. This displacement is more pronounced in the 3 mm diameter Nd:YAG rod, pumped through the previous scheme, resulting in increased loss of absorbed pump power compared to the 4 mm diameter Nd:YAG rod pumped through the present pumping scheme.
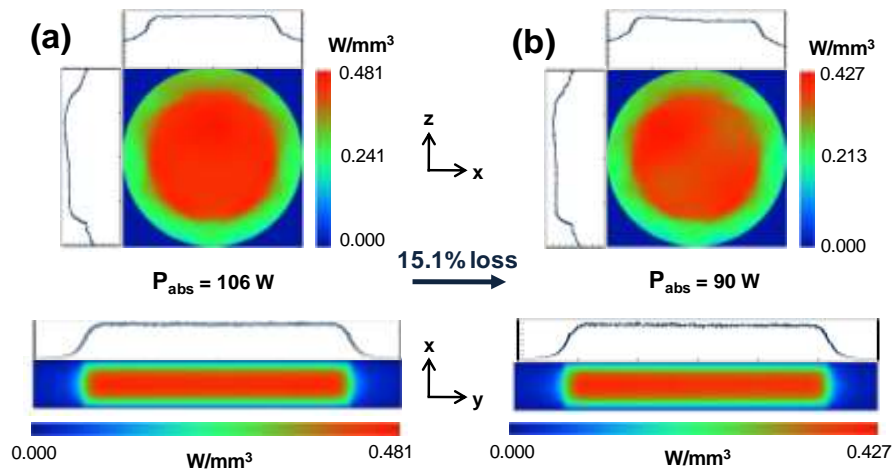
**FIG. 6.11** - Numerical absorbed pump flux distributions along the central and longitudinal cross-sections of the 4 mm diameter, 30 mm length, 1.1 at.% Nd:YAG rod pumped through the present scheme **(a)** with no tracking error and **(b)** considering 0.1° combined tracking error in X,Y axes.
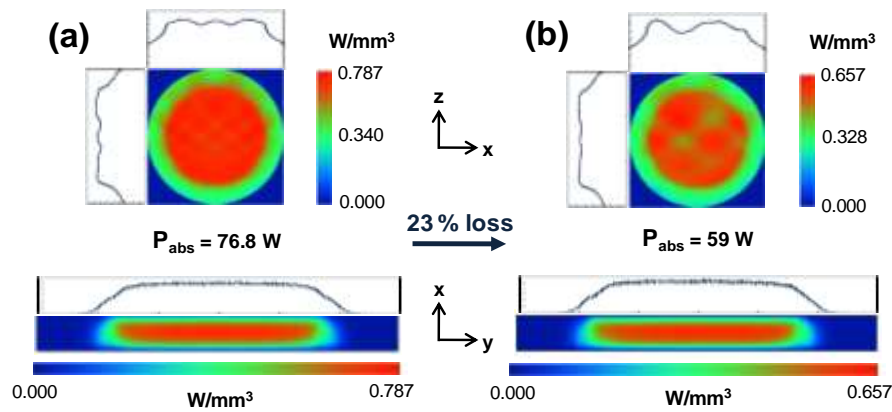


**FIG. 6.12** - Numerical absorbed pump flux distributions along the central and longitudinal cross-sections of the 3 mm diameter, 30 mm length, 1.1 at.% Nd:YAG rod pumped through the previous scheme *(37)* **(a)** with no tracking error and **(b)** considering 0.1° combined tracking error in X,Y axes.

The two-dimensional 2V-shaped cavity, in FIG. 6.13, has an entrance aperture of 16 mm × 22 mm and 15.3 mm depth. It is composed of a V-shaped reflector $V_1$, with $\alpha_1 = 60°$ opening angle, and two upper planar reflectors $V_2$, making an inclination of $\alpha_2 = 17.5°$ in relation to $V_1$. This 2V combination is much more efficient in coupling the pump rays, with different incidence angles from the light guide to the laser rod, as compared to a single V-shaped reflector. As shown in FIG. 6.12 (b), ray A passes through the rod once and is bounced back by $V_1$, so that double-pass absorption is accomplished. The rays that don´t hit directly the laser rod can be redirected by either $V_1$, making one passage (ray B) or two passages (ray C) through the laser rod, or by $V_2$ (ray D). The upper reflectors play also an important role in redirecting the rays (ray E) that exit the inclined faces of the water-flooded light guide output section towards the 2V cavity, so that at least one passage through the laser rod is accomplished. The inner walls of both $V_1$, $V_2$ and upper reflectors were bonded with a protected silver-coated aluminum foil with 94% reflectivity.

By combining the pumping features of the 2V-shaped pump cavity with the homogenization capacity of the rectangular light guide, uniform pump power deposition within the laser rod is achieved. For low-average-power operation, in which thermal lensing is moderate, the overlap of the laser mode with an excitation peaked at the center of the rod can be advantageous. However, at

high average output power, when the absorption profile is centrally peaked, the temperature on the axis increases further, resulting in stronger thermal lensing at the center, higher-order aberrations at the periphery, and larger stress in the laser rod compared with those of uniform excitation *(111)*. Consequently, to scale our solar-pumped rod laser to high TEM$_{00}$-mode average power, it is of utmost importance for us to start with a uniform pump power deposition within the laser rod.



**(a)**                                                                 **(b)**
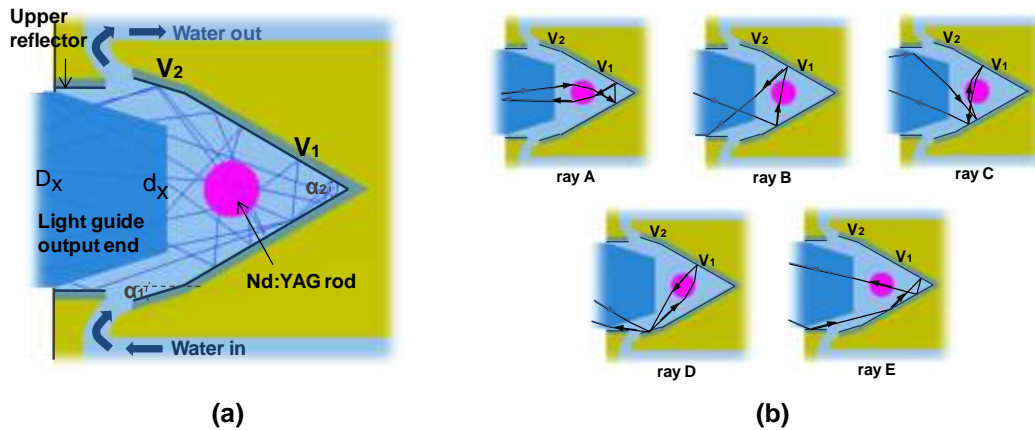
**FIG. 6.13** - **(a)** The 2V-shaped pump cavity, within which the 4 mm diameter Nd:YAG rod is efficiently pumped due to multi-pass absorption of pump radiation. **(b)** Examples of the passage of the pump rays with different incidence angles within the 2V-cavity.

## 6.3.2 NUMERICAL OPTIMIZATION OF THE SOLAR LASER PERFORMANCE

FIG. 6.14 shows the influence of the light guide width ($D_X$) on the absorbed pump power in the rod. Maximum absorbed pump power of 106 W is numerically achieved with $D_X = 14$ mm light guide. Optimized output aperture $d_X = 9$ mm is found in this case.
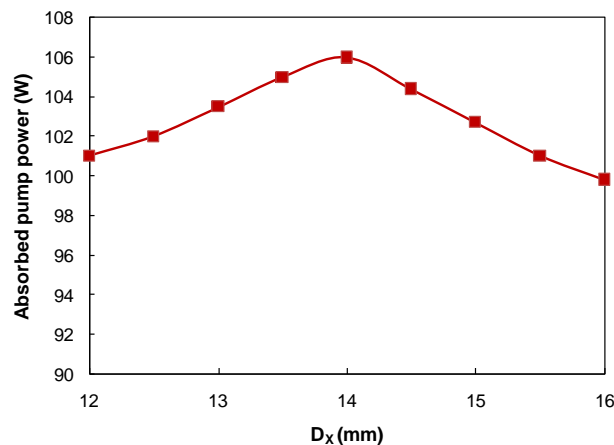


**FIG. 6.14** - Numerically obtained absorbed pump power as function of the light-guide width $D_X$.

Analogously to the previous TEM$_{00}$-mode schemes, the optical resonator is comprised of two opposing parallel mirrors, HR mirror and PR mirror, at right angles to the axis of the active medium. In LASCAD$^{©}$ program, the focal length of the rod lens can be determined through the stability limits of a flat-flat resonator. Analogously to the resonator design in FIG. 6.3, one end mirror is fixed at a close distance to the rod lens, L$_2$. For a fixed pump power, the focal length of the rod lens is hence given by L$_1$ at the point in which the resonator becomes unstable. FIG. 6.15(a)

shows the numerically calculated rod focal length as function of the pump power at the focus. The focal length decreases as pump power increases. The numerically calculated values of temperature and heat load in the rod, for the different input powers, are also given in FIG. 6.15(b) and FIG. 6.15(c), respectively.
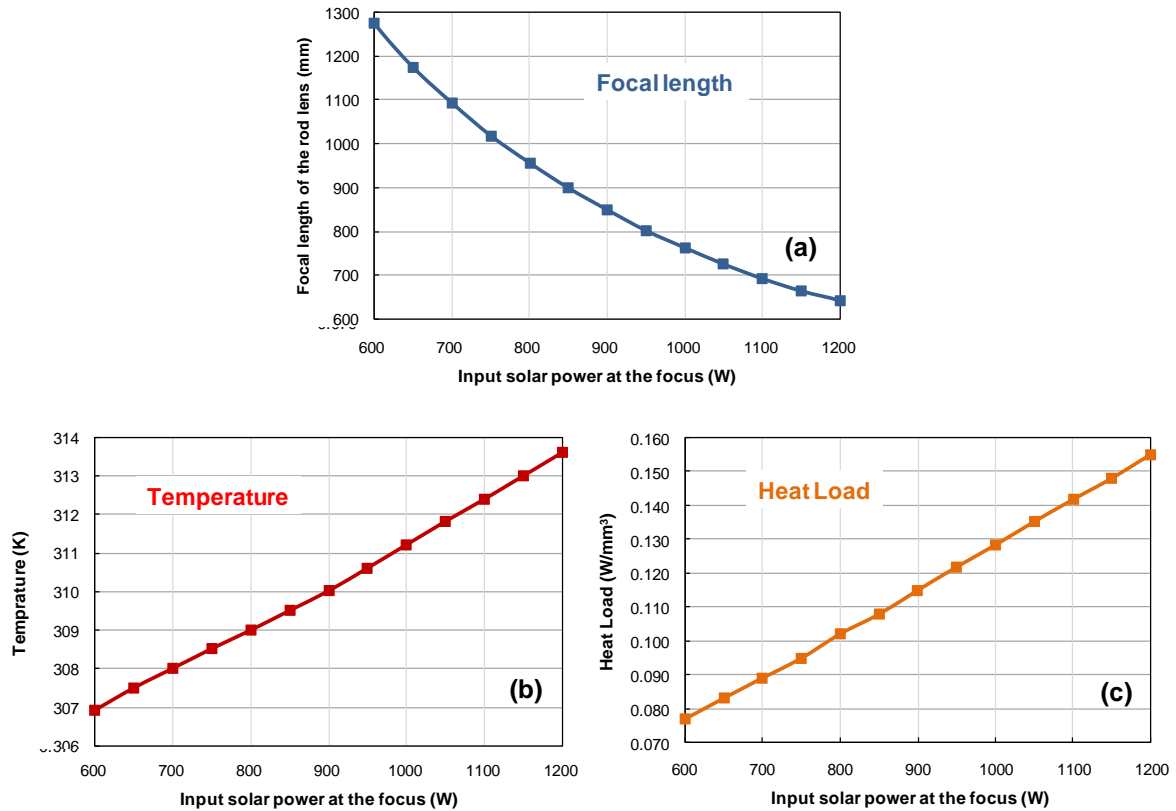


FIG. 6.15 - Numerically calculated (a) rod focal length, (b) temperature and (c) heat load in the rod, for different input solar powers, assuming T = 300 K water cooling.

### 6.3.3  SOLAR LASER EXPERIMENTAL RESULTS

Based on ZEMAX$^©$ and LASCAD$^©$ numerically optimized design parameters of the solar laser system, a prototype was built in Lisbon and tested in PROMES – CNRS. The 4 mm diameter, 30 mm length Nd:YAG is supplied by Altechna Co., Ltd. It has 1.1 % Nd$^{3+}$ concentration. Both ends of the rod are anti-reflection (AR) coated (R < 0.2% @ 1064 nm). The resonator mechanics was designed to allow the displacement of the HR mirror (from $L_1$= 120 mm to $L_1$=580 mm), while maintaining the PR mirror at a fixed $L_2$ = 120 mm position. Direct solar irradiance varied between 810 and 995 W/m$^2$during the experiments.

For TEM$_{00}$-mode operation, the HR mirror is shifted to $L_1$ = 580 mm. A 94% reflectivity output coupler with large RoC = -5 m was used in this case. FIG. 6.16 shows the laser output power as function of the input solar power at the focus. Laser starts to oscillate at an input power of 570 W approximately and grows almost linearly until the pump power reaches about 1000 W. With further increase of pump power, laser output power approaches to a peak value and then drops abruptly, meaning that the resonator has moved out of stability zone. Compared with the increment of rod gain, which is proportional to the pump power, the diffraction loss, that is caused by thermally induced aberration, increases more rapidly as the pump power increases, and consequently the laser

output power is limited. The small concave curve at higher input powers possibly results from birefringence *(51)*. 1.27% slope efficiency is experimentally measured, representing an 1.6 times improvement over that of the previous $TEM_{00}$-mode solar laser within the same solar facilty *(37)*.
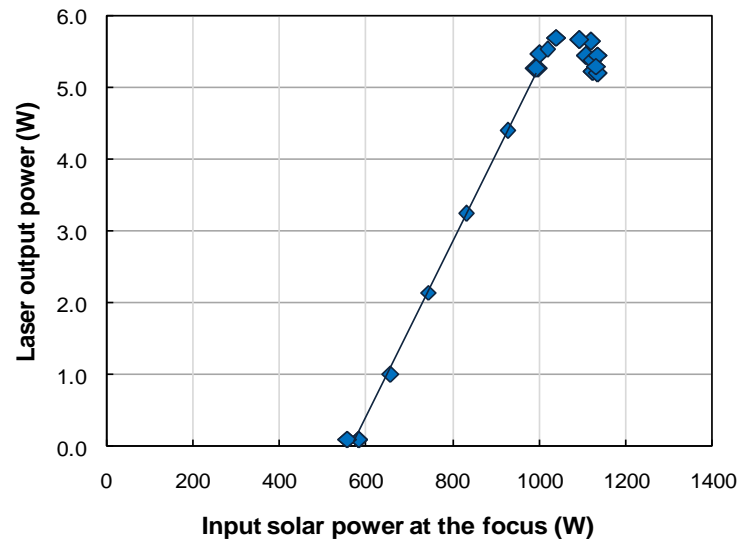


**FIG. 6.16** - Laser output power (at $L_1$ = 580 mm) as function of the solar input power at the focus.

The CINOGY UV-NIR beam profiler - CinCam CMOS was used for monitoring the laser beam profile during the experiments. FIG. 6.17 (a)-(d) shows the evolution of the laser beam profile with pump powers higher than 1000 W.
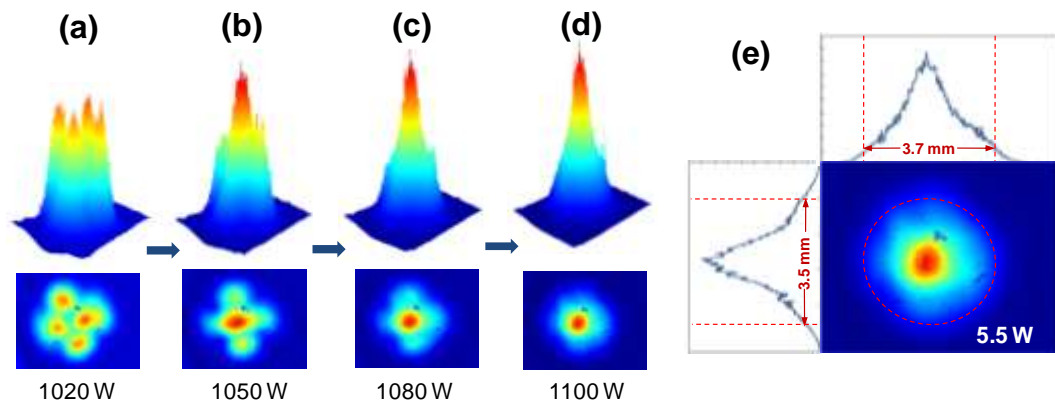


**FIG. 6.17** - **(a)-(d)** Evolution of output laser beam profile (taken 1.7 m away from the output coupler) with pump power as it approaches the resonator stability limit. **(e)** 2D analysis of the measured $TEM_{00}$-mode profile.

Since no aperture is used in the laser resonator besides the rod itself, oscillation of higher-order modes occurs at low output powers due to the relatively small overlap between the fundamental mode volume and the pumped region. With the increase of pump power, and thus diffraction loss, only few modes become possible to oscillate, as shown in FIG. 6.17 (a). While pump power is going near thermal stability limit, the resonator modes give rise to only one mode of higher intensity, in FIG. 6.17 (d). 5.5 W $TEM_{00}$-mode laser power was registered in this case, for an effective collection area of 1.92 $m^2$ (with the shutter opened at 80%), corresponding to 2.84 $W/m^2$ $TEM_{00}$-mode solar laser collection efficiency. This value is 1.5 times higher than the previous result *(37)*. The slight discrepancy in laser beam diameters at $1/e^2$ along X and Y axis (FIG. 6.17(e)) can be justified by the slight pump profile misalignment due to heliostat orientation error.

Laser beam quality factors were determined by measuring the beam diameter at $1/e^2$ in a near-field position (40 mm from the output coupler) and a far-field position (3 m away from the output coupler). $M_x^2 \approx 1.25$, $M_y^2 \approx 1.14$ factors were determined. Considering the heliostat orientation error during laser emission, $M_x^2 \approx M_y^2 \leq 1.25$ are considered as adequate values for describing the laser beam quality.

## 6.4   4.0 W/M$^2$ TEM$_{00}$-MODE SOLAR LASER COLLECTION EFFICIENCY

To improve the previous TEM$_{00}$-mode solar laser efficiency we used a solar laser head composed of the ellipsoid-shaped fused silica concentrator, the 2V-shaped pump cavity, a 1.0 at% grooved Nd:YAG rod (with 4 mm diameter, 34 mm length, grooved pitch of 0.6 mm and grooved depth of 0.1 mm) *(41)*. The grooved surface offers a larger interface with cooling liquid, compare to common rods, and hence better heat dissipation, reducing the thermal lensing effect, which in turn can improve the laser beam quality of a solar laser *(80)*.

### 6.4.1   SIDE-PUMPING SCHEME WITH TRUNCATED ELLIPSOID-SHAPED CONCENTRATOR

The solar laser head is composed of the truncated ellipsoid-shaped fused silica concentrator and the 2V-shaped pump cavity, and most importantly, the grooved Nd:YAG laser rod, as indicated in FIG. 6.18 (a), was fixed on the automatic X-Y-Z axis mechanical support by the multi-angle vice.
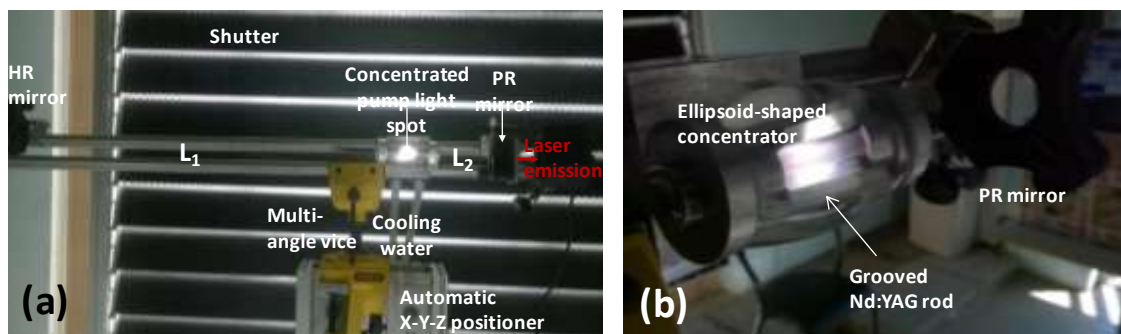


**FIG. 6.18 -** The solar laser head, composed of the truncated ellipsoid-shaped fused silica concentrator and a 2V-shaped pumping cavity within which the grooved Nd:YAG rod is efficiently pumped.

The truncated ellipsoid-shaped concentrator is mathematically defined by a = b = 17.5 mm, c = 50 mm and is truncated from two sides to L = 60 mm length. The two-dimensional 2V-shaped cavity has an entrance aperture of 10 mm × 22 mm and 8 mm depth. As shown in FIG. 6.19 (b), it is composed of a V-shaped reflector V$_1$, with 43º half-angle, and two upper planar reflectors V$_2$, with 20º half-angle relative to V$_1$. The 2V combination is more efficient in coupling highly concentrated light rays with different incidence angles, ranging from 0º to 60º, into the laser rod, as compared to a single V-shaped reflector. The 2V-shaped cavity ensures an efficient pumping to the laser rod by redirecting unabsorbed pump radiation back to the rod again. A significant part of pump radiation can be more efficiently absorbed by double-pass pumping approach.
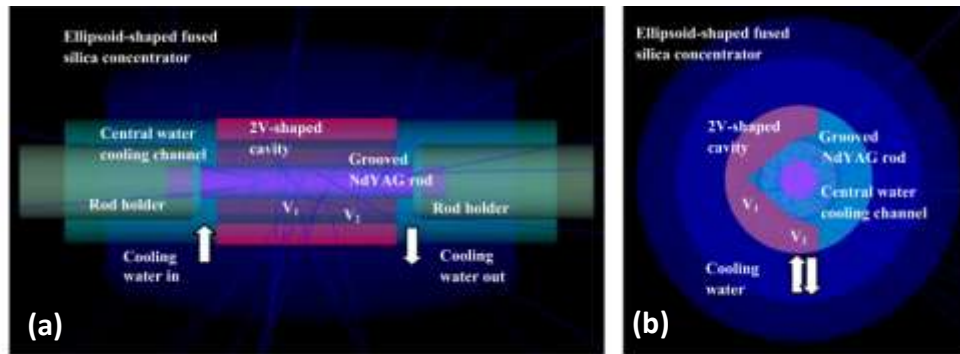
FIG. 6.19 - (a) Front-view and (b) side-view of the simple solar laser pumping approach are illustrated by ZEMAX$^©$ shaded models.

To manufacture the ellipsoid-shaped secondary concentrator, a fused silica rod with 37 mm diameter, 60 mm length, 99.999% optical purity, was used as starting material. A 16 mm diameter central water cooling channel was firstly drilled and polished along the central axial of the 37 mm diameter, 60 mm length fused silica rod. The external faces of this rod were then machined and polished to the form the final truncated ellipsoidal dimensions defined by a = b = 17.5 mm, c = 50 mm and L = 60 mm. The 2V-shaped pumping cavity was then installed within the cooling channel. The 1.0 at.% grooved Nd:YAG rod, with 4 mm diameter, 34 mm length, grooved pitch of 0.6 mm and grooved depth of 0.1 mm, was supplied by Chengdu Dongjun Laser Co., Ltd. Both end faces of the rod are anti-reflection (AR) coated for the laser emission wavelength (R < 0.2% @ 1064 nm). The grooved rod was mechanically fixed by the two holders within the channel, where it was cooled by distilled water at 6 Liter/min flow rate.

## 6.4.2  NUMERICAL OPTIMIZATION OF THE SOLAR LASER PERFORMANCE

To weaken the thermal problems of our solar laser setup, it is very important for us to achieve a circularly symmetric absorbed pump flux distribution in the laser rod, as shown in FIG. 6.20(a), by optimizing carefully both the truncated ellipsoidal and the 2V–shaped cavity dimensions.
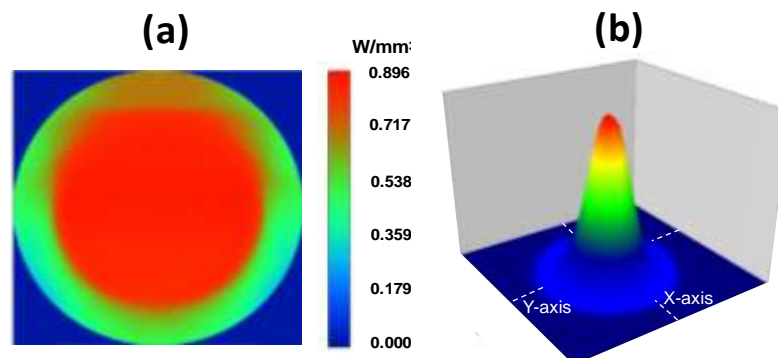


FIG. 6.20 - (a) A circularly symmetric uniform absorbed pump flux distribution of the 4.0 mm diameter grooved rod by ZEMAX$^©$ numerical simulation. (b) Numerically simulated TEM$_{00}$-mode laser beam pattern on the output mirror of the asymmetric laser resonator with RoC = –5 m for the 3.5 mm diameter grooved rod in LASCAD$^©$ BPM propagation.

For the 4.0 mm diameter Nd:YAG grooved rod, the LASCAD$^©$ beam propagation method (BPM) gives 3.74 % diffraction loss, resulting in a total round-trip loss of  6.18 % for calculating the fundamental mode solar laser power. 4.6W TEM$_{00}$ laser power is numerically calculated with

the following optimized cavity parameters of $L_1$ = 100 mm, $L_2$ = 545 mm, R = 94 % and RoC = -5 m for the PR mirror, R = 99.8 % and RoC = -5 m for the HR mirror. It was also worth noting that only excellent absorbed beam profile along the rod from ZEMAX©, in Fig. 6.20(a), could ensure a satisfactory Gaussian shape laser beam distribution in LASCAD©, in Fig. 6.20 (b).

### 6.4.3 Solar laser experimental results

For 1.13 m² effective collection area and 900W/m² solar irradiance, the heliostat parabolic mirror system collected 630W solar powers to its focal zone. The output mirror was fixed at $L_1$ = 100 mm, while the HR rear mirror was positioned at $L_2$ = 545 mm from the rod center. Maximum TEM$_{00}$ laser output power of 4.5 W was measured for - 5 m RoC PR mirror with 94 % reflectivity at $L_1$ = 100 mm and - 5 m RoC HR mirror at $L_2$ = 545 mm, when pumped by the maximum solar input power of 615 W, which matched well with the LASCAD© numerical simulation result of 4.6 W. The threshold solar power of 380W was measured in the focal zone. 2.36 % laser slope was determined, which is 1.9 times higher than the previous by the parabolic mirror *(38)*. 4.0 W/m² collection efficiency was also calculated with the experimental values in Fig. 6.21, constituting a new record for high brigtness solar laser emission, which can be considered as a stimulating value for many interesting applications with fundamental mode solar-powered lasers.
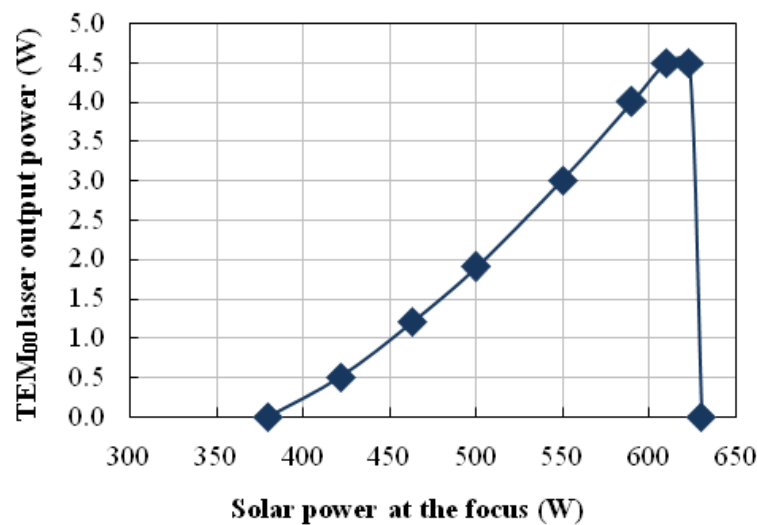


**Fig. 6.21** - TEM$_{00}$ mode laser output power versus concentrated solar input power at the focus of the parabolic mirror.

As shown in Fig. 6.21, there is a slight nonlinearity in the output power for TEM$_{00}$ operation. This can be explained by considering the change in the eigenmode radius of the cavity at the 1064 nm HR mirror and at the laser rod, which is caused by the thermal lensing effect. Both mode overlap and diffraction loss at the HR mirror depend on the thermal lensing effect and consequently on the pump intensity; hence the nonlinearity in the output power *(112)*. When there is a larger diffraction loss, the extracted power from the laser rod decreases, so that the thermal lensing effect gets stronger until finally the laser resonator becomes unstable and the laser stops oscillating, as indicated in Fig. 6.21.

The laser beam quality factors are determined by measuring the beam diameter at $1/e^2$ at both a near-field position (40 mm from the output coupler) and a far-field position near the laboratory

ceiling (2.5 m away from the output coupler). The CINOGY UV-NIR beam profiler - CinCam CMOS was used for monitoring the laser beam profile during the experiments.
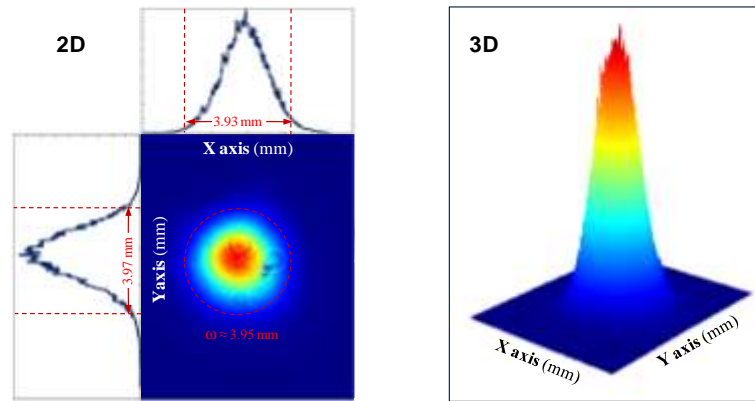


**FIG. 6.22** - Measured $TEM_{00}$ mode output laser beam 2D and 3D profiles 2.5 m away from the output coupler.

The measured average near-field laser beam diameter is $\phi_1$ = 2.4 mm. The measured average beam diameter at $1/e^2$ width at the far-field is $\phi_2$ = 3.95 mm. $\omega_0$ = 1170 µm, as calculated by LASCAD$^\copyright$ laser beam propagation method for the 4 mm diameter, 34 mm length rod. Since L = 2.46 m, $M^2$ factor can be determined as 1.087 by using eq. (6.1) and (6.2) in TABLE 6.1. Considering the heliostat orientation error during laser emission, $M_x^2 \approx M_y^2 \leq 1.1$ are considered as adequate values for describing the laser beam quality.

## 6.5  7.9 W/M$^2$ TEM$_{00}$-MODE SOLAR LASER COLLECTION EFFICIENCY

With the same solar laser prototype with end-pumping configuration described in SUBCHAPTER 5.4, it was possible to achieve a record $TEM_{00}$-mode solar laser collection efficiency of 7.9 W/m$^2$ *(31)*. The laser resonant cavity length $L_1$ was the key parameter for achieving the highest fundamental mode power.

### 6.5.1 NUMERICAL OPTIMIZATION OF THE SOLAR LASER PERFORMANCE

The pump-flux distributions along both one longitudinal central cross-section and five transversal cross-sections in end-side-pumping configuration are given in FIG. 6.23. Absorbed pump light distributions presented a strong non-uniform distribution along the laser rod, as shown by the central longitudinal absorbed pump flux distribution along the laser rod. Yet, this was the distribution that ensured the maximum absorbed pump power by the rod. Moreover, this peak flux is only half of that of end-side pumping scheme with larger rod, addressed in SUBCHAPTER 5.2 *(34)*, reducing significantly the thermal problems of solar lasers setups with end-side pumping configuration.
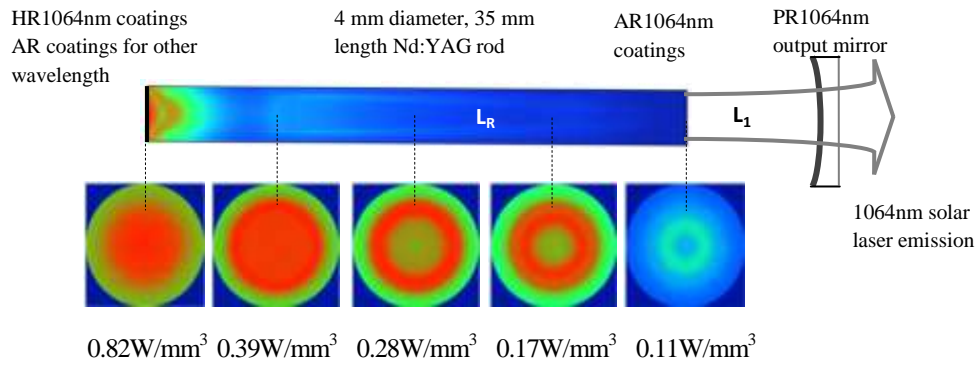
**FIG. 6.23** - Absorbed pump-flux distributions along both one longitudinal central cross-section and five transversal cross-sections of the 4 mm diameter, 35 mm length Nd:YAG rod, obtained by ZEMAX© analysis.

In LASCAD© analysis, PR mirrors of different reflectivity and radius of curvature were tested individually to optimize both multimode and TEM$_{00}$-mode laser power. For the 4 mm diameter, 1.0 at % Nd:YAG rod with $L_R$ = 35 mm, the amount of absorption and scattering losses was $2\alpha L_R$ = 2.1%. Assuming 0.4% of imperfect HR and AR coating loss, the round-trip losses were increased to 2.5%. LASCAD© beam propagation method (BPM) gave 0.2% diffraction loss, resulting in a total round-trip loss of 2.7% for calculating the fundamental mode solar laser oscillation. 9.6 W maximum TEM$_{00}$–mode laser power was numerically calculated with optimized cavity parameters of $L_1$ = 430 mm, R = 94% and RoC = -5 m for the PR mirror, as shown in FIG. 6.24.
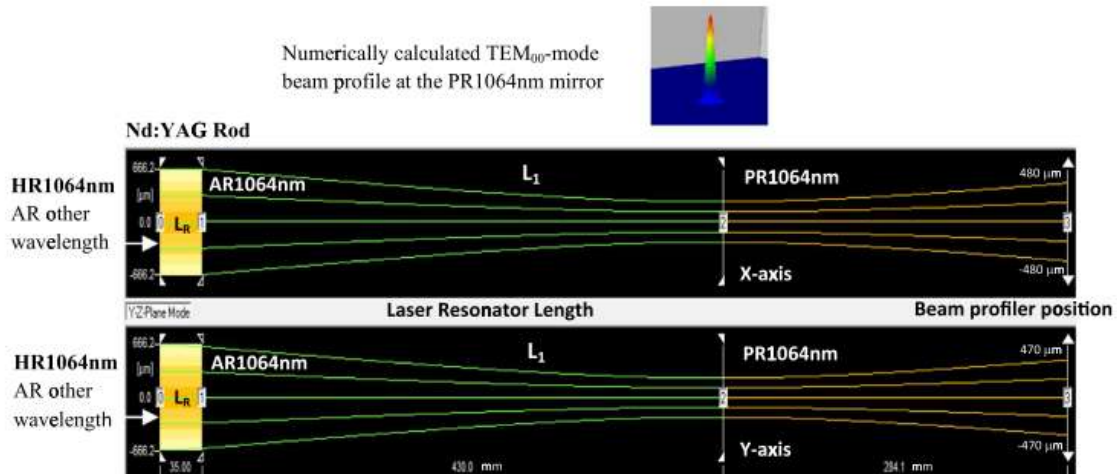


**FIG. 6.24** - Laser resonator configuration for the efficient extraction of fundamental mode solar laser power. Numerically calculated TEM$_{00}$-mode BPM beam profile at the PR1064 nm mirror is given in the inset image.

## 6.5.2 SOLAR LASER EXPERIMENTAL RESULTS

In TEM$_{00}$ mode solar laser oscillation experiments, - 5 m RoC output mirror with 94% reflectivity at $L_1$ = 430 mm offered the maximum TEM$_{00}$-mode laser output power of 9.3 W, as when pumped by the maximum solar input power of 700 W, which matched well with the LASCAD© numerical simulation result of 9.6 W. 7.9 W/m$^2$ collection efficiencies were therefore calculated, which is nearly the double of the previous record by the parabolic mirror *(41)*.

Since fundamental mode laser beam was at its highest flux level right at the PR output mirror, as shown in FIG. 6.25, the CINOGY UV-NIR beam profiler - CinCam CMOS was placed 284mm away from the mirror in order to avoid damaging of the CMOS detector. To measure the beam

diameters at $1/e^2$ width under extremely high 1064 nm laser radiation, another 95% 1064 nm RoC = ∞ output mirror was added before the CMOS detector, acting as an extra laser beam attenuator and reducing the 1064 nm laser power level to only mW level for the detector. Considering the heliostat orientation error during laser emission, $M_x^2 \approx M_y^2 \leq 1.2$ were considered as adequate values for describing the laser beam quality in FIG. 6.25. Solar laser beam figure of merit was therefore calculated as 6.46 W, 1.6 times more than the previous record *(37)*. There were good agreement between the measured beam widths (0.94 mm) in FIG. 6.26 and the numerically analyzed ones (± 470-480 μm) at beam profiler position in FIG. 6.25.
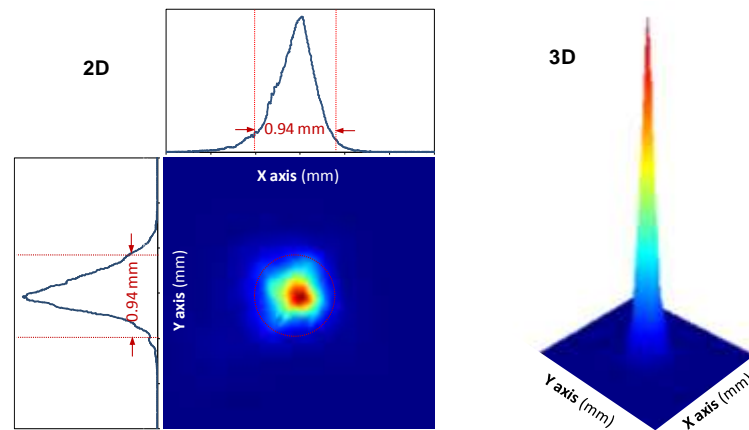


**FIG. 6.25** - Measured TEM$_{00}$-mode output laser beam 2D and 3D profiles 284 mm away from the PR 1064 nm mirror.

Stable emission of the most efficient solar laser power in fundamental mode regime, could constitute one step further for many interesting applications for solar-powered lasers.

The advances in solar laser beam brightness within the framework of this PhD project are summarized below in FIG. 6.26 and compared to that of the previous records. Substantial improvement in solar laser beam brightness was only obtained by the production of TEM$_{00}$ mode solar laser operation through a large-mode volume resonator configuration, reported for the first time in 2013 *(42)* under this PhD project. A two-fold increase was later achieved in 2015 with heliostat-parabolic mirror system, demonstrating the advantages of heliostat-parabolic-mirror system for pumping small diameter rods. Indeed, in 2016 the TEM$_{00}$ mode solar laser collection efficiency was improved by 1.4 times compared to that with Fresnel lens. Most recently, in 2017, 7.9 W TEM$_{00}$ mode power per unit area was reported *(31)*, representing a two-fold increase in collection efficiency. 6.5 W record solar laser beam brightness was also obtained, being 3.4 times more than the record value with Fresnel lens.

Although the latest advances in both solar laser efficiency and beam brightness were achieved by end-side-pumping configurations, it is also very important to take into consideration the solar laser beam stability. This parameter was, however, more favored by the solar prototypes with side-pumping configuration, particularly with light guides. The most recent advances in solar laser beam stability with the first production of a solar pumping scheme with twisted light guides is described in Chapter 7.

## 6.6 SUMMARY OF THE ADVANCES IN SOLAR LASER BRIGHTNESS
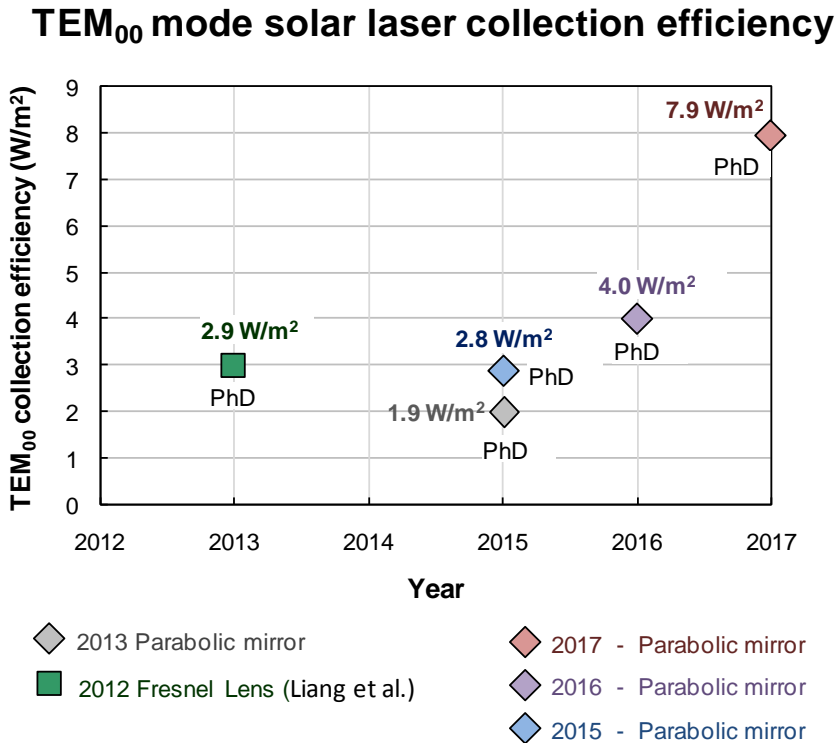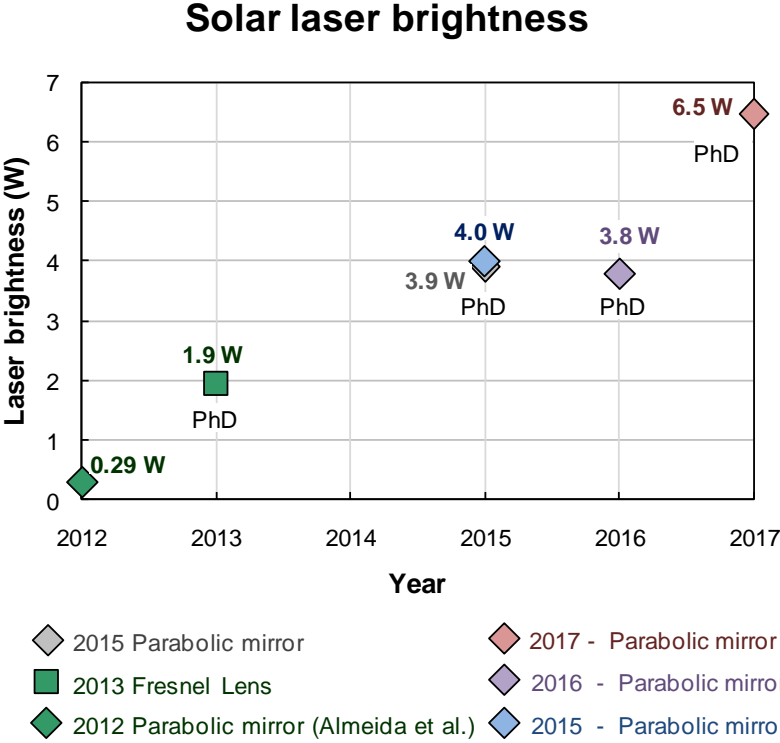


**FIG. 6.26** - Summary of the brightness and $TEM_{00}$-mode collection efficiency advances during the PhD project and comparison with the previous record.
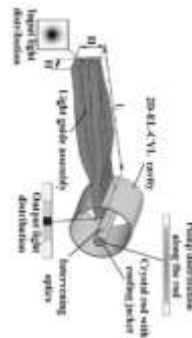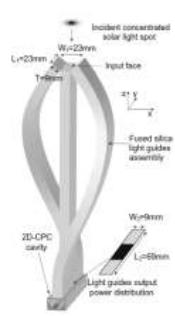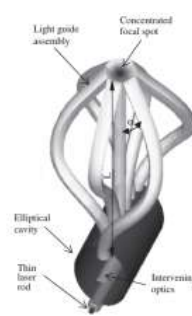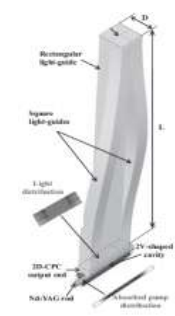
# 7 ADVANCES IN SOLAR LASER STABILITY

Heliostat orientation error is a critical factor influencing the resonator stability of a solar laser. It moves the center of the absorption distribution inside the crystal, resulting in both less output power and a non-uniform beam profile. To improve the solar laser beam brightness, direct solar laser pumping configurations have been tested, where the concentrated solar radiation at the focus was efficiently coupled within the laser rod, through either a fused silica aspheric lens *(31,42)*, or a semi-cylindrical lens *(40)* or an ellipsoidal-shaped lens *(41)*, allowing the efficient generation of $TEM_{00}$ mode laser power, as shown in CHAPTER 6. Unfortunately, resulting also in stronger thermal lensing and a non-uniform distribution along the laser rod. Besides, in solar lasers, thermal focusing of a laser rod greatly modifies the modes, and the pump-induced fluctuations of the focal length may strongly perturb the laser output, even preventing any practical or reliable use of the laser. Efficient exploitation of the rod volume of a solar laser operating in $TEM_{00}$ mode requires the solution of the following problem: The $TEM_{00}$-mode volume in the rod has to be maximized, but the resonator should remain as insensitive as possible to focal length and alignment perturbations. Early solutions proposed the compensation of the thermal lens by: a convex mirror *(113)*; a resonator featuring an internal telescope *(114,115)*; bifocusing-compensation technique with two identically pumped rods *(116)*; the insertion of a negative lenses, either in the resonator *(117)* or ground at the ends of the rod, that exactly eliminate the focusing effect of the rod *(48)*. With these methods, high power in a single-mode beam were obtained. However, it was only effective for one particular value of the focal length. To minimize this problem, single fused silica light-guides with large square input/output ends were proposed and tested *(37) (38)*. Pump light uniformity at the output end of the square light-guide was achieved. However, the transfer efficiency from the focal spot to the laser rod was reduced due to the relatively low efficient light coupling between the large output end of the light guide and the laser rod.

Since 2008, many solar laser pumping schemes were proposed to generate stable $TEM_{00}$-mode laser emission *(118,119,120,121)*, as listed in TABLE 7.1. Solar laser pumping through a twisted fused silica light-guide was considered to be an effective solution to solar laser beam stability problem. Based on the refractive and total internal reflection principles, the light guide, by serving also as a beam homogenizer, transformed the near Gaussian profile of the concentrated light spot at its large square input face into a uniform pump light distribution at a narrower rectangular output end, facilitating further efficient light coupling into a long and thin laser rod. Compared to the light-guide schemes, where the concentrated solar radiation is mainly collected and transported by the central light-guide *(118,119,120)*, the twisted light guide from 2012 *(121)*, provides a uniform way in both sharing and transporting the concentrated solar radiation at the focus. 50% radiation is easily transmitted through the single light-guide with rectangular cross-section, while the other 50% is also efficiently transmitted through the two twisted light-guides with square cross-section. This lead to both a largely enhanced transmission efficiency and a more homogenous pump light

distribution along the output end of the assembly, as observed in TABLE 7.1. Less variation in pumping density is also detected, resulting in a more stable solar laser scheme. Nevertheless, even though optimum light-guide solar laser pumping parameters were found through ZEMAX© and LASCAD© numerical analysis codes, no prototypes lasers were built to validate these proposals until 2016 *(90)*.

TABLE 7.1 - Proposed solar laser schemes with twisted guides.

| Solar laser schemes |  |  |  |  |
|---|---|---|---|---|
| | Light guide assembly /elliptical-cylindrical cavity | Light-guide assembly /2D-CPC cavity | Light guide assembly /elliptical cavity | Compact light-guide assembly /2V- pump cavity |
| Year | 2008 | 2009 | 2009 | 2012 |
| Authors / Reference | Geraldes and Liang *(118)* | Pereira and Liang *(119)* | Liang and Pereira *(120)* | Almeida and Liang *(121)* |
| Input area | $20\times20$ mm$^2$ | $18\times18$ mm$^2$ | $15.4\times16$ mm$^2$ | $14\times14$ mm$^2$ |
| Output area | $6.7\times60$ mm$^2$ | $7\times54$ mm$^2$ | $7\times49$ mm$^2$ | **7**$\times28$ mm$^2$ |
| Transmission efficiency | 76.9% | 73.9% | 83.1% | 88.8% |
| Pumping density variation | 85% | 80% | 80% | 30% |
| Rod length | 80 mm | 76 mm | 70 mm | 40 mm |

## 7.1 SIDE-PUMPING SCHEME WITH TWISTED LIGHT-GUIDE

Analogously to the previous twisted light-guide of 2012 *(121)*, to improve the laser beam stability of the solar-pumped laser by the heliostat–parabolic mirror system, two side-pumping schemes with monolithic fused silica twisted light guides were built in 2016 and tested in PROMES-CNRS *(90,91)*. Both solar laser heads were composed by the fused-silica twisted light

guide, a secondary 2D-CPC concentrator, a tertiary 2V-shaped pump cavity, and a long and thin Nd:YAG rod, as shown in FIG. 7.1.
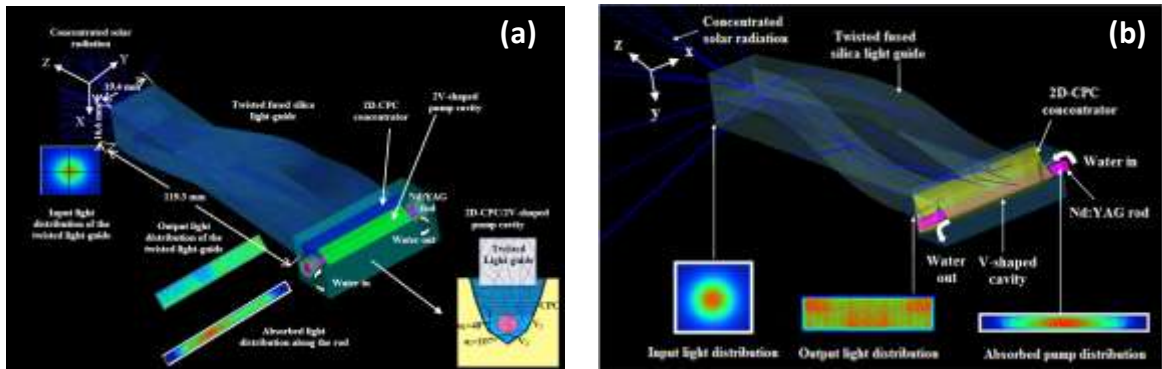


**FIG. 7.1** - Design of **(a)** non-symmetric *(90)* and **(b)** symmetric *(91)* solar-pumped Nd:YAG laser heads twisted light guides, in ZEMAX[©].

To provide the desired form of the twisted light guides, two techniques are possible: 1. shaping the light guide in either high-temperature environment or 2. directly sculpturing from a fused silica slab at room temperature. For the first technique, high-temperature environment (hydrogen flame, more than 1500°C) and pure graphite moulds are needed for controlling the bending curvatures of the light guide for lamp-pumped lasers *(103)*. High temperature light guide shaping technique would be effective if each single curved light guide were produced separately, but the problem of water leakage would appear if several curved light guides were joined together. Direct glass sculpturing technique was chosen because it allowed the fabrication of the twisted light guides at room temperature and hence avoiding water leakage problem. To the best of our knowledge, these were the first reports of the successful sculpturing of monolithic fused silica twisted light guides (FIG. 7.2) for solar laser research *(90,91)*.

**(a)** **(b)**
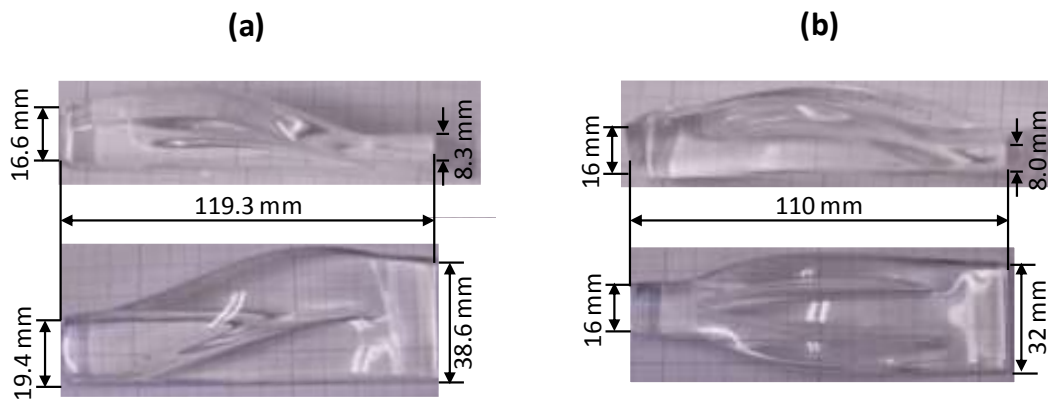


**FIG. 7.2** - Photos of the **(a)** non-symmetric and **(b)** symmetric twisted fused silica light guides with final dimensions.

The monolithic twisted fused silica light-guides in FIG. 7.2 were produced directly from a fused silica slab of 99.999% optical purity with 40 mm × 17 mm × 120 mm dimensions. The production of both the twisted light-guides was time consuming and delicate. The process was subdivided into three steps: 1. The fused silica slab was firstly cut and sculpted by diamond tools and gradually ground into the shape of twisted light-guide, optimized by both ZEMAX[©] and LASCAD[©] numerical analysis codes. 2. Secondly, the twisted light-guide was further dimensioned by coarse grinding paper. 3. Finally, optically transparent input, output and side surfaces, in FIG. 7.2, were achieved by fine polishing paper and suspension liquid.

The 2D-CPC, and consequently the 2V-shaped pump cavity, were optimized for each twisted light guide. The 2D-CPC/2V-shaped cavity of the non-symmetric light guide, in FIG. 7.3(a) had an entrance aperture of 11 mm × 35 mm and was 10 mm in depth. The hollow 2D-CPC had 11 mm input aperture, 7 mm output aperture, and 6.5 mm height, while for the 2V-shaped cavity, the reflector $V_1$ was mounted at $\alpha_1 = 107°$ full-angle and the reflector $V_2$ at $\alpha_2 = 48°$ half-angle. For the symmetric twisted light guide, the 2D-CPC concentrator had 11 mm × 36 mm rectangular large input aperture, 7 mm ×36 mm small output aperture and 10 mm in depth, as shown in FIG. 7.3(a). The two-dimensional 2V-shaped cavity had an entrance aperture of 7 mm × 36mm and 5 mm depth. It was composed of a V-shaped reflectors, $V_1$ with 47.5° half-angle and two upper planner reflectors, $V_2$ with 14° half-angle relatively to $V_1$.

**(a)**                                                                    **(b)**
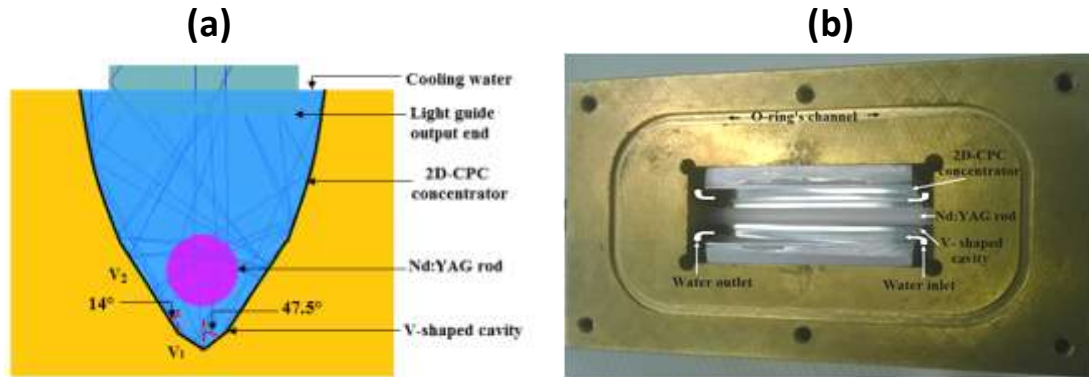


**FIG. 7.3** - **(a)** 2D-CPC concentrator and2V-shaped pump cavity with the 3 mm diameter, 50 mm length rod for the symmetric twisted light guide (b) Photo of the pump cavity with the $Nd^{3+:}YAG$ laser rod.

In ZEMAX$^©$ analysis, the 2D-CPC/2V-shaped cavity combination was found to be more efficient for coupling the light rays of different angles from the twisted light-guides to the thin laser rod, as compared to either a single V-shaped reflector or a 2V-shaped reflector. The inner walls of both 2D-CPC and 2V-shaped reflectors were bonded with a protected silver-coated aluminum foil with 94% reflectivity. By combining the light concentration capacity of both the 2D-CPC concentrator and the 2V-shaped pump cavity with the light homogenization capacity of the twisted light guides, relatively uniform pump power deposition within the laser rod was achieved.

## 7.2   NUMERICAL OPTIMIZATION OF THE SOLAR LASER PERFORMANCE
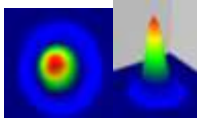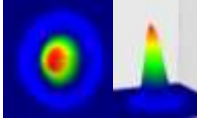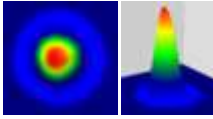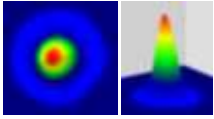
The terrestrial solar irradiance of 1000 W/m$^2$ was considered in the ZEMAX$^©$ analysis. The effective pump power of the light source was 189 W for the parabolic mirror with 1.4 m diameter. It took into account the 16% overlap between the Nd:YAG absorption spectrum and the solar spectrum, the reflection and absorption losses of both the heliostat and the parabolic mirror, the shading effects of the shutter, the mechanical support unit and the laser head.

Analogously to the previous side-pumping schemes in CHAPTER 6, in LASCAD$^©$ analysis, the optical resonator was comprised of two opposing parallel mirrors at right angles to the axis of the active medium. One end mirror was high-reflection coated with 99.8% reflectivity (HR1064 nm). The other output mirror was partial reflection coated (PR1064 nm). The solar laser performance was numerically studied by positioning the PR mirror at 60 - 90 mm from the nearest end face of the laser rod, while the HR mirror varied between 500 mm and 520 mm. For efficient extraction of

$TEM_{00}$-mode solar laser power, large RoC = -5 m end mirrors were adopted. The 3 mm diameter rod presented the highest $TEM_{00}$-mode laser power within the asymmetric laser resonator of $L_1$ = 518.3 mm and $L_1$ = 506.6 mm for the non-symmetric and symmetric twisted light guide, respectively. In these cases, BPM analysis gave a diffraction loss of 0.48% and 0.42%, and thus, the total round-trip loss of 3.88% and 3.82%, respectively.

The numerically calculated $TEM_{00}$-mode laser power and output laser beam profiles for both schemes are given in TABLE 7.2. The influence of the combined tracking error displacement on the absorbed pump flux distributions of the Nd:YAG single-crystal rods and on $TEM_{00}$-mode laser performance were also studied.

**TABLE 7.2** - Numerical orientation error dependent $TEM_{00}$-mode laser performance of non-symmetric and symmetric twisted light guides.

| Tracking error | Non-symmetric Twisted Light Guide | | Symmetric Twisted Light Guide | |
|---|---|---|---|---|
| | **Without** ($\Delta x = \Delta y = 0$ mm) | **With** ($\Delta x = \Delta y = 2.55$ mm) | **Without** ($\Delta x = \Delta y = 0$ mm) | **With** ($\Delta x = \Delta y = 2.55$ mm) |
| $TEM_{00}$ mode 2D/3D profile |  |  |  |  |
| $TEM_{00}$ mode laser power | 2.64 W | 2.57 W | 3.14 W | 3.09 W |
| $TEM_{00}$ mode laser stability | 3.7 % | | 1.6 % | |

Heliostat orientation error displaced the circular light spot away from the central point at the input face of the light guide. For the focal distance of 850 mm of the PROMES-CNRS parabolic mirror, a typical 0.2° orientation error (2 mrad) corresponds to approximately 2.55 mm displacement in both X and Y axes. Zero-orientation error corresponded to the optimum alignment between the heliostat and the primary parabolic concentrator. Pump light in this case was efficiently transmitted and uniformly redistributed along the rod through the twisted light guide, which is especially true for the symmetric twisted light-guide, as shown in FIG. 7.1, resulting in 3.14 W numerically calculated $TEM_{00}$-mode solar laser output power and an excellent Gaussian fundamental mode beam profile in TABLE 7.2. For the non-symmetric twisted guide, less $TEM_{00}$-mode laser power of 2.64 W was numerically calculated. For the combined tracking errors in both X and Y axes, the focal spot was shifted obliquely from the center of the input face of the lower straight part of the light guide of the symmetric twisted guide, then the homogeny of the pump light distribution within the rod was affected, causing a slight reduction in laser output power to 3.09 W and a little modification of the $TEM_{00}$ mode beam profile as shown in TABLE 7.2. Nevertheless, only 1.6% $TEM_{00}$-mode laser beam stability was achieved, which was better than the 3.6% beam stability of the non-symmetric twisted guide.

## 7.3  NUMERICAL ANALYSIS OF INPUT SOLAR POWER DEPENDENT TEM$_{00}$– MODE SOLAR LASER PERFORMANCE

Both ZEMAX$^{©}$ and LASCAD$^{©}$ software were used to study the input solar power dependent TEM$_{00}$-mode laser powers and beam profiles of both the previous TEM$_{00}$-mode end-side-pumped solar laser *(31)*, in FIG. 7.4(a), and the side-pumped solar laser by the twisted light guide *(91)*, FIG. 7.4 (b).
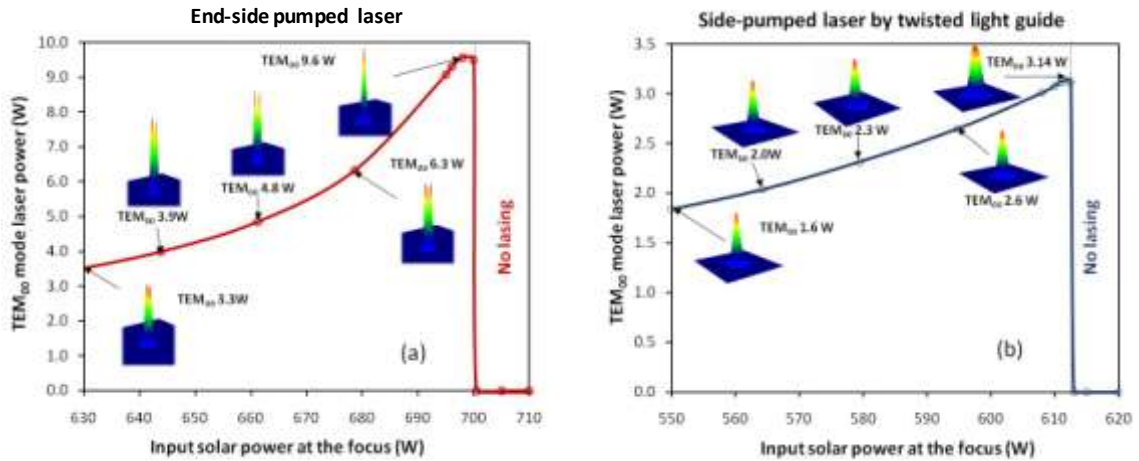


**FIG. 7.4** - Input solar power dependent TEM$_{oo}$-mode solar laser powers and beam profiles from both **(a)** the conical-shaped end-side-pumped laser *(31)* and **(b)** the side-pumped laser by the symmetric twisted light guide *(91)*.

In FIG. 7.4(a), low-order mode solar laser beam profiles were changed to a Gaussian TEM$_{00}$-mode profile when input solar power at the focus approached 700W (when the shutter was removed). 9.6 W fundamental mode laser power was numerically calculated. The TEM$_{00}$-mode solar power was found to be very sensitive to the variation of input solar power at the focus. Slight increase in input solar power above 700W led to a shorter thermal length, causing the extinction of solar laser output power. Reduction in solar power alleviated considerably the thermal lensing effect, permitting either two-mode, or other low-order mode laser operation within the laser cavity. Significant reduction in fundamental mode power, from 9.6W to 3.3W were numerically calculated when solar power at the focus was reduced from 700W to 630W, corresponding to 2.9 times reduction. For FIG. 7.4(b), however, the Gaussian TEM$_{00}$-mode profile remained nearly stable when the input solar power at the focus was increased from 550W to 612W (by controlling the shutter), demonstrating a remarkable laser beam profile stability until the input solar power level exceeded 612W after which solar laser stopped lasing due to the thermal lensing effect. When the input solar power was reduced gradually from 612W to 550W, the numerically calculated TEM$_{00}$-mode laser power was gradually reduced from 3.14W to 1.6W, corresponding to near 2 times reduction. From FIG. 7.4, it was clear that change in input solar power could cause much less variation in both TEM$_{00}$-mode laser power and beam profile by the twisted light guide solution than by the conical-shaped end-side-pumped laser.

## 7.4 SOLAR LASER EXPERIMENTAL RESULTS

The solar laser head was mechanically mounted to the laser resonator, which was fixed on an X-Y-Z axis positioning system by using the multi-angle vice, as shown in FIG. 7.5. The resonator mechanics were designed to allow the displacement of the HR mirror, while maintaining the PR mirror at fixed $L_2 = 60$ mm position. An accurate optical alignment in the focal zone was hence ensured. The 3 mm diameter, 50 mm length $Nd^{3+}$:YAG was supplied by Altechna Co., Ltd. It had 1.0 % $Nd^{3+}$ concentration. Both ends of the rod were anti-reflection (AR) coated (R < 0.2% @ 1064 nm). The thin Nd:YAG rod was actively cooled by water at 6 l/min flow rate.



**FIG. 7.5** - The solar laser head within the asymmetric resonator.

Direct solar irradiance varied between 970-1000 $W/m^2$ during the experiments. Laser power was measured simultaneously with a Thorlabs PM1100D power meter. The correspondingly input solar power at the focus was measured by a Molectron PowerMax 500D power meter. To reduce the maximum input solar power at the focus, the external annular area of the 2.0 m diameter parabolic mirror was limited by a mask, so that only 1.4 m diameter central circular area was utilized. For 1000 $W/m^2$ solar irradiance and 1.18 $m^2$ effective collection areas, 610W was measured at the focal spot with the shutter totally opened. The experimental $TEM_{00}$-mode solar laser performances of both twisted light guide schemes are shown in TABLE 7.3.

**TABLE 7.3** - Experimental $TEM_{00}$ mode laser performance of non-symmetric and symmetric twisted light guides.

| | Non-symmetric Twisted Light Guide | Symmetric Twisted Light Guide |
|---|---|---|
| **Asymmetric resonator parameters** | $L_1 = 518.3$ mm / $L_2 = 60$ mm | $L_1 = 506.6$ mm / $L_2 = 85$ mm |
| **Threshold power** | 276 W | 285 W |
| **Maximum input power** | 600 W | 610 W |
| **Maximum $TEM_{00}$ mode laser power** | **2.3 W** | **2.7 W** |

| $TEM_{00}$ mode collection efficiency | 1.95 W/m$^2$ | 2.29 W/m$^2$ |
|---|---|---|
| **M$^2$ factors** | $M_x^2 \approx M_y^2 \leq 1.05$ | $M_x^2 \approx M_y^2 \leq 1.05$ |
| **Brightness figure ofmerit** | 2.1 W | 2.4 W |

The CINOGY UV-NIR beam profiler –CinCam CMOS was used for monitoring the laser beam profile. To measure the beam diameters at $1/e^2$ width under high 1064 nm laser intensity, a PR1064 nm (95%), RoC = ∞ output mirror was added before the CMOS detector, to act as an extra laser beam attenuator.
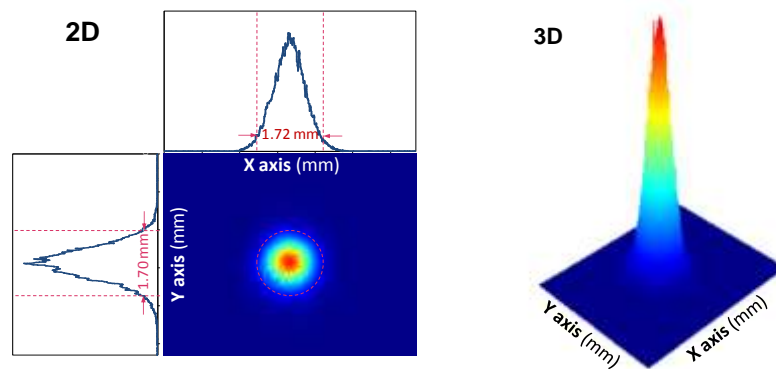


**FIG. 7.6** - 2D and 3DTEM$_{00}$-mode output laser beam 2D and 3D profiles, measured 50 mm away from the PR1064 nm mirror.

The thermal lens effect is a serious issue in solar laser systems, small diameter rods can minimize considerably this problem. The combination of both monolithic twisted light guide and small diameter $Nd^{3+}$:YAG rod have considerably overcome these thermal lensing problems, providing a uniform pumping distribution along the thin laser rod, which allowed the generation of much more stable continuous-wave TEM$_{00}$-mode solar laser power with maximum 2.3 W/m$^2$ collection efficiency. This in turn, led to significantly reduced solar pumping intensity, and consequently less heat load, less thermal stress and working temperature, as compared to all the previous schemes *(31,37,38,41,42)*.

Time dependent TEM$_{00}$ mode solar laser power variations of both the end-side-pumped laser *(31)* and the side-pumped laser by the symmetric twisted light guide were measured in PROMES-CNRS during the first two weeks of July in 2017. For the side-pumped laser by the twisted light guide at 970 W/m$^2$ solar irradiance and 1.18 m$^2$ effective collection area, the asymmetric resonator with RoC = - 5 m PR (94%) mirror fixed at $L_2 = 85$ mm and RoC = -5m HR mirror placed at $L_1 = 500$ mm, similar to that shown in FIG. 7.5. 2.5W TEM$_{00}$-mode solar laser power were measured during 240 seconds, with the maximum output power variation being less than 1.7%. The Gaussian TEM$_{00}$ mode profile was also found stable during the measurement. For the TEM$_{00}$-mode end-side-pumped scheme *(31)* at 950 W/m$^2$ solar irradiance and 1.18 m$^2$ effective collection area, a - 5 m RoC output mirror with 94% reflectivity at $L_1 = 430$ mm, provided the maximum TEM$_{00}$ mode laser output power of 8.9 W. Strong oscillation of 12% were observed during the measurement process of 240 seconds. The end-side-pumped configuration offered the maximum TEM$_{00}$-mode solar laser collection efficiency, but also suffered from a stronger thermal lensing

effect. Much more than the 1.7% of the twisted light guide laser. FIG. 7.7 represented a favorable result in TEM$_{00}$ mode laser beam stability of less than 12% for the end-side-pumped laser. During the measurement process, however, it was not easy to maintain a perfect Gaussian mode profile due to the strong thermal lensing effect of the type of laser. Solar irradiance variation of less than 0.5%, cooling water temperature oscillation of less than 2 degrees during the measurement were found sufficient to change a solar laser beam with Gaussian profile into either a low-order mode beam or a two-mode, sometimes a four-mode.
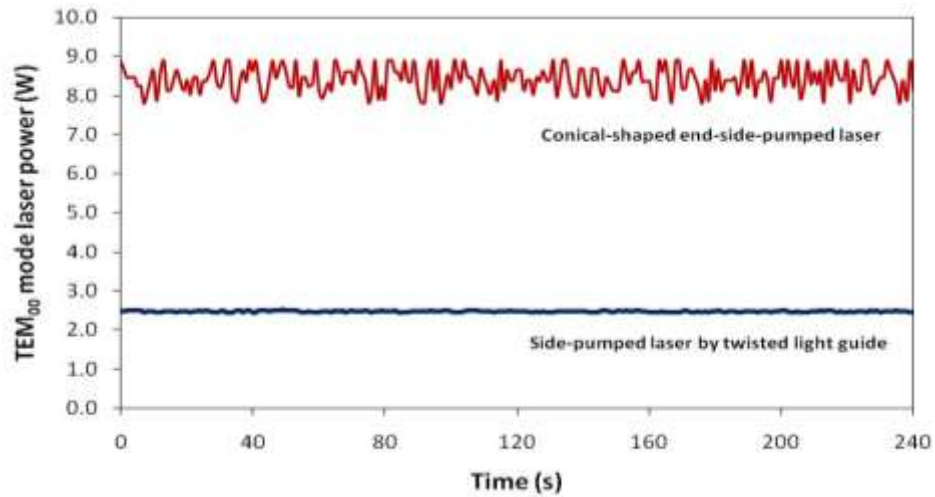


**FIG. 7.7** - Time dependent TEM$_{00}$ mode solar laser power variations of both the end-side-pumped TEM$_{00}$ mode laser *(31)* and the present side-pumped laser by the twisted light guide *(91)*.

The previous TEM$_{00}$-mode laser schemes with no light guides *(39,40,41,42)*demonstrated poor stability compared to that with single light guide *(37,38)*. Strong thermal lensing effects, which affected largely the TEM$_{00}$-mode laser power stability of previous solar lasers were not observed in our measurement. Therefore, by improving polishing accuracy of the dimension of the twisted light guide, enhanced TEM$_{00}$-mode solar laser efficiency and stability can hopefully be achieved.

# 8 Doughnut-shape solar laser beam

Gaussian $TEM_{00}$-mode beams are by far the most common laser beam shape used in materials processing *(43)*. Nevertheless, non-Gaussian beam profiles such as annular beams, also called doughnut-shaped beams, are also a very important class of beams for many applications *(43)*. They enable novel fundamental insights in light-matter interactions and have the potencial to extend the possibilities of laser-based processing *(122)*. When using doughnut-shaped beam, the lateral spreading of the heated area is still larger while the maximum temperature rise is lower in the center. These temperature profiles are crucial for applications in which temperature is a key parameter, such as laser heat treatment or laser heardening *(43)*. Doughnut-shaped laser beams have also recently attracted significant attention for applications in advanced trapping techniques, acting as optical tweezers for trapping atoms and molecules *(123,124)*.

To form a doughnut-shaped beam, the traditional way is to cut the Gaussian $TEM_{00}$-mode *(125)*. It has also been demonstrated by inserting additional phase elements in a laser cavity *(126)*. However, these methods require precise laser cavity alignment, and they involve a significant waste of output power due to insertion losses *(125,126)*.

We reported, to the best of our knowledge, the first emission of a doughnut-shaped solar laser beam from a side-pumped grooved Nd:YAG laser rod. A solar laser prototype was built and tested by the NOVA heliostat–parabolic mirror system.

## 8.1  Side-pumping scheme with large aspheric lens

The solar laser head was consisted of a fused silica semi-spherical lens, a two-dimensional trapezoidal-shaped pumping cavity, and a 4.0 mm diameter, 34 mm length, 1.0 at.% grooved Nd:YAG rod, as shown in FIG. 8.1. The fused silica semi-spherical lens collected and compressed the concentrated solar radiation along the laser rod. To manufacture the large spherical lens, an 80 mm diameter, 40 mm length fused silica rod of 99.999% optical purity (supplied by Beijing Kinglass Quartz Co., Ltd.) was ground and polished to its final dimensions: 80 mm output face diameter, 40 mm radius of curvature and 35 mm length. The two-dimensional trapezoidal-shaped pumping cavity had an entrance aperture of 12.2 mm × 22 mm and 13.3 mm depth. The laser rod optical axis was 3.5 mm separated from the pumping cavity bottom and 11 mm from the output face of the fused silica lens. The pumping cavity was composed of a trapezoidal-shaped reflector $V_1$, with α = 25° opening angle, and two upper planar reflectors $V_2$, perpendicular to the bottom face of the pumping cavity. This combination was very effective in coupling the concentrated light rays with different incidence angles into the laser rod.
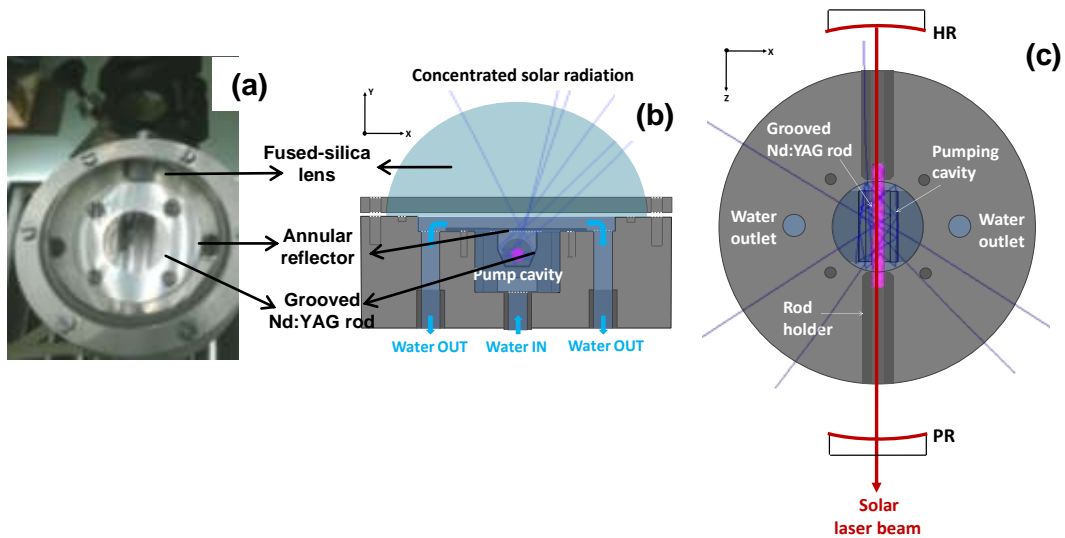
**FIG. 8.1** - **(a)** Photograph of the Nd:YAG solar laser head. **(b)** Front-view and **(c)** top-view of the laser head design.

As shown in FIG. 8.2, ray A passes through the rod once and is bounced back by $V_1$, so that double-pass absorption is accomplished. The rays that does not hit directly the laser rod are redirected by either $V_1$, making one passage (ray B) or two passages (ray C) through the laser rod, or $V_2$, hitting once (ray D) or twice (ray E) the laser rod through $V_1$. The upper annular reflector played also an important role in redirecting some rays (ray F) that exit the pumping cavity, so that one or two passages through the laser rod is accomplished. The inner walls of both $V_1$, $V_2$ and annular reflectors were bonded with a protected silver-coated aluminum foil with 94 % reflectivity.
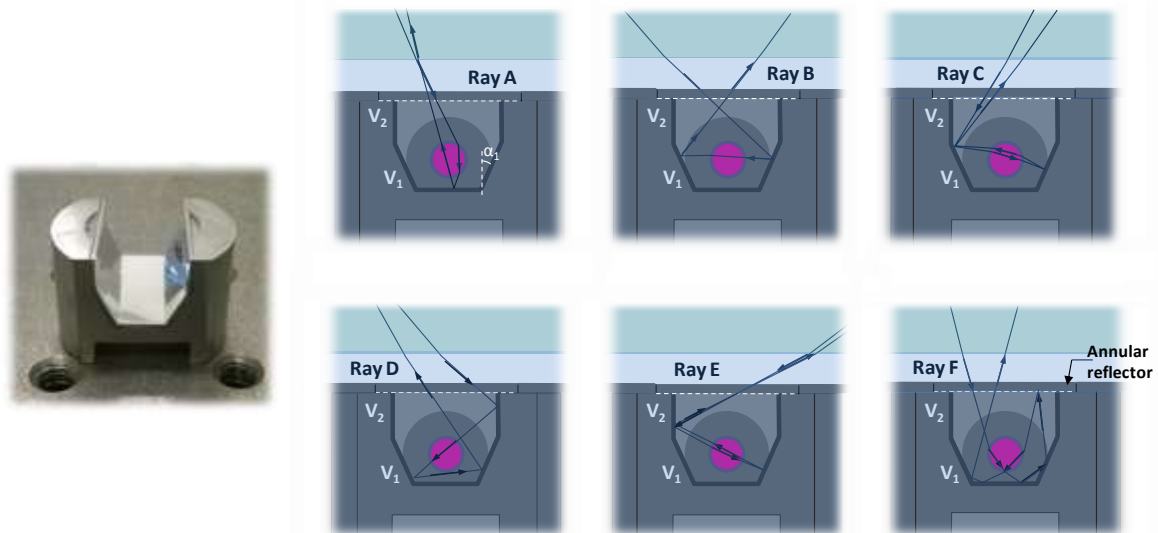


**FIG. 8.2** - Photograph of the trapezoidal pumping cavity and examples of the passage of the pump rays with different incidence angles in ZEMAX$^©$ analysis.

The 1.0 at% grooved Nd:YAG rod with 4 mm diameter, 34 mm length, grooved pitch of 0.6 mm and grooved depth of 0.1 mm, was supplied by Chengdu Dongjun Laser Co., Ltd. Both end faces of the rod were anti-reflection (AR) coated for laser emission wavelength (R<0.2% @ 1064 nm). The rod was fixed by two rod holders and cooled by distilled water at 6 L/min flow rate. The laser head was mechanically mounted to a laser resonator, which was fixed on an X–Y–Z axis mechanical support by using a multi-angle vice.

## 8.2 NUMERICAL OPTIMIZATION OF THE SOLAR LASER PERFORMANCE

Similar to our previous solar pumping approaches, all the above-mentioned design parameters of the solar laser system were firstly optimized by non-sequential ray-tracing ZEMAX$^{©}$ software for achieving the best compromise between the absorbed pump power and suitable pump profile within the laser rod.

In the proposed side-pumped solar laser scheme, tested within the same solar facility $(39)$, a fused silica tube lens was combined with a 2V-shaped pumping cavity to provide efficient pumping along the grooved 1.0 at.% Nd:YAG rod, also with 4 mm diameter and 34 mm length. The absorbed pump flux distributions along seven transversal cross sections and one central longitudinal cross section of the grooved Nd:YAG rod pumped through the previous $(39)$ and present schemes are shown in FIG. 8.3(a) and FIG. 8.3(b), respectively. The correspondingly thermally induced effects - heat load, temperature and stress intensity - from LASCAD$^{©}$ analysis are also shown in FIG. 8.3(c) and FIG. 8.3(d). To scale our solar-pumped laser rod to high average power, it is of utmost importance to attain a more uniform pump power deposition along the laser rod, as in FIG. 8.3 (b). Heat load, temperature gradient and stress intensity in the laser rod were all reduced to more than a half, FIG. 8.3 (d), as compared to that of the previous scheme, FIG. 8.3 (c).
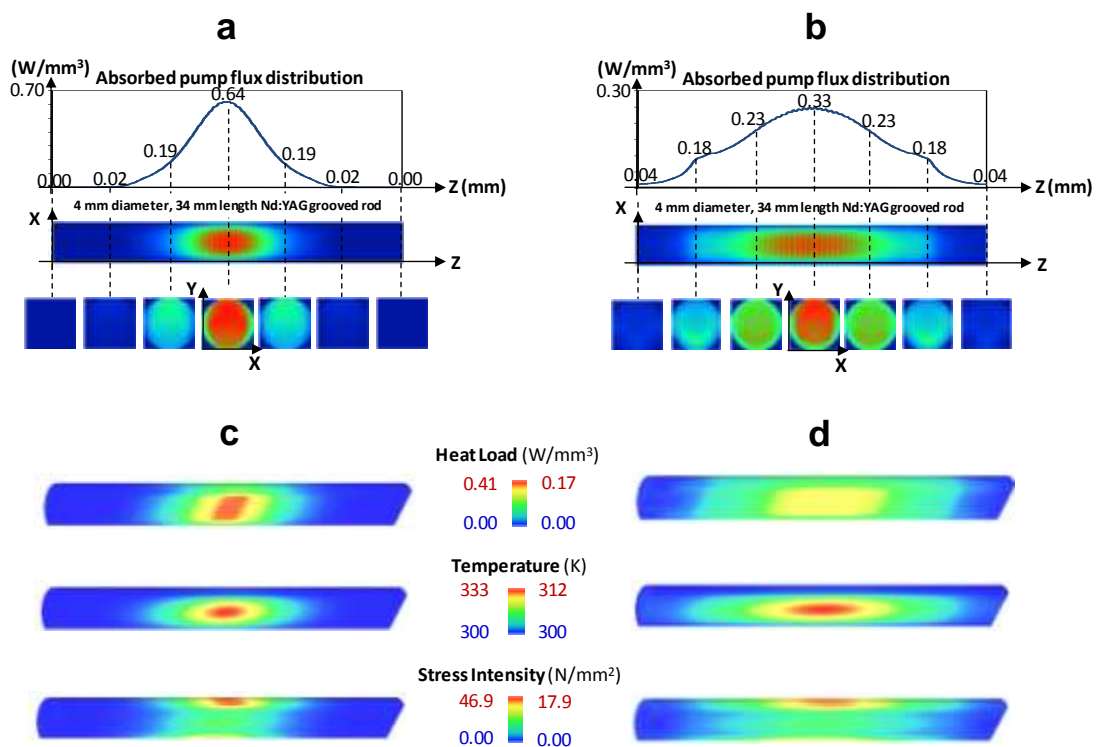


FIG. 8.3 - (a), (b) Numerical absorbed pump flux distributions along central and longitudinal cross-sections of the 4 mm diameter, 34 mm length, 1.0 at.% Nd:YAG rod pumped through the previous $(39)$ and the present scheme, respectively, obtained through ZEMAX$^{©}$ analysis. (c), (d) Correspondent heat load, temperature and stress intensity, obtained through LASCAD$^{©}$ analysis.

In LASCAD$^{©}$ program, the optical resonator was comprised of two opposing parallel mirrors at right angles to the axis of the active medium, as illustrated in FIG. 8.3. $L_1$ and $L_2$ together with HR and PR mirrors reflectivity and radius of curvature were optimized to achieve the lowest laser beam divergence and, thus, the highest fundamental mode power.
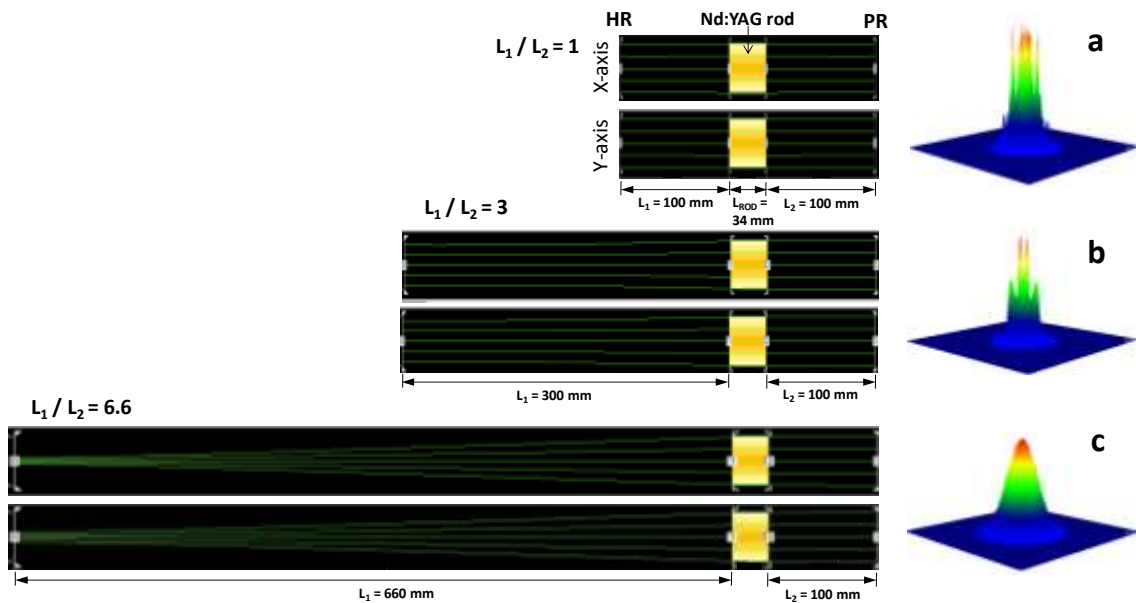
**FIG. 8.4** - Laser resonator design in LASCAD$^{©}$ analysis at different $L_1/L_2$ ratios and correspondingly numerical output laser beam profiles.

Compared to the previous scheme *(39)*, the edge of optically stable region is longer in the present scheme ($L_1/L_2$= 6.6). Thus, the mode-matching efficiency is less sensitive to small changes in thermal lensing near the asymptote and, consequently, stable solar laser emission at lower modes can be more often observed.

## 8.3   SOLAR LASER EXPERIMENTAL RESULTS

The resonator mechanics was designed to allow the displacement of the HR mirror (from $L_1$= 100 mm to $L_1$=680 mm), while maintaining the PR mirror at a fixed $L_2$ = 100 mm position.
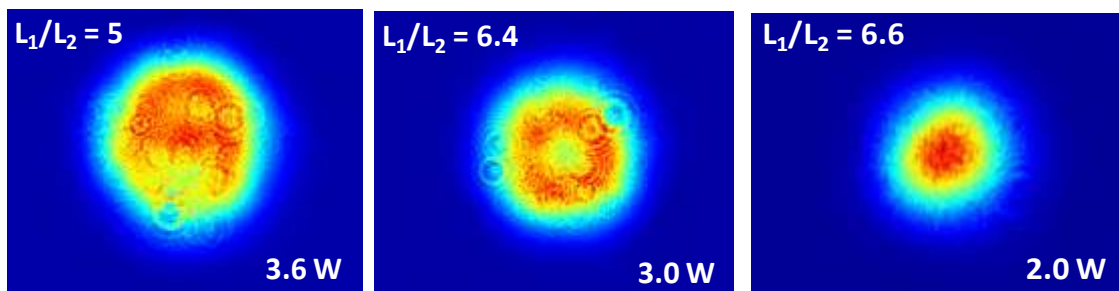


**FIG. 8.5** - Output solar laser beam profile, and correspondingly laser output power, at three different $L_1/L_2$ asymmetric resonators: $L_1/L_2$ = 5, $L_1/L_2$ = 6.4, and $L_1/L_2$ = 6.6.

The CINOGY UV-NIR beam profiler CinCam CMOS, placed 40 mm away from the output coupler, monitored the laser beam profile during the experiments. By varying the rotation angle of a shutter standing between the heliostat and the parabolic mirror, different input solar power and output laser power were measured with a Molectron PowerMax 500D and a Thorlabs PM1100D power meters, respectively.

At relatively large $L_1/L_2$, only few modes oscillated, as what happened with $L_1/L_2 = 5$ ratio. By displacing the HR mirror to $L_1 = 640$ mm ($L_1/L_2 = 6.4$ ratio), doughnut-shaped solar laser beam oscillation was registered for the first time, corresponding to 3.0 W solar laser power, as shown in FIG. 8.6 (b) and FIG. 8.6. Maximum solar input power of 730 W was measured in this case.
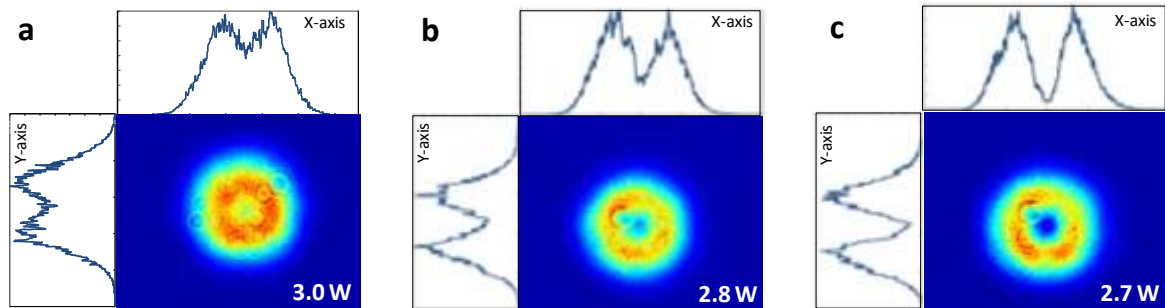


**FIG. 8.6** - Different doughnut-shaped output laser beam profiles at $L_1/L_2 = 6.4$ ratio. Influenced by the slight angular adjustment of the HR mirror.

Slight adjustments in the optical resonator alignment by precisely rotating either PR or HR mirror influenced significantly the beam profiles of the doughnut-shaped beams, as shown in FIG. 8.6. For example, with a slight angular adjustment of the PR mirror, it was possible to obtain a doughnut-shaped with an almost null intensity at the center, FIG. 8.6(c). However, this came at the expense of lowering slightly the laser output power. For achieving $TEM_{00}$-mode solar laser oscillation, the HR mirror was placed at $L_1 = 660$ mm ($L_1/L_2 = 6.6$), closer to the border of the resonator stable zone. Maximum $TEM_{00}$-mode solar laser output power of 2.0 W was finally measured.

The novel side-pumping scheme had enabled a more uniform pump profile as compared to that of the previous side-pumping approach *(39)*, with the same solar facility, reducing significantly the pump peak intensity and thus the thermal induced effects within the laser rod. This contributed to increasing the asymmetric laser resonator length and consequently providing a more stable solar laser emission at lower modes. Therefore, it was able to demonstrate the first emission of doughnut-shaped laser beam from the solar-pumped laser with the grooved Nd:YAG rod. The selective modes oscillation were achieved by the optimization of the spatial overlap between the desired resonator mode and the pump mode volumes, and which was obtained by adopting the asymmetric laser resonator, allowing the formation of the doughnut-shaped beam without the need of inserting additional optical phase elements to the laser cavity. The successful production of doughnut-shaped and Gaussian laser beam may widen the applications areas of solar-pumped lasers.

# 9 CONCLUSIONS AND FUTURE VISIONS

Since our ultimate power source in space is the Sun *(1)*, shining 24 hours, a desirable laser for use in space-based applications would be one that derives all its power from the Sun. Therefore, the idea of broadband solar radiation conversion into coherent, narrow-band laser radiation by free solar pumping is of ever-increasing importance. On the Earth, solar-pumped lasers can also lead to a new generation of fuel-free energy-efficient and cost-effective transport system with zero $CO_2$ and $SO_2$ emissions *(8,9,27)*, becoming a natural choice in many Sun-rich countries.

For solar-pumped laser technology to be an alternative renewable energy system, its development of high-efficiency is of primary importance. For the practical application, the laser output for the unit surface area of collector is important as the assessment of the sunlight laser. The solar laser beam brightness is also a crucial figure of merit to characterize the performance of solar-pumped lasers, for applications that need energy transferred at long distances.

During this doctoral programme, several solar laser prototypes were performed to increase both the solar laser efficiency and brightness of present-day solar lasers. They were built and tested, according to the optimized parameters through ZEMAX$^©$ and LASCAD$^©$ numerical analysis. Almost all of the solar laser setups developed in this thesis employed an heliostat-parabolic mirror system (PROMES-CNRS MSSF and NOVA solar furnace) for collecting and concentrating the sunlight into a small spot without dispersion, which was essential for efficient solar-pumping of small diameter and thin laser rods, leading to a substantial progress in solar laser beam quality, and brightness. Yet, the first report on $TEM_{00}$ mode solar laser emission occurred with the use of cost-effective Fresnel lens as a primary concentrator, helping to guide our way for further improvement in solar laser beam brightness.

The main achievements addressed in this PhD thesis are summarized as follow:

1. **Advances in solar laser efficiency:**

- Due to the research projects supported by SFERA I (*Laser-Osci-Amp*) and SFERA II (*P1404090033*), we have reported a significant improvement in solar laser collection efficiency with parabolic mirror system, in 2013 *(33)* and 2015 *(34)*, through the access of PROMES-CNRS MSSF solar facility. 13.9 $W/m^2$ and 21.1 $W/m^2$ solar laser collection efficiencies were respectively registered, by end-side-pumping a 5 mm diameter, 25 mm length, 1.0 at.% Nd:YAG laser rod using either a double stage light guide lens / conical pump cavity or a double stage conical lens / conical pump cavity.

- With the final construction of the NOVA heliostat-parabolic mirror system, 25.5 $W/m^2$

solar laser collection efficiency was reported in 2016, by end-side pumping a thinner Nd:YAG laser rod *(35)*. In addition to the enhancement of solar laser collection efficiency, the thermal performance of solar laser with end-side-pumping configuration was also improved.

- In 2017, record solar laser collection efficiency of 31.5 W/m$^2$ was reported by end-side-pumping a 4 mm diameter, 35 mm length, 1.0 at.% Nd:YAG laser rod in PROMES-CNRS MSSF, through the research project *P1602010181* supported by SFERA II *(31)*. This result surpassed the previous record with Fresnel lens in direct solar tracking system. Also, record slope efficiency of 8.9 % was achieved.

**2. Advances in solar laser brightness:**

- The first emission of TEM$_{00}$-mode solar laser was reported in 2013, by side-pumping a 3 mm diameter, 30 mm length, 1.1 at.% Nd:YAG rod with NOVA Fresnel lens system *(42)*. This has lead to 6.5 times improvement in solar pumped laser beam brightness. The choice of asymmetric resonator, closer to the border of resonator instability zone, for maximum extraction of TEM$_{00}$-mode solar laser was also an essential breakthrough for improving significantly the solar laser brightness.

- Through the research projects *P1404090033* and *P1502270118* supported by SFERA II, record solar laser beam brightness of 4.0 W *(37)* and record TEM$_{00}$ mode collection efficiency of 2.8 W/m$^2$ *(38)* were reported in PROMES-CNRS, in 2015. Both laser heads were composed of a single fused silica light guide to pump either a 3 mm diameter *(37)* or a 4 mm diameter, 30 mm length, 1.1 at.% Nd:YAG rod *(38)* for compensation of tracking error and thermal lensing to ensure stable solar laser emission.

- 1.5 times enhancement in TEM$_{00}$ mode solar laser collection efficiency was further reported in PROMES-CNRS, in 2016, by employing a Nd:YAG grooved for the first time in a side-pumping scheme, composed by a simple double-stage barrel-type fused silica concentrator / 2V-shaped pumping cavity *(41)*.

- In 2017, a substantial progress in both solar laser collection efficiency and solar laser brightness in TEM$_{00}$-mode regime was registered, through the research project *P1602010181* supported by SFERA II *(31)*. By end-side-pumping a 4 mm diameter, 35 mm length, 1.0 at.% Nd:YAG rod, the TEM$_{00}$ mode solar laser collection efficiency was almost doubled, reaching 7.9 W/m$^2$. Record-high solar laser brightness of 6.5 W was achieved.

**3. Advances in solar laser stability:**

- Homemade sculptured fused silica twisted light guides were produced for the first time, in order to provide an efficient light coupling and uniform redistribution of pump light into a thin and long laser rod *(90,91)*. Through the research projects *P1602010181* and *P1701190231* supported by SFERA II, enhanced TEM$_{00}$ mode solar laser beam stability was achieved.

**4. First doughnut shaped solar laser emission:**

- By side-pumping a Nd:YAG grooved rod within a long asymmetric resonator in NOVA heliostat-parabolic mirror system, the first production of doughnut-shaped solar laser beam, without the need of additional phase elements in laser cavity, was reported. 3.0 W solar laser power was measured, 1.5 times more than TEM$_{00}$ mode solar laser power.

It should be noted that the solar laser efficiency advances were achieved by employing end-side-pumping configurations *(26,29,30,31,33,34,35)*, since they can lead to much higher efficiencies compared to side-pumping configurations *(127)*. Nevertheless, in order to avoid overheating of the Nd:YAG active medium, which can worsen both solar laser efficiency and beam quality, almost all of the solar laser prototypes performed in this PhD work for improving solar brightness *(37,38,41,42)*, as well as solar laser beam stability *(90,91)* and doughnut-shape solar laser emission, have side-pumping configurations. It is an effective configuration for power scaling as it allows uniform absorption along the rod axis within the laser medium, hence improving the thermal performance of solar lasers, which is especially true for the side-pumping schemes using single *(37,38)* and twisted light guides *(90,91)*. Although both record $TEM_{00}$-mode solar laser collection efficiency and record solar laser brightness were further achieved by adopting an end-side-pumping configuration *(31)*, $TEM_{00}$ mode solar laser power, and thus brightness, was less sensitivity to pump power fluctuations by using side-pumping configurations, especially with twisted light guides *(90,91)*.

Until 2013, space-based and terrestrial applications for a renewable energy laser were not seriously considered *(20)*. Yet, these efforts for enhancing solar laser efficiency *(31,33,35)* and brightness *(31,37,38,41,42)* resulted in several world records, which have gained international recognitions in: *Laser Focus World* in 2013 *(20)*. and 2016 *(89)*; *Renewable Energy Global Innovations* in 2016 *(88)*; *Laser Physics Highlights* in 2013 *(79)*. Some of this reports were also shared in the websites: *Nextbigfuture* website *(2)*, *Photonics Online* and *Photonics Solutions*. This has lead to change that notion, drawing the attention of several solar laser researchers *(81,82,87,92,93,128)* which may widen the  applicability of solar-pumped lasers.

### Future visions:

Despite the several efforts addressed in this PhD thesis, solar-pumped lasers have yet to reach the levels of efficiency that would make these applications feasible.

The highest-performance solar lasers to date are based on Nd:YAG *(31)*, which is a proven laser medium with excellent optical and thermal properties, but when pumped directly by solar light the resulting efficiency is limited due to the poor overlap between its pump absorption bands and the solar spectrum *(45)*.

The utilization of solid-state laser materials with broadband absorption in the visible range, such as alexandrite, is also very attractive *(22)*. However, there was only one study on solar-pumped alexandrite laser reported by Lando et. al. in 1999 *(68)*. A laser output power of 12 W was obtained, requiring however a high final concentration of 4000–6000 times the incoming solar flux *(68)*. The main problem of Alexandrite is its low stimulated emission cross-section ($0.7 \times 10^{-20}$ cm$^2$) *(48,58,59,60,61,62)*, which requires high pump fluence for efficient gain extraction, making this laser material a real challenge for solar-pumped lasers *(22,68,69)*.

The improvement of solar laser conversion efficiency by adding $Cr^{3+}$ ions as a codopant in Nd:YAG has been pointed out for a long time *(26,56,72)* since it provides broader absorption bands, compared to Nd:YAG, for capturing the sunlight *(47,57)*. However, the preceding attempts to increase the conversion efficiency of solar pumped lasers with chromium co-doping did not give rise to further progress in solar-to-laser power conversion for now.

To take advantage of Cr:Nd:YAG ceramics in solar lasers an alternative is to study its amplification property. Contrary to the case of using Nd:YAG, it is easier to perform laser amplification using Cr:Nd:YAG ceramic owing to the broad spectral bandwidth of over 2 nm

*(129)*. By using a multi-stage of Cr:Nd:YAG ceramic thin disks *(93)*, the focusing sunlight can be injected into the laser housing of the multi-stage active mirror amplifiers, where the laser beam path can be designed orthogonally for multi-pass amplification.

In order to improve substantially the solar laser performance of Nd:YAG single-crystal, an architecture for that uses a luminescent solar concentrator (LSC), to decouple the conventional trade-off between solar absorption efficiency and the mode volume of the optical gain can be also explored *(81)*. The incident light absorbed by the LSC is then re-emitted as photoluminescence, in which a fraction can be absorbed by the active medium. The main advantages in using such materials are: the efficient coupling of incoherent, spectrally broad sunlight in small gain volumes, which should allow the generation of coherent laser light from intensities of less than 100 suns; less rigid requirements for thermal properties; potential use in non-tracking regime; and also the possibility of use different host materials for active medium *(81)*.

Another alternative to find a solution to achieve simultaneously a high efficiency and beam quality of solar-pumped lasers is the possibility to pump a vertical external cavity surface emitting laser (VECSEL) *(82)* as a continuation of the proven mode-converting capabilities of diode-pumped VECSELs *(83,84,130)*, also known as semiconductor disk lasers. The idea of solar-pumped semiconductors laser is attractive, primarily due to their broadband optical absorption but also due to their very short absorption lengths, which simplify the problem of overlapping pump and output beam *(85,86)*. Yet, to get watt level power out of a solar pumped VECSEL is very challenging, in terms the pump power density needed, heat dissipation and limited lifetime. The pump intensity needed to reach lasing threshold in high-power VECSELs is typically in excess of $\sim$20 MW/m$^2$ *(83,131)*. It is therefore clear that sunlight must be concentrated by a factor of at least 31,000 in order to reach lasing threshold, and by a larger factor to achieve useful power output *(82)*. The heat removal of semiconductor solar lasers is also a very challenging issue to be studied in detailed, since only a fraction of the spectrum is used/absorbed efficiently.

# References

1. (March 2013) Space Solar Power: Limitless clean energy from space. In: *National Space Society.* Available at: http://www.nss.org/settlement/ssp/

2. (October 2014) Towards Megawatt Solar Powered Lasers for Magnesium Production and future space applications. In: *Nextbigfuture.* Available at: https://www.nextbigfuture.com/2014/10/solar-powered-lasers-for-magnesium.html

3. Galle, P. (2008) *Estimating Laser Diode Lifetimes and Activation Energy.*, ILX Lightwave Corporation.

4. Lando, M., Kagan, J., Shimony, Y., Kalishy, Y., Noter, Y., Yogev, A., Rotman, S., Rosenwaks, S. (1997) Solar-pumped solid state laser program. *Proc. SPIE* **3110**, 196-201.

5. Massimiliano, V., Maddock, C. A. (2012) Pure design of a formation of solar pumped lasers for asteroid deflection. *Adv. Space Res.* **50**, 891 – 905.

6. Liang, D., Almeida, J., Oliveira, M., Gonçalves, F., Vistas, C. R. (April 2015) *Advances in high-efficiency TEM00-mode solar-pumped laser.* 1st Workshop on Laser solutions for Orbital Space Debris - Paris - France.

7. Almeida, J., Liang, D., Oliveira, M., Gonçalves, F., Vistas, C. R. (April 2015) *Progress in solar-pumped laser efficiency by heliostat-parabolic mirror system.* 1st Workshop on Laser solutions for Orbital Space Debris - Paris - France.

8. Yabe, T., Ohkubo, T., Dinh, T., Kuboyama, H., Nakano, J., Okamoto, K. (2012) Demonstration of solar-pumped laser-induced magnesium production from magnesium. Wiley 55 – 58.

9. Yabe, T., Uchida, S., Ikuta, K., Yoshida, K., Baasandash, C., Mohamed, M. S., Sakurai, Y., Ogata, Y., Tuji, M., Mori, Y., Satoh, Y., Ohkubo, T., Murahara, M., Ikesue, A., Nakatsuka, M., Saiki, T., Motokoshi, S., Yamanaka, C. (2006) Demonstrated fossil-fuel-free energy cycle using magnesium and laser. *Appl. Phys. Lett.* **89**, 261107.

10. Maiman, T. H. (1960) Stimulated optical radiation in ruby. *Nature* **187**, 493.

11. (1962) Sun-powered lasers. *J. Frankl. Inst.* **274**, 531–532.

12. Kiss, Z. J., Lewis, H. R., Duncan, R. C. (1963) Sun pumped continuous optical maser. *Appl. Phys. Lett.* **2**, 93-94.

13. Young, C. W. (1966) A sun-pumped cw one-watt laser. *Appl. Opt.* **5**, 993-997.

14. Schneider, R. T., Kurzweg, U. H., Cox, J. D., Weinstein, N. H. (1983) *Research on solar pumped liquid lasers.* NASA Technical Reports Server (NTRS).

15. Yesil, O., Christiansen, W. H. (1979) Optically pumped carbon dioxide laser mixtures. *J. Energy* **3**, 315–318.

16. Lee, J. H., Weaver, W. R. (1981) Solar-pumped gas laser. *IEEE J. Quantum Electron.* **17**, 2438–2440.

17. Insuik, R. J., Christiansen, W. H. (1984) Blackbody-Pumped CO2 Laser Experiment. *AIAA J.* **22**, 1271-1274.

18. DeYoung, R. J. (1986) Low Threshold Solar-Pumped Iodine Laser. *IEEE J. Quant. Electron.* **QE-22**, 1019-1023.

19. DeYoung, R. J., Weaver, W. R. (1986) Low-threshold solar-pumped laser using C2F5I. *Appl. Phys. Lett.* **49**, 369-370.

20. Overton, G. (December 2013) NOVEL LASERS: Solar-pumped Nd:YAG Lasers Getting Brighter. In: *LaserFocusWorld.* Available at: http://www.laserfocusworld.com/articles/print/volume-49/issue-12/world-news/novel-lasers-solar-pumped-nd-yag-lasers-getting-brighter.html

21. Arashi, H., Oka, Y., Sasahara, N., Kaimai, A., Ishigame, M. (1984) A solar-pumped cw 18 W Nd:yag laser. *Jpn. J. Appl. Phys.* **23**, 1051–1053.

22. Weksler, M., Shwartz, J. (1988) Solar-pumped solid-state lasers. *IEEE J. Quantum Electron.* **24**, 1222–1228.

23. Benmair, R. MJ., Kagan, J., Kalisky, Y., Noter, Y., Oron, M., Shimony, Y., Yogev, A. (1990) Solar-pumped Er, Tm Ho: YAG, Laser. *Opt. Lett.* **15**, 36–38.

24. Jenkins, D., Lando, M., O'Gallagher, J., Winston, R. (1996) A solar-pumped Nd:YAG laser with a record efficiency of 4.7 watt/m2. *Bulletin of Israel Physics Society* , 101.

25. Lando, M., Kagan, J., Linyekin, B., Dobrusin, V. (2003) A solar pumped Nd:yag laser in the high collection efficiency regime. *Opt. Commun.* **222**, 371–381.

26. Yabe, Y., Ohkubo, T., Uchida, S., Nakatsuka, M., Funatsu, T., Mabuti, A., Oyama, A., Nakagawa, Y., Oishi, T., Daito, K., Behgol, B., Nakayama, Y., Yoshida, M., Motokoshi, S., Sato, Y., Baasandash, C. (2007) High efficiency and economical solar energy pumped laser with Fresnel lens and chromium co-doped laser medium. *Appl. Phys. Lett.* **90**, 261120–261123.

27. Yabe, T., Suzuki, Y., Satoh, Y. (2014) Working prototype of magnesium batteries for cell phone and cars and magnesium recycling by lasers for renewable energy cycle. *Renewable Energy and Power Quality Journal (RE&PQJ)* **12**, 2172-038.

28. Oliveira, M., Liang, D., Almeida, J., Vistas, C. R., Gonçalves, F., Martins, R. (2016) A path to renewable Mg reduction from MgO by a continuous-wave Cr:Nd:YAG ceramic solar laser. *Sol. Energ. Mat. Sol. Cells* **155**, 430-435.

29. Liang, D., Almeida, J. (2011) Highly efficient solar-pumped Nd:YAG laser. *Opt. Express* **19**, 26399–26405.

30. Dinh, T. H., Ohkubo, T., Yabe, T., Kuboyama, H. (2012) 120 W continuous wave solar-pumped laser with a liquid light-guide lens and a Nd:YAG rod. *Opt. Lett.* **37**, 2670–2672.

31. Liang, D., Almeida, J., Vistas, C. R., Guillot, E. (2017) Solar-pumped Nd:YAG laser with 31.5 W/m2 multimode and 7.9 W/m2 TEM00-mode collection efficiencies. *Sol. Energ. Mat. Sol. Cells* **159**, 435–

439.

32. Jing, L., Liu, H., Wang, Y., Xu, W., Zhang, H., Lu, Z. (2014) Design and optimization of Fresnel lens for high concentration photovoltaic system. *Int. J. Photoenergy* **14**, 539891.

33. Almeida, J., Liang, D., Guillot, E., Abdel-Hadi, Y. (2013) A 40 W cw Nd:yag solar laser pumped through a heliostat: a parabolic mirror system. *Laser Phys.* **23**, 065801-065801.

34. Almeida, J., Liang, D., Vistas, C. R., Guillot, E. (2015) Highly efficient end-side-pumped Nd:YAG solar laser by a heliostat-parabolic mirror system. *Appl. Opt.* **54**, 1970–1977.

35. Liang, D., Almeida, J., Vistas, C. R. (2016) 25 W/m2 collection efficiency solar-pumped Nd:YAG laser by a heliostat - parabolic mirror system. *Appl. Opt.* **55**, 7712–7717.

36. Almeida, J., Liang, D., Guillot, E. (2012) Improvement in solar-pumped Nd:YAG laser beam brightness. *Opt. Laser Tech.* **44**, 2115-2119.

37. Liang, D., Almeida, J., Vistas, C. R., Guillot, E. (2015) Solar-pumped TEM00 mode Nd:YAG laser by a heliostat-parabolic mirror system. *Sol. Energy Mat. Sol. Cells* **134**, 305–308.

38. Almeida, J., Liang, D., Vistas, C. R., Bouadjemine, R., Guillot, E. (2015) 5.5W continuous-wave TEM00-mode Nd:YAG solar laser by a light guide/2V pump cavity. *Appl. Phys. B. - Lasers and Optics* **121**, 473-482.

39. Vistas, C. R., Liang, D., Almeida, J. (2015) Solar-pumped TEM00 mode laser simple design with a grooved Nd:YAG rod. *Sol. Energ.* **122**, 1325-1333.

40. Vistas, C. R., Liang, D., Almeida, J., Guillot, E. (2016) TEM00 mode Nd:YAG solar laser by side-pumping a grooved rod. *Opt. Commun.* **366**, 50-56.

41. Liang, D., Almeida, J., Vistas, C. R., Oliveira, M., Gonçalves, F., Guillot, E. (2016) High-efficiency solar-pumped TEM00 mode Nd:YAG laser. *Sol. Energy Mater. Sol. Cells* **145**, 397–402.

42. Liang, D., Almeida, J. (2013) Solar-pumped TEM00 mode Nd:YAG laser. *Opt. Express* **21**, 25107–25112.

43. Duocastella, M., Arnold, C. B. (2012) Bessel and annular beams for materials processing. *Laser Photonics Rev.* **6**, 607-621.

44. In: *Procédés, Matériaux et Énergie Solaire UPR 8521.* Available at: http://www.promes.cnrs.fr/index.php?page=mssf-horizontal

45. Bin, Z., Zhao, C., He, J., Yang, S. (2007) The study of active medium for solar-pumped solid-state lasers. *Acta Opt. Sin.* **27**, 1797-1801.

46. Reference Solar Spectral Irradiance: ASTM G-173. Available at: http://rredc.nrel.gov/solar/spectra/am1.5/astmg173/astmg173.html

47. Endo, M. (2010) Optical characteristics of Cr3+ and Nd3+codoped Y3Al5O12 ceramics. *Opt. & Laser Tech.* **42**, 610–616.

48. Koechner, W. (1999) *Solid-state laser engineering*. Springer, Berlin.

49. In: *RPphotonics.* Available at: http://www.rp-photonics.com

50. Magni, V. (1986) Resonators for solid-state lasers with large-volume fundamental mode and high alignment stability. *Appl. Opt.* **16**, 107–117.

51. Feng, Y., Bi, Y., Xu, Z., Zhang, G. (2003) Thermally near-unstable cavity design for solidstate lasers. *Proc. SPIE* **4969**, 227–232.

52. Welford, D., Rines, D. M., Dinerman, B. J. (1991) Efficient, TEM00-mode operation of a laser-diode side-pumped Nd:YAG laser. *Opt. Lett.* **16**, 1850–1852.

53. Almeida, J., Liang, D. (2014) Design of TEM00 mode side-pumped Nd:YAG solar laser. *Opt. Commun.* **333**, 219-225.

54. Liang, D., Almeida, J., Vistas, CR. (2014) Scalable pumping approach for extracting the maximum TEM00 solar laser power. *Appl. Opt.* **53**, 7129-7137.

55. Lando, M., Jenkins, D. G., Bernstein, H., O' Gallagher, J. J., Winston, R., Lewandowski, A. (1995) High-brightnesssolar-pumped Nd:YAG laser design. *Proc. SPIE* **2426**, 478 – 490.

56. Liang, D., Almeida, J., Guillot, E. (2013) Side-pumped continuous-wave Cr:Nd:YAG ceramic solar laser. *Appl. Phys. B. - Lasers and Optics* **111**, 305-311.

57. Yagi, H., Yanagitani, T., Yoshida, H., Nakatsuka, M., Ueda, K. (2006) Highly efficient flashlamp-pumped Cr3+ and Nd3+Codoped Y3 Al5 O12 ceramic laser. *Jpn. J. Appl. Phys.* **45**, 133–135.

58. Walling, J. C., Jenssen, H. P., Morris, R. C., O´Dell, E. W., Peterson, O. G. (1979) Tunable-laser performance in BeAl2O4:Cr3+. *Opt. Lett.* **4**, 182-183.

59. Walling, J. C., Peterson, O. G., Jenssen, H. P., Morris, R. C., O´Dell, E. W. (1980) Tunable Alexandrite lasers. *IEEE J. Quantum Electron.* **16**, 1302 - 1315.

60. Walling, J. C., Heller, D. F., Samelson, H., Harter, D. J., Pete, J. A., Morris, R. C. (1985) Tunable Alexandrite lasers: development and performance. *IEEE J. Quantum Electron.* **21**, 1568 - 1581.

61. Weber, M. J., Milam, D., Smith, W. L. (1978) Nonlinear refractive index of Glasses and Crystals. *Opt. Engineering* **17**, 463.

62. Kuper, J. W., Chin, T., Aschoff, H. E. (1990) Extended tuning range of Alexandrite at Elevated Temperatures. *Proc Advanced Solid State Lasers (OSA)* **6**, paper CL3.

63. Torizuka, K., Yamashita, M., Yabiku, T. (1993) Continuous-wave alexandrite laser-pumped by a direct-current mercury arc lamp. *Appl. Opt.* **32**, 7394–7398.

64. Scheps, R., Myers, J. F., Glesne, T. R., Serreze, H. B. (1993) Monochromatic end-pumped operation of an alexandrite laser. *Opt. Commun.* **97**, 363–366.

65. Peng, X., Marrakchi, A., Walling, J. C., Heller, D. F. (2005) Watt-level red and UV output from a CW

diode array- pumped tunable alexandrite laser. *Conference on Lasers and Electro-Optics (OSA)*, paper CMAA5.

66. Beyatli, B., Baali, I., Sumpf, B., Erbert, G., Leitenstorfer, A., Sennaroglu, A., Demirbas, U. (2013) Tapered diode-pumped continuous-wave alexandrite laser. *J.Opt. Soc. Am. B* **30**, 3184 - 3192.

67. Teppitaksak, A., Minassian, A., Thomas, G. M., Damzen, M. J. (2014) High efficiency >26W diode end-pumped alexandrite laser. *Opt Express* **22**, 16386-16392.

68. Lando, M., Shimony, Y., Benmair, R. MJ., Abramovich, D., Krupkin, V., Yogev, A. (1999) Visible solar-pumped lasers. *Opt. Mater.* **13**, 111–115.

69. Hwang, I. H., Lee, J. H. (1991) Efficiency and threshold pump intensity of cw solar-pumped solid-state lasers. *Opt. Mater.* **13**, 111–115.

70. Noter, Y., Oron, M., Shwartz, J., Weksler, M., Yogev, A. (1988) Solar-pumped Nd:Cr: GSGG laser. *SPIE* **1038**.

71. Endo, M. (2007) Feasibility study of a conical-toroidal mirror resonator for solar-pumped thin-disk lasers. *Opt. Express* **15**, 5482-5493.

72. Liang, D., Almeida, J., Garcia, D. (2013) Comparative study of Cr:Nd:YAG and Nd:YAG solar laser performances. *Proc. SPIE* **8785**.

73. Liang, D., Almeida, J. (2012) Design of ultra-high brightness solar-pumped disk laser. *Appl. Opt.* **51**, 6382-6388.

74. Giesen, A., Hügel, H., Voss, A., Wittig, K., Brauch, U., Opower, H. (1994) Scalable concept for diode-pumped high-power solid-state lasers. *Appl. Phys. B* **58**, 365–372.

75. Giesen, A., Speiser, J. (2007) Fifteen years of work on thin-disk lasers: results and scaling laws. *IEEE J. Sel. Top. Quantum Electron.* **13**, 598 – 609.

76. Kuzmin, A. N. (September 2012) *Design of ultrahigh brightness solar-pumped disk laser.* Spotlight on Optics.

77. Mizuno, S., Ito, H., Hasegawa, K., Suzuki, T., Ohishi, Y. (2012) Laser emission from a solar-pumped fiber. *Opt. Express* **20**, 5891-5896.

78. (2014) Side-pumped continuous-wave Cr:Nd:YAG ceramic solar laser. In: *Renewable Energy global innovations.* Available at: [https://reginnovations.org/key-scientific-articles/side-pumped-continuous-wave-crndyag-ceramic-solar-laser/](https://reginnovations.org/key-scientific-articles/side-pumped-continuous-wave-crndyag-ceramic-solar-laser/)

79. (2013) *Novel Laser Materials and Lasers.* Highlights of 2013 - Laser Physics - IOPscience.

80. Xu, P., Yang, S., Zhao, C., Guan, Z., Wang, H., Zhang, Y., Zhang, H., He, T. (2014) High-efficiency solar-pumped laser with a grooved Nd:YAG rod. *Appl. Opt.* **53**, 3941–3944.

81. Reusswig, P. D., Nechayev, S., Scherer, J. M., Hwang, G. W., Bawendi, M. G., Baldo, M. A., Rotschild, C. (2015) A path to practical Solar Pumped Lasers via Radiative Energy Transfer. *Nature Scientific Reports*

**5**, 1-6.

82. Quarterman, A. H., Wilcox, K. G. (2015) Design of a solar-pumped semiconductor laser. *Optica* **2**, 56-61.

83. Heinen, B., Wang, T. L., Sparenberg, M., Weber, A., Kunert, B., Hader, J., Koch, S. W., Moloney, J. V., Koch, M., Stolz, W. (2012) 106 W continuous-wave output power from vertical-external-cavitysurface-emitting lase.. *Electron. Lett.* **48**, 516 – 517.

84. Khiar, A., Rahim, M., Fill, M., Felder, F., Hobrecker, F., Zogg, H. (2010) Continuously tunable monomode mid-infrared vertical external cavity surface emitting laser on Si. *Appl. Phys. Lett.* **97**, 151104.

85. Landis, G. A. (1992) New approaches for a solar-pumped GaAs laser. *Opt. Commun.* **92** , 261 – 265.

86. Tsidulko, I. M. (1992) Semiconductor laser pumped by solar radiation. *Sov. J. Quantum Electron.* **22**, 463 – 466.

87. Payziyev, S., Makhmudov, K. (2016) Solar pumped Nd:YAG laser efficiency enhancement using Cr:LiCAF frequency down-shifter. *Opt. Commun.* **380**, 57–60.

88. (October 2016) Most efficient continuous-wave 1064nm solar laser emission within a laboratory. In: *Renewable Energy Global Innovations.* Available at: https://reginnovations.org/key-scientific-articles/most-efficient-continuous-wave-1064nm-solar-laser-emission-laboratory/

89. (December 2016) New Breaks: 1064 nm solar laser achieves record power output and efficiency. In: *LaserFocusWorld.* Available at: http://www.laserfocusworld.com/articles/print/volume-52/issue-12/newsbreaks/1064-nm-solar-laser-achieves-record-power-output-and-efficiency.html

90. Bouadjemine, R., Liang, D., Almeida, J., Mehellou, S., Vistas, C. R., Kellou, A., Guillot, E. (2016) Stable TEM00-mode Nd:YAG solar laser operation by a twisted fused silica light-guide. *Opt. Laser Tech.* **97**, 1-11.

91. Mehellou, S., Liang, D., Almeida, J., Bouajmine, R., Vistas, C. R., Guillot, E., Rehouma, F. (2017) Stable solar-pumped TEM00-mode 1064nm laser emission by a monolithic fused silica twisted light guide. *Sol. Energy* **155**, 1059-1071.

92. Masuda, T., Iyoda, M., Yasumatsu, Y., Endo, M. (2017) Low-concentrated solar-pumped laser via transverse-excitation fiber-laser geometry. *Opt. Lett.* **42**, 3427-3430.

93. Saiki, T., Fujiwara, N., Matsuoka, N., Nakatuka, M., Fujioka, K., Iida, Y. (2017) Amplification properties of KW Nd/Cr:YAG ceramic multi-stage active-mirror laser using white-light pump source at high temperatures. *Opt. Commun.* **387**, 316–321.

94. Guan, Z., Zhao, C., Yang, S., Wang, Y., Ke, J., Gao, F., Zhang, H. (2016) Low-threshold and high-efficiency solar-pumped laser with Fresnel lens and a grooved Nd:YAG rod. *Proc. of SPIE* **10016** , 1001609-9.

95. Dihn, T. H., Ohkubo, T., Yabe, T. (2014) Development of solar concentrators for high-power solar-pumped lasers. *Appl. Opt.* **53**, 2711 - 2719.

96. Garg, H. P., Prakash, J. (2000) *Solar energy: fundamentals and applications.* Tata McGraw-Hill

Publishing Company Limited, New Delhi.

97. Xie, W. T., Dai, Y. J., Wang, R. Z., Sumathy, K. (2011) Concentrated solar energy applications using Fresnel lenses: A review. *Renewable and Sustainable Energy Reviews* **15**, 2588–2606.

98. (2012) *Standard tables for reference solar spectral irradiances: direct normal, and hemispherical on 37° tilted surface.* ASTM Standard G173-03.

99. *||, The FEA Code of LASCAD.* LAS-CAD GmbH, Brunhildenstrasse 9 D-80639 Munich, Germany.

100. *||, Computation of Laser Power Output for CW Operation.* LAS-CAD GmbH, Brunhildenstrasse9 D-80639 Munich, Germany.

101. *LASCAD - The Laser Engineering Tool.* LAS-CAD GmbH.

102. Fox, A. G., Li, T. (1960) Resonant modes in a maser interferometer. *Bell.Sys.Tech.* **40**, 453-488.

103. Bernardes, P. H., Liang, D. (2006) Solid-state laser pumping by light guides. *Appl. Opt.* **45**, 3811-3817.

104. Welford, W. T., Winston, R. (1989) *High Collection Nonimaging Optics*. Academic Press, New York.

105. Jafrancesco, D., Sani, E., Fontani, D., Mercatelli, L., Sansoni, P., Giannini, A., Francini, F. (2012) Simple Methods to Approximate CPC Shape to Preserve Collection Efficiency. *Int. J. Photoenergy* **2012**, 863654-863661.

106. Clarkson, W. A. (2001) Thermal effects and their mitigation in end-pumped solid-state lasers. *J. Phys. D: Appl. Phys.* **34**, 2381-2395.

107. Weber, R., Neuenschwander, B., Mac Donald, M., Roos, M. B., Weber, H. P. (1998) Cooling schemes for longitudinally diode laser-pumped Nd:YAG rods. *IEEE J. Quantum Electron.* **34**, 1046-1053.

108. Fan, T. Y. (1993) Heat generation in Nd:YAG and Yb:YAG. *IEEE J. Quantum Electron.* **29**, 1457 - 1459.

109. Tsunekane, M., Taguchi, N., Kasamatsu, T., Inaba, H. (1997) Analytical and experimental studies on the characteristics of composite solid-state laser rods in diode-end-pumped geometry. *IEEE J. Select. Topics Quantum Electron.* **3**, 9 - 18.

110. Liang, D., Bernardes, P., Martins, R. (2005) Sun-pumped Nd:YAG laser with excellent tracking error compensation capacit. *Technical Digest Series of CLEO/Europe-EQEC* **29 B**, CA7-5-TUE.

111. Brand, T. (1995) Compact 170-W continuous-wave diode-pumped Nd:YAG rod laser with a cusp-shaped reflector. *Opt. Lett.* **20**, 1776-1778.

112. Kaneda, Y., Oka, M., Masuda, H., Kubota, S. (1992) 7.6 W of continuous-wave radiation in a TEM00 mode from a laser-diode end-pumped Nd:YAG laser. *Opt. Lett.* **17**, 1003-1005.

113. Ma, J., Duanmu, Q., Wang, G., Qiao, Z. Diode-side-pumped TEM00 mode Nd:YAG laser with plane-convex resonator. *Proc. SPIE* **7276** , 72761Q-1.

114. Hanna, D. C., Sawyers, C. G., Yuratich, M. A. (1981) Large volume TEM00 mode operation of Nd:YAG

lasers. *Opt. Commun.* **37**, 359-362.

115. Yang, H. (2002) 41 W cw TEM00 (M2 = 1.2) 1064 nm beam generation from a diode-side-pumped Nd:YAG laser by use of a dual-telescopic optics configuration. *Opt. Commun.* **204**, 263–266.

116. Hirano, Y., Koyata, Y., Yamamoto, S., Kasahara, K., Tajime, T. (1999) 208-W TEM 00 operation of a diode-pumped Nd:YAG rod laser. *Opt. Lett.* **24**, 679-681.

117. Lee, S. (2003) A Compact Asymmetric TEM00-Mode Resonator with a Single Negative Lens. *J. Kor. Phys. Soc.* **43**, 507-512.

118. Geraldes, J. P., Liang, D. (2008) An alternative solar pumping approach by a light guide assembly elliptical-cylindrical cavity., 836-843.

119. Pereira, R., Liang, D. (2009) Maximizing TEM 00 solar laser power by a light guide assembly-elliptical cavity. *Opt. Laser Tech.* **41**, 687-692.

120. Liang, D., Pereira, R. (2009) High conversion efficiency solar laser pumping by a light-guide/2D-CPC cavity. *Opt. Commun.* **(282)**, 1385-1392.

121. Almeida, J., Liang, D. (2012) Design of a high brightness solar-pumped laser by light-guides. *Opt. Commun.* **285**, 5327-5333.

122. Prakash, O., Astadjov, D. N., Kumar, P., Mahakud, R., Kumar, J., Nakhe, S. V., Dixit, S. K. (2013) Effect of spatial coherence on the focusability of annular laser beams. *Opt. Commun.* **290**, 1 – 7.

123. (December 2007) Donut-shaped beam could trap particles. In: *LaserFocusWorld.* Available at: http://www.laserfocusworld.com/articles/print/volume-43/issue-12/newsbreaks/donut-shaped-beam-could-trap-particles.html

124. Chu, SC., Ohtomo, T., Otsuka, K. (2008) Generation of doughnutlike vortex beam with tunable orbital angular momentum with controlled Hermite-Gaussian modes. *Appl. Opt.* **47**, 2583 – 2591.

125. Cherezova, T. Y., Chesnokov, S. S., Kaptsov, L. N., Kudryashov, A. V. (1998) Doughnut-like laser beam output formation by intracavity flexible controlled mirror. *Opt. Express* **3**, 180 – 189.

126. Okida, M., Hayashi, Y., Omatsu, T., Morita, R. (2009) Characterization of 1.06 μm optical vortex laser based on a side-pumped Nd: GdVO4 bounce oscillator. *Appl. Phys. B* **95**, 69 – 73.

127. Almeida, J., Liang, D., Garcia, D. (2013) Comparative study of Nd:YAG solar laser performance in end-pumping and side-pumping configurations. *Lasers and Electro-Optics Europe (CLEO EUROPE/IQEC)*.

128. Nechayev, S., Rotschild, C. (2017) Detailed Balance Limit of Efficiency of Broadband-Pumped Lasers. *Nature Scientific Reports* **7**, 1-6.

129. Saiki, T., Nakatsuka, M., Fujioka, K., Motokoshi, S., Imasaki, K. (2011) Cross-relaxation and spectral broadening of gain for Nd/Cr:YAG ceramic lasers with white-light pump source under high-temperature operation. *Opt. Commun.* **284**, 2980-2984.

130. Calvez, S., Hastie, J. E., Guina, M., Okhotnikov, O. G., Dawson, M. D. (2009) Semiconductor disk lasers

for the generation of visibleand ultraviolet radiation. *Laser Photon. Rev.* **3**, 407 – 434.

131. Wang, TL., Kaneda, Y., Yarborough, J. M., Hader, J., Moloney, J. V., Chernikov, A., Chatterjee, S., Koch, S. W., Kunert, B., Stolz, W. (2010) High-power optically pumped semiconductor laser at 1040 nm. *IEEE Photon. Technol. Lett.* **22**, 661 – 663.

# ANNEXES

## HIGHLIGHTS DURING THE PHD PROJECT (2013-2017)

Overton, G. (December **2016**) *1064 nm solar laser achieves record power output and efficiency.* Laser Focus World.
http://www.laserfocusworld.com/articles/print/volume-52/issue-12/newsbreaks/1064-nm-solar-laser-achieves-record-power-output-and-efficiency.html

Reference: D. Liang, D., <u>Almeida</u>, J., Vistas, C. R., Guillot, E. (2017) Solar-pumped NdYAG laser with 31.5 $W/m^2$ multimode and 7.9 $W/m^2$ $TEM_{00}$-mode collection efficiencies. *Sol. Energ. Mat. Sol. Cells* **159**

(October **2016**) *Most efficient continuous-wave 1064nm solar laser emission within a laboratory.* Renewable Energy Global Innovations
https://reginnovations.org/key-scientific-articles/most-efficient-continuous-wave-1064nm-solar-laser-emission-laboratory/

Reference: D. Liang, D., <u>Almeida</u>, J., Vistas, C. R., Guillot, E. (2017) Solar-pumped NdYAG laser with 31.5 $W/m^2$ multimode and 7.9 $W/m^2$ $TEM_{00}$-mode collection efficiencies. *Sol. Energ. Mat. Sol. Cells* **159**
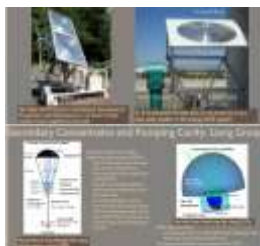
(October **2014**) *Towards Megawatt Solar Powered Lasers for Magnesium Production and future space applications*, Nextbigfuture
https://www.nextbigfuture.com/2014/10/solar-powered-lasers-for-magnesium.html
References: Liang, D, Almeida, J. (2011)Highly efficient solar-pumped Nd:YAG laser. *Opt. Express* **19** and Liang, D., Almeida, J. (2013) Solar-pumped $TEM_{00}$ mode Nd:YAG laser. *Opt. Express* **21**

Liang, D., <u>Almeida, J</u>., Guillot, E. (2013) Side-pumped continuous-wave Cr:Nd:YAG ceramic solar laser. *Appl. Phys. B - Lasers and Optics* **111** was selected by Renewable Energy Global Innovations as a Key Scientific Article (February **2014**).
https://reginnovations.org/key-scientific-articles/side-pumped-continuous-wave-crndyag-ceramic-solar-laser/
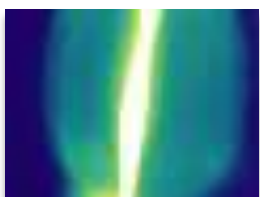
Almeida, J., Liang, D., Guillot, E., Abdel-Hadi, Y. (2013) A 40 W cw Nd:YAG solar laser pumped through a heliostat: a parabolic mirror system. *Laser Phys.* **23** was featured Laser Physics Highlights in (**2013**).
http://iopscience.iop.org/journal/1555-6611/page/Highlights-of-2013

Overton, G. (December **2013**) *Novel Lasers: Solar-Pumped Nd:YAG Lasers Getting Brighter.* Laser Focus World
http://www.laserfocusworld.com/articles/print/volume-49/issue-12/world-news/novel-lasers-solar-pumped-nd-yag-lasers-getting-brighter.html

Reference: Liang, D., Almeida, J. (2013) Solar-pumped $TEM_{00}$ mode Nd:YAG laser. *Opt. Express* **21**
Shared in Photonics Online and Photonics Solutions (December **2013**).
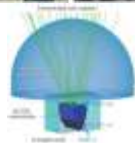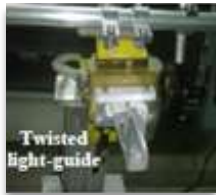
## PUBLICATIONS DURING THE PHD PROJECT (2013 -2017)

**In Peer-reviewed Journals:**

I. Mehellou, S., Liang, D., <u>Almeida, J.</u>, Bouadjemine, R., Vistas, C. R., Guillot, E., Rehouma, F. (2017) Stable solar-pumped $TEM_{00}$-mode 1064 nm laser emission by a monolithic fused silica twisted light guide. *Sol. Energ.* **155**, 1059-1071. doi:10.1016/j.solener.2017.07.048



II. Bouadjemine, R., Liang, D., <u>Almeida, J.</u>, Mehellou, S., Vistas, C. R., Kellou, A., Guillot, E.,(2017) Stable $TEM_{00}$-mode Nd:YAG solar laser operation by a twisted fused silica light-guide. *Opt. Laser Tech.* **97**, 1-11. doi:10.1016/j.optlastec.2017.06.003



III. Liang, D., <u>Almeida, J.</u>, Vistas, C. R., Guillot, E.(2017) Solar-pumped NdYAG laser with 31.5 $W/m^2$ multimode and 7.9 $W/m^2$ $TEM_{00}$-mode collection efficiencies. *Sol. Energ Mat. Sol. Cells* **159**, 435-439. doi:10.1016/j.solmat.2016.09.048



IV. Liang, D., <u>Almeida, J.</u> Vistas, C. R. (2016) 25 $W/m^2$ collection efficiency solar-pumped Nd:YAG laser by a heliostat-parabolic mirror system. *Appl. Opt.* **55**, 7712-7717. doi:10.1364/AO.55.007712
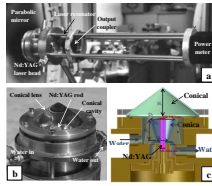


V Vistas, C. R., Liang, D., <u>Almeida, J.</u>, Guillot, E. (2016) $TEM_{00}$ mode Nd:YAG solar laser by side-pumping a grooved rod. *Opt Commun.* **366**, 50-56.doi:10.1016/j.optcom.2015.12.038



VI. Liang, D., <u>Almeida, J.</u>, Vistas, C. R., Oliveira, M., Gonçalves, F.,Guillot, E.(2016)High-efficiency solar-pumped $TEM_{00}$-mode Nd:YAGLaser. *Sol. Energ Mat. Sol. Cells* **145**, 397-402. doi:10.1016/j.solmat.2015.11.001
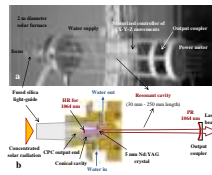


VII. <u>Almeida, J.</u>, Liang, D., Vistas, C. R., Bouadjemine, R., Guillot, E. (2015) 5.5 W continuous-wave $TEM_{00}$-mode Nd:YAG solar laser by a light guide / 2V pump cavity. *Appl. Phys. B - Lasers and Optics* **121**, 473-482. doi:10.1007/s00340-015-6257-z

VIII .     Almeida, J., Liang, D., Vistas, C. R., Guillot, E. (2015) Highly efficient end-side-pumped Nd:YAG solar laser by a heliostat-parabolic mirror system. *Appl. Opt.* **54**, 1970-1977. doi: 10.1364/AO.54.001970
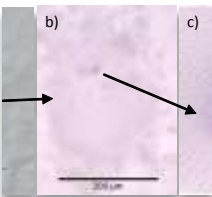


IX.     Liang, D., Almeida, J., Vistas, C. R., Guillot, E. (2015) Solar-pumped $TEM_{00}$ mode Nd:YAG laser by a heliostat-parabolic mirror system. *Sol. Energ. Mat. Sol. Cells* **134**, 305-308. doi:10.1016/j.solmat.2014.12.015



X     Almeida, J., Liang, D., Guillot, E., Hadi, Y. (2013) A 40W cw Nd:YAG solar laser pumped through a heliostat: a parabolic mirror system. *Laser Phys.* **23**, 065801. doi:10.1088/1054-660X/23/6/065801
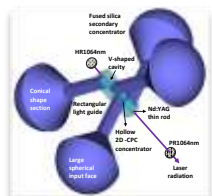


XI.     Liang, D., Almeida, J. (2013) Solar-pumped $TEM_{00}$ mode Nd:YAG laser. *Opt. Express* **21**, 25107–25112.
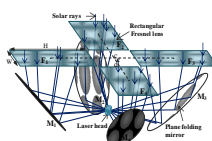
doi: 10.1364/OE.21.025107



XII.     Oliveira, M., Liang, D., Almeida, J., Vistas, C. R., Gonçalves, F., Martins, R. (2016) A path to renewable Mg reduction from MgO by a continuous-wave Cr:Nd:YAG ceramic solar laser. *Sol. Energ Mat. Sol. Cells* **155**, 430-435 doi:10.1016/j.solmat.2016.06.046
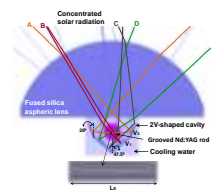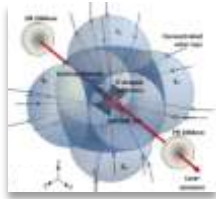


XIII.     Vistas, C. R., Liang, D., Almeida, J. (2015) Solar-pumped $TEM_{00}$ mode laser simple design with a grooved Nd:YAG rod. *Sol. Energ.* **122**, 1325-1333. doi:10.1016/j.solener.2015.10.049



XIV.     Liang, D., Almeida, J., Vistas, C. R.(2014)Scalable pumping approach for extracting the maximum $TEM_{00}$ solar laser power. *Appl. Opt.* **53**, 7129-7137. doi:10.1364/AO.53.007129
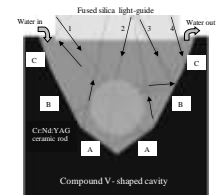


XV.     Almeida, J., Liang, D. (2014) Design of $TEM_{00}$ mode side-pumped Nd:YAG solar laser. *Opt. Commun.* .**333**, 219 225. doi:10.1016/j.optcom.2014.07.091

XVI. Liang, D., Almeida, J., Garcia, D. (2014) Design of high-power, high-brightness Nd:YAG solar laser. *Appl. Opt.* **53**, 1856-1861. doi: 10.1364/AO.53.001856



XVII. Liang, D., Almeida, J. (2013)Multi Fresnel lenses pumping approach for improving high-power Nd:YAG solar laser beam quality. *Appl. Opt.***52**, 5123-5132 doi:10.1364/AO.52.005123



XVIII. Liang, D., Almeida, J., Guillot, E. (2013) Side-pumped continuous-wave Cr:Nd:YAG ceramic solar laser. *Appl. Phys. B - Lasers and Optics***111**, 305-311. doi:10.1007/s00340-013-5334-4

**In conference proceedings:**

I. Almeida, J. Liang, D. (2017)  Recent advances in solar-pumped lasers. *2nd Doctoral Congress in Engineering* (DCE) poster #249.

II. Almeida, J., Liang, D., Vistas, C. R., Guillot, E. (2015) 56W cw Nd:YAG solar laser by a heliostat-parabolic mirror system.*2015 European Conference on Lasers and Electro-Optics - European Quantum Electronics Conference* (OSA), paper CA_11_6.

III. Vistas, C. R., Liang, D. Almeida, J.(2015) Renewable forsterite production by a solar furnace*. European Conference on Lasers and Electro-Optics - European Quantum Electronics Conference (OSA),* paper CE_P_26.

IV. Liang, D., Almeida, J., Oliveira, M., Gonçalves, F., Vistas, C. R. (27-28th April 2015)Advances in high-efficiency TEM$_{00}$-mode solar-pumped laser. *Workshop on Laser Solutions for Orbital Space Debris, Paris, France*.

V. Almeida, J., Liang, D., Oliveira, M., Gonçalves, F., Vistas, C. R. (27-28th April 2015)Progress in solar-pumped laser efficiency by heliostat-parabolic mirror system. *Workshop on Laser Solutions for Orbital Space Debris, Paris, France*.

VI. Liang, D., Almeida, J.(2014) Design of high-brightness TEM$_{00}$-mode solar-pumped laser for renewable material processing. *Proc. SPIE* **9286**. doi:10.1364/AO.53.001856

VII. Almeida, J., Liang, D.(2014)High-power high-brightness solar laser approach for renewable Mg recovery from MgO. *Proc. SPIE* **9286**, 2nd International Conference on Applications of Optics and Photonics. doi:10.1117/12.2063442

VIII. Garcia, D., Liang, D., Almeida, J. Core-doped Nd:YAG disk solar laser uniformly pumped  by six Fresnel lenses. *Proc. SPIE***8785**, 8th Ibero american Optics Meeting and 11th Latin American Meeting on Optics, Lasers, and Applications doi:10.1117/12.2030434

IX. Tomás, G., Liang, D., Almeida, J. (2013). Side-pumping Nd:YAG solar laser by six

Fresnel lenses. *Proc. SPIE* **8785**, 8th Ibero american Optics Meeting and 11th Latin American Meeting on Optics, Lasers, and Applications. doi:10.1117/12.2026082

X.   Liang, D., Almeida, J., Garcia, D. (2013) Comparative study of Cr:Nd:YAG and Nd:YAG solar laser performances. *Proc. SPIE* **8785** doi:10.1117/12.2027673

XI.   Almeida, J., Liang, D., Garcia, D. (2013) Comparative study of Nd:YAG solar laser performance in end-pumping and side-pumping configurations. *Conference on Lasers and Electro-Optics - International Quantum Electronics Conference (OSA)*, paper CA_P_19 doi:10.1109/CLEOE-IQEC.2013.6800658